Prototype Development and Simulation of the Cosmic-Ray Electron Synchrotron Telescope (CREST)

by

Atsushi Yagi

A dissertation submitted in partial fulfillment
of the requirements for the degree of
Doctor of Philosophy
(Physics)
in The University of Michigan
2009

Doctoral Committee:

Professor Gregory Tarlé, Chair
Professor Fred Adams
Professor Carl W. Akerlof
Professor Fred D. Becchetti
Professor Joel N. Bregman

To my family and Porscha L. McRobbie

ACKNOWLEDGEMENTS

It was great enjoyment and pleasure to spend my graduate study at the University of Michigan, Ann Arbor. It would not be possible without everybody who supported the completion of my Ph.D.

I would like to thank my family for financially and mentally supporting me to come to the United States in order to pursue my education and career over a decade and my friends from all over the world who stimulated me throughout my school years even though their area of expertise might be quite different. Lastly, I want to thank Porscha L. McRobbie for spending precious time with me and bringing excitement in my life.

I would like to thank all the people in the CREST collaboration. I want to thank my adviser, Greg Tarlé, for insightful advice and assistance. Also, I want to thank Mike Schubnell, and Jon Ameel from the University of Michigan for helping me to understand technical hardware and software details. I want to thank Jim Musser, Chuck Bower, and Mark Gebhard for my stay at Indiana University for the CREST-I flight and frequent visits. I want to thank Scott Nutter from Northern Kentucky University, Stéphane Coutu, T. Anderson., and M. Geske from Pennsylvania State University, Dietrich Müller, Scott Wakely, A. Martell, R. Northrop, N. Park, and C. Smith from the University of Chicago, B. Ball and A. Tomasch from the University of Michigan, Micheal DuVernois and T. Childers from the University of Minnesota for all the aspects of the CREST project.

TABLE OF CONTENTS

CHAPTER

LIST OF TABLES

Table

LIST OF FIGURES

Figure

LIST OF APPENDICES

Appendix

CHAPTER I

Introduction

1.1 Introduction

The electron components (e^- and e^+) of cosmic rays (CRs), distinguished by their low mass and leptonic nature, are relatively rare. Their intensities are approximately one percent of the CR proton intensity at GeV energies. While it is still not fully understood why there are so few of them in CRs, the origins of CR electrons and CR positrons are becoming increasingly apparent from direct measurements [1]. At energies greater than a few GeV, it is believed that CR electrons are accelerated from supernova remnants (SNRs), while CR positrons are mostly secondary products of charged pions interacting with the interstellar medium (ISM).

CR electrons with energies greater than 3 TeV have never been detected directly at Earth, although there is strong indirect evidence for their existence [2] from non-thermal X-ray emissions from high energy electrons observed in a number of SNRs. Detecting these high energy CR electrons at Earth would yield significant physical information regarding their sources, their acceleration and propagation. Compared with CR nuclei, which are the dominant components in the ISM, high energy CR electrons are suppressed because of rapid energy loss due to synchrotron radiation in the galactic magnetic field and inverse Compton scattering with the background radiation. As a result of these energy loss processes, a 1 TeV CR electron, for instance, must have originated within 1 kpc to be detected at the Earth. If supernova shocks are responsible for cosmic ray acceleration, they produce the observed power law spectrum, and only a few known SNRs within 1 kpc from the Earth can generate high energy CR electrons. Consequently, the features of the high energy CR electron spectrum depend on the distribution of nearby SNRs.

Unlike most CR electrons that are primary in origin, most CR positrons are generally attributed to secondary production in the Galaxy, mostly from $\mathrm{p}-\mathrm{p}$ hadronic interactions that lead to π^+ generation. Although the CR positron component of all CR electrons is approximately 10 percent at a few GeV, their percentage should decrease monotonically at higher energies. A number of experiments (HEAT [3], AMS [4], and PAMELA [5]) have observed deviations from this indicating the possibility of additional primary contributions to the positron, and this is a subject of ongoing research [3].

1.2 CREST Overview

The Cosmic Ray Electron Synchrotron Radiation Telescope (CREST) is a balloon payload designed to measure the flux of primary CR electrons at energies greater than 2 TeV. The CREST detector concept is presented in Figure 1.1. The CREST instrument detects primary electrons indirectly through observation of the synchrotron radiation generated by these electrons in the Earth's magnetic field. This technique has previously been suggested [6], but has never been fully exploited. By this method, CREST will be able to obtain a much larger effective detector area, since the detector samples only a portion of the line of synchrotron radiation. In contrast, the previous direct measurements were limited by small physical detector areas. The

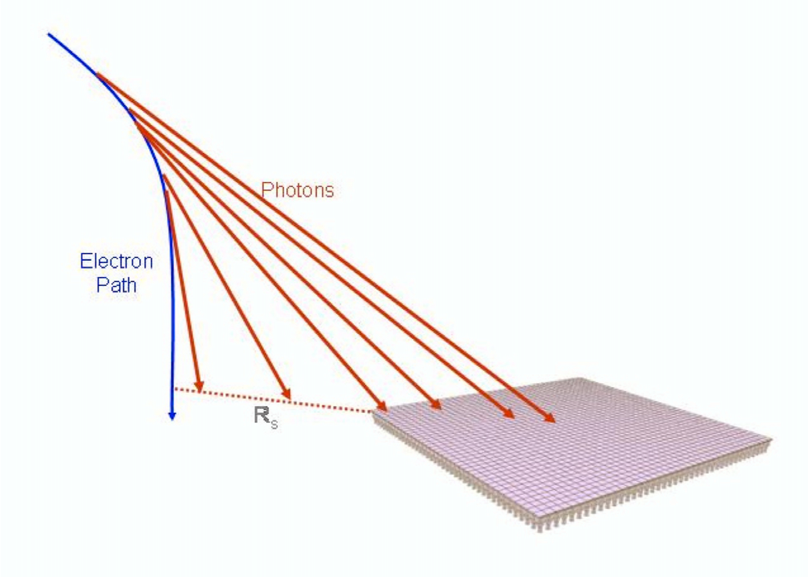

Figure 1.1: CREST indirect detection concept

effective aperture of the CREST instrument is determined by the spatial extent of the synchrotron photons, not by the physical size of the instrument. At the same time, the separation between real and background X-ray events requires knowledge of two characteristics of synchrotron radiation. These are the formation of a line of synchrotron photons at the detector and the very short time intervals over which these photons are detected. Consequently, the CREST instrument was proposed to be a spatially segmented detector with good timing resolution.

The CREST project has three phases: CREST-I (Ft. Sumner, NM in Fall 2005) is a prototype array of 96 BGO and BaF_2 crystals that was used to validate the technique and to measure the X/γ ray background. CREST-II (Spring 2009) will be flown with a smaller array of 64 BaF_2 crystals and improved electronics similar to that which we will utilize in Antarctica. The full detector, Antarctic CREST (Winter 2010-2011, Antarctica), will be a long duration instrument with a 1024 BaF_2 crystal array.

A summary of my work on the CREST project is as follows:

Year: 2004-5

- Photomultiplier tubes/BGO selection, development and testing
- Development of improved BaF_2 detectors and wave-shifter
- CREST-I flight

Year: 2006

- CREST-I flight data analysis
- Study of high energy cosmic ray electrons
- Discriminator board evaluation and testing

Year: 2007-8

- Study of synchrotron radiation and CREST detector simulation via GEANT4

1.3 Organization of the thesis

This thesis is organized as follows:

Chapter 2 presents a brief introduction to cosmic rays, theoretical aspects of high energy cosmic ray electrons, and characteristics of synchrotron radiation from those high energy CR electrons. First, the historical significance of cosmic rays and an overview of cosmic ray research are presented. Next, for high energy electrons, widely accepted theories of sources of cosmic ray electrons, the process of electron acceleration by these sources and the propagation from those sources to the Earth are discussed. Based on these processes, a few theoretical predictions for the differential flux of electrons from nearby SNRs are shown. Basic formulas of synchrotron radiation are also shown for reference.

Chapter 3 presents discussions on designing of the CREST instrument and estimations of one dimensional effective width and the number of synchrotron photons.

Chapter 4 introduces the main components of the full size Antarctic CREST detector, and discusses the crystal/photomultiplier tube (PMT) assembly, which was initially developed and tested by me at the University of Michigan. Among different inorganic crystals, BGO and BaF_2 were chosen for CREST-I due to their availability, decay time, energy resolution, and price. Similarly, the PMTs were chosen from different vendors based on their gain, noise, timing resolution, and most importantly vacuum survivability. After the first CREST flight (CREST-I), improvement and modification of the assembly was transfered to our collaborators at Indiana University for CREST-II and the Antarctic CREST instruments.

Chapter 5 shows performance and results for the CREST-I flight. CREST-I is a smaller detector, and its main purpose was to measure diffuse and atmospheric X/γ ray background at flight altitude. Previous and current observations on diffuse and atmospheric X/γ ray are presented for comparison. Testing of the crystal/PMT assembly performance and electronics functionality under near vacuum were critical objectives for this flight.

Chapter 6 presents GEANT4 simulation results of an Antarctic CREST flight. First, background effects on the detector are shown to determine latch time of the discriminator to reduce dead time. This result is incorporated into the new version of the discriminator for the CREST-II flight in 2009. Second, a synchrotron radiation simulation based on GEANT3 is presented to determine the effectiveness of the collection of secondary synchrotron radiation in the Antarctic magnetic field. In the last section, the performance of the Antarctic CREST detector to synchrotron radiation is presented.

Chapter 7 presents summaries of the thesis and the expected number of synchrotron events by the Antarctica CREST flight.

CHAPTER II

Cosmic Ray and Cosmic Ray Electrons

2.1 Cosmic Ray Physics

This section will first give a brief overview of cosmic ray physics. Then, the current understanding of CR electrons will be presented through previous experimental results and theoretical aspects of acceleration and propagation.

2.1.1 Overview of Cosmic Ray Physics

Historically, the field of cosmic ray physics originated in the year 1912 when Victor F. Hess performed a series of balloon experiments where he indirectly observed ionization of unknown particles causing an increase in the discharge rate of the two gold leaves of an electroscope. Most importantly, the existence of CR from outer space became conclusive when the separation of the electroscope leaves decreased at a greater rate at higher altitude. In 1925, Robert Millikan coined the terms *cosmic rays* or *cosmic radiation* for the first time to describe these observed unknown ionizing particles. Further observations of the constituent particles of cosmic rays led to the discovery of elementary particles, such as the positron in 1932 and the muon in 1937.

Figure 2.1 presents the current global structure of the observed all-particle cosmic ray spectra, which extends eleven decades in energy and over 18 decades in flux.

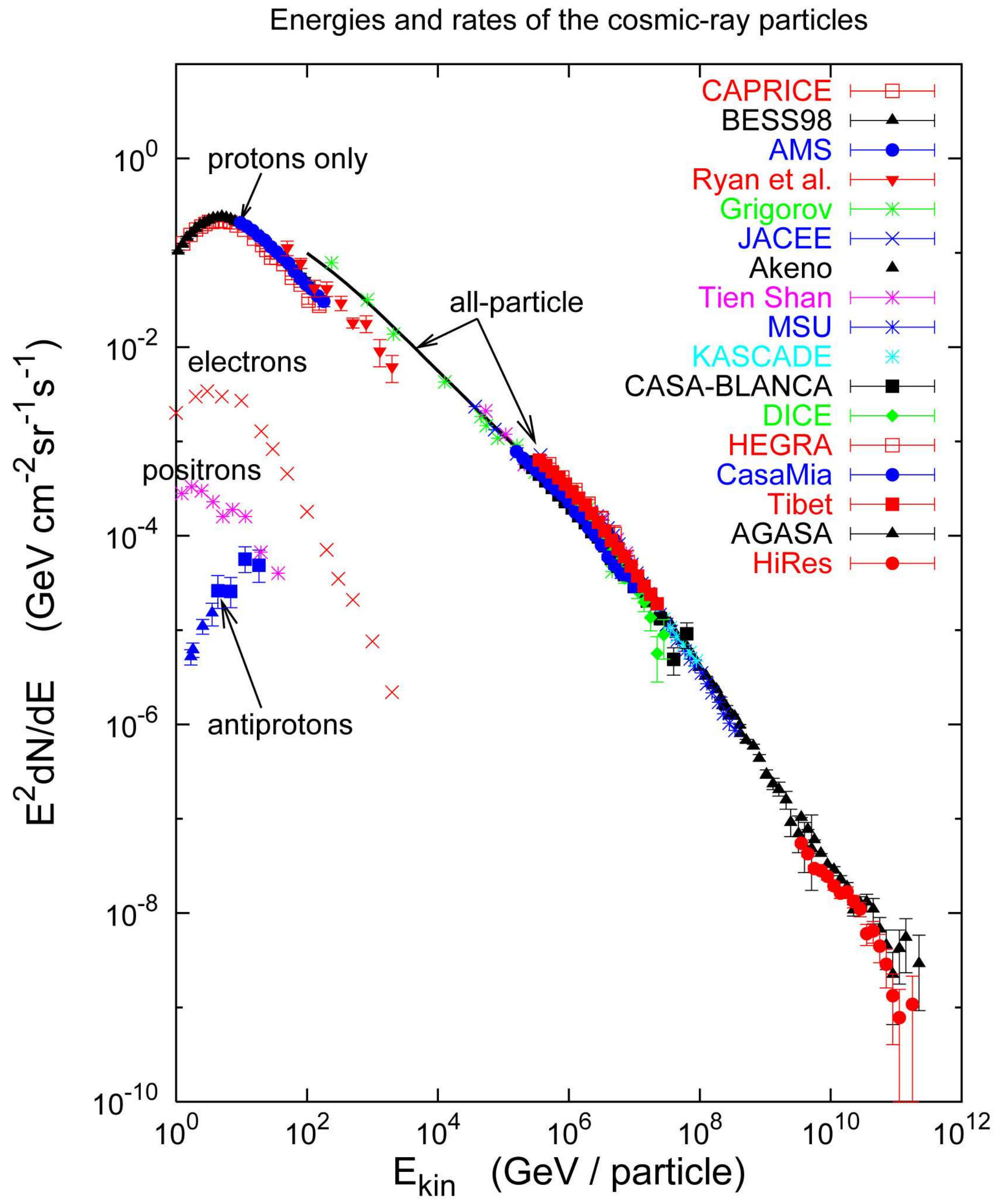

Figure 2.1: Global compilation of all particle CR spectra in the year 2005 [7]. These spectra show the differential flux multiplied by E^2.

Cosmic ray particles mainly consist of nuclei (proton, helium, and the other nuclei), fermions (mainly $e^{\pm}$), and their anti-particles. Among these particles, protons, which constitute approximately 86% of total cosmic rays, are most abundant. Helium ($\sim$ 12% of total CRs) is the second most abundant element. The remaining few percent of total CRs are heavier nuclei, fermions (e^- and μ^-), and anti-particles. The observed cosmic ray composition ratio among different particles above the Earth's atmosphere is very similar to that observed in Solar system material, except that some nuclei of CRs are enhanced via spallation during propagation through the interstellar medium.

The main structural feature of the all-particle CR spectrum is that it follows a simple power law: $dN/dE \propto E^{\alpha}$. In this spectrum there are two slight changes in the parameter α called the knee (from -2.7 to -3.1) and the ankle (from -3.1 to -2.1), whose corresponding energies are approximately 3×10^{15} eV and 3×10^{18} eV, respectively. These changes in the power index, α, are most likely caused by different physical acceleration mechanisms from different sources of cosmic rays. It is generally accepted that below and around the knee, CRs are accelerated up to these energies by Supernova remnants (SNRs). Therefore, one current experimental front is to look for energy cutoffs of different species of cosmic rays by extending measurements to energies above those where direct measurements by scientific balloon and satellite experiments have been employed in the past.

At very high energies (beyond the knee to $\sim 10^{20}$ eV), the rate of incident cosmic rays becomes very low and is approximately 1 particle m^{-2} $year^{-1}$ at the knee, and it is even lower at the ankle, $\sim$ 1 particle km^{-2} $year^{-1}$. Because of this, very high energy CR particles are only indirectly detected by reconstructing cosmic ray showers caused by primary CRs interacting with atmospheric nuclei. At the highest energy region ($\sim 10^{21}$ eV where experimental data points are quite sparse), the so-called (*Greisen-Zatsepin-Kuzmin* cutoff [8, 9]) has been observed by the High Resolution Fly's Eye experiment [10] and by the AUGER experiment [11]. Here, the GZK energy cutoff (6×10^{19} eV) is the energy where Lorentz-boosted cosmic microwave background photons result in photopion production on rest-frame cosmic ray protons ($\gamma + \mathrm{p} \rightarrow \Delta^{+} \rightarrow$ either $\mathrm{p} + \pi^{0}$ or $\mathrm{n} + \pi^{+}$). As a result, cosmic rays with energies greater than the GZK cutoff cannot originate from distances more than 50 Mpc from the Earth.

It can be seen from the Figure 2.1 that CR electrons consist of only $\sim$ one percent of the total CR spectrum at 10 GeV, and this proportion further decreases with energy ($\sim$ 0.1 percent of CR protons at 1 TeV) resulting in a harder power index, α.

2.2 Cosmic Ray Electron

2.2.1 SNRs as Candidate for Sources of High Energy CR Electron

Among the numerous astronomical objects responsible for accelerating electrons to high energy ($\sim$ a few TeV), several possible candidates are summarized in Figure 2.2. A typical length L of the acceleration region must be much larger than the gyro radius of electrons. The gyro radius is defined as $\mathrm{r_g} = 1.1 \times E_{15}/B_{\mu G}$ pc, where E_{15} is the energy of the accelerated electrons in units of 10^{15} eV, and $B_{\mu G}$ is the magnetic field strength of the accelerating region in μG. The energies of the electrons which the objects can accelerate [13] are constrained by,

$$E_{15} < \frac{L_{pc} B_{\mu G} \beta}{2} \tag{2.1}$$

where L_{pc} is the size of the accelerating region in pc and β is the characteristic velocity of the scattering centers of the electrons. For relativistic protons with β

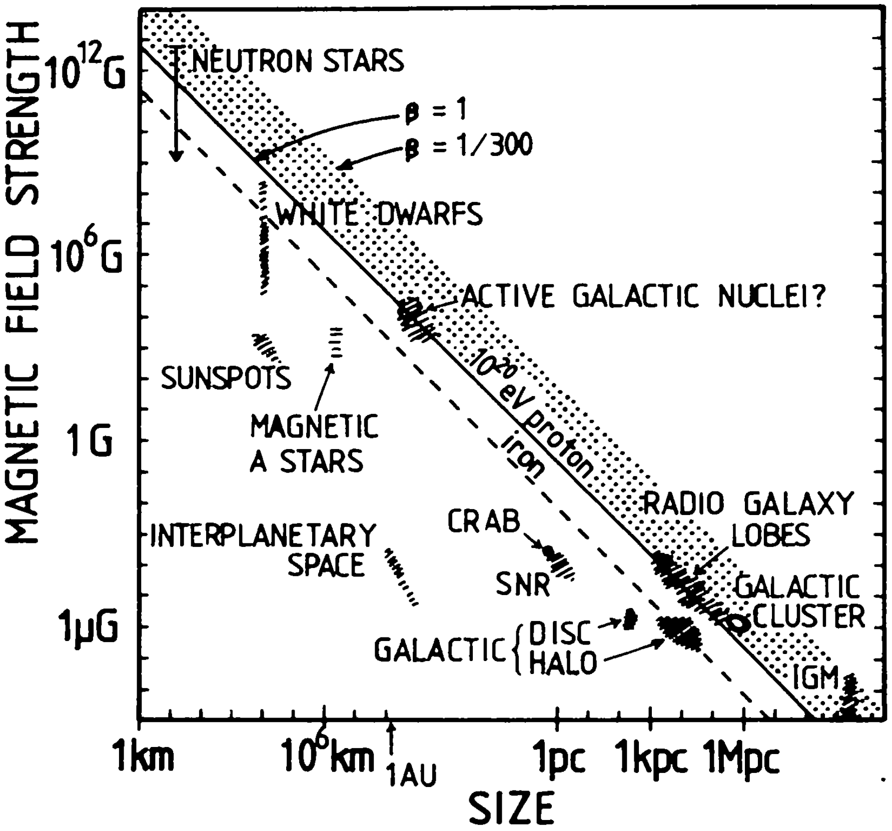

Figure 2.2: Size and magnetic field strength of possible candidate sites responsible for CR particle acceleration [12]. The meshed diagonal region indicates the approximate size and magnetic field required to accelerate protons to 10^{20} eV.

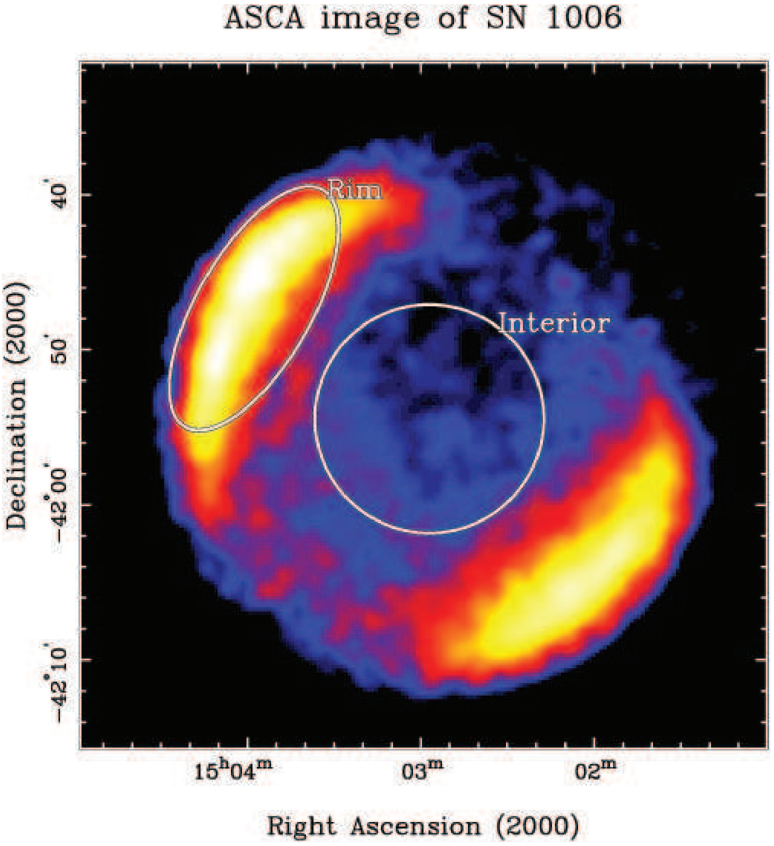

Figure 2.3: CCD image of SN1006 from 0.4 to 8 keV in the X-ray band observed by ASCA. [2]

= 1, the astronomical objects lying in the diagonal meshed region of Fig. 2.2 are possible candidates for acceleration of protons up to 10^{20} eV. The most likely source of high energy CR electrons are SNRs with $L_{pc} \sim 10$ pc, $B_{\mu G} \sim 10$, and $\beta \sim 3 \times 10^{-3}$. With these parameters, Eq. (2.1) provides an estimate of $E \sim 100$ TeV for the maximum energy of accelerated electrons.

At the same time, the strength of the internal magnetic field of the object independently limits the maximum energy achieved by electrons via synchrotron radiation processes. By invoking synchrotron radiation energy loss, Gaisser [14] estimates that the strength of the internal magnetic field must be less than ~ 1 G for electrons to be accelerated to TeV energies.

In 1995 Koyama et al. [2] observed the non-thermal radiation generated by high energy electrons (Fig. 2.3) in the shell of the remnant of SN 1006 with the ASCA satellite. This provided the first evidence for the existence of high energy electrons in SNRs. In this shell, the energy spectra of the bright rims show power law spectra due to synchrotron radiation from high energy electrons.

Another possible source of high energy CR electrons is via decay of π^-: $\pi^- \rightarrow \mu^- \rightarrow e^-$. In such a process, the number of CR positrons ($\pi^+ \rightarrow \mu^+ \rightarrow e^+$) should be almost equal to the number of CR electrons. However, it has been observed that the positron fraction, $e^+/(e^+ + e^-)$, is approximately 10% at energies of 1 to 10 GeV. Consequently, it can be concluded that high energy CR electrons have a significant primary component assuming all CR positrons are secondary.

2.2.2 Direct Experimental Measurements

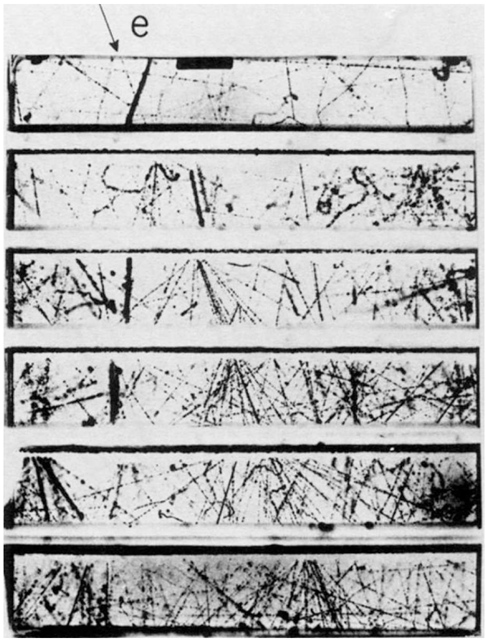

Figure 2.4: A cloud-chamber picture of a shower produced by a high energy cosmic ray electron [15].

Figures 2.5 shows direct experimental measurements of cosmic ray electrons by balloon experiments since 1975. In 1961, Earl James [15] performed the first detection

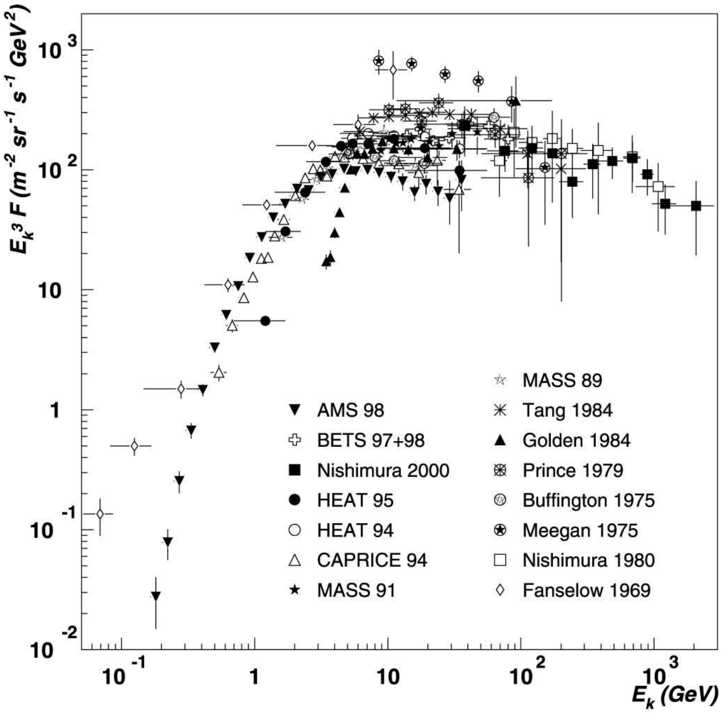

(a)

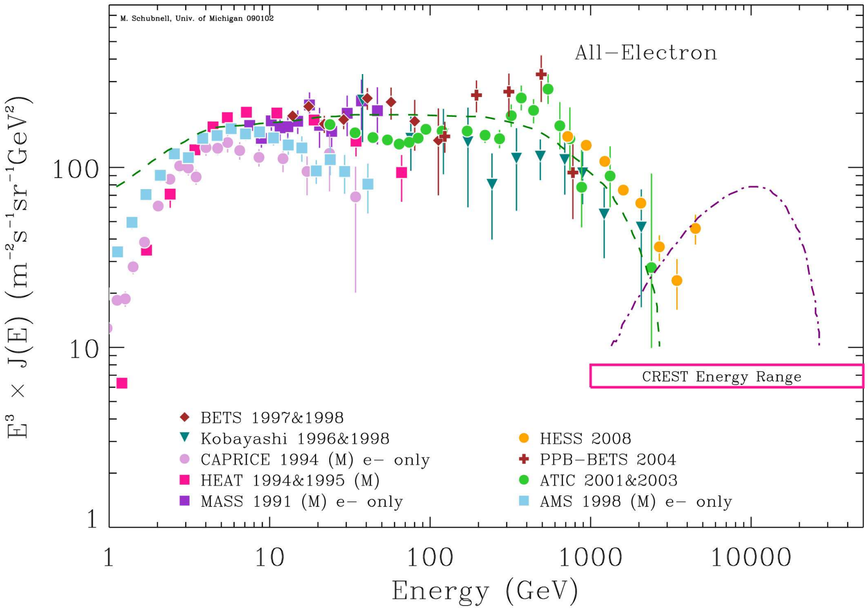

(b)

Figure 2.5: CR electron differential flux, F (m^2 sr^{-1} s^{-1} GeV^{-1}), multiplied by E^3 by direct measurement since 1975 [1] and with more recent results complied by Michael Shubnell.

of CR electrons using multi-plate cloud chambers (made out of five layers of lead plates) carried on a balloon at an average atmospheric depth of 4.5 g/cm^2 (Fig. 2.4). He observed the showers produced in the chambers by CR electrons whose energies were above 0.5 GeV. Since then, CR electrons have been measured with balloon and satellite experiments over a wide energy range. The highest energy CR electrons ($\sim$ 4.5 TeV) ever observed was indirectly by imaging atmospheric Cherenkov telescope by HESS experiment [16], and they used Random Forest method by comparing real air shower data with simulated ones.

The measured CR electron spectrum can be roughly categorized into three regions. Up to a few 100's of GeV, the spectrum consists of a diffuse CR electron component from SNRs throughout the Galaxy. At lower than a few 10's of GeV, this diffuse component is strongly modified by the solar magnetic field. At higher energies ($\geq$ a few 100's of GeV), the high energy CR electron spectrum is believed to originate from nearby SNRs.

At higher than a few GeV, the power law index, α, of the CR electron spectrum is found to range approximately from -3.0 to -3.3 [17]. With a force-field model to correct for solar modulation, Casadei and Bindi [1] found that the corrected power index of the spectrum is -3.44 ± 0.03 from 3 GeV to 2 TeV. Note that this power index is harder than the one for CR protons (-2.7), because CR electrons lose their energy much more rapidly during propagation.

2.3 High Energy CR electron Propagation and Acceleration

Since the changes in the particle energies per collision with the ISM are relatively small, the diffusion equation (Fokker-Planck equation) is most commonly used to describe the propagation of CRs from their sources. In our case, we use this equation to describe high energy CR electron propagation from SNRs:

$$\frac{dN_e}{dt} - \nabla(D\nabla N_e) + \frac{\partial}{\partial E}(\frac{dE}{dt}N_e) = \sum_{i=1}^{n} Q_i \tag{2.2}$$

where $N_e = N_e(E, \vec{x}, t)$ is the density of CR electrons with energy, E, at $(\vec{x}, t)$. $D \simeq D(E)$, is the energy dependent uniform diffusion coefficient (in general, the coefficient can also be position sensitive), and the second term of Eq. (2.2), therefore, describes the diffusion of CR electrons during their propagation. The third term represents their energy loss, and the details of diffusion and energy loss will be given in the next Section. $Q_i = Q_i(E, \vec{x}, t)$ is the source strength at position $\vec{x_i}$, and time t_i, and n is the number of the sources responsible for generating CR electrons. Consequently, Eq. (2.2) describes the fact that acceleration by sources increases the electron density, but both diffusion and energy loss (the second and the third terms respectively) during propagation decrease its density. In this model, the high energy CR electrons can be generated from both discrete sources and continuously distributed ones.

The following sections describe the details of each of the three terms (energy loss, diffusion, and acceleration sources) in Eq. (2.2).

2.3.1 Energy Loss and Diffusion of Propagation

Traveling through the interstellar medium, CR electrons experience energy losses of different forms: ionization, bremsstrahlung, synchrotron radiation and inverse Compton scattering. Each such energy loss mechanism has a different dependence on the electron energy, and the total electron energy loss in the ISM can be simply expressed [18] as,

$$-\frac{dE}{dt} = \mathrm{a} + \mathrm{b}(\ln E) + \mathrm{c}E + \mathrm{d}E^2 \tag{2.3}$$

where a, b, c, and d are constants, and E is the energy of the CR electron. Note that this equation is the third term of Eq. (2.2) except for the negative sign to express energy loss. The terms of constant, a, and logarithmic dependence on E, $\mathrm{b}\ln(E)$, describe ionization loss of the electron from atomic hydrogen in the ISM [18],

$$-\frac{dE}{dt}_{ion} = 7.64 \times 10^{-15} \mathrm{N_H} \left(19.8 + 3\ln\left(\frac{E}{\mathrm{m}_e\mathrm{c}^2}\right)\right) \quad \mathrm{eV/s} \tag{2.4}$$

where $\mathrm{N_H}(\sim 10^6$ atoms/m$^3)$ is the number density of hydrogen atoms/m^3 in the ISM. This is a quite negligible effect for high energy electrons in the Galaxy. By integrating Eq. (2.4), the lifetime of electrons can easily be estimated. For instance, for a 3 GeV electron in the Galaxy, the rate of ionization loss is only ∼10 eV/year. Bremsstrahlung between CR electrons and the hydrogen nuclei in the ISM is responsible for the linear term of the energy loss, $\mathrm{c}E$ [18],

$$-\frac{dE}{dt}_{brems} = 3.66 \times 10^{-22} \mathrm{N_H} \left(\frac{E}{\mathrm{eV}}\right) \quad \mathrm{eV/s} \tag{2.5}$$

Energy loss in the quadratic term, $\mathrm{d}E^2$, is most important for high energy CR electron propagation (especially, above 10 GeV). Synchrotron radiation and inverse Compton scattering are the physical processes responsible for this energy loss. Synchrotron radiation is caused by interaction with the magnetic field through which the electron propagates. On the other hand, the interaction with low energy photons from interstellar radiation (2.7 K CMB, radiation from dust grains, and stellar radiation) in the Galaxy causes inverse Compton scattering of high energy CR electrons. The expression that describe these processes is [19],

$$-\frac{dE}{dt}_{sync/IC} = \frac{4\sigma_T c}{3\left(\mathrm{m}_e \mathrm{c}^2\right)^2}\left(\frac{B^2}{8\pi} + w_{photon}\right)E^2 \tag{2.6}$$

where σ_T is the Thomson cross section, B is the magnetic field strength in the Galaxy ($B_\perp \simeq 5\mu G$ and ${B_\perp}^2 = 2B^2/3$) for synchrotron radiation energy loss, (Here, $B_\perp$ is the magnetic field perpendicular to the velocity direction of CR electron.), and w_{photon} is the energy density of the interstellar photons ($w_{photon} \simeq 1.0$ eV/cm^3) for inverse Compton scattering energy loss. Additionally, the correction to Thomson scattering, σ_T, accounts for the Klein-Nishina effect for high energy CR electrons. Klein-Nishina effect is the lowest order correction from quantum electrodynamics for the interaction between photons and an high energy electron. This correction introduces an energy dependent coefficient of E^2 that decreases with energy [19]. For instance, d $\simeq 1.85 \times 10^{-16}$ GeV^{-1}s^{-1} at 1 GeV, but decreases to $\simeq 1.4 \times 10^{-16}$ GeV^{-1}s^{-1} at 1 TeV. The details of calculations including the Klein-Nishina formula can be found in many references [20–23].

The diffusion coefficient, $D(E)$, in Eq. (2.2) is energy dependent, and can be estimated from the measured secondary to primary ratios of nuclei such as B/C (Fig. 2.6). For a few tens of GeV nucleon, $D(E) = \text{constant}\times E^\delta$, where δ can range from 0.3 to 0.85. In the simplest case, $\delta = 0$ indicates energy independent diffusion, while $\delta = 0.3$ indicates Kolmogorov-type turbulence in the ISM.

Earlier studies of the solutions to the diffusion Eq. (2.2) applied to high energy CR electron propagation have been performed by Syrovatskii [25] and Shen and Mao [26] with energy independent diffusion ($\delta = 0$). However, with recent observation of the secondary to primary ratio (sub Fe(Z = 21,22,23)/Fe) from the RUNJOB experiment [27, 28], Kobayashi et. al. [19] estimate $D(E) = 2 \times 10^{28}(E/5\text{ GeV})^{0.6}$ cm^2/s around 100 GeV and $D(E) = 2 \times 10^{29}(E/\text{TeV})^{0.3}$ cm^2/s in the TeV region.

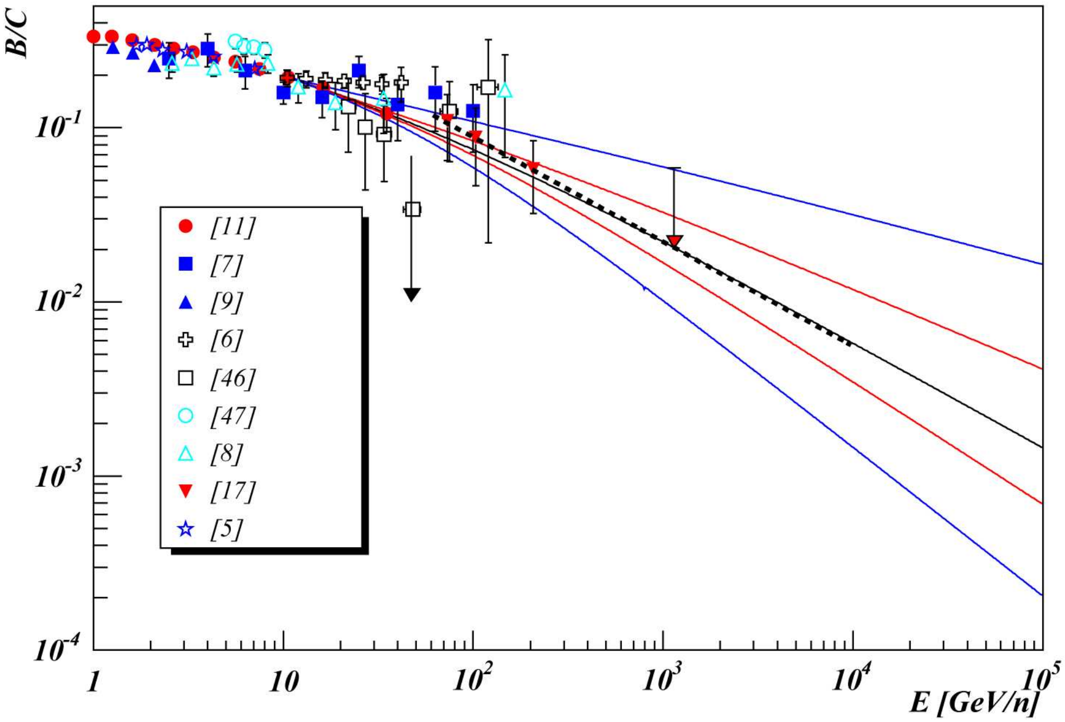

Figure 2.6: B/C ratio (solid curves) with diffusion coefficient slope $\delta = 0.3$, 0.46, 0.6, 0.7, 0.85 (from top blue line) as a function of kinetic energy/nucleon. Dashed line is for B/C $\propto E^{-0.60}$. Refer to [24] for the B/C ratio data points.

2.3.2 CR Acceleration

The topic of shock acceleration of cosmic rays is quite involved and complex (reviews can be found at the end of this Chapter). The following sections introduce a few of the basic and widely accepted methods of CR shock acceleration, which can be applied to CR electrons as well.

2.3.2.1 Fermi Acceleration

In 1949 Enrico Fermi first proposed a mechanism to explain the observed non-thermal power law CR spectrum. Here, we briefly introduce his idea of CR acceleration. The CR particles are accelerated by interactions with a moving plasma cloud (called 2^{nd} order Fermi acceleration) or with a plane shock front (called 1^{st} order Fermi acceleration) where CR particles experience slight energy increases, δE, for each encounter with the boundaries (Fig. 2.7). These boundaries of the plasma cloud and shock front can be seen by the CR particles as discontinuities, since the gyro-radii of the accelerated particles are much larger than those of thermal ions, which form these boundaries.

In these mechanisms, elastic scattering by the magnetic field inside the plasma clouds and upstream of the shock fronts by Alfvén waves or other forms of magnetic turbulence, ensure that the CR particles cross these boundaries multiple times. These multiple boundary crossings are considered to be responsible for generating the power spectrum of CRs. The main difference between 1^{st} order and 2^{nd} order acceleration mechanisms is that their power indices of average energy gain per collision are proportional to β (=V/c refers to the relative velocity of the plasma/shock) or β^2, respectively. That is,

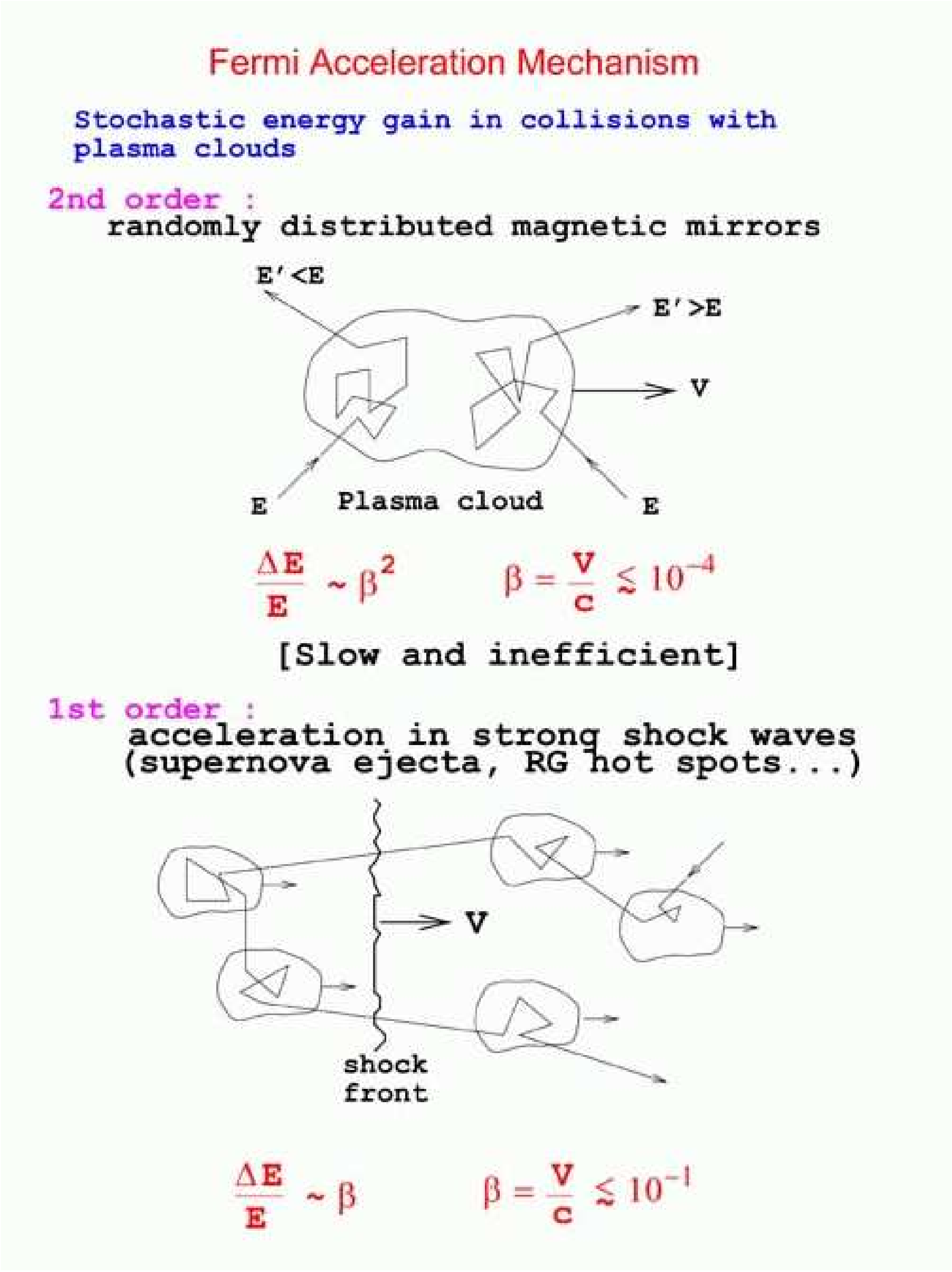

Fermi Acceleration Mechanism

Stochastic energy gain in collisions with plasma clouds

2nd order : randomly distributed magnetic mirrors

$$\frac{\Delta E}{E} \sim \beta^2 \qquad \beta = \frac{V}{c} \lesssim 10^{-4}$$

[Slow and inefficient]

1st order : acceleration in strong shock waves (supernova ejecta, RG hot spots...)

$$\frac{\Delta E}{E} \sim \beta \qquad \beta = \frac{V}{c} \lesssim 10^{-1}$$

Figure 2.7: Illustrations of 2^{nd} order and 1^{st} order Fermi acceleration mechanisms. E and E' are the energies of the particle before and after the interaction with the plasma cloud and shock front.

$$\left\langle \frac{\triangle E}{E} \right\rangle \propto \beta \tag{2.7}$$

per collision (the detailed derivations and references of the Fermi acceleration mechanisms can be found in [14, 18]) for 1st order Fermi acceleration, and

$$\left\langle \frac{\triangle E}{E} \right\rangle \propto \beta^2 \tag{2.8}$$

per collision for 2nd order Fermi acceleration. This difference in the acceleration efficiencies is due to the fact that in 2nd order Fermi acceleration, the CR particles gain energy for head-on collisions, but lose energy for tail-end collisions. Since overall, head-on collisions are statistically more probable. CR particles gain energy on average. For 1st order Fermi acceleration, no-tail end collisions occur. Consequently, CR particles only gain energy crossing the shock front multiple times. The problem of 2nd order Fermi acceleration is that the acceleration process is very slow, since random velocities of plasma clouds are the order of $\beta \leq 10^{-4}$, and thus, $\beta^2 \leq 10^{-8}$, while $\beta \leq 10^{-2}$ for the 1st order acceleration process.

To conclude this section, the power spectrum will be derived from Equations (2.7) and (2.8). The average energy of the particle per collision can be expressed by $E = \mathrm{f}(\beta)E_0$ for both 1st and 2nd order acceleration mechanisms. $\mathrm{f}(\beta)$ is the energy gain per collision as a function of β, and E_0 is some initial energy taken from a thermal distribution of electrons. Also, P is defined as a probability per collision of the particle remaining within the acceleration region. Therefore, after n collisions, there are $N = N_0 P^n$ particles with energies $E = \mathrm{f}(\beta)^n E_0$. By eliminating the number of collisions, n, we obtain,

$$N = N_0 \left(\frac{E}{E_0}\right)^{\frac{\ln P}{\ln(\mathrm{f}(\beta))}} \tag{2.9}$$

and, therefore,

$$N(E)dE = \text{constant} \times E^{-\left(\frac{\ln P}{\ln(\mathrm{f}(\beta))}+1\right)} dE \tag{2.10}$$

as a result. The next section will examine the physics of the shock front in detail to extract the physical meaning of the exponent of Eq. (2.10).

2.3.2.2 Physics of Shock Front

Shock waves can be understood by the shock front separating two regions of different velocities, densities, and pressures (See Fig. 2.7). By going to the rest frame of the shock front and defining velocities ($\vec{v_1}$ and $\vec{v_2}$), densities (ρ_1 and ρ_2), and pressures (p_1 and p_2) in each region, the boundary conditions at the shock front require three conservation laws:

$$\nabla \cdot (\rho \vec{v}) = 0 \Rightarrow \rho_1 v_1 = \rho_2 v_2 \tag{2.11}$$

$$\nabla \cdot (\rho \vec{v})\, \vec{v} = -\nabla p \Rightarrow p_1 + \rho_1 {v_1}^2 = p_2 + \rho_2 {v_2}^2 \tag{2.12}$$

$$\nabla \cdot \left[\left(\frac{1}{2}v^2 + \epsilon_{int} + \frac{p}{\rho}\right)\rho\vec{v}\right] = 0 \Rightarrow \left(\frac{1}{2}{v_1}^2 + \epsilon_{int_1} + \frac{p_1}{\rho_1}\right)\rho_1\vec{v_1} = \left(\frac{1}{2}{v_2}^2 + \epsilon_{int_2} + \frac{p_2}{\rho_2}\right)\rho_2\vec{v_2} \tag{2.13}$$

where Equations (2.11), (2.12), and (2.13) are the mass, momentum, and energy conservation, respectively. The directions of $\vec{v_1}$ and $\vec{v_2}$ are perpendicular to the shock front, and ϵ_{int_1} and ϵ_{int_2} are internal energies per unit mass in the two regions.

Along with the ideal gas law, $p = (\gamma - 1)\epsilon_{int}\rho$, these conservation equations lead to relationships between velocities, densities, and pressures of both sides of the shock front (Rankine-Hugoniot relation),

$$r = \frac{\rho_2}{\rho_1} = \frac{v_2}{v_1} = \frac{(\gamma + 1)}{(\gamma - 1) + \frac{2}{{M_1}^2}} \tag{2.14}$$

$$\frac{p_2}{p_1} = \frac{2\gamma {M_1}^2 - (\gamma - 1)}{(\gamma + 1)} \tag{2.15}$$

where $M_1 = v_1/c_1$ ($c = \sqrt{(\gamma p)/\rho}$: sound speed) is the Mach number. The r in Eq. (2.14) is called the compression ratio of the shock front. In the case of a mono-atomic non-relativistic gas where $\gamma = 5/3$, the compression ratio, r, approaches 4 as M_1 becomes larger.

2.3.2.3 Diffusive Shock Acceleration

To understand the physical meaning of the power index of shock acceleration, the diffusive shock acceleration (DSA) method can be exploited. DSA is quite similar to the 1^{st} order Fermi acceleration mechanism: A fraction of the CR particles are trapped by scattering around the shock front, where they are accelerated. Also, there could be some particles, which are both injected into and escaping from the region of the shock front. Hence, the main difference of the formulations between DSA and Fermi acceleration is that DSA describes the CR particles by the distribution function, $f = f(\vec{x}, \vec{p}, t)$, while the Fermi acceleration mechanism deals with the behaviors of individual particles. To describe the DSA process, a one dimensional time independent diffusion-convection equation can be used [29],

$$\frac{\partial}{\partial x}\left[uf - \kappa\frac{\partial f}{\partial x}\right] = \frac{1}{3}\left(\frac{\partial u}{\partial x}\right)\frac{\partial}{\partial p}(pf) \tag{2.16}$$

where $\kappa = \kappa_{\|} cos^2\theta_{Bn} + \kappa_{\perp} sin^2\theta_{Bn}$ is the diffusion coefficient. The angle, θ_{Bn}, is between the direction of the magnetic field and the normal to the shock front, and the coefficient, κ, holds information about the local magnetic field. The left and right hand terms in Eq. (2.16) describe diffusion and adiabatic compression of the CR particles respectively. For simplicity it assumes that there are no injection and escape terms [30, 31]. In most contexts, Alfvén waves are responsible for scatterings of the particles, and the diffusion coefficient, κ, can be simplified in the case where the magnetic field is parallel to the shock normal [32, 33] ($\theta_{Bn} = 0$),

$$\kappa = \frac{1}{3}\left(\frac{B}{\delta B}\right)^2 r_g v_e \overset{B \sim \delta B}{\longrightarrow} \frac{1}{3} r_g c \tag{2.17}$$

where r_g is the gyro radius of the particle and δB is the fluctuation of the local magnetic field. For the special case when $B \sim \delta B$ (called the Bohm diffusion limit), the diffusion coefficient approaches $\frac{1}{3} r_g c$.

The boundary conditions to solve the Eq. (2.16) for CR particle acceleration around the shock front are given by

$$\frac{\partial u}{\partial x} = -(u_u - u_d)\delta(x) \tag{2.18}$$

at the shock front, and at $x = \pm\infty$

$$\begin{cases} \frac{\partial f}{\partial x} = 0 & \text{for } x = \pm\infty \\ f = f_u(p) & \text{for } x = -\infty \\ f = f_d(p) & \text{for } x = +\infty \end{cases} \tag{2.19}$$

where $f_u(p)$ and $f_d(p)$ are the distribution functions upstream and downstream of the shock front respectively. The one dimensional diffusion-convection equation

(Eq. (2.16)) can be solved using these boundary conditions, and the spectrum downstream of the accelerated particles [34] becomes,

$$N(p) \propto p^2 f_d \propto p^{-\frac{r+2}{r-1}} \tag{2.20}$$

In the case of the high energy electrons where $p \propto E$,

$$N(E)dE \propto E^{-\left(\frac{2r+1}{r-1}\right)} dE. \tag{2.21}$$

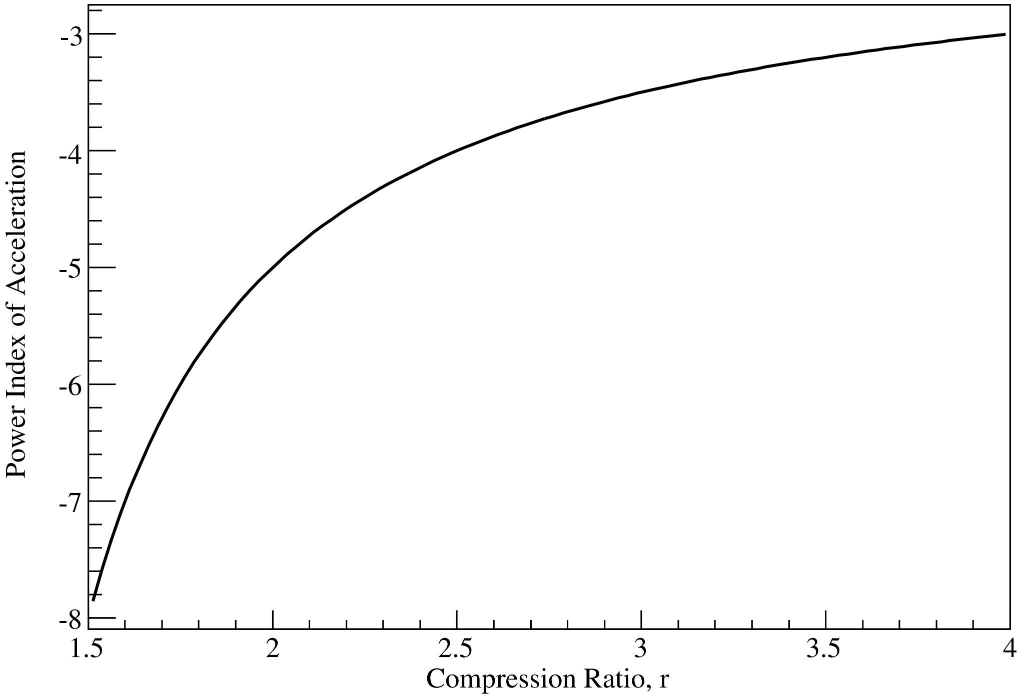

Figure 2.8: Power index of the downstream spectrum as a function of the compression ratio.

Again, we obtain a power law spectrum, but additionally in this DSA formulation, the power index is found to be a function of the compression ratio, r of the shock front. When the compression ratio approaches 4 for a non-relativistic strong shock (note that *non-relativistic* means that the speed of the shock is much less than the speed of the light, and *strong* means a very large M_1 in Eq. (2.14)), the power index of the downstream spectrum leads to r = −3 from the negative side. Fig. 2.8 presents this behavior of the power index at the acceleration site as a function of compression ratio in this DSA scheme.

2.3.2.4 Other Methods of Shock Acceleration

Other types of shock acceleration, such as relativistic shock acceleration (Kirk & Duffy [35]; Kirk et al. [36]), non-linear shock (Drury & Völk [37]; Berezhko & Ellison [38]), and the test particle Markov stochastic method (Zhang [39]), can be found in many references. They can be applied to different astronomical objects under unique physical conditions, which in turn yield different power indices of the spectra. For instance, relativistic shock acceleration can be applied to relativistic jets from AGNs and gamma-ray bursts. Non-linear strong shock accounts for the influence of CR particles on the shock front, when pressure from CR particles becomes significant.

2.4 Nearby SNRs as candidates for HE CR electron accelerators

For the high energy electrons ($\geq \sim$1 TeV), the most dominant energy loss processes are synchrotron radiation and inverse Compton scattering, where energy loss of the CR electron is proportional to the square of their energy. By solving the energy loss Eq. (2.6), Kobayashi et al. [19] found an estimate for the time scale for high energy CR electrons to travel from their sources to the Earth,

$$T \approx 2.1 \times 10^5 \left(\frac{E}{1\mathrm{TeV}}\right)^{-1} \quad \mathrm{yr} \tag{2.22}$$

and also a distance, r,

$$r \sim \sqrt{(2D(E)T)} \approx 1.0 \left(\frac{E}{1\mathrm{TeV}}\right)^{-1} \quad \mathrm{kpc} \tag{2.23}$$

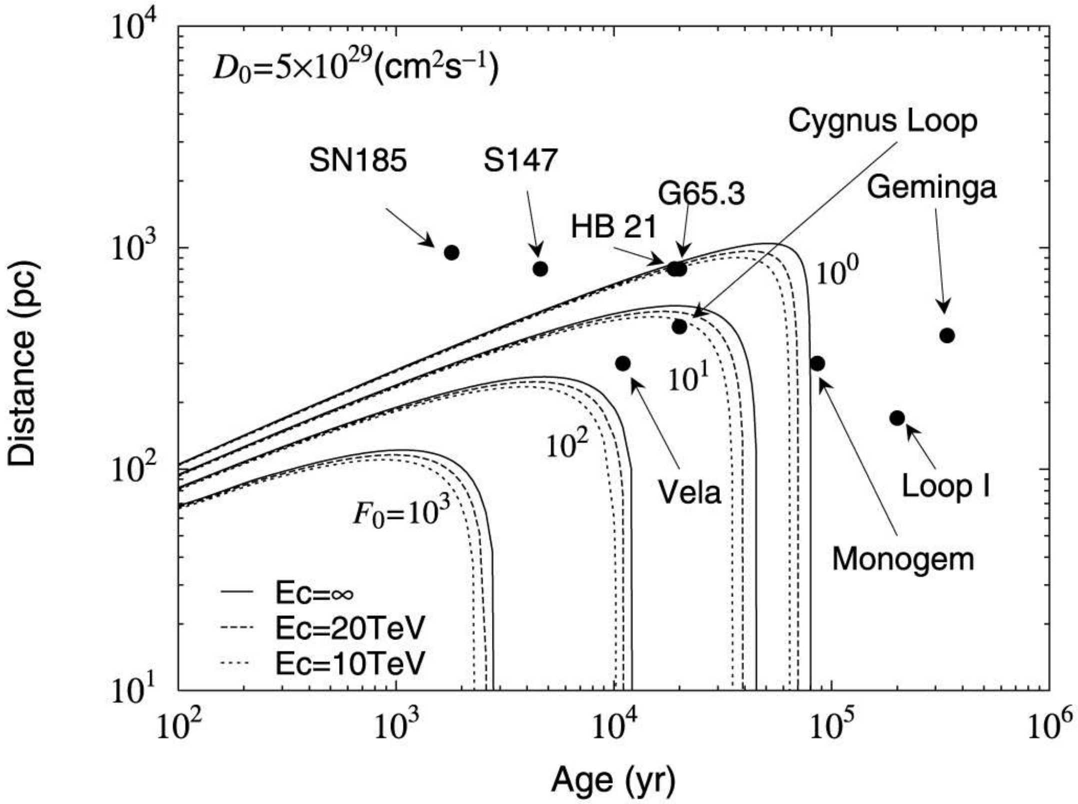

Figure 2.9: Contours of the CR electron flux at 3 TeV with $F_0 = (E/\mathrm{GeV})^3 \times$ (the electron flux at 3 TeV) (GeV^2/m^2/s/sr) with the diffusion coefficient, $D_0 = 5\times10^{29}$ (cm^2/s), and different exponential cutoffs, E_c (explained in a later section), after prompt release of the electron [19].

D(E) is energy dependent diffusion coefficient (See Sec. 2.3.1). To be observed at the Earth, TeV CR electrons must have been accelerated within approximately 1 kpc and within $\sim10^5$ years. As primary sources of TeV CR electrons, a list of nearby SNRs and contours of the CR spectrum are shown in Table 2.1 and Fig. 2.9. Notice that only a few such candidates exist, and Vela and the Cygnus Loop are the ones, which most likely contribute to the high energy CR electron spectrum. Also, E_{max} is restricted by the propagation of high energy electrons and is given by 1/(d $\times$ T) where d is the energy-loss coefficient of the E^2 term in Eq. (2.6) and T is the age of the SNR assuming the prompt release of high energy electrons after the SNR

Table 2.1: List of nearby SNRs ([19] and references within) E_{max} is the maximum energy for prompt release after the explosion.

SNR	Distance (kpc)	Age (years)	E_{max} (TeV)
S147	0.80	4.6×10^3	63
HB21	0.80	1.9×10^4	14
G65.3+5.7	0.80	2.0×10^4	13
Cygnus Loop	0.44	2.0×10^4	13
Vela	0.30	1.1×10^4	25
Monogem	0.30	8.6×10^4	2.8
Loop1	0.17	2.0×10^5	1.2
Geminga	0.15	3.4×10^5	0.67

explosion.

2.5 Solutions to Fokker-Planck propagation equation

With the understanding of the energy loss and diffusion processes of CR electron propagation in the previous sections, we are now at the point where solutions to the Fokker-Planck equation (Eq. (2.2)) can be found. For lower energy ($\leq$ a few 100's of GeV), the equation can be solved using a two dimensional cylindrical Fourier expansion with boundary conditions [40]. These conditions are determined by the size of our local Galaxy and an average SN explosion rate of 1/30 yrs^{-1} [40] and an explosion energy of 10^{48} erg/SNR to uniformly fill the Galaxy with CR electrons. For higher energies ($\geq$ a few 100's of GeV), a three dimensional Green's function method without boundary conditions can be exploited, since high energy CR electrons cannot propagate very far due to their rapid energy loss. This method has been developed first by Shen [41] and followed by other authors [26, 42].

For high energy electrons, we follow the Green's function method provided by Kobayashi et al. [19]. First, as described in the previous sections, the diffusion and energy loss terms in the Fokker-Planck propagation Eq. (2.2) can be taken as

$$\begin{aligned} D(E) &= D_0 \left(\frac{E}{\mathrm{TeV}}\right)^{\delta} && (2.24) \\ \frac{dE}{dt} &= -\mathrm{d}\ E^2 && (2.25) \end{aligned}$$

where

$$D_0 = (2-5) \times 10^{29} (\mathrm{cm}^2/\mathrm{g}) \tag{2.26}$$

and

$$d = \frac{4\sigma_T c}{3\left(\mathrm{m}_e \mathrm{c}^2\right)^2} \left(\frac{B^2}{8\pi} + w_{photon}\right). \tag{2.27}$$

Note that only synchrotron radiation and inverse Compton scattering terms, which are proportional to E^2 in the energy loss, are kept in the calculation.

The source of the accelerated CR electrons described in the right-hand term of Eq. (2.2) can be exploited in the following way: For the case of burst source injection at ($\vec{r}$,t) = ($\vec{0}$,0) with the source energy spectrum of $Q(E) \propto E^{-\gamma}\exp(-E/E_c)$, the source term of the Green's function becomes,

$$Q(E, \vec{r}, t) = Q_0 E^{-\gamma} exp(-\frac{E}{E_c}) \times \delta(\vec{r})\delta(t) \tag{2.28}$$

where the cutoff energy, E_c, in the source term was added to restrict the maximum energy of the accelerated electrons inside SNRs due to both synchrotron radiation energy loss and the acceleration rate, and Q_0 is normalized such that the output energy for the electrons above 1 GeV is $\sim 1 \times 10^{48}$ ergs. Hence, the density of high energy electrons, $N_e = N_e(E, \vec{r}, t)$, can be derived [40, 42] as

$$N_e(E, \vec{r}, t) = \frac{1}{(4\pi D_1)^{\frac{3}{2}}} \frac{e^{\frac{\vec{r}^2}{4D_1}}}{1 - dEt^2} \times Q(\frac{E}{1 - dEt}) e^{-\frac{E}{E_c(1-dEt)}} \tag{2.29}$$

where $D_1 = D_1(E')$ is defined as

$$D_1(E) = \int_{E}^{\frac{E}{1-dtE}} \frac{E' D(E')}{b} \, dE' \tag{2.30}$$

As a result, the flux of high energy CR electrons from nearby discrete sources can be obtained through,

$$J_n(E, \vec{r}, t) = \frac{c}{4\pi} N_e(E, \vec{r}, t) \tag{2.31}$$

at the distance, $|\vec{r}|$, from the source to the Earth with release time, t.

Some of the expected results involving the power indices of acceleration and diffusion, γ and δ, respectively ($\gamma + \delta = 2.7$) from individual SNR contributions to the CR electron spectrum are shown in Fig. 2.10 for the prompt release of CR electrons after SNR explosions. Only a few (Vela, Monogem, and Cygnus Loop in this case) of the nearby SNRs listed in Table 2.1 are expected to significantly contribute to the high energy portion ($\geq \sim$1TeV) of the spectrum. Note that the diffusive (distance) component is also shown in the Figure.

Other than the power indices, γ and δ, the variations of three additional parameters (diffusion coefficient (D_0), energy cutoff (E_c), and release time (τ)) can be investigated. First, a larger diffusion coefficient allows CR electrons to propagate diffusively to larger distances. The diffusion coefficient generally affects both the lower energy end and the normalization of the spectrum. On the other hand, the energy cutoff of the source, E_c, has effects on the high energy end of the spectrum as seen in Figure 2.10.

Kobayashi et al. examined different scenarios for continuous and delayed release times of CR electrons from SNRs. They concluded that a spectrum with the mean value of the continuous release time can correspond to the same value of the burst-like

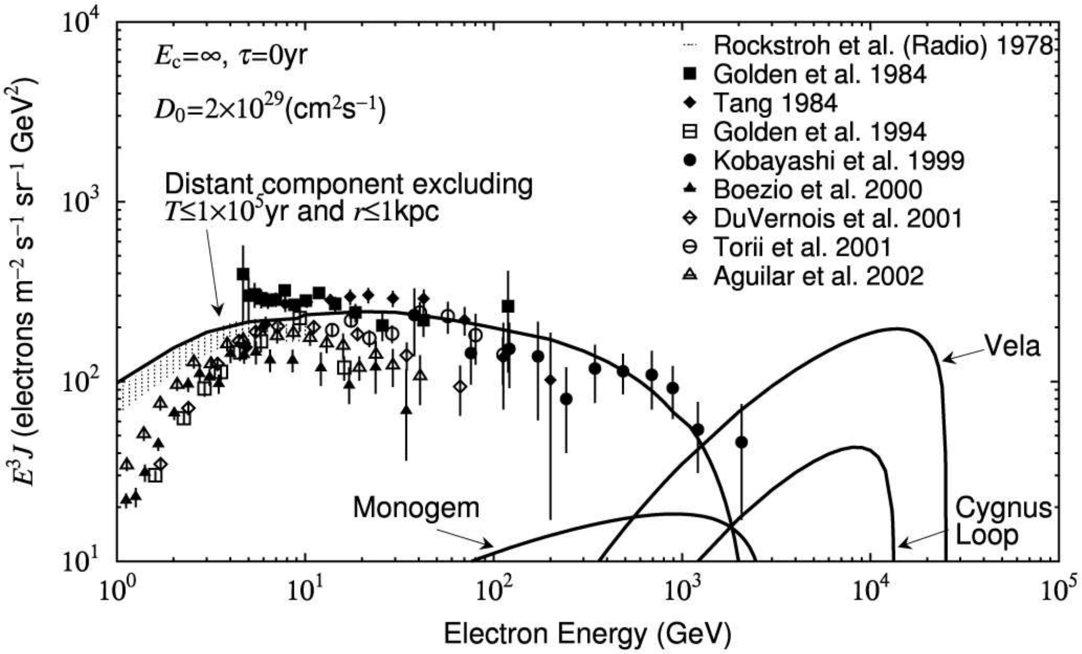

(a)

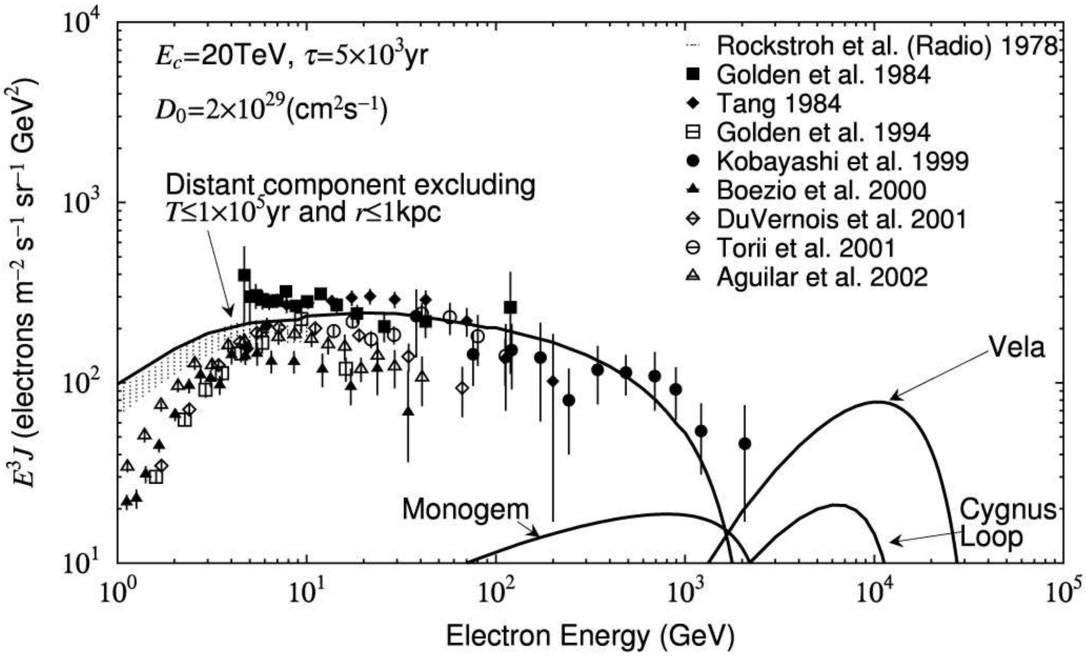

(b)

Figure 2.10: Two examples of possible electron spectra with different parameters, diffusion coefficient (D_0), release time (τ), energy cutoff (E_c) from individual nearby SNRs with $\gamma + \delta = 2.7$.

release time. They also found that delayed release times have a significant influence on the normalization of the spectrum. For some delayed release times, we will not be able to observe any high energy electrons ($\geq \sim$1 TeV), and the electron spectrum will die down continuously from the diffusive component.

A wealth of information can be discovered by observations of high energy CR electrons ($\geq$ a few TeV). Acceleration mechanisms at their sources as well as energy dependent diffusion processes from their sources can be extracted from the power index of the spectrum. Observation of the energy cutoff in the spectrum gives us information on the strength of the magnetic field and the rate of acceleration processes of SNRs and the release time of the high energy CR electrons from these SNRs. Furthermore, the normalization of the spectrum informs us as to the strength of the diffusion process during propagation, the output energy of the SNRs and release time of high energy electrons. Lastly, specific sources of high energy CR electrons can be identified by such observations.

2.6 Synchrotron Radiation from High Energy Electrons

Synchrotron radiation photons are generated as charged particles travel through magnetic fields. Emission of synchrotron radiation is well understood [18, 43]. In this section, we focus on the features of synchrotron radiation relevant to the CREST experiment.

The number of synchrotron photons per path length, s, per relative energy, $x = E_\gamma/E_c$ where the critical energy is $E_c = 3\hbar/2m\gamma^2 eB_\perp$, with magnetic field strength, $B_\perp$, perpendicular to instantaneous direction of a charged particle is expressed by [44, 45],

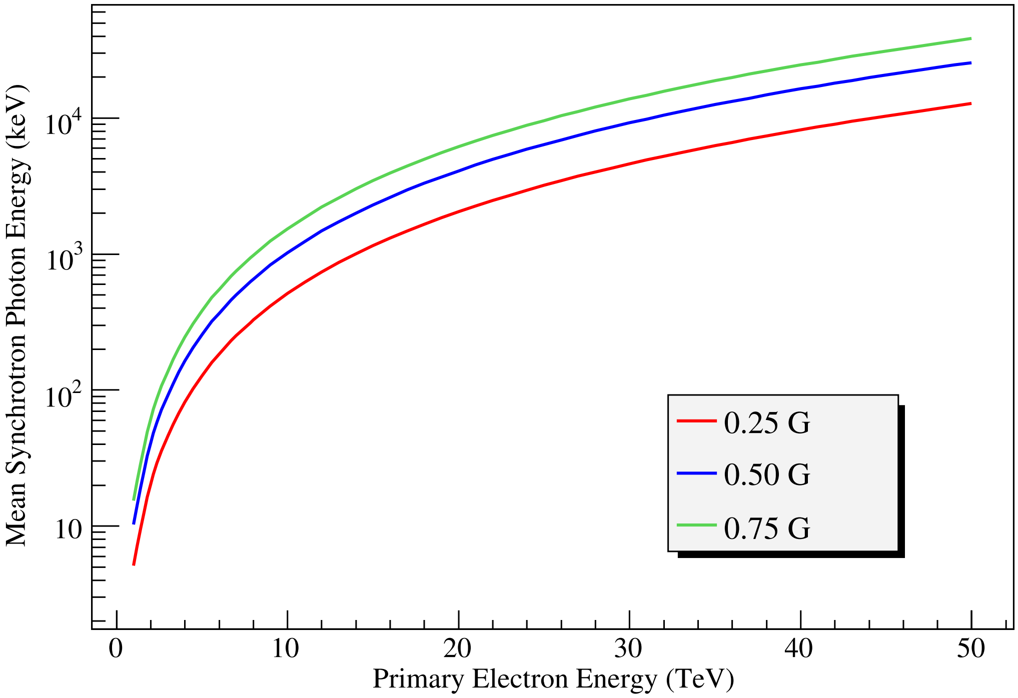

Figure 2.11: Maximum value of the mean synchrotron photon energy per mean free path at three different uniform magnetic field strengths where the directions of the electrons and of the magnetic fields are perpendicular.

$$\frac{d^2N}{dsdx} = \frac{\sqrt{3}\alpha}{2\pi}\frac{eB_\perp}{m\beta c}\int_x^\infty K_{\frac{5}{3}}(\xi)\,d\xi \tag{2.32}$$

where $\alpha = e^2/4\pi\varepsilon_0\hbar c \simeq 1/137$ is the fine structure constant, and $K_{\frac{5}{3}}(\xi)$ is a modified Bessel function of the third kind. Integration of Eq. (2.32) over the relative energy, x, from 0 to ∞ gives the mean number of synchrotron photons per path length,

$$\frac{dN}{ds} = \frac{5\alpha}{2\sqrt{3}}\frac{eB_\perp}{m\beta c} = \frac{1}{\lambda} \tag{2.33}$$

Hence, λ represents the mean free path between emitted photons. Notice that when the particles are in the ultra-relativistic regime ($\beta \approx 1$), λ depends only on $B_\perp$, and is independent of the energy of the particle. For synchrotron photons from primary high energy CR electrons at the altitude of the CREST experiment where the magnetic field is approximately 0.5 G, the mean free path can be approximated (for $\beta \approx 1$) as,

$$\lambda \simeq \frac{0.1618\ \ (\mathrm{T})}{B\ \mathrm{Sin}(\theta)} \mathrm{m} \geq 3.23\ \ \mathrm{km} \tag{2.34}$$

where θ is the angle between the local magnetic field and the direction of the electron. Therefore, in the Antarctic magnetic field, the mean free path for high energy CR electrons is at least ∼3.2 km.

By defining a normalized probability function of the modified Bessel function of the third kind as,

$$n_\gamma(x) = \frac{3}{5\pi} \int_x^\infty K_{\frac{5}{3}}(\xi)\, d\xi \tag{2.35}$$

the mean relative energy can be obtained,

$$\mu = \int_0^\infty x n_\gamma(x)\, dx = \frac{8}{15\sqrt{3}} = 0.30792. \tag{2.36}$$

Consequently, the mean energy of synchrotron photons per mean free path, λ, is simply,

$$\overline{E} = \mu\, E_c \propto \gamma^2 B_\perp \leq \gamma^2 B \tag{2.37}$$

Thus, the mean energy of synchrotron photons is proportional to γ^2 in the limit of an infinite number of photons. This property of synchrotron radiation can be used to estimate the energy of the high primary energy CR electron, even though only a small number of synchrotron photons are measured. Fig. 2.11 shows the maxima of the mean synchrotron photon energy per mean free path (when the angle between the magnetic field and the direction of electron is perpendicular, $\theta = \pi/2$) for different uniform magnetic fields as a function of the electron energy.

2.6.1 Further Reading

There are useful simulation tools, textbooks, and references regarding cosmic ray propagation and acceleration. These helpful resources are:

2D and 3D CR Propagation Simulation in the Galaxy

- Strong and Moskalenko, *GALPROP* [46]

Cosmic Ray Astrophysics

- Berezinskiĭ et al. , *Astrophysics of Cosmic Rays* [40]
- Gaisser, *Cosmic Rays and Particle Physics* [14]
- Longair, *High energy astrophysics* [18, 47]
- Schlickeiser, *Cosmic Ray Astrophysics* [48]

Review of CR Acceleration

- Blandford and Eichler

  Particle acceleration at astrophysical shocks: A theory of cosmic ray origin [49]
- Malkov and Drury

  Nonlinear theory of diffusive acceleration of particles by shock waves [29]

CHAPTER III

Detection Method of CREST Payload

3.1 Designing the Instrument

The CREST instrument was designed to detect individual synchrotron photons from primary CR electrons with a its synchrotron characteristic described in the previous Chapter. Since the instrument only needs to intercept a portion of these synchrotron photons, it enjoys a larger effective area than the actual physical size of the instrument. Past satellite and balloon experiments have been quite limited by both the geometrical size of the instrument and its exposure time.

The physical size and the weight of the CREST instrument employed in Antarctica is determined by the nature of the balloon experiment. Both transportation of the payload from the U.S.A. to Antarctica and NASA safety requirements restrict the physical dimension of the payload. Among all the carriers flying from New Zealand to Antarctica, the C-17 is the only cargo plane which can contain the full size of the CREST instrument (114 inches × 114 inches). The integration of the instrument at the McMurdo base in Antarctica is very tight in schedule and limited in space.

The weight limitation is also an important factor. The increase in the weight of the instrument decreases the flight altitude and, therefore, it results in increasing atmospheric absorption of the signal synchrotron events and increased background

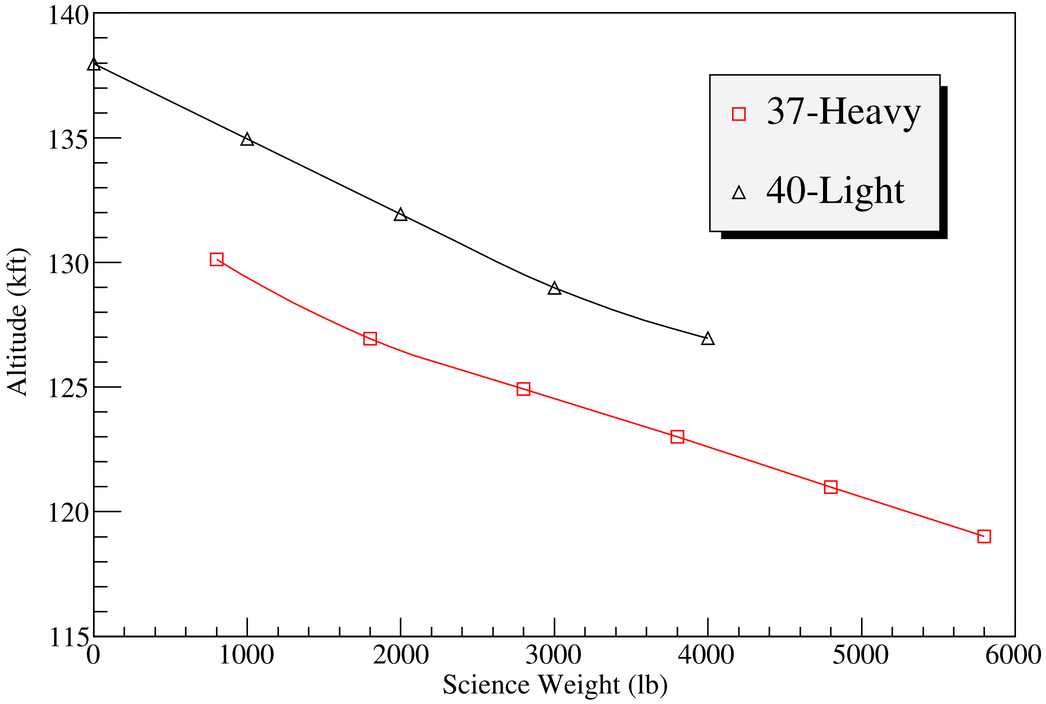

Figure 3.1: LDB Antarctica flight altitude

from bremsstrahlung photons. It also increases atmospheric x/γ-ray backgrounds. Among the possible long during balloons, the Columbia Scientific Balloon Facility (CSBF) has two (40-light and 37-light) available for the weight class of the CREST instrument (science weight ~4,000 lb). Figure 3.1 shows the possible CREST altitude potential for an Antarctica flight, based on the data provided by CSBF. Chuck Bower from Indiana University estimated that use of the 37-light would produce 30% less signal events, but a 10% increase in the single background rate. The overall background will increase ~35% for 4-hold conicidence hits. The weight restriction became a serious issue after it was realized that it was necessary to put a pound lead (Pd) shields around each crystal/PMT assembly to reduce the false event rate due to Compton scattering (See Appendix C). This lead shielding added an additional 900 lb (= 1 lb × 900 inner crystal/PMT assemblies) the instrument.

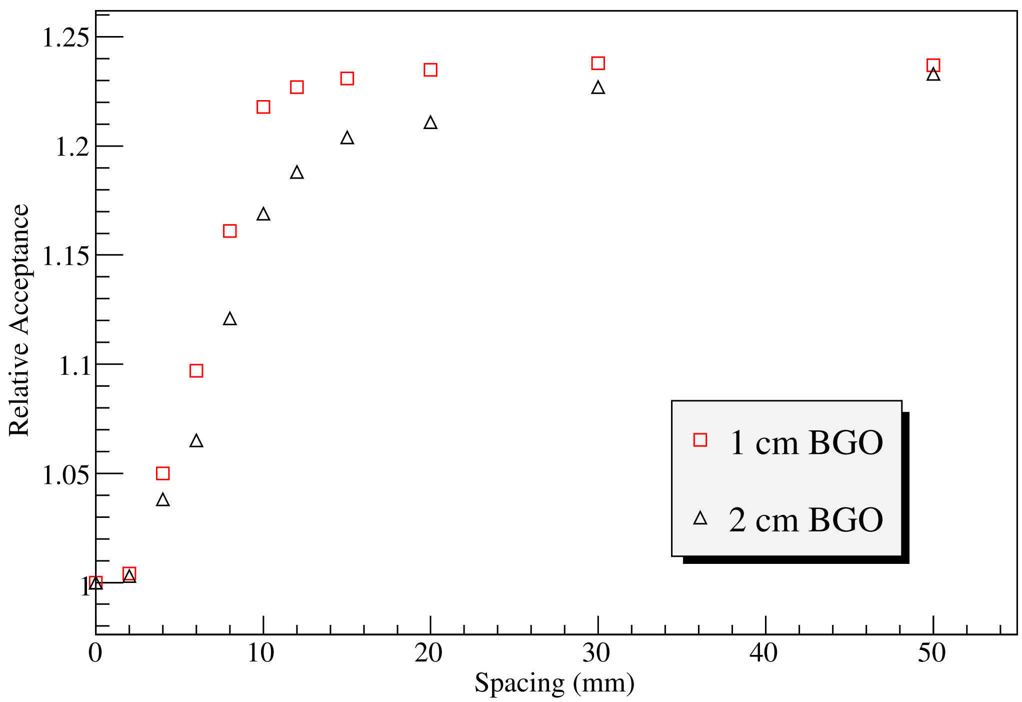

Figure 3.2: Relative acceptance of instrument to isotropical photon incidence with respect to the spacing between the center of the BGO crystals.

To detect individual synchrotron photons, the CREST instrument has multiple crystal/PMT assemblies with crystal facing upwards in the supporting foam structure (Figures 4.1 and 4.3). Segmenting the instrument using multiple crystal/PMT assemblies enables us to achieve much larger detection area with smaller active crystal detection area (only $\sim$ 25% of the instrument is filled with the crystals). The optimal spacing of the crystal/PMT assemblies was determined by our previous collaborator, Micheal DuVernois, using a Geant4 simulation. With fixed instrument area, the spacing was first determined to maximize the relative acceptance of the instrument to an isotropic photon flux. Figure 3.2 shows the simulated relative acceptance (normalized at 0 (mm) spacing) for cylinderical 2.54 cm radius BGO crystals with different thickness. The acceptance initially increases as the spacing increases due to the increased acceptance at higher incidence angles from the sides of the crystals. The ideal spacing is achieved when the spacing becomes comparable to the thickness where the acceptance levels off.

With fixed spacings for different thickness and type of crystals (1 cm and 2 cm for both BGO and BaF_2) as well as for different bulk order prices for PMTs and crystals, the cost per event was optimized. Below $\sim$ 8 TeV, the thinner 1 cm BaF_2 crystals became cheaper per event. Above 8 TeV, the 2 cm BaF_2 crystal becomes the least expensive. The comparison between BGO and BaF_2 crystals also show that 2 cm thick BaF_2 crystals have more detected events than 1 cm BGO crystals, having approximately same number of radiation lengths. It was concluded that the use of 2 cm thick BaF_2 crystals was optimal (due to timing resolution, compared with BGO crystals as discussed in Sec 4.5.2) for the CREST instrument. To maintain modularity of the electronics, the spacing between the centers of the crystal/PMT assemblies was set at 7.5 cm (2.5 cm spacing distance).

Because of the large flux of cosmic ray protons (Figure 2.1), rejection of charged particles is a critical issue. Detection of high energy electrons through their synchrotron emission naturally provides good proton rejection but a high charged particle flux, if not rejected, can lead to a substantially increased rate of accidental events. The CREST instrument can take care of these charged particles with a nearly hermetic 4π ster-radian veto plastic scintillator shield. A monolithic calorimeter type of experiment such as GLAST instrument will have difficulty rejecting CR protons from electrons, since a small fraction of the time protons can produce electromagnetic showers through early neutral pion production and decay. Even a small ($\sim 10^{-4}$) fraction of such events can overwhelm the electron measurement with proton contamination.

Furthermore, Figure 3.3 shows the effective geometrical factors between the CREST-type instrument [6] and a monolithic calorimeter. The geometrical factor for detecting secondary synchrotron radiation from electrons was derived by integrating the electron flux over zenith and azimuthal angles for a 2 m diameter aperture, requiring more than 3 photons to fall inside the instrument. This was calculated at an altitude of 4 g/cm^2 and a cutoff energy of 20 keV at Ft. Sumner, NM. The geometrical factor for the balloon-born calorimeter assumed 14 X_0 of lead and a science instrument weight limitation of 1500 kg. The significant increase of the geometrical factor for detecting secondary synchrotron radiation is quite apparent, and the CREST instrument takes advantage of this method.

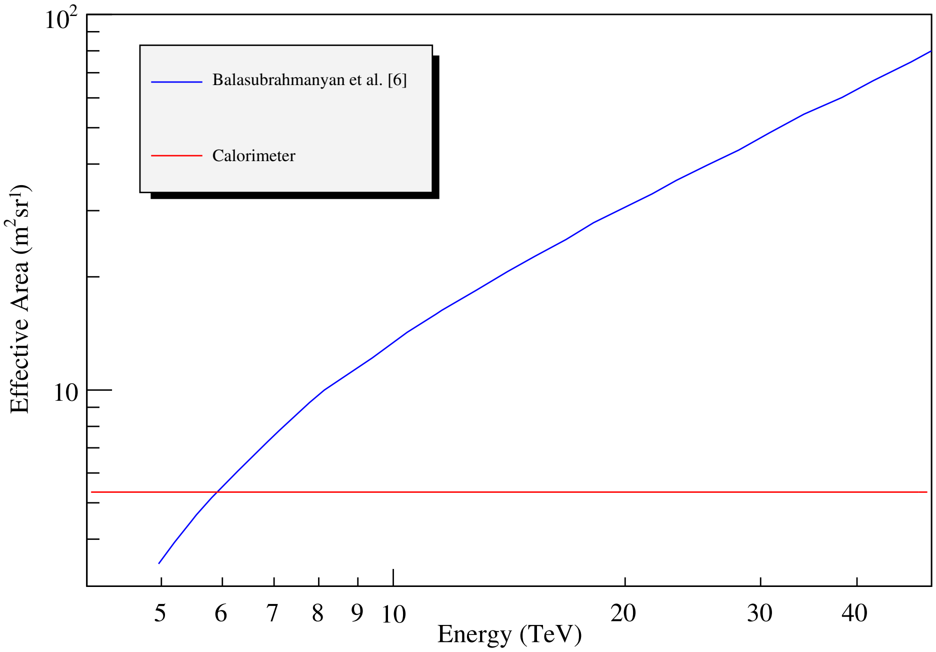

Figure 3.3: Effective area comparison between the CREST-like instrument and simple calorimeter.

Currently, the CREST collaboration is studying the impact of bremsstrahlung from the primary CR electrons which also generate synchrotron photons.

3.2 Estimation of Number of Synchrotron Photons and Effective Detector Width

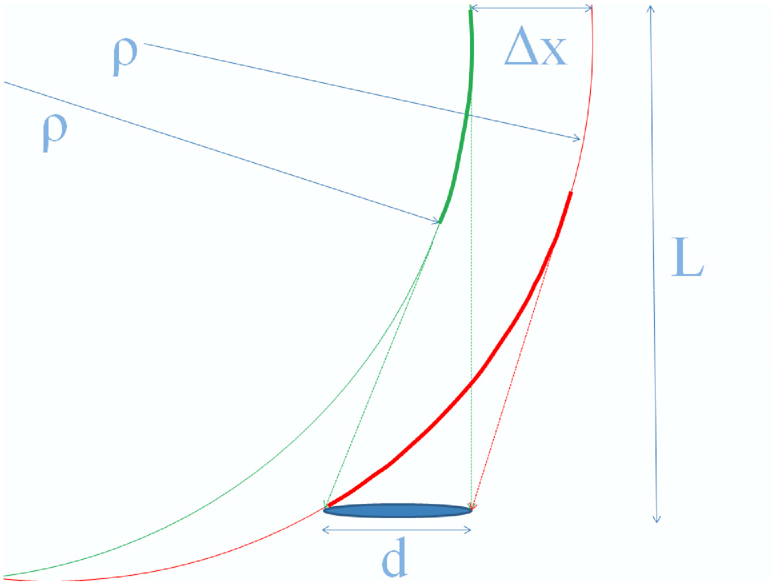

Figure 3.4: Simple geometry used for this estimation: ρ is radius of curvature, d is one-dimensional size of the instrument, L is characteristic height, and $\Delta\text{x} = \rho - d - \sqrt{\rho^2 - L^2}$ is the horizontal distance, which geometrically encompasses the maximum and minimum effective path lengths (shown in red and green, respectively).

The number of synchrotron photons incident on the CREST instrument can be estimated for vertical incidence of primary electrons. This estimation scheme was developed by Professor Carl Akerlof from University of Michigan and presented in this Section. Figure 3.4 shows the geometry concerned for detection of synchrotron radiation from the vertically incident electrons. The radius of curvature, ρ, is expressed as 3.336 (m) $\times p(\text{GeV}/c)/(\text{B(T)} <\sin(\theta)>)$ [44], and the average angle between the magnetic field and the direction of the particle $<\sin(\theta)>$ can be taken to be 0.816 for simplicity. The effective path length is the distance of the arc (shown in thicker lines), which can be caluclated exactly using geometry. The mean number of detected synchrotron photons generated at each trajectory is calculated by the product of the number of the photons per path length (Eq. 2.33), path length, and the fraction of the detection area. The maximum path length can be seen when the primary particle passes through the end of the instrument as in red in Figure 3.4.

Figure 3.5 shows the mean number of detected synchrotron photons for maximum and minimum path lengths (shown in red and blue, respectively) and the average path length over Δx (in yellow). This calculation was performed by taking the Earth magnetic field to be 0.5 G, an energy cutoff of 20 keV, $L = 2000$ km and $d = 2.62$ m (for equivalent circular detector of the CREST instrument). It is shown here that for vertically incident primary particles the CREST instrument is insensitive to synchrotron radiation until large enough path length exists above the instrument. At maximum path length, the estimated mean number of photons is approximately 3.1 at 10 TeV.

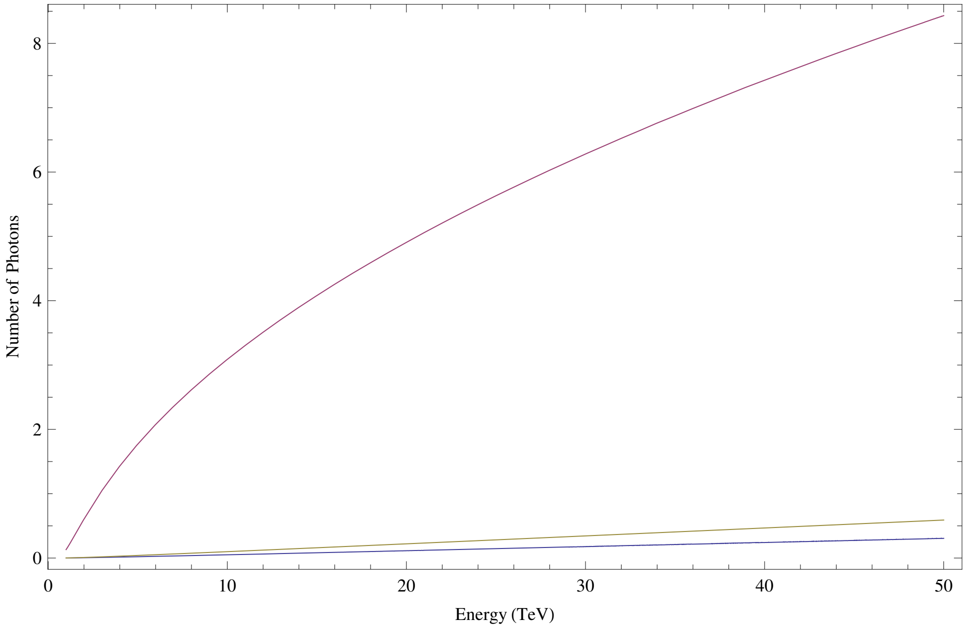

Figure 3.5: The number of synchrotron photons within the instrument as a function of the energy of the primary electron with maximum, minimum, and average path lengths for vertical incidence of the primary particle.

Figure 3.6 shows one dimensional effective detector widths observing sufficient number of the photons as a function of primary particle energy. These are the cases

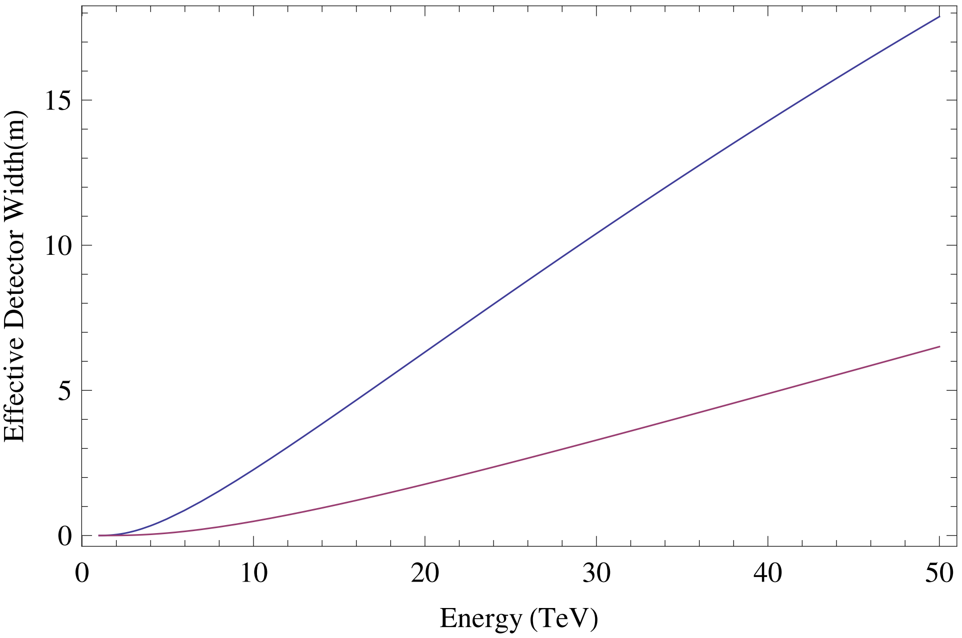

Figure 3.6: One-dimensional effective detector width for finding 3 or more photons in blue and finding 4 or more photons in red as a function of the energy of the primary particle at vertical incidence.

for finding more than two photons and for finding more than three photons (shown in blue and red, respectively) in a function of the energy of the primary particle. Here, the effective detector width is obtained by,

$$\Delta x_{\text{effective}} = \int_0^{\Delta x} \text{probability}_{>m}(x)dx \tag{3.1}$$

where the probability is to detect more than m photons in terms of the average observed number of photons, <n>, and can be expressed as,

$$\text{probability}_{>m}(x) = 1 - \sum_{i=0}^{m} \frac{< n >^i}{i!} e^{-<n>}. \tag{3.2}$$

The effective detector width increases linearly with the energy of the primary electron, and the effective widths of the CREST instrument are 6.5 and 17.9 m at 50 TeV for probability$_{>3}$ and probability$_{>2}$, respectively.

Knowledge of the effective detector width from Fig. 3.6 allows us to estimate the number of events as follows. This expected number of the events can be expressed by

$$\mathrm{N}_{e^\pm} = T \int_{E_{\mathrm{low}}}^{E_{\mathrm{high}}} \mathrm{GF}\,(E)\, J(E)\, dE \tag{3.3}$$

where T is the duration of the measurement, $\mathrm{GF} = \mathrm{GF}(E)$ is the geometrical factor, and $\mathrm{J}(E)$ is the electron flux. For non-vertical incidence of primary electrons, observed average number of photon from Fig. 3.5, <n>, is in general proportional to the effective radiation path, which scales like a square root of the physical detector width, $\sqrt{d}$. Since d is proportional to $\cos(\theta)$, <n> is proportional to $\sqrt{\cos(\theta)}$. probability$_{>m}$ in Eq. 3.2 is therefore approximately proportional to $\left(\sqrt{\cos(\theta)}\right)^{m+1}$ in the highest order, and the angular dependancy of the GF can be simply integrated by,

$$\mathrm{GF}(E) = 2\pi d \int_0^{\frac{\pi}{2}} \Delta x_{\mathrm{effective}}(\theta, E)\, d\theta. \tag{3.4}$$

In the case of a 100 day flight with a flux of $(1.17 \pm 0.02) \times 10^{-4} \times E^{-3.05\pm0.02} \times e^{-E/(2.1\mathrm{TeV})}$ $(\mathrm{m}^{-2}\mathrm{sr}^{-1}\mathrm{s}^{-1}\mathrm{TeV}^{-1})$ from the HESS experiment [16], Equation 3.3 then provides a rough estimate of approximately 18.9 and 1.9 events from 2.5 to 50 TeV primary electrons for probability$_{>2}$ and probability$_{>3}$, respectively. This corresponds to 0.2 and 0.02 events per day.

The next Chapter presents the individual hardware and software components of the CREST instrument.

CHAPTER IV

CREST Front-End Detector Development and Testing

The CREST instrument must intercept a portion of the line-like signature from synchrotron photons emitted by high energy CR electrons as they travel through the magnetic field of the Earth. This detection method requires an instrument which is able to identify individual synchrotron photons. To do this, the CREST instrument is composed of segmented photon-sensitive detectors. A typical method of detection of these photons, whose energies range from ∼20 keV to a few 10's of MeV, utilizes a high density inorganic scintillator viewed by a photomultiplier tube (PMT). The scintillator/PMT assembly has to be sensitive to photons of interest, but at the same time it needs good timing resolution to both identify individual synchrotron photons and to separate them from background. The electronics of the CREST instrument must be able to handle the data rates from these events. These are the basic scientific requirements for the design and the construction of the CREST instrument.

This chapter will first present the CREST instrument hardware and electronics for the Antarctic flight. Next, the results of the initial development of the crystal/PMT assemblies and their performance tests for the CREST-I flight will be given. At the end of the chapter, a close examination of the front-end electronics will be presented.

4.1 Antarctic CREST Instrument

4.1.1 Mechanical Structure and Electronics of the Instrument

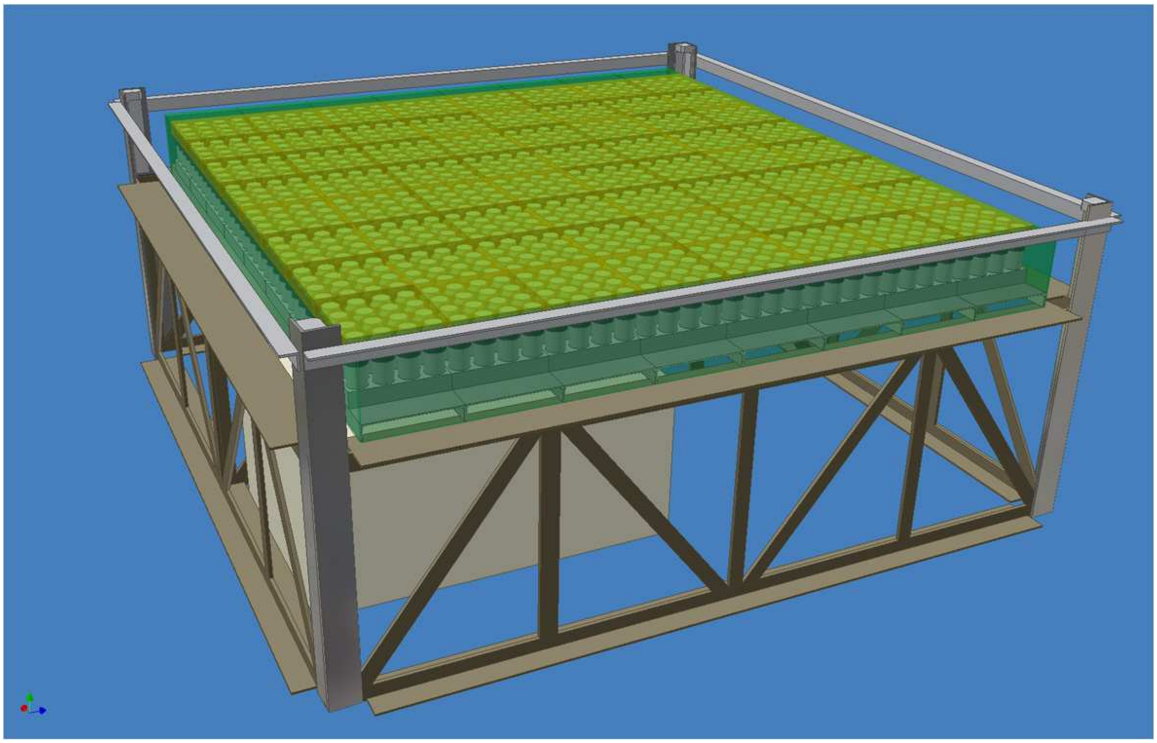

Figure 4.1: Schematic drawing of the Antarctic full-size CREST instrument. 1024 crystal/PMT assemblies, completely covered by veto scintillators (in dark green), are supported by aluminum alloy and carbon fiber composite structure (shown in grey). The total size of the instrument is 2.86 m × 2.86 m × 1.18 m. The electronics and solar panels are not shown in this figure.

Figure 4.1 shows overall structure of the Antarctic CREST instrument. Its size and weight were constrained by the NASA scientific balloon requirements. Synchrotron photons from high energy CR electrons are expected to come from above the horizon of the instrument, and the number of crystal/PMT assemblies (shown in light green) and their spacings were optimized by a simulation initially performed by Michael DuVernois to minimize the dollar cost per synchrotron event at the fixed size of the instrument. Currently, there are a total of 1024 BaF_2 crystal/PMT assemblies on the instrument. These assemblies are enclosed over the complete 4π solid angle by 5 mm thick plastic scintillators to separate synchrotron photons from charged cosmic ray background particles such as protons and heavier nuclei. The front-end electronics is located right underneath the crystal/PMT assemblies (Fig. 4.3). The flight computer, the main digital control electronics board (called the XEM carrier board), and the other supporting electronics are located below the bottom scintillators. To provide power to this electronics, there are solar panels and batteries on the instrument (not shown in the Figure 4.1).

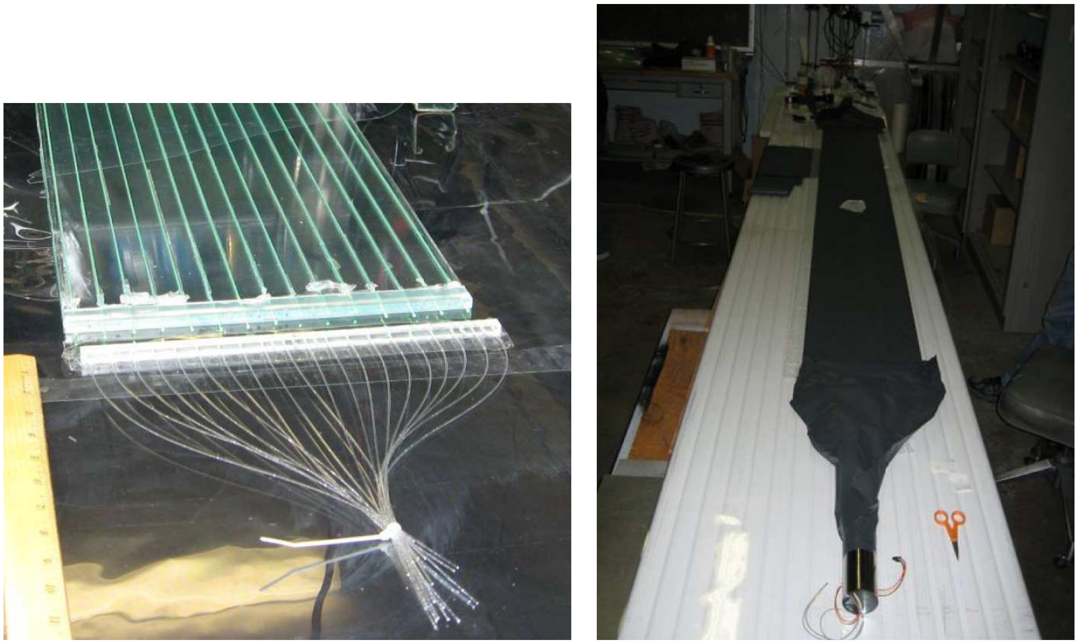
(a) (b)

Figure 4.2: Pictures of (a) Kurary wavelength shifting fibers embedded in the transparent plastic veto scintillator. Stray UV photons in the room cause these fibers glow in the green. (b) One complete scintillator package wrapped with black Tedlar film. Both pictures were taken by Matt Geske and Tyler Anderson from Penn State Unversity.

Manufactured by Eljin Technology, there are 21 veto plastic scintillators (EJ-200): 8 on the top, 4 on the sides, and 9 on the bottom (one extra veto scintillator is needed to cover the electronic cables) in the current scheme. The size of the top veto plastic scintillator is 2.6 m × 32 cm × 5 mm, but each plastic scintillator has slightly different dimensions, depending on its location on the instrument. To read out blue scintillation photons generated by charged particles, the plastic scintillators are optically coupled with 15 Kuraray Y-11 double-clad wavelength shifting fibers (Fig. 4.2(a)). These fibers absorb blue scintillation photons from the scintillator, re-emit green scintillation photons, and then pipe them down to the PMTs (Hamamatsu R7724CW) at the both ends of the scintillator. To maximize light output and to avoid light leakage, these plastic scintillators are wrapped in three layers of Teflon tape and two layers of black Tedlar polyvinyl fluoride film (DuPont), a highly reflective Teflon-based material. Light collection performance measured by our collaborators from Pennsylvania State University showed that ∼20 photoelectrons are observed at each end of the scintillator in response to a normally incident singly charged particle at the center.

For convenience of construction and disassembly at the recovery site, the CREST instrument was designed to be modular. The array of crystal/PMT assemblies is divided into eight identical aluminum alloy C-channels. On the top of each channel (Fig. 4.3(a)), there are 128 crystal/PMT assemblies (32 by 4 PMTs). A veto scintillator is located on the top of each the 128 assemblies along the direction of the channel, while the bottom veto scintillators (not shown in the Figure 4.3(a)) run in a perpendicular direction to the channels underneath the C-channel. Figure 4.3(b) is a schematic representation of the inside of the C-channel where the front-end electronics are suspended. These front-end electronics consist of a sedecim[1] discriminator module, a sedecim ADC (sADC), Sedecim Voltage Interpreter (SVI), and Sedecim Timing and Analog Control (STAC). Each of these front-end electronics boards handles 16 crystal/PMT assemblies, and these electronics are inter-connected through control cables (CRESTBus and VETOBus: Bussed LVDS) and voltage interpreter

---

[0] Sedecim means sixteen in Latin

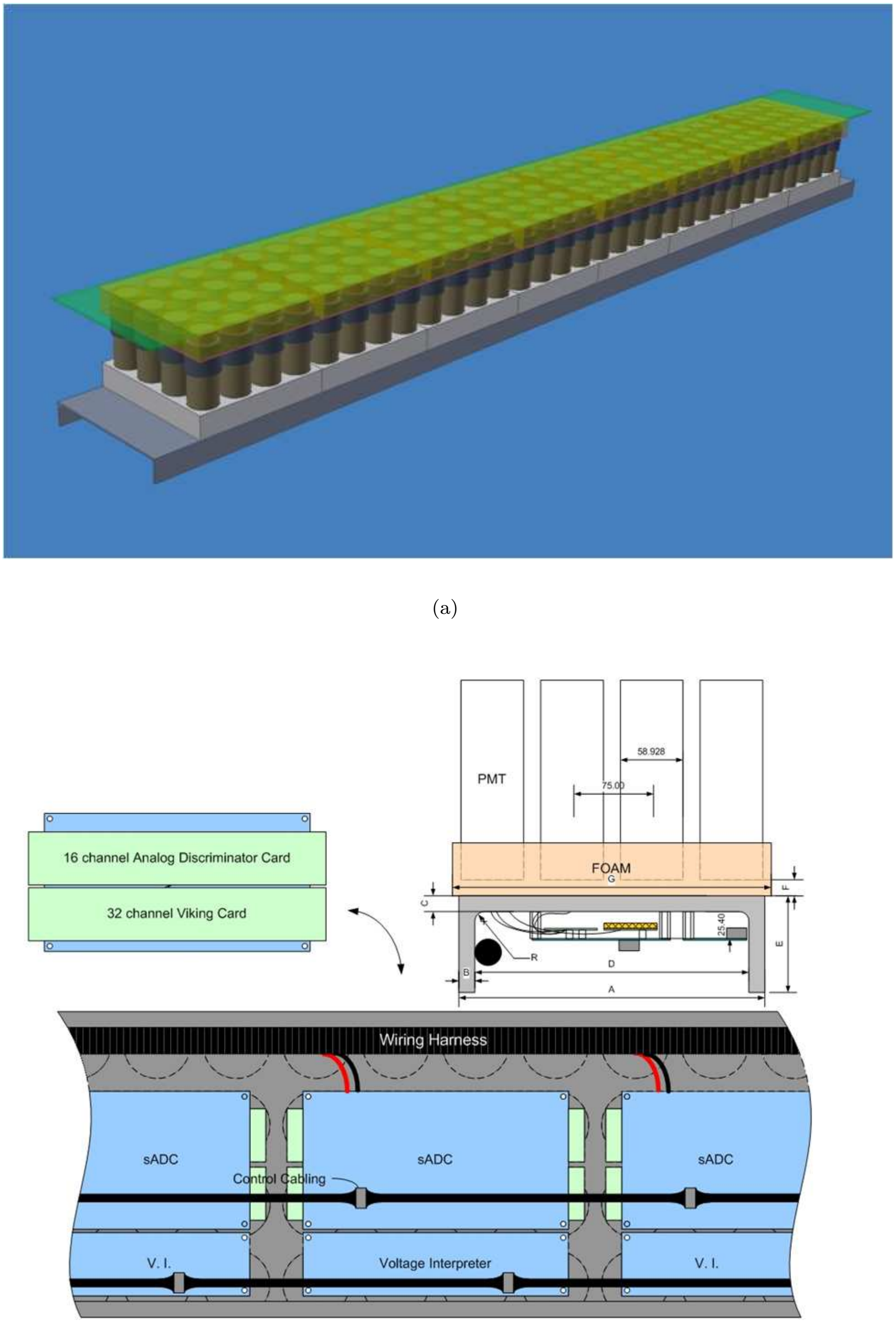

(a)

(b)

Figure 4.3: Drawings of the CREST channel: (a) one channel with 128 crystal/PMT assemblies (2.60 m × 35.7 cm × 25.7 cm tall) with one top veto scintillator. (b) mechanical locations of the front-end electronics with respect to the crystal/PMT assemblies.

cables (SVI cables) to the XEM carrier board, which is located outside the channel.

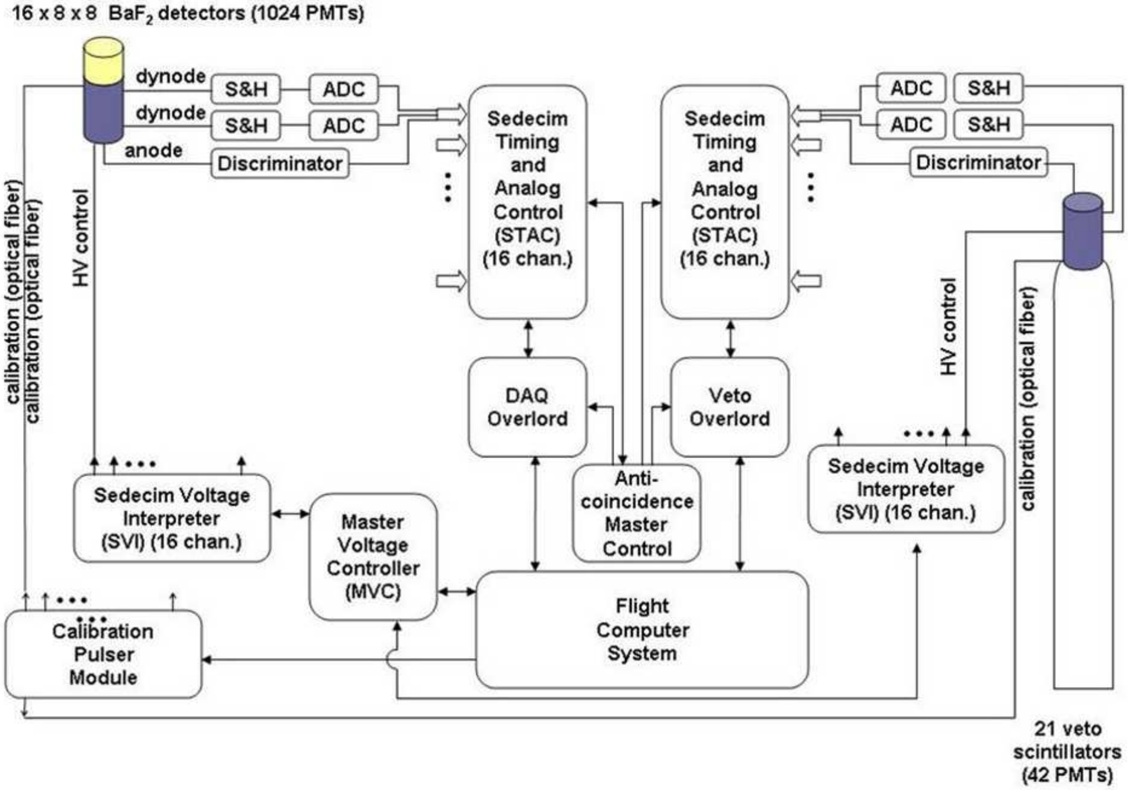

Figure 4.4: CREST data stream block diagram.

The heart of the CREST experiment lies in the electronics. Basic data flow of the CREST experiment is presented in the block diagram (Fig. 4.4) as follows: A signal generated from the crystal/PMT assembly is separated into three analog signals: one for the timing and the other two for the charges, which covers different energy ranges. As a result of baseline noise induced by the Cockcroft-Walton voltage divider (See Sec. 4.1.4.1) of the PMT, the charge from the 5th dynode is not currently able to be read out. To resolve this, an anode signal from the PMT is separated into two: one for the timing and the other one for the charge. The PMT anode thus provides both the timing and the charge at lower energy range, while the PMT 8th dynode provides the charge at higher energy range.

The timing portion of the anode signal from a crystal/PMT assembly initiates triggering of the discriminator. This time is recorded and digitized in the STAC to a least count of 1 ns (TDC). Next, this STAC, responsible for 16 crystal/PMT assemblies, reports a crystal hit and/or hits to the Anti-coincidence Master Control. The Master Control generates *charge digitize* commands back to all the STACs when either of the following conditions exist within a 32 ns time window: If it receives a pre-scaled number of single hits or more than 2 coincidence hits for the whole array. When the sADC with a hit and/or hits receives digitize commands from the STAC, it reads off the charges from both anode and 8^{th} dynode of the PMT (ADC), and reports two ADC values back to the STAC. The STAC sends the two ADC values and the TDC value to the DAQ Overload. The Overload packages these digitized values and sends the collection of these packages to the flight computer. At the end of the data pipeline, the flight computer records these event data into a solid-state flash hard disk, and sends selected portions of these data back to the ground through telemetry.

One of the critical features of the CREST electronics is to achieve better than 1 ns timing resolution within the limited power consumption of the balloon experiment (In terms of the digital electronics, one bit of data should at most correspond to 1 ns). This resolution can be accomplished by the extensive use of Spartran-3 Clocked Programmable Logic Devices (CPLDs) manufactured by Xilinx. By clocking four CPLDs at 125 MHz, using both clock-edges and shifting each phase by 90 degrees (Fig. 4.5), the Xilinx Field Programmable Gate Array (FPGA) firmware is able to reconstruct a rising edge from a discriminator to 1 ns least count. It was estimated that < 1 ns timing resolution is necessary to identify the directionality for line-like crystal hits from synchrotron radiation.

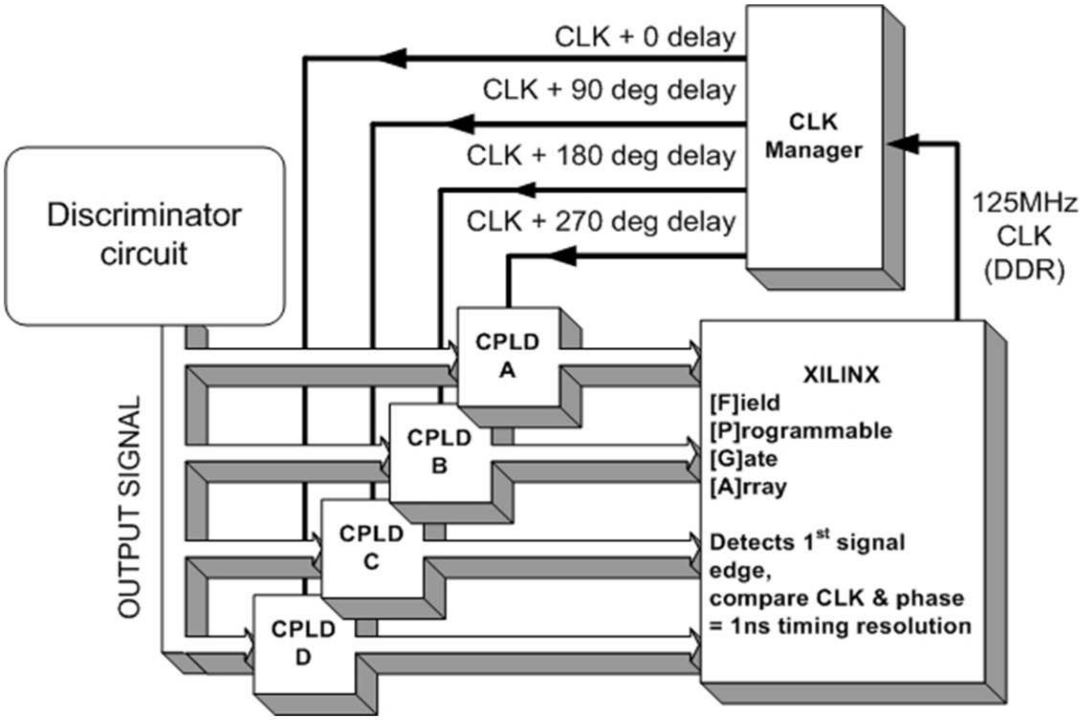

Figure 4.5: Principle of 1 GHz timing Clocked Programmable Logic Devices (CPLDs) drawn by John Ameel

Charge collection is based on two multi-channel VA chips from IDE Corp., Norway (IDE VA32_HDR11: 32 channels with 25 pC to −30 pC full scale) on the sADC board to cover a dynamic range of $\sim 10^4$. This chip, originally developed for silicone strip detectors, provides a charge sensitive preamplifier, a shaper and a sample and hold with output multiplexer. Two VA chips read off the charges from the 8^{th} dynode and the anode of the PMT upon receiving a *digitize* command from the Anti-coincidence Master Control through the STAC. The process of sequential digitization for each of the 32 channels results in a total of ~ 2 μs dead time. This becomes the main source of the total dead time for the CREST instrument (See. Section 6.1.5 for a discussion of the dead time from the simulation).

Verilog and VHDL (firmware programming languages) provide the control of all the digital electronics in STAC, DAQ and Veto Overload, MVC, and Anti-coincidence Master Control. These programs reside in standalone FPGA integration modules XEM3010 with Xilinx Spartan-3 from Opal Kelly (`http://www.opalkelly.com`). This module was selected, based on previous experience in NASA scientific balloon experiments, convenience of communication through USB (USB 2.0) with API, and PROM and SDRAM functionalities already included on the board.

Other than data accumulation, the flight computer has two other functionalities (Fig. 4.4): The flight computer controls and monitors all the preset voltages of the 1024 crystal/PMT assemblies with nominal gain of 5×10^6 through the Master Voltage Controller (MVC). The MVC, in turn, commands the Sedicim Voltage Interpreter (SVI), responsible for providing control voltages to 16 crystal/PMT assemblies. The flight computer also controls the Calibration Pulser Module. This generates calibration LED pulses into all the PMTs not only for monitoring individual gain drifts but also for calibrating relative timing offsets during the flight.

The data chain for the plastic veto scintillators works in the same way as that for the crystal/PMT assemblies. One difference is that discriminator triggers from the veto scintillators do not participate in the coincidence decision of the Anti-coincidence Master Control. As a result, only discriminator triggers from the crystal/PMT assemblies on the array can initiate coincidence logic to read off the charges from both crystal/PMT and veto scintillator assemblies. Otherwise, this would result in a significant increase of the instrument dead time and the collection of irrelevant data.

The next three sections will present the descriptions of the CREST hardware for which I had significant involvement.

Table 4.1: Characteristics of NaI, BGO, and BaF_2 [50].

Crystal	Density (gm/cm^3)	μ^{-1} (cm)[2]	λ_{max} (nm)	Index of Refraction	Photons (/MeV)	Decay time (ns)	Photons (/MeV/ns)
NaI(TI)	3.67	3.05	415	1.85	38,000	230	165
BaF_2	4.89	2.29	195,220	1.49	1,800	0.8	3,000
			310		10,000	630	15
total					11,800		3,015
BGO	7.13	1.11	480	2.15	700	60	12
			480		7,500	300	25
total					8,200		37

4.1.2 Scintillator Crystals: BGO and BaF_2

The choice of the scintillator crystal is an integral part of X/γ-ray photon detection. The CREST experiment requires three main characteristics of the scintillator crystal to accomplish its scientific goal. First, the crystal has to be dense enough to measure synchrotron photons in the energy range from a few 10's of keV to a few 10's of MeV. The bismuth germanate, $Bi_4Ge_3O_{12}$, (BGO) crystal was selected for this reason for the initial CREST proposal and the first CREST flight (CREST-I). Compared with commonly used thallium-doped sodium iodide, NaI(TI), (Table 4.1), the BGO is $\sim$three times denser and has $\sim$three times lower attenuation length at 511 keV.

The photon energy deposited inside the crystal has to be efficiently converted into scintillation photons. This, combined with spectral distribution of quantum efficiency of the PMT, determines the energy resolution of the crystal/PMT assembly. In this respect, the number of the scintillation photons from BGO crystals is approximately three times less than those for a NaI crystal at a given energy. As a consequence, the energy resolution of the BGO crystal is $\sim$ 43% poorer than that of the NaI crystal (if all the scintillation photons are converted into photoelectrons). Lastly and most importantly, it is necessary for the timing distribution of the scintillation

---

[2] Attenuation length for 511 keV photons

photons from the crystal to have enough photoelectrons in the first ns to accomplish $\leq \sim 1$ ns timing resolution. This becomes problematic for BGO crystals, because of the smaller number of scintillation photons generated at lower deposited energy. Additionally, the timing distribution of BGO has a long exponential decay. The timing resolution of the BGO crystal at low energy was measured by me, and the result will be presented in Sec. 4.5.

Among the available scintillation crystals, BaF_2 crystal is a great candidate to resolve this matter: It has the fastest decay time among inorganic crystals, and this in turn yields excellent timing resolution even at lower energy. Moreover, the amount of scintillation photons in the fast component does not depend on temperature. This is especially beneficial for the CREST instrument which expects to have large temperature fluctuations during its flight. (BGO crystals have a rather large dependence of total light output with temperature [51].) One of the disadvantages for the use of BaF_2 crystals is that the radiation length is twice as large as for BGO crystals. As a result, this requires twice the thickness for BaF_2 crystals to obtain one radiation length of thickness. The wavelengths of the scintillation photons from the BaF_2 crystal (fast components 195 nm and 220 nm at maximum wavelengths) are too low for transmission through regular borosilicate glass window PMTs. Various possibilities for resolving this problem were investigated and tested by me, and the results of these measurements will be shown in Section 4.5. Note that the price and availability of the scintillation crystals were also major limiting factors for selection in the CREST experiment.

4.1.3 Interaction of X/γ-ray Photons

For the detection of synchrotron photons from high energy electrons, the physical interaction processes between photons whose energies in X/γ-ray range and the ab-

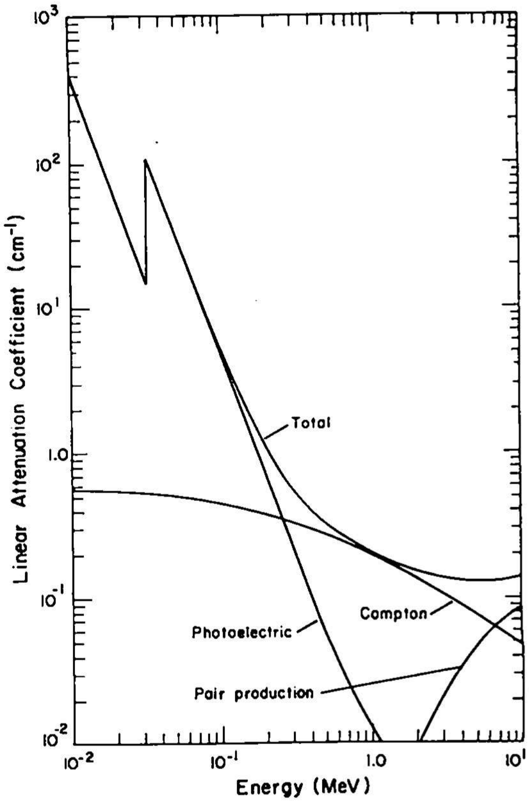

Figure 4.6: X/γ-ray energy dependence of linear attenuation coefficient in NaI from "Harshaw Scintillation Phosphors," Harshaw Chemical Company.

sorber material must be understood. First, three major interaction mechanisms of x/γ-ray photons with the material will be presented. Next, the effect of the finite size of the material on the measurement of photon energies will be discussed.

Figure 4.6 presents the energy dependence of the linear attenuation coefficient, μ, for photon interaction with NaI. The linear attenuation coefficient describes the probability of photon interaction involving absorption, scattering, and pair production per unit path length of the material. It can be defined through $I = I_0 e^{-\mu t}$ where I and I_0 are the number of transmitted photons with and without the absorbing material respectively, and t is the thickness of the material. At different photon energies the dominant interaction mechanism is quite different: At relatively low energies, photo-electric absorption is the dominant mode of the photon interaction. In Figure 4.6, slightly above 30 keV, K-shell characteristic X-rays resulting from the binding energy of the electron are shown as a sharp edge for NaI. Note that photo-electric absorption in the linear attenuation coefficient can be roughly expressed as constant × $Z^n/{E_\gamma}^{3.5}$ where Z is atomic charge of the material and E_γ is photon energy. Higher Z is thus preferable for X/γ-ray detection material. At higher energies, Compton scattering between photons and the electrons in the material takes over. Above a threshold energy of 1.022 MeV, pair production of $e^\pm$ is possible, and at much higher energies, it becomes the most dominant mechanism. As a result, the linear attenuation coefficient can generally be expressed as the sum of these three processes and μ = probability of (photoelectronic absorption + Compton scattering + Pair production) per length.

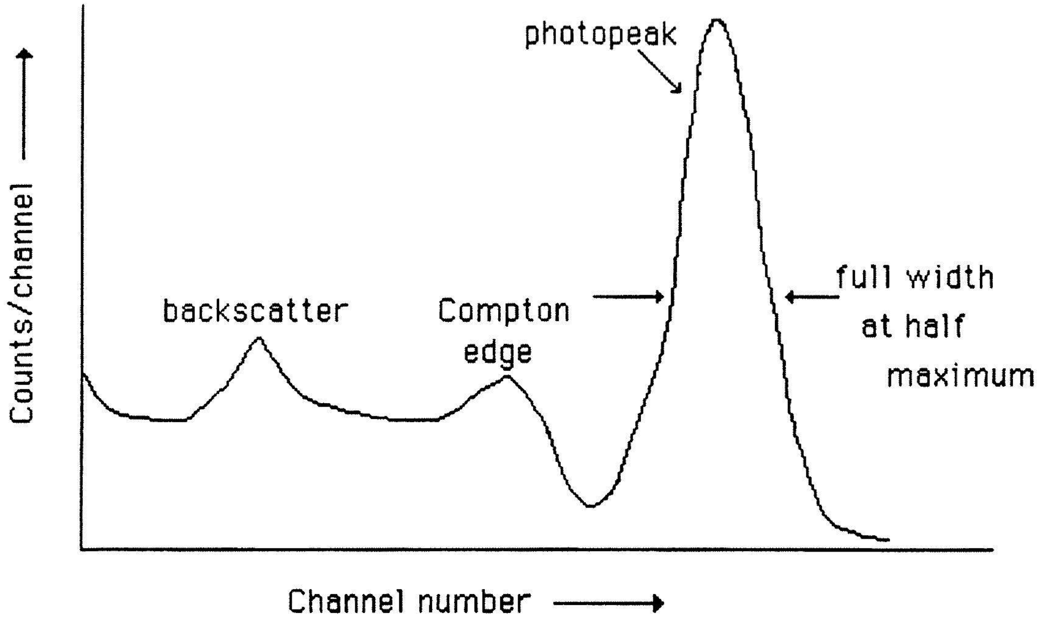

Figure 4.7: Example of x/γ-ray spectrum (from Undergraduate Class Note at Rutgers University)

The containment of deposited energy by the photon inside of the finite size of the absorber material must be taken into consideration. For an ideal, infinitely large detector, all the energy of the incident photon can be transfered into the material through the three processes described above. However, in reality the finite size of the material allows deposited energy to leak out without generating a signal. Figure 4.7 shows the typical X/γ-ray spectrum in the scintillator. A *photopeak* is at where all the energy of the photon is transfered into the material. Then, it generates a Poisson distribution of scintillation photons, with a width in the measurement (typically defined as a full width at half maximum). A *Compton edge* and a *Compton continuum* at energies below the Compton edge results when some portion of the photon energy is transfered into the scintillator through the combined effect of Compton scattering and photo-electric absorption. A back scattering peak occurs when photons are first Compton scattered by the surrounding materials, and then are absorbed by the detector material. Also, incident photons whose energies are above the 1.022 MeV produce positrons inside the material, and it then annihilates to produce a pair-production peak at 0.511 MeV (not shown). Throughout this argument, it is apparent that the atomic number, Z, and the size of the scintillator are important factors for the detection of X/γ-ray photons.

4.1.4 Photomultiplier Tube (PMT)

The photomultiplier tube (PMT) with its general characteristics of high sensitivity, low noise and fast response to photons is also critical for the CREST experiment. Figure 4.8 (taken from `http://en.wikipedia.org/wiki/Photomultiplier`) illustrates the simplest photon detection method with a scintillator and PMT: At the scintillator, incident photons are converted into multiple scintillation photons with lower energies. Next, these scintillation photons interact with the photocathode of the PMT and are converted into photoelectrons by the photoelectric effect Then, the photoelectrons are accelerated by the voltage differences between the dynodes of

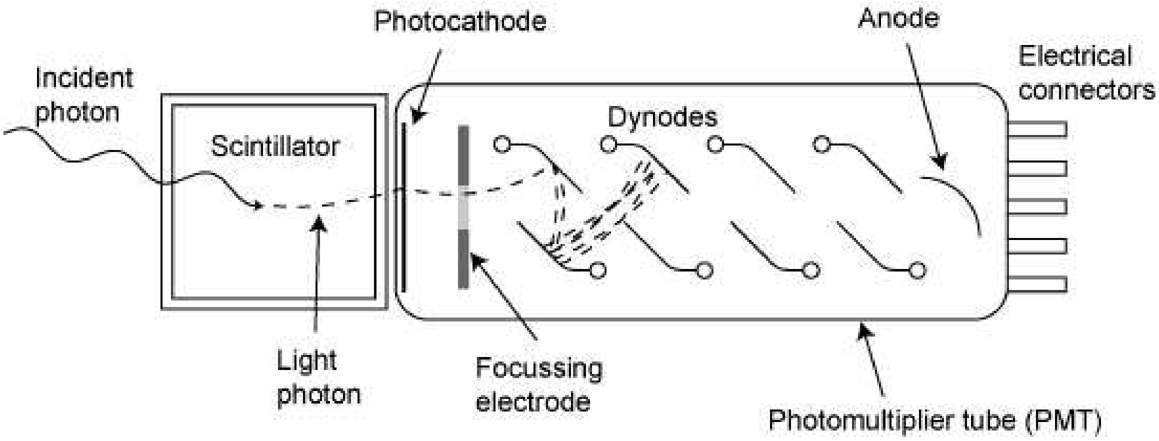

Figure 4.8: Schematic illustration of photon detection method (Colin Eberhadt from wiki page)

the PMT and then are multiplied by generating secondary electrons in the dynodes. By this multiplication process, the number of the photoelectrons are significantly increased (typically on the order of $10^5 \sim 10^7$ per incident photo-electron at the anode), and form a measurable electrical signal by the time they reach the PMT anode.

The performance requirements of the PMT to perform the CREST balloon experiment can be summarized as the following:

1. High gain: Gains of all the PMTs are set at 3×10^6 for the CREST-I flight and at 5×10^6 for the Antarctic CREST flight. They are high enough to keep the signal for single photoelectrons above the baseline noise level of the discriminator so that it can trigger at the 0.5 photo-electron level needed for good timing resolution.

2. Pulse height resolution: The PMT should not degrade the pulse height resolution of the scintillator crystal. It is necessary to match the spectral distribution of the photons generated from the scintillator crystal with the transmission of the PMT window and the photocathode response.

3. Low magnetic sensitivity to reduce gain variations: Less than 5% gain varaition for any orientation with respect to the Earth's magnetic field for CREST-I, and less than 30% at 1 Oersted for the Antarctic CREST PMT. Weight restrictions of the Antarctic payload preclude the use of μ-metal shield. The plan is to monitor these variations and correct for them.

4. Good timing resolution to distinguish individual synchrotron photons as well as to reject background photons. The general requirement is less than 1 ns timing resolution.

5. Low noise: Since signals from PMT are triggered at a fraction of photoelectrons, the level of dark noise from PMT above the threshold of the discriminator has to be small. At a threshold of 1 mV, the PMT trigger rate should be less than 1 kHz.

6. Low power consumption: $\leq$ 60 mW per PMT at maximum.

7. Vacuum durability under near vacuum operation and light tightness: PMTs must survive for more than 3 months.

8. Price $\leq$ \$ 600 per PMT for 1024 PMTs.

These performance specifications were sent to different PMT vendors and evaluation PMTs were produced. I then tested these prototype PMTs to verify compliance with the specifications (presented in Sec. 4.2). Detailed specifications for the original CREST-I PMT and the Antarctic PMT can be found in Appendix A.

The current design of the Antarctic BaF_2 crystal/Hamamatsu PMT package is presented in Figure 4.9. The critical portion of this development was to have the crystal/PMT assembly both light-tight and vacuum-tight. This was achieved by

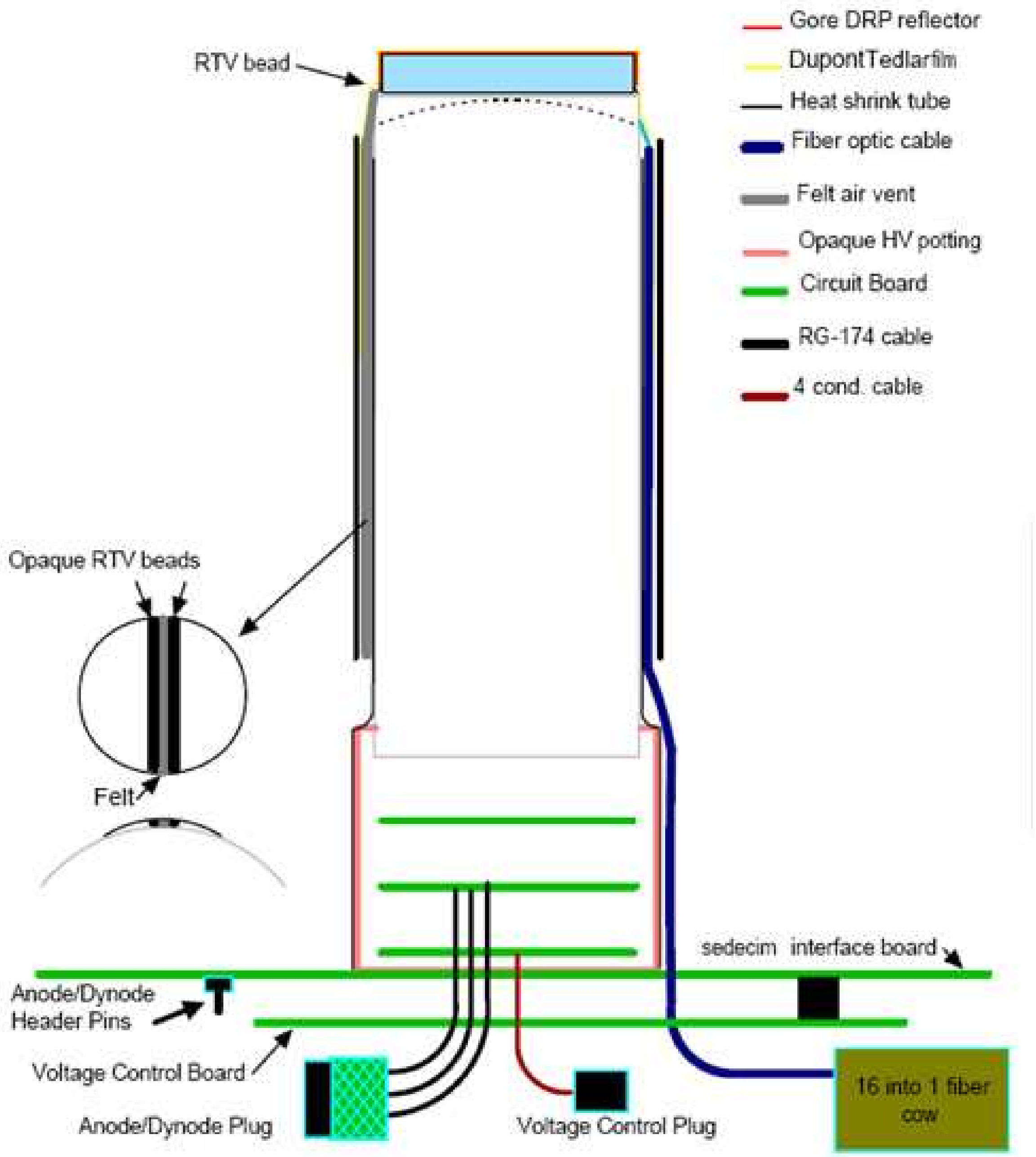

Figure 4.9: Schematic of the Antarctic CREST crystal/PMT assembly. A large effort was put into making this assembly light and vacuum tight with stabilization of the 2 cm BaF_2 crystal on the top of the PMT window. The fiber optics cable is for the calibration of both the gain of the PMT and the timing.

potting the Cockcroft-Walton base and by using layers of black felt, Tedlar film, and heat shrink. Gore DRP acts as a good UV photon reflector and is wrapped around the BaF_2 crystal and was covered by Tedlar film for light-tightness. At the bottom of the PMT, red opaque RTV was used for high voltage potting. Note that there is a fiber optic cable running along the side of the PMT to provide gain variation and timing offset calibration measurements during the flight. I developed this technique first by depositing aluminum in a vacuum chamber on the surface of the 45 degree fine-cut optical fiber. The thickness of the deposited aluminum and the angle of the fine cut on the tip of the optical fiber were examined to optimize light output into the PMT. This method of calibration was first used for the CREST-I flight. Indiana University then developed a different method by using a transparent ring attached at the end of the optical fiber, and this ring was placed around the top window of the PMT.

To complete the crystal/PMT package, a simulation study was performed by Jim Musser to estimate the effect of random coincidence of Compton scattered photons (Appendix C for more details). Random X/γ-ray background along with Compton scattering can mimic a line-like signature in the CREST instrument, and this could be misidentified as real synchrotron event. The simplest way to reduce this effect is to put a lead shield (Pb) around the crystal/PMT assembly. Since the weight of the Antarctic CREST payload constrained, the amount of Pb shielding must be minimized. By varying the thickness and positioning of the lead shield in the simulation, it was estimated that a 6 cm by 5 mm thick lead foil placed 6 mm above the face plate of the PMT around the crystal/PMT assembly significantly reduces the random coincidence without exceeding weight limitations. By requiring a 40 keV threshold and 4 crystal hits within 6 ns with rates estimated from the CREST-I flight, the misidentified event rate can be reduced to roughly one event per 30 day Antarctic flight.

4.1.4.1 Cockcroft-Walton Voltage Divider

One of the main features of the CREST PMT is a Cockcroft-Walton (CW) high voltage power supply potted in the base. With this power supply, the PMT can be individually programmed and controlled with a low voltage (∼a few volts), while regular PMTs require quite high voltages (∼a few thousands volts). Under the CREST experimental environment, it would be too heavy and impractical to operate with thousands of high voltage cables for the PMTs, and it would be much more likely for the high voltage to cause corona and current leakage under near vacuum flight conditions. Consequently, a CW power supply at the base of the PMT is ideally suited to the CREST experiment.

As shown previously, the photoelectrons are accelerated in the high voltage differences between dynodes of the PMT. Conventional PMTs (Fig. 4.8(a)) generate these voltage differences by a resistive divider network, while PMTs with a CW power supply (Fig. 4.8(b)) create high voltages via an oscillator and the combinations of capacitors and diodes in the base. By supplying low voltage to the oscillator, inter-dynode high voltages can be built up by the CW voltage network. An important design consideration is to limit the oscillator noise that feeds through to the PMT outputs.

4.1.5 Front-End Electronics: Discriminator and SVI

4.1.5.1 Discriminator

The CREST discriminator board (Fig. 4.11), based on the MINOS design, takes the input signals from the anodes of 16 PMTs and generates trigger output signals to the

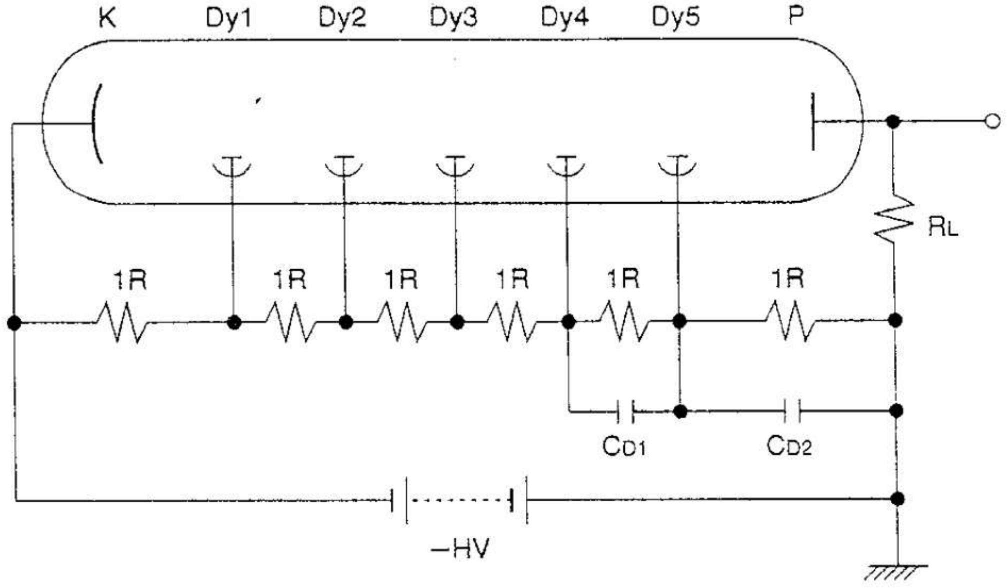

(a)

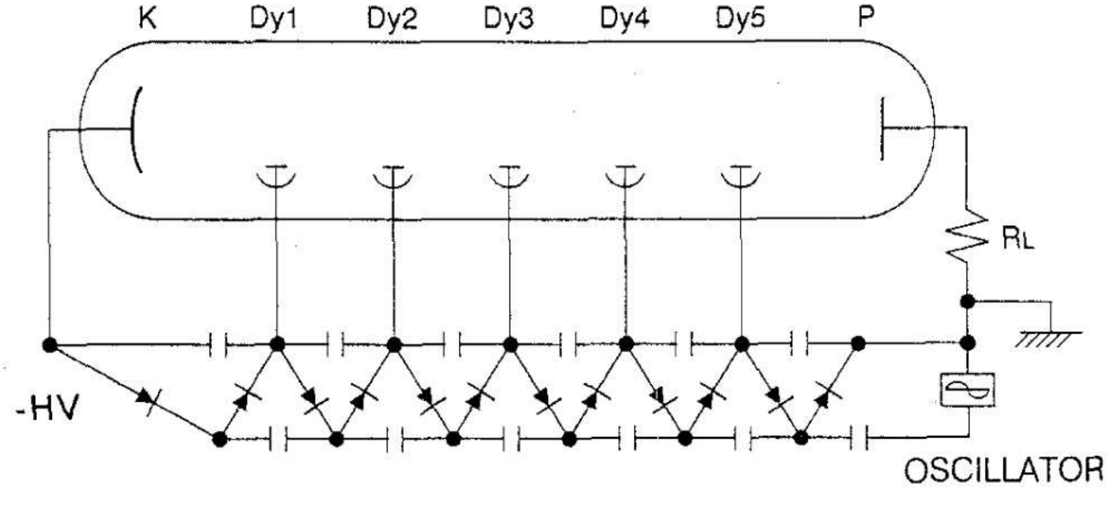

(b)

Figure 4.10: Schematics of PMT voltage dividers for (a) resistor base (b) Cockcroft-Walton base [52].

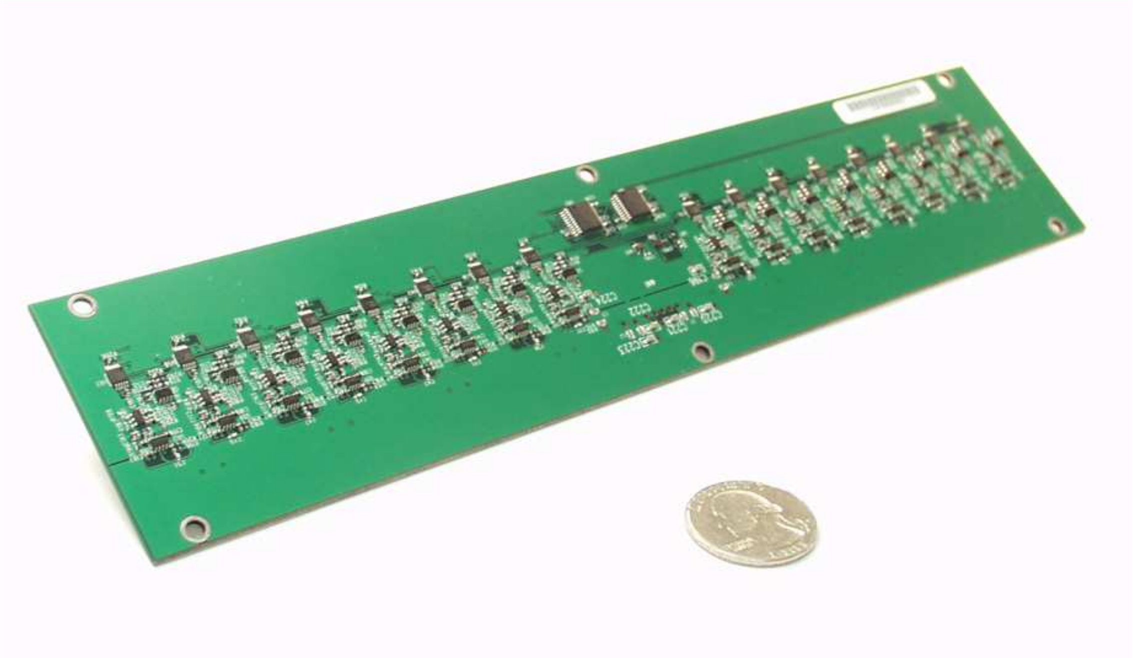

Figure 4.11: Picture of the discriminator board.

STAC board. Fig. 4.12 presents the schematic of the discriminator circuit for one channel. This discriminator circuit can be understood by following this schematic:

The current signal (negative in voltage) from the PMT anode comes in from ANODE 0 (terminated at 50 Ω at R9), and is multiplied ten times at the MAX4224 amplifier (U1) section, to be compared at MAX9203 (U2) with the discriminator threshold. For the discriminator threshold level setting, an 8 bits Digital-to-Analog Converter (DAC) AD5161 (U4) sets a voltage level in 19.5 mV steps from a 5 V stable power source. This voltage setting can be monitored by an ADC (DAC0) as needed. After dividing (AD6039 at U3-A and at R3 and R10) and inverting (AD8039 at U3-B) this level, one digital step at AD5161 (U4) becomes -4.9 mV at the comparator MAX9203 (U2). The ×10 anode signal from the PMT and the threshold level set by AD5161 are compared at MAX9203 (U2). If the signal from the PMT goes below threshold, the comparator generates a trigger signal (active low), whose hold time is

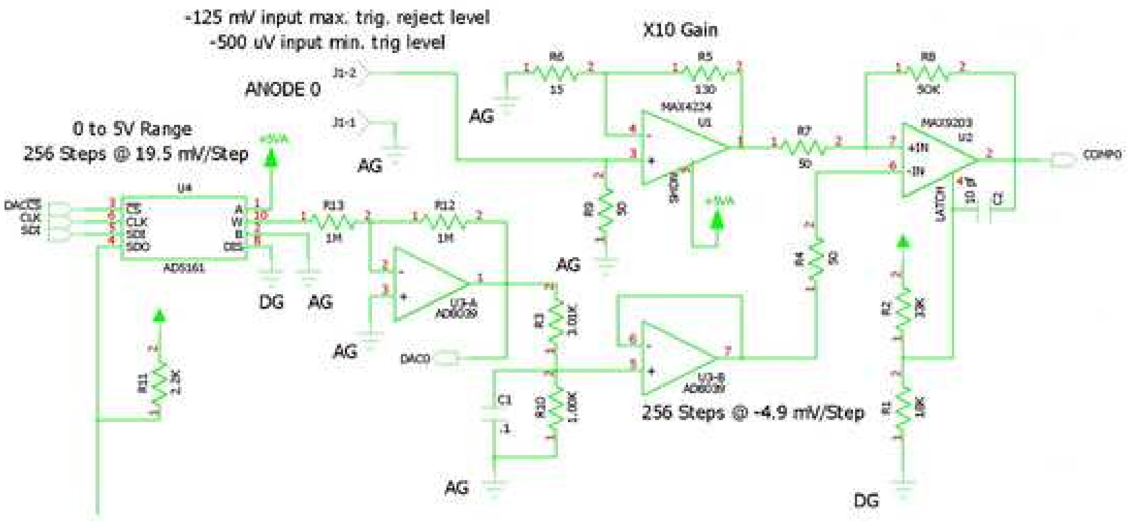

Figure 4.12: Schematic of discriminator circuit by Mark Gephard.

determined by capacitor C2 and the voltage divider (R1 and R2).

At the University of Michigan, I was responsible for testing the discriminator boards for the CREST-II flight. Discriminator functionalities such as setting and reading discriminator thresholds and generating trigger signals were checked. Similarly, the ability of triggering at a half of one photo-electron was successfully observed, and power consumption (the discriminator is one of the most power hungry boards in the whole experiment) was also measured. The results of testing the discriminator boards will be summarized in Sec. 4.6 of this Chapter.

Note that the hold time is kept active during a fixed length of time in this discriminator. This is necessary, because the analog signal from the crystal/PMT assembly is discretely distributed in time. Optimization of the TDC hold time in the discriminator with the ADC dead time induced by the readout time of the VA Readout Controllers (VARCs) was performed by me using a Geant4 simulation at the expected background rates for the Antarctic flight and is described in Sec. 6.1.5.

4.1.5.2 SVI

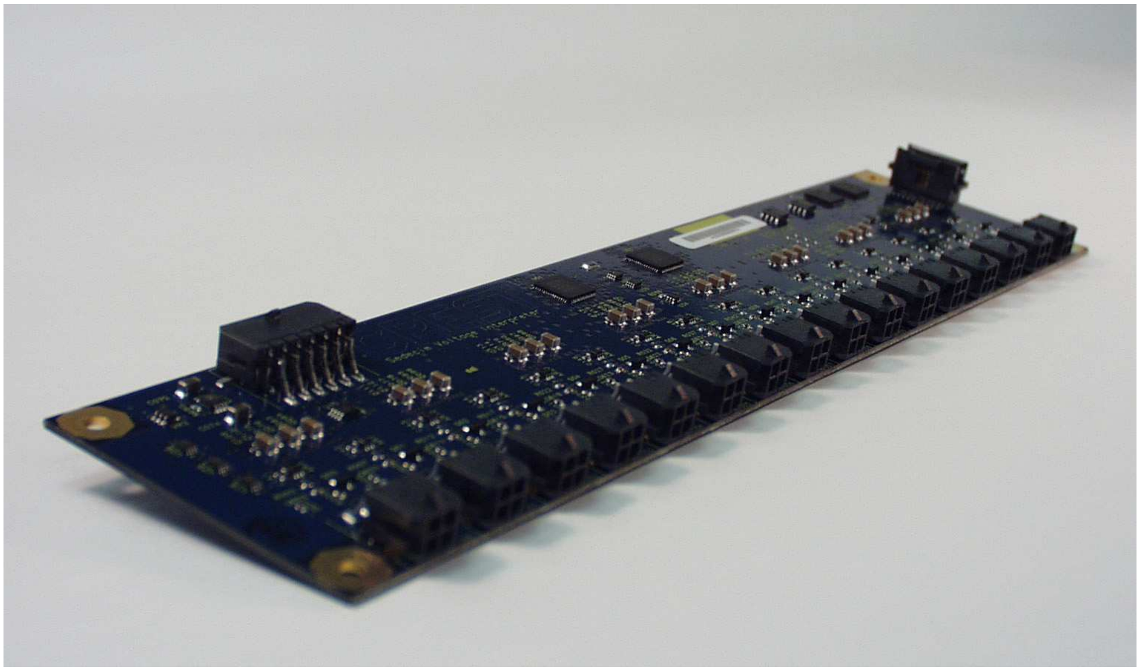

Figure 4.13: Picture of the SVI board

One Sediciem Voltage Interpreter (SVI) board provides both a 5.0 V power supply and adjusted control voltages (0.0−2.0 V) to set gains for the 16 PMTs in each module. The SVI provides ADC read-backs for all the voltages to monitor control voltage variation during flight. Each SVI is connected by the SVI Buss cables, and all the SVIs are controlled by the Master Voltage Controller (MVC) on the XEM carrier board (Fig. 4.4). To test these boards, I have written a C++ based interface code, which connects the communication between the hardware, SVI boards, and the firmware VHDL codes.

4.2 CREST-I: BGO/PMT Test Procedure and Results

4.2.1 Summary of Inorganic Crystal/PMT Development

I was responsible for testing the performance of the evaluation PMTs from different vendors and selecting two of them for the CREST-I flight. I was also responsible for testing all of the flight PMTs and BGO crystals from the selected vendors in collaboration with the University of Chicago.

BGO was initially chosen for its high density and low attenuation length at the time when the CREST experiment was initially proposed. Two vendors (Proteus, Inc, and Saint-Gobain) provided us with BGO crystals for evaluation, and the crystals from both companies yielded similar results (within a few percent in pulse height resolution). Based on availability, delivery schedule and price, Proteus was chosen to be the provider for the BGO crystals for the CREST-I instrument.

Four vendors (Burle Industries, Electron Tubes Enterprises Limited, Hamamatsu Photonics, and Photonis) provided us with evaluation photomultiplier tubes. These evaluation PMTs are characterized by gain, pulse height resolution, magnetic sensitivity, vacuum durability, and timing resolution. For this evaluation procedure, Electron Tubes Enterprises was not able to provide a vacuum durable evaluation PMT with a μ-metal magnetic shield, and they declined participation in the selection process. Similarly, the PMT provided from Hamamatsu failed to function after a few minutes of regular operation and was not included in the selection for the CREST-I flight. The experimental test setup, procedures, and results will be presented.

Based on the results of the PMT performance testing, the CREST collaboration decided to use half Burle PMTs and half Photonis PMTs for the array of the CREST-I instrument (57 PMTs from Burle and 58 PMTs from Photonis were provided). Individual Burle and Photonis PMTs were tested and characterized by me at the University of Michigan, and BGO crystals and Burle/Photonis PMTs were assembled as vacuum/light sealed modules at the University of Chicago. After completion of the characterization of the crystal/PMT assemblies, they were shipped to Indiana

University for the CREST-I instrument integration. During this time, the possibility of an use of the alternative crystal to accomplish a better timing resolution was considered and tested by me, and the performance comparisons between BGO and BaF_2 crystals will be shown in Sec. 4.5.

After the CREST-I experiment, Hamamatsu provided us with one more operational PMT for reconsideration. In the end, based on superior timing resolution of the PMT, Hamamtsu was chosen as the supplier of the PMTs for CREST-II and Antarctic CREST flights. Also, further development of the crystal/PMT assemblies in terms of vacuum/light tightness and improvement of wave-shifter on BaF_2, was handed down to Indiana University. The final design of the crystal/PMT assembly package is shown in Fig. 4.8.

The following sections are organized as follows: First, the four evaluation PMTs from the vendors are introduced, and the experimental test setups, procedures, and their testing results are presented. Then, the summary of the characterizations of the Burle and Photonis PMTs for CREST-I experiment will be presented. Lastly, the results of the comparison of timing resolutions between BGO and BaF_2 crystals and of the optimization of scintillation photon collection from the BaF_2 crystal will be shown.

4.2.2 Four Evaluation PMTs

Based on our PMT performance specification (See the Appendix A for details), each PMT vendor provided us with one or two evaluation PMTs to measure their performance (The pictures of these evaluation PMTs are shown in Fig. 4.14). Their physical and electrical operational characteristics are quite different (See Table 4.2), especially the number of dynode stages to achieve 1×10^6 gain. The Electron Tube and Hamamatsu PMTs were not selected CREST-I for the following reasons: Elec-

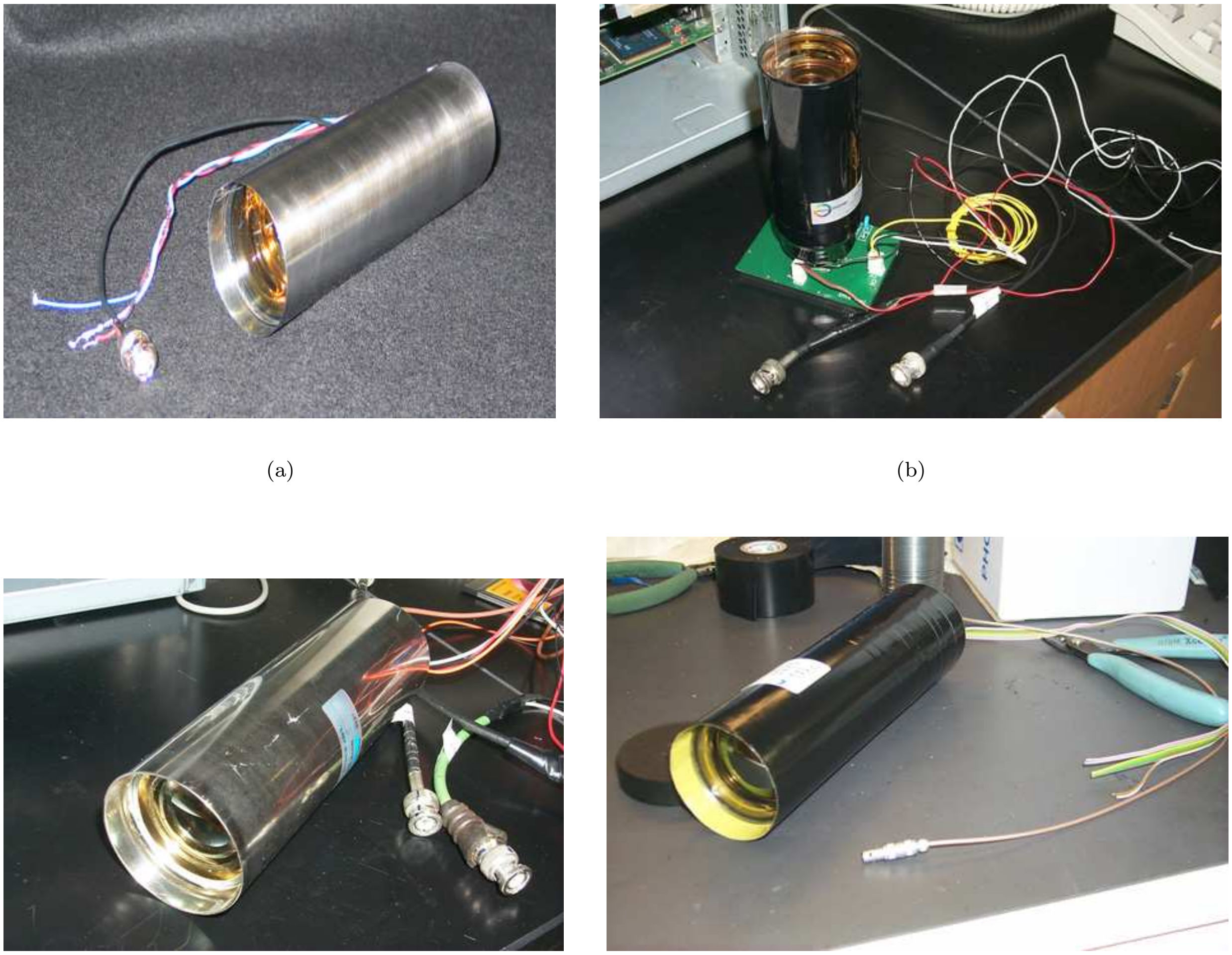

(a) (b)

(c) (d)

Figure 4.14: Pictures of (a) Burle PMT: 8575B(800) (b) Electron Tube PMT with separated module for voltage base: 9954SB(DM0044) (c) Hamamatsu PMT: R7724CW (d) Photonis PMT: XP20Y0

Table 4.2: Physical and operational electronic characteristics of four evaluation PMTs

	Burle 8575B(800)	Electron Tube 9954SB(DM0044)	Hamamatsu R7724CW	Photonis XP20Y0
Date of Arrival (yr 2008)	August 8th	July 30th	August 6 th	September 1st
Weight (g)	306.3	263.3	499.8	331.8
Full Length (mm)	170.0	156.0	170.0	179.5
Supply Voltage (V)	12	5	5	12
Number of Stages	12	12	10	8
Max. Operating Voltage (V)	1,950	1,800	2,000	1,500
Control:Output Voltage Ratio	1:1,000	1:1,000	1:1,000	1:400
μ metal thickness (inch)	0.01	×	0.032	0.02

tron Tube was not able to provide us the vacuum/light sealed PMT by the date we requested. Furthermore, their PMT did not have a monitor output for the high voltage nor a μ-metal shield. Hamamatsu could not provide an operational PMT by the deadline for the CREST-I PMT evaluation cycle.

4.2.3 Gain and PHR Resolution

Figures 4.15 shows the schematic of the experimental setup for the gain and pulse height resolution (PHR) measurement and presents an example of the ^{137}Cs ($\tau_{1/2}$: 30.2 yrs) spectrum measured with a multichannel analyzer (MCA: Amptek 8000A). First, the PHR (typically quoted as Full Width Half Maximum (FWHM)) for three evaluation PMTs (except Hamamatsu) were measured as follows: After the electronics and the sample PMT had been allowed to stabilize, a radioactive source, ^{137}Cs, was placed five inches in front of a 2.54 cm × 1 cm thick cylindrical BGO crystal coupled to the evaluation PMT. One millimeter thick cured RTV silicone (RTV615 from GE Silicones) was inserted to optically couple the BGO crystal with the PMT, and the same BGO crystal was used for all the evaluations. By adjusting both input impedance in the charge sensitive preamplifier (Ortec 113) and the fine/course gain in the amplifier (Ortec 575A), a peak at 661.7 keV from the ^{137}Cs source was found

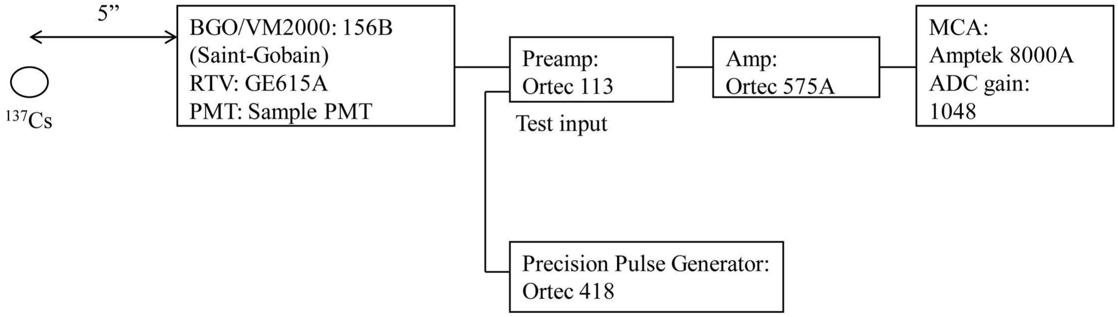

(a)

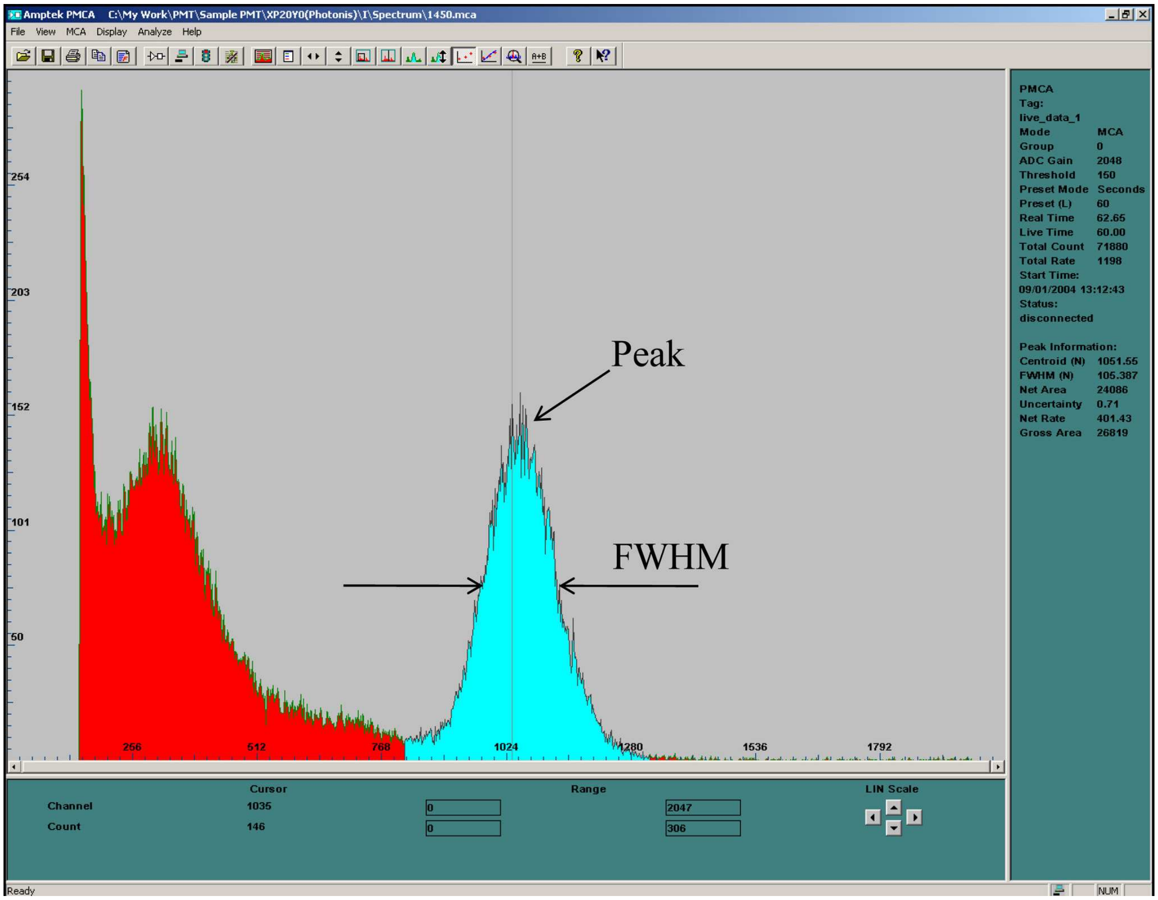

```
PMCA
Tag:
live_data_1
Mode          MCA
Group         0
ADC Gain      2048
Threshold     150
Preset Mode   Seconds
Preset (L)    60
Real Time     62.65
Live Time     60.00
Total Count   71880
Total Rate    1198
Start Time:
09/01/2004 13:12:43
Status:
disconnected

Peak Information:
Centroid (N)  1051.55
FWHM (N)      105.387
Net Area      24086
Uncertainty   0.71
Net Rate      401.43
Gross Area    26819
```

```
          Cursor          Range
Channel   1035      0             2047
Count     146       0             306
```

(b)

Figure 4.15: (a) Schematic of the experimental setup for the gain and PHR resolution measurement. (b) Screen shot of the peak and FWHM at 661.7 keV of ^{137}Cs (shown in blue) at MCA.

in the spectrum at the MCA. Measuring both the channel number of the peak and the number of channels corresponding to the FWHM, the resolution can be expressed as,

$$\text{FWHM Resolution at 661.7 keV} = \frac{\text{FWHM (channel number)}}{\text{peak (channel number)}} \tag{4.1}$$

For the gain measurement, with the same input impedance in the preamplifier and the fine/course gain in the amplifier from the FWHM resolution measurement, a voltage pulse from a precision pulse generator (Ortec 418) is generated. It is important to note that this voltage pulse generates a pulse shape with similar exponential decay time to that of the evaluation PMT right after the preamplifier. By measuring the peak voltage from this generator, the charge, which corresponds to the peak channel at MCA, was simply obtained by $\mathrm{Q} = \mathrm{C} \times \mathrm{V}$, where C is the input capacitance of the test input of the preamplifier, and V is the voltage pulse measured from the pulse generator. Since the average number of the photoelectrons, $\overline{\mathrm{N}}$, generated at the photocathode of the PMT can be obtained from the FWHM resolution (=2.35σ for a Gaussian distribution), and peak and σ in channel numbers are $g \times \overline{\mathrm{N}}$ and $g \times \sqrt{\overline{\mathrm{N}}}$ respectively where g is the electronics gain, the gain of the PMT as a function of the input control voltage (effectively changing the inter-dynode voltage differences) can be obtained as

$$\begin{aligned} \text{Gain of PMT(control voltage)} &= \frac{\mathrm{Q}}{e\overline{\mathrm{N}}} \\ &= \frac{\mathrm{CV}}{e} \times \left(\frac{\text{FWHM Resolution (\%)}}{2.35}\right)^2 \end{aligned} \tag{4.2}$$

where e is the charge of an electron ($= 1.602\times10^{-19}$ C) and C is a carefully measured capacitor at the test input of the Ortec 113 (= 2220 pF replacement for the original

20 pF test input capacitor to avoid saturation of the test input).

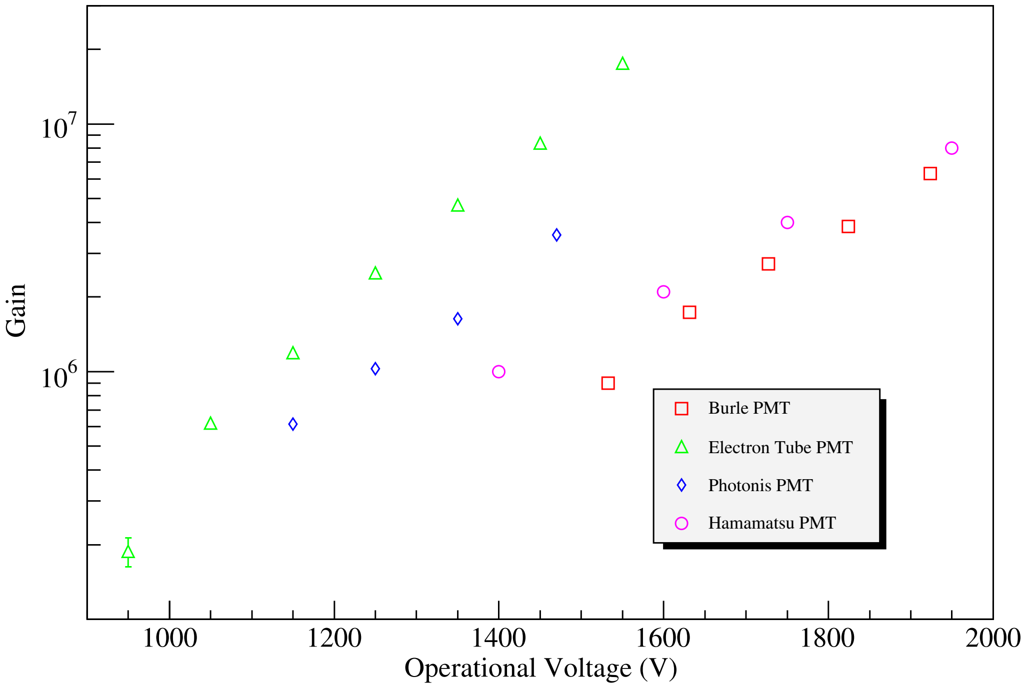

Figure 4.16: Result of the gain measurement for the three evaluation PMTs (Burle, ET, and Photonis) as a function of operational voltages. Data points for the Hamamatsu PMT were taken from their data sheet. Notice that they have different maximum voltages by design.

Figure 4.16 shows the result of the gain measurement of the three evaluation PMTs with different operational output voltages. Note that each evaluation PMT has a different maximum operational voltage. Since the gain of PMT can be expressed in terms of the voltage differences: $\propto \mathrm{V}^{\mathrm{N}}$, where V is the inter-dynode voltages (by assuming equal dynode voltage differences) and N is the number of stages (= number of dynodes +1, since secondary electrons are accelerated between the last dynode and anode at the last stage), the logarithmic gain of the PMT is proportional to the operational voltage.

The results of these resolution and gain measurements are summarized in Table 4.3. All three evaluation PMTs were able to achieve gains of $1{\times}10^6$ and beyond

Table 4.3: FWHM Resolution (%) at 661.7 keV and the maximum gain of the four evaluation PMTs with BGO crystal

	Burle 8575B (800)	Electron Tube 9954SB(DM0044)	Hamamatsu R7724CW	Photonis XP20Y0
FWHM Resolution (%)	9.99 ± 0.22	9.84 ± 0.11	×	10.13 ± 0.07
Number of stages	12	12	10	8
Max Gain	6.31×10^6	1.76×10^7	[3] 8.00×10^6	3.56×10^6

as requested (Data points from Hamamatsu were taken from their data sheet). At the same time, we did not measure any significant degradation of the resolution. In this evaluation, the Electron Tube PMT achieved the highest gain among the three evaluation PMTs.

4.2.4 Magnetic Sensitivity

Photoelectrons accelerated in the photocathode to first dynode region are very sensitive to the magnetic field, and as a result, the gain of the PMT can be varied by exposure to the Earth's magnetic field. To reduce this gain variation from the field, a μ-metal magnetic shield was wrapped around the side of the cylindrical PMT. All the PMT vendors except E.T. provided their evaluation PMTs (according to their own estimates) with enough μ-metal shielding so that no more than 5% gain variations occured at the expected magnetic field strength at float in Antarctica (~0.5 G at maximum). In Ann Arbor, it happens to be that the strength of magnetic field is approximately the same as the expected magnetic field in Antarctica (although their directions are quite different).

The experimental setup (Fig. 4.17) for measuring sensitivity to magnetic field was very similar to the one for the gain and resolution measurement. To measure gain variation to the magnetic field, the evaluation PMT was rotated every 45 degrees along the local magnetic field measured to be 0.45 G at maximum. Note that the

---

[3] This is from the Hamamatsu PMT data sheet, not a measured value.

Table 4.4: The result of the maximum peak to peak PMT magnetic field sensitivity

	Burle 8575B (800)	Electron Tube 9954SB(DM0044)[4]	Hamamatsu R7724CW	Photonis XP20Y0
μ metal (inch)	0.01	2×0.0004	0.032	0.02
Gain Variation (%)	6	6	×	5

maximum gain is where the axis of the magnetic field coincides with that of the PMT. In this orientation, photoelectrons are channeled along the magnetic field lines. Table 4.4 presents the results of these measurements, and shows that the maximum peak-to-peak gain variations are 6% for Burle and E.T. PMTs and 5% for Photonis PMT.

Investigation of the μ-metal magnetic shield thickness optimization was continued by our colleagues at Indiana University. Their results showed that without μ-metal shielding, for the worst cases there were ~30% and ~20% losses in the anode signals from the Hamamatsu PMT at 1.0 G and 0.7 G uniform magnetic field respectively. For the Antarctic CREST instrument, serious weight reduction is necessary to fly at higher altitude to reduce the X/γ-ray secondary background. Therefore, we have concluded that the Antarctic CREST PMTs would not be wrapped with μ-metal sheilding, as long as gain variations are properly monitored during the flight.

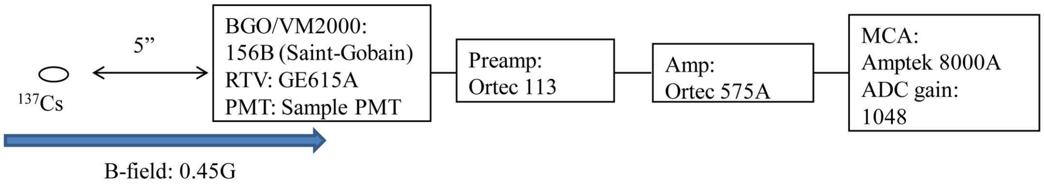

Figure 4.17: Schematic of the experimental setup for the magnetic field sensitivity measurement.

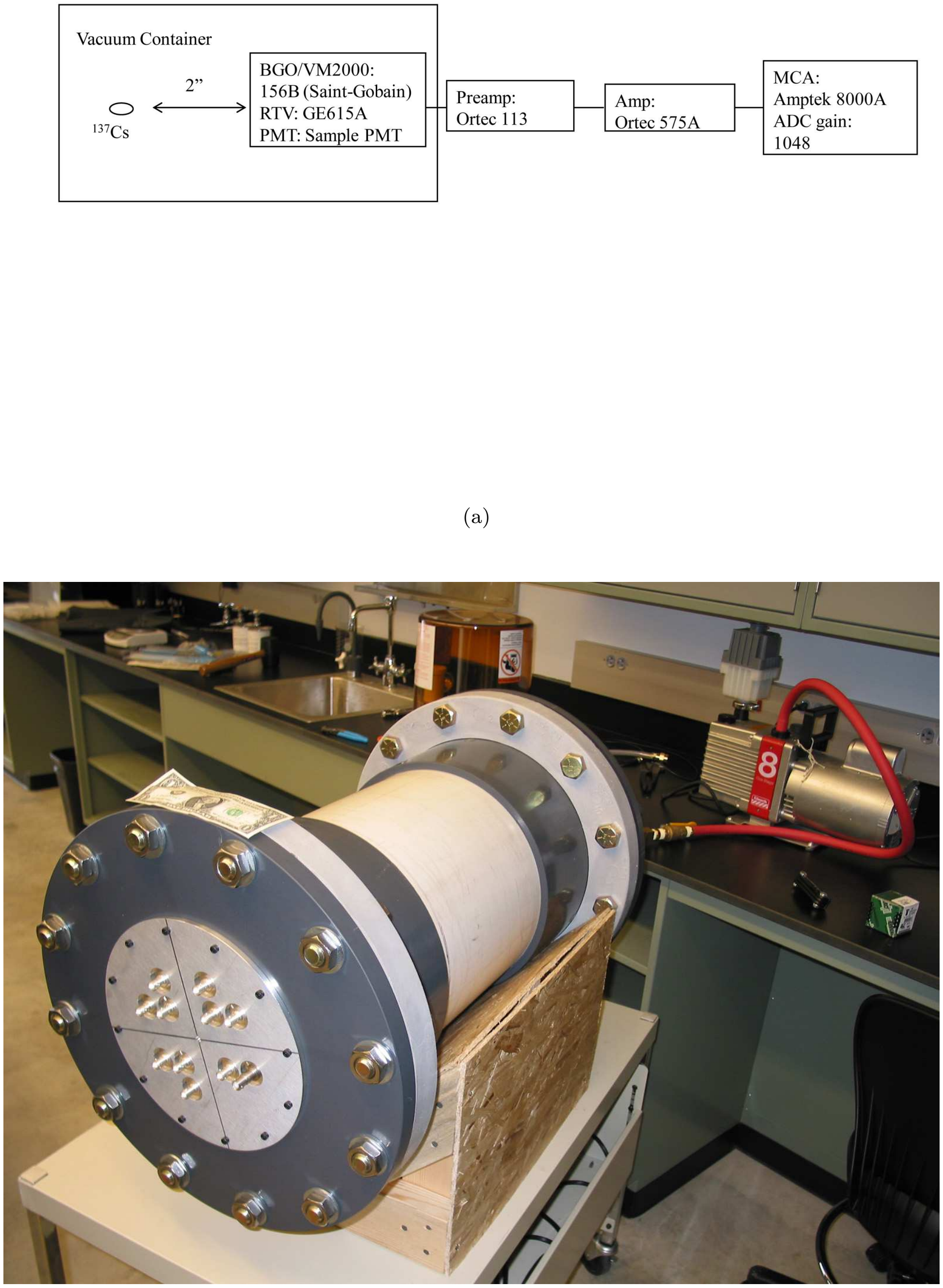

(a)

(b)

Figure 4.18: (a) Schematic of the experimental setup for the vacuum durability measurement. (b) Photograph of the vacuum chamber borrowed from Scott Nutter from Northern Kentucky University that I used for these tests.

4.2.5 Vacuum Durability

Under the near vacuum environment where the CREST instruments were flown and will be flown, corona or/and current leakage at the base of the PMT has to be seriously considered. Since CREST PMTs have CW high voltage power supplies, encapsulation of the base is critical. The PMT vendors were required to provide us potted base PMTs which are able to operate for at least three months under ∼2 mbar. At the University of Michigan, these evaluation PMTs were operated under ∼2.5 mbar in a vacuum chamber (Fig. 4.16(b)) for two weeks, and their signals were monitored every day.

The results of the evaluation of the PMTs under near vacuum are as follows: Burle provided us with two PMTs. One PMT, which they had not tested under near vacuum, failed to function at approximately 200 mbar on the way to 2.5 mbar, while the other one successfully operated for 2 weeks. The Photonis PMT operated normally at 2.5 mbar for 2 weeks, but on the way back to standard atmospheric pressure (ATM), it failed to function. Photonis fixed their failed PMT, and it worked for a one hour test with pressure changes from 1.0 ATM to 2.5 mbar and from 2.5 mbar to 1.0 ATM. The evaluation PMT from ET was not potted for vacuum testing, and the Hamamatsu evaluation PMT operated under ∼2.5 mbar for a one hour test after they had fixed their CW base problem.

4.2.6 Time Resolution

Timing resolution is the most critical characteristic of the PMT for the CREST experiment to separate $e^{\pm}$ and to reject background. To measure the timing resolution of the evaluation PMTs with BGO crystals, the time difference measured for two simultaneous photons from ^{22}Na was utilized. ^{22}Na ($\tau_{1/2}$: 2.6 yrs) in metal generates

---

[4] The magnetic field sensitivity test was done by wrapping the E.T. PMT with two layers of 0.004" μ-metal shield.

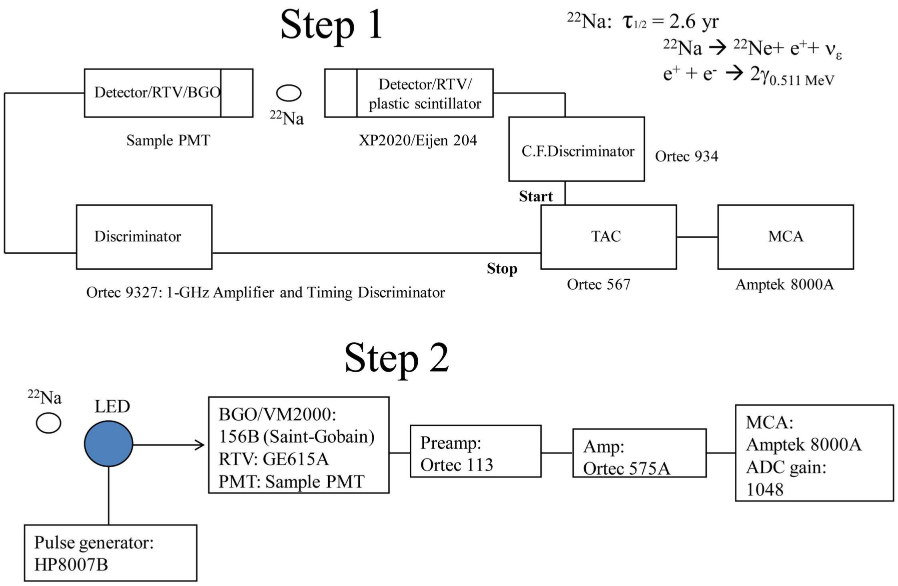

(a)

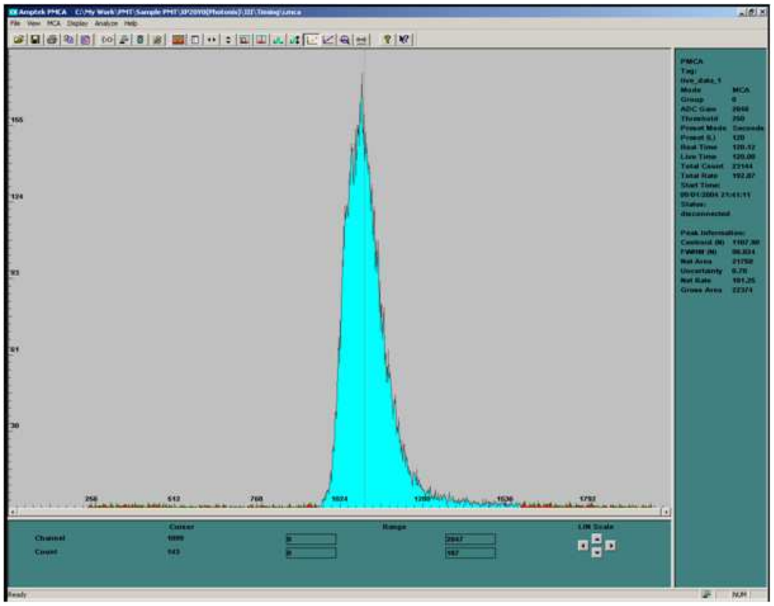

(b)

Figure 4.19: (a) Schematic of the experimental setup for the timing resolution measurement. In Step 1, the distribution of the timing difference between two signals from the XP2020 and the sample PMT was measured. In Step 2, the corresponding energy was measured by the light output limiting washer. (b) Distribution of the timing differences at MCA (0.0244 ns/ADC count). σ of this distribution defines the timing resolution of the crystal/evaluation PMT.

two back-to-back simultaneous 511 keV γ's by first decaying into ^{22}Ne through a 1.27 MeV-decay and a positron and then this positron interacts with a free electron in the metal and annihilates into a pair of γ's each with an energy of 511 keV.

Figure 4.19 illustrates the experimental setup used for measuring the timing resolution of the evaluation PMTs. From two simultaneous photons, the start reference signal of a Time to Analog Converter (TAC, Ortec 567) was generated by a 2.00" diameter × 2.00" long organic plastic scintillator (Eljen 204) coupled with a fast timing Photonis XP2020 PMT through a constant fraction discriminator (Ortec 934). The evaluation PMT, operated at gain of a 3×10^6 and coupled with a 2.54 cm radius × 1 cm thick cylindrical BGO crystal from Saint-Gobain, provided the stop signal of the TAC, and the output signal triggered a discriminator (Ortec 9327) at a threshold of 1/2 photo-electron. At the TAC, the time differences between the start and the stop discriminator signals were measured and recorded by the MCA. An example of this measured timing difference distribution is shown in Fig. 4.19. The standard deviation, σ_{timing}, of this distribution determines the timing resolution of the BGO/evaluation PMT assembly by assuming σ_{timing} from the plastic scintillator with the XP2020 PMT alone is negligible.

To measure the energy dependence of the timing resolution, very thin washers with different sized holes of the opening holes were inserted between the BGO crystal and the top of the window of the evaluation PMT. This artificially reduced the number of scintillation photons. With this method, the time difference distribution and the timing resolution were easily measured with a reduced number of photons. The equivalent crystal deposited energy was found by the pulse height resolution method (Step 2 in Fig. 4.19) using a green LED. First, the ADC channel at the peak of the energy spectrum from ^{22}Na was measured with the washer in place. By pulsing the LED directly into the glass window of the PMT such that the peak was in the same ADC channel, the number of generated photoelectrons was calculated from the resolution for the LED spectrum. Thus, by using the known number of photoelectrons at 661.7 keV from the ^{137}Cs source, the equivalent deposited energy with the washer in place was calculated.

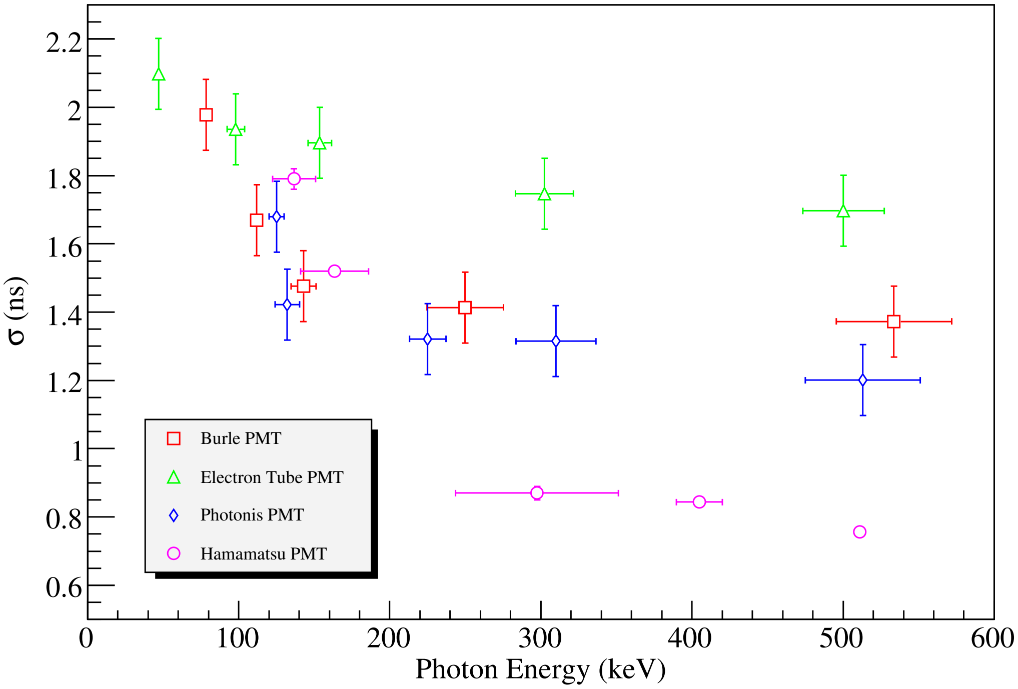

Figure 4.20: Measurement of timing resolution (ns) with the BGO crystal.

Figure 4.20 presents the result of the timing resolution measurements for the four evaluation PMTs using the washer method. There were five washers with different sized openings. In the graph, data points for each PMT have the same features: In the higher energy range ($\geq \sim$200 keV), the timing resolution of the PMTs are constant. This is due to the fact that the resolution at higher energy is limited by the intrinsic geometry of the dynode structure of the PMT. On the other hand, at lower deposited energy, timing resolutions become degraded, because the probability of the number of the scintillation photons generated by the BGO crystals in the first ns drops below unity. This result led to the investigation of an alternate crystal with better scintillation photon yield in the first ns. The result clearly shows that the Hamamatsu PMT has the best intrinsic timing resolution (sub nanosecond), compared with the other vendors (Burle, ET, and Photonis) with $\sigma_{\text{timing}} \geq 1$ ns.

Importance of σ_{timing} less than 1 ns can be illustrated as follows. With an approximately 2 m instrument, it takes ~ 6 ns to cross the detector at the speed of light (30 cm/ns). Thus, to separate the directionality of the hits on the crystals with $\pm 3\ \sigma_{\text{timing}}$ requires ~ 1 ns timing resolution.

4.3 Summary Table of Evaluation PMT Performance

Table 4.5: Performance comparisons of the four evaluation PMTs

Vendor	Burle 8575B (800)	Electron Tube 9954SB(DM0044)	Hamamatsu R7724CW	Photonis XP20Y0
Date of Arrival (year 2008)	August 8th	July 30th	August 6th	September 1st
Physical Description				
Weight (g)	306.3	263.3	499.8	331.8
Full Length (mm)	170.0	156.0	170.0	179.5
Gain and FWHM Resolution				
Supply Voltage (V)	12	5	5	12
Number of stages	12	12	10	8
Max. Operating Voltage (V)	1,950	1,800	2,000	1,500
Control:Output Voltage Ratio	1:1,000	1:1,000	1:1,000	1:400
FWHM Resolution (%)	9.99 ± 0.22	9.84 ± 0.11	×	10.13 ± 0.07
Max Gain	6.31×10^{6}	1.76×10^{7}	8.0×10^{6}	3.56×10^{6}
Magnetic Field Sensitivity				
μ metal (inch)	0.01	2×0.0004	0.032	0.02
peak to peak variation (%)	6	6	×	5
Vacuum Testing				
Vacuum ($\sim$ 2.5 mbar)	failed/2 weeks	×	1 hr	1 hr
Timing Resolution with BGO crystal				
σ_{time} (ns) at 511 keV	1.37	1.70	0.76	1.20

4.4 CREST-I: Crystal/BGO Test Result

Based on the results of the evaluation PMT measurements, Burle and Photonis were chosen to be the suppliers of the PMTs for the CREST-I flight. They provided a total of 115 PMTs (57 from Burle and 58 from Photonis). Among these PMTs, 96 PMTs and 8 PMTs were used for the crystal array and for the plastic scintillator, respectively. The remainder (11 PMTs) were left for spares.

In the 96 PMT array, half were Burle PMTs: 32 Burle PMTs were coupled to BGO crystals and 16 Burle PMTs were coupled to BaF_2 crystals. The rest of the PMT array were from Photonis and these were all coupled to BGO crystals. For the plastic veto scintillators two PMTs were utilized to read out scintillation photons from each side. As a result, two pairs of two Burle PMTs and two pairs of two Photonis PMTs were used for a total of four CREST-I veto scintillators (See Figure 4.2(b) and Figure 5.7).

Upon arrival of these PMTs at the University of Michigan, they were individually characterized and their data was archived in SQL. The PMT characterization measurements were performed to determine the input control voltage required to achieve a gain of 3×10^6 (instead of 1×10^6 originally requested for the evaluation PMTs), the resolution at 662 keV from ^{137}Cs, the maximum power consumption at maximum gain, and the noise rate (Hz) at a 0.5 photoelectron trigger threshold. In addition, I performed two weeks of vacuum operational testing by the methods described in the previous sections. Figures 4.21 and 4.22 represent the characterization distributions of the 104 PMTs.

The first two histograms (Fig. 4.21) show the distributions of the output operational voltages needed to obtain gains of 3×10^6 and the maximum gains of the 104

PMTs. In the top histogram, the two distributions (Burle in black and Photonis in red) show that the operational voltages at PMT gains of 3×10^6 are clustered around their means, but their spreads are relatively large (∼350 V for the Burle PMTs and ∼500 V for Photonis PMTs). Note that the manufacture-rated maximum operational voltages for the Burle and Photonis PMTs are quite different (1,950 V and 1,500 V for the Burle and Photonis PMTs respectively). The distributions of the maximum gains from both Burle and Photonis PMTs are shown in the bottom histogram. They are statistically the same except a few Photonis PMTs have much higher maximum gains. This is because these values (operational voltage at 3×10^6 gain and maximum gain) are extrapolated from five different operational voltage data points with the assumption that the logarithmic gain of the PMT is proportional to the operational output voltage. Hence, more than 80% of both PMT groups were able to achieve gains of 5×10^6 successfully.

The next two histograms (Fig. 4.22(a)) show the distributions of the resolutions of the BGO crystal/PMT assemblies and the noise rates (Fig. 4.22(b)) at a −5 mV discriminator threshold. Since the measured quality of the BGO crystals are approximately the same (∼ 10% FWHM at 662 keV using one evaluation PMT), it is apparent from the top histogram that neither the Burle nor the Photonis PMTs significantly degraded the PHR from the BGO crystals. The bottom histogram shows the noise rates of the PMTs operated at 3×10^6 gain with a −5 mV discriminator threshold. Note that at PMT gain of 3×10^6, a −5 mV threshold level is approximately 2/3 of a photoelectron. Noise rates of both Burle and Photonis PMTs were about the same (∼1 kHz), although a few much noiser Photonis PMTs existed. The main cause of these noise triggers were from photo-electrons released inside of the tube, the background radiation in the lab, and cosmic rays (mainly muons). At

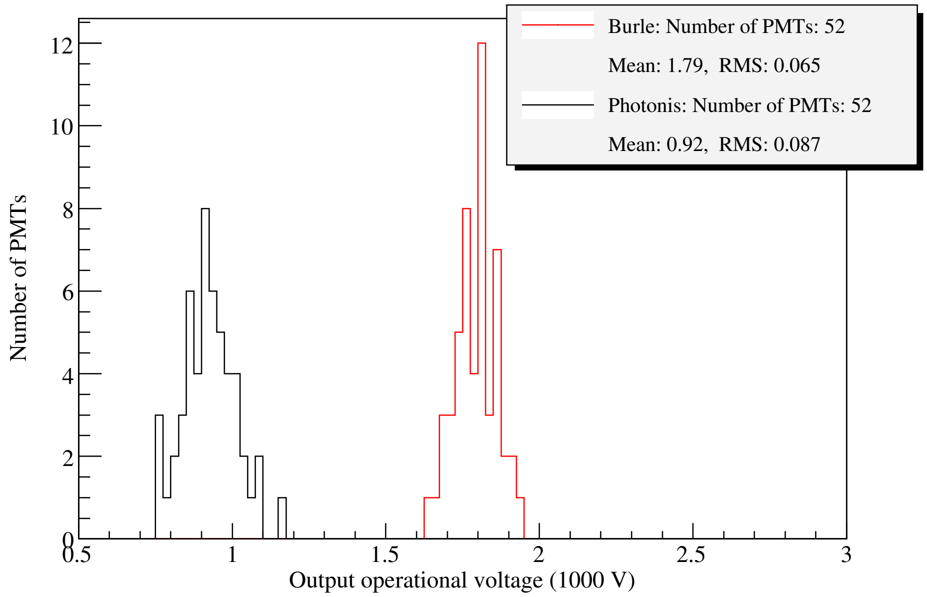

(a)

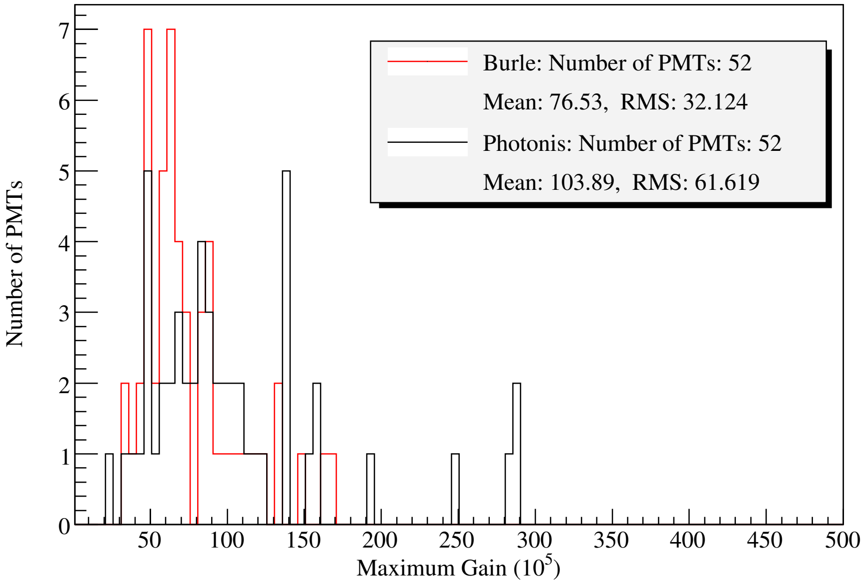

(b)

Figure 4.21: (a) Distributions of the PMT operational voltages needed to obtain a gain of 3×10^6 for both Burle and Photonis PMTs. (b) Distributions of maximum gains of the PMTs.

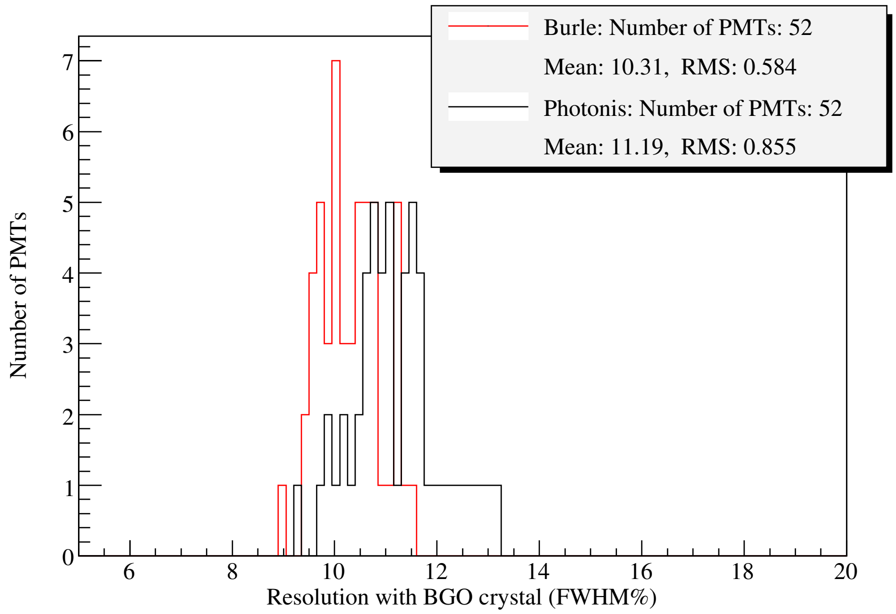

(a)

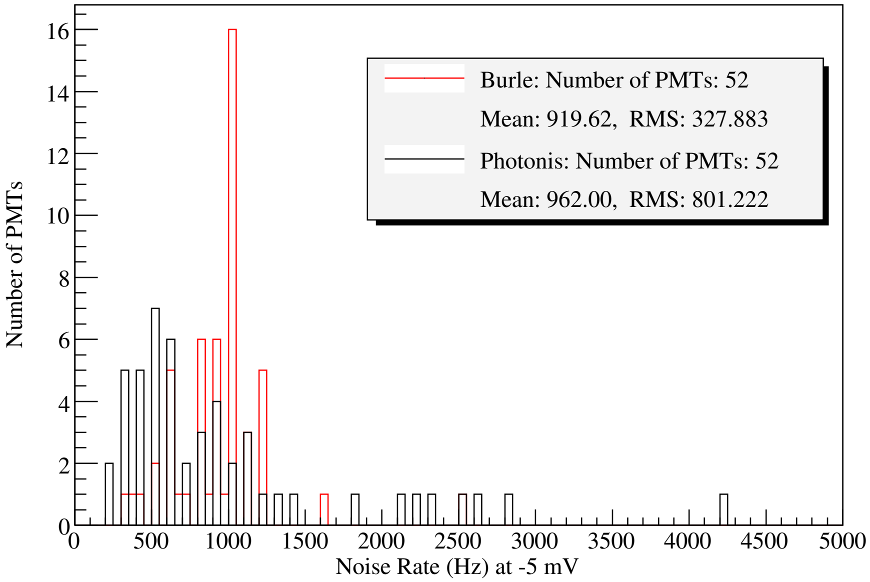

(b)

Figure 4.22: (a) Distributions of the resolution for the Burle and Photonis PMTs with BGO crystals at 662 keV (b) Distributions of the noise rates at a −5 mV discriminator threshold, measured in Rm 3222 at the University of Michigan.

the CREST-I flight site in Ft. Sumner, NM, the noise rates of all the PMTs were re-measured and found to be slightly lower than those measured in Ann Arbor. To reduce the data loads to the electronics, the discriminator thresholds for a few of the high noise rate PMTs were set higher until their rates became ≤ 1.5 kHz.

The power consumption of the PMTs was measured by running them at the manufacture-rated maximum operational voltages. The Burle PMTs had a power consumptions of only 12 mW, while the Photonis PMTs consumed 37 mW. At the end of the PMT characterizations for the CREST-I flight, two Burle PMTs had mechanical failures: One had a much lower gain and the other one suffered degradation of resolution. In addition, two Photonis PMTs failed to operate under vacuum testing. These failed Burle and Photonis PMTs were sent back to their vendors and they either fixed them or supplied new ones to us.

4.5 CREST-I and CREST-II: Timing Resolution Comparison between BGO and BaF$_2$, and BaF$_2$ Light Output Optimization

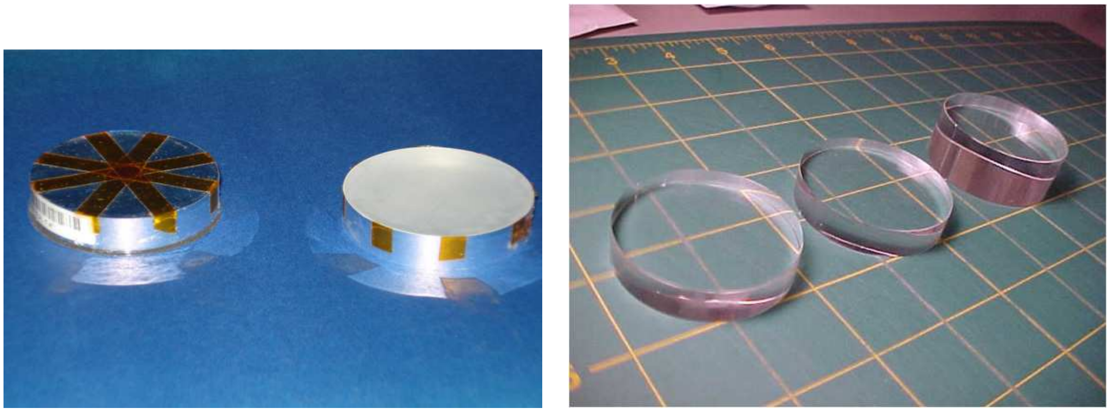
(a) (b)

Figure 4.23: Pictures of (a) two 1 cm thick BGO crystals with VM2000 reflector and (b) two 1 cm and one 2 cm thick BaF$_2$ crystals supplied by Proteus.

As shown in the previous Section 4.2.6, timing resolution of the BGO crystal is significantly degraded at lower energies. In the following section, BaF_2 is investigated as an alternative to BGO to improve timing resolution and light collection.

4.5.1 BGO and BaF2

One of the drawbacks of the use of BaF_2 crystals is that the UV scintillation photons (195 and 220 nm for the fast component and 310 nm for the slow component at their maximum wavelengths) do not have good transmission through borosilicate glass PMT windows. To efficiently convert these UV photons to photo-electrons either a UV extended PMT (quartz window PMT) or a wave-shifter from UV to visible must be inserted between the crystal and photocathode.

A quartz window for a PMT can extend its spectral sensitivity down to $\sim$100 nm, which comfortably covers the wavelengths of the UV scintillation photons from BaF_2 crystals. Quartz window versions of the CREST PMTs were purchased from both Burle and Photonis. To reduce costs we considered various wave-shifters that would allow us to use the cheaper borosilicate glass window. Chuck Hurlbut from Eljen Technology recommended 4,4'-Diphenylstilbene (DPS: $C_{16}H_20$) as a wave-shifter. It has an absorption spectrum from 280 to 380 nm (340 nm at peak), and its emission spectrum is from 380 to 460 nm where the regular borosilicate glass-window PMT is sensitive. To use this wave-shifter it needs to be deposited on the BaF_2 crystal. Among the different deposition methods (evaporation, spraying, etc.), the vacuum evaporation/deposition technique (pictures of the evaporator shown in Fig. 4.24) was used. This is because it is the cleanest method, which can yield the most light output [53].

The collection of scintillation photons from the crystal into the window of the PMT is also an important factor to improve the timing and pulse height resolution. For the CREST-I flight, the top and side surfaces of all the BGO crystals (480 nm at

Figure 4.24: Pictures of the vacuum evaporator and the evaporation table/supporting structures inside the glass dome in the inset at bottom-left.

max. wavelength) were wrapped with VM2000 (multi-layered polymeric film from 3M). This radiant mirror film has an excellent reflectivity in the visible region ($\geq$ 95% for wavelengths $\geq$ 425 nm and $\leq$ 10% for wavelengths $\leq$ 400 nm [54], resulting in superior light collection for the BGO crystals. Light collection for the BaF_2 crystal is more complex: For the UV scintillation photons from the BaF_2 crystal, this VM2000 film is not a good choice before the DPS waveshifter converts the UV photons into the visible. This reflector performs very well however, after the wavelength conversion has taken place. Here, woven teflon-based films are great reflectors in the UV region, but they are not quite as good for visible photon reflection. To compare their reflective performances (VM2000 and Teflon films), I tested various types of coatings (bottom surface and all the surfaces) to maximize the light collection of the reflector.

One more subtle but important thing to consider was stabilization of the crystal on the top of the glass window of the PMT. Typically, RTV silicone is used for this purpose. This is because it optically couples the crystal (BGO: 2.15 and BaF_2: 1.49) and the borosilicate glass window of the PMT whose index of refraction is 1.5. For the CREST-I instrument, RTV 615 from GE (index of refraction: 1.402) was used for the BGO crystal as well as for the BaF_2 crystal packages (with SS4120 primer for stronger adhesion between the glass window and the crystal).

4.5.2 Timing Resolution Comparison

The experimental setup and the procedure for measuring the timing resolution of the BGO and BaF_2 crystals were the same as in the previous Sec. 4.2.6. The reference PMT used for this timing measurement was a Hamamatsu R7724CW, which was also used for the optimization of the light output from the BaF_2 crystal, as described in the following section. The Hamamatsu PMT was chosen for CREST-II and the

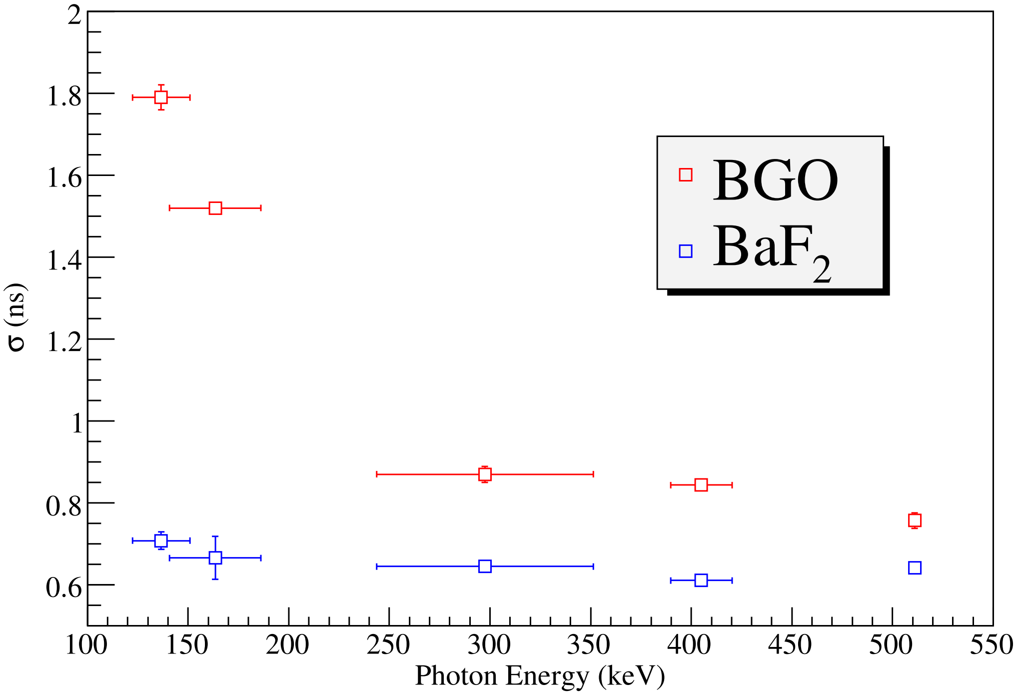

Figure 4.25: Timing resolution comparison between BGO and BaF_2 crystals.

Antarctic CREST experiments, since it displayed the best timing resolution with BGO crystals. The BaF_2 crystal used for this comparison measurement was a 2.54 cm radius × 1 cm thick cylinder (same as the BGO crystal) whose bottom-surface was vacuum coated with 0.084 g/cm^2 DPS (See the properties of BaF_2 at Table 4.1). It also was wrapped with three layers of Tetratex Teflon as a reflector of UV photons.

In Figure 4.25, the excellent timing resolution of the BaF_2 crystal is quite apparent. It has better timing resolution at all energies, but it is even more pronounced at lower energy where the timing resolution of the BGO crystal degrades. As explained before, this is because the BGO has fewer photo-electrons in the first ns due to its long decay time. At higher energies, the timing resolution of the BaF_2/Hamamatsu PMT is limited by the intrinsic resolution of this PMT ($\sim$ 0.65 ns). This timing resolution is expected to continue down to $\sim$ a few keV for a waveshifted BaF_2 crystal with estimated yield from simple estimate of 612 photons/MeV in the first ns (Table 4.1).

4.5.3 Optimization of Light Outputs for the BaF_2 Crystal

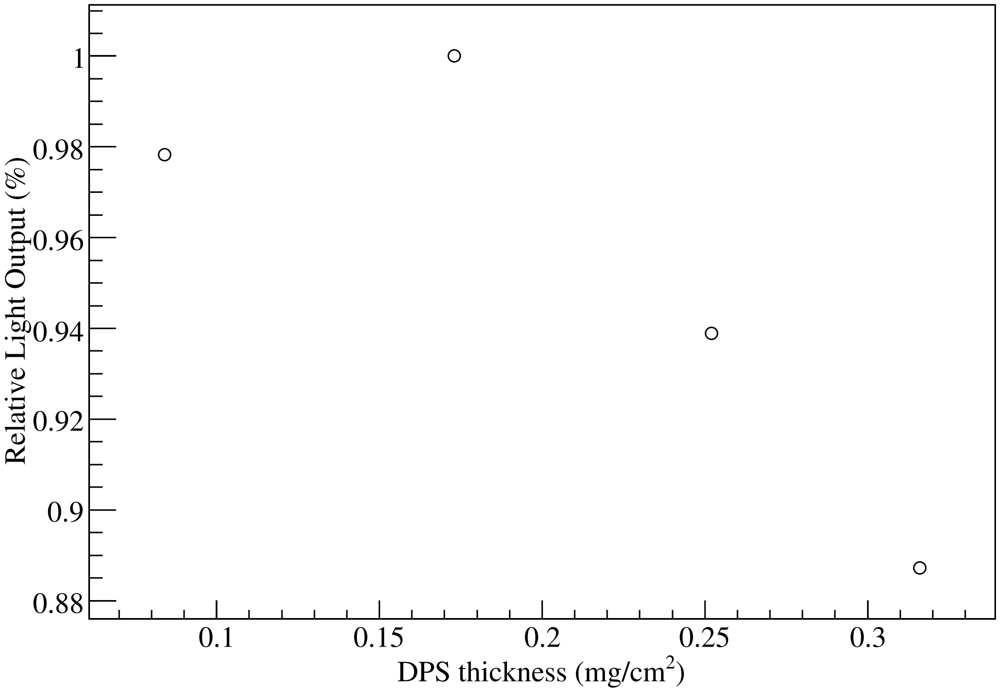

Figure 4.26: Relative light output for the bottom surface coating of 2.54 cm radius × 2 cm thick BaF_2 crystal with 3 layers of Tetratex Teflon for different DPS thickness.

Table 4.6: Relative light output with respect to the BGO crystal. For the bottom surface, the DPS deposited thickness is 0.10 g/cm^2. With all surfaces coated, the average thickness of the DPS is 0.21 g/cm^2 on the top and bottom, and ∼0.63 g/cm on the sides.

All Surface	no reflector	Mil Spec	VM2000	Tetratex
R.L.O.	0.52	1.16	1.39	1.27
Bottom Surface	no reflector	Mil Spec	VM2000	Tetratex
R.L.O.	0.46	1.20	1.03	1.28

First, I optimized the DPS deposition thickness (g/cm^2) on the bottom surface of the 2.54 cm radius × 2 cm tall cylindrical BaF_2 crystal. If the DPS thickness is too small, the UV light will not be absorbed. If the DPS deposition is too thick, the scintillation photons are absorbed. With sufficient separation between the evaporation boat and the crystal, a uniform coating can be obtained. The thickness of the DPS coating was determined by measuring the weight difference before and after vacuum evaporation/deposition and dividing this difference by the product of the area of the bottom surface of the crystal and the density of the DPS. Although it was quite difficult to control the amount of DPS deposited by vacuum evaporation, Figure 4.26 shows that the relative maximum light output of the BaF_2 crystal resulted when the coating thickness was approximately 0.17 mg/cm^2. This result agrees with other measurements [53], where the maximum light output occurred at ~ 0.2 mg/cm^2. A similar trend of a decrease of light output with thicker DPS coatings was obtained.

Next, I investigated different photon reflector films to maximize light collection from the BaF_2 crystal. These were:

- BaF_2 with bialkali PMT (sensitivity: 400 nm peak, $300 - 600$ nm) with RTV
    - Bottom surface coating or all surfaces
    - VM2000 or Teflon based diffuse reflectors (Tetratex Teflon, Mil Spec (thicker than Tetratex) or no reflector
- BaF_2 with a quartz window PMT (sensitivity extending to 100 nm)

The relative light output for these configurations relative to a 2.54 cm radius $\times$ 1 cm thick cylindrical BGO crystal with VM2000 are summarized in Table 4.6. The process by which the scintillation photons are converted to visible photons can be made even more efficient by the choice of the reflector (VM2000 or Teflon films) and choosing which surfaces of the crystal are coated (the entire surface or only the bottom surface). Apparently, without reflector films, the light collection of the crystal is not great ($\leq 50\%$). It was found that the VM2000/full surface combination was more efficient than the Teflon/bottom surface combination. As a result, the 16 BaF_2 crystals were coated on all surfaces for the CREST-I experiment and VM2000 reflectors were used.

The light output from two different BaF_2 crystal surface polishings (UV and diffuse polish) were also compared. With all the crystal surfaces coated with DPS and with VM2000 wrapping, the UV-polished crystal yielded 0.6% better light output than the crystal with diffuse polished surfaces, although this slight difference was larger than the effect from the DPS deposition thickness variation. The light output from the quartz window PMT and the regular PMT with waveshifter DPS deposition were also compared. For the quartz PMT, the crystal was wrapped with Tetratex Teflon (good reflector for UV photons). In short, the DPS waveshifter method yielded a few percent better resolution, which was also observed in [55].

4.6 CREST-II: Discriminator Testing

4.6.1 Discriminator Testing Setup

Testing the CREST discriminator board required an independent testing board to supply the voltages and the commands to the ADC/DAC chips on the discriminator. This testing board (Fig. 4.27) was designed by Jon Ameel at the University of Michigan. The functionalities of the discriminator testing board were as follows: It provided both DC voltages and charge injection into all the input channels of the discriminator and it also provided an instant visual check of the outputs of the discriminator through the use of LED indicators. It could also monitor power consumption from the discriminator. It also housed the Opal Kelly board, which controlled the ADC/DAC chips on the discriminator, and this board was in turn controlled by a desktop PC through USB.

Both Verilog code and C++ GUI interface codes were written by me to control

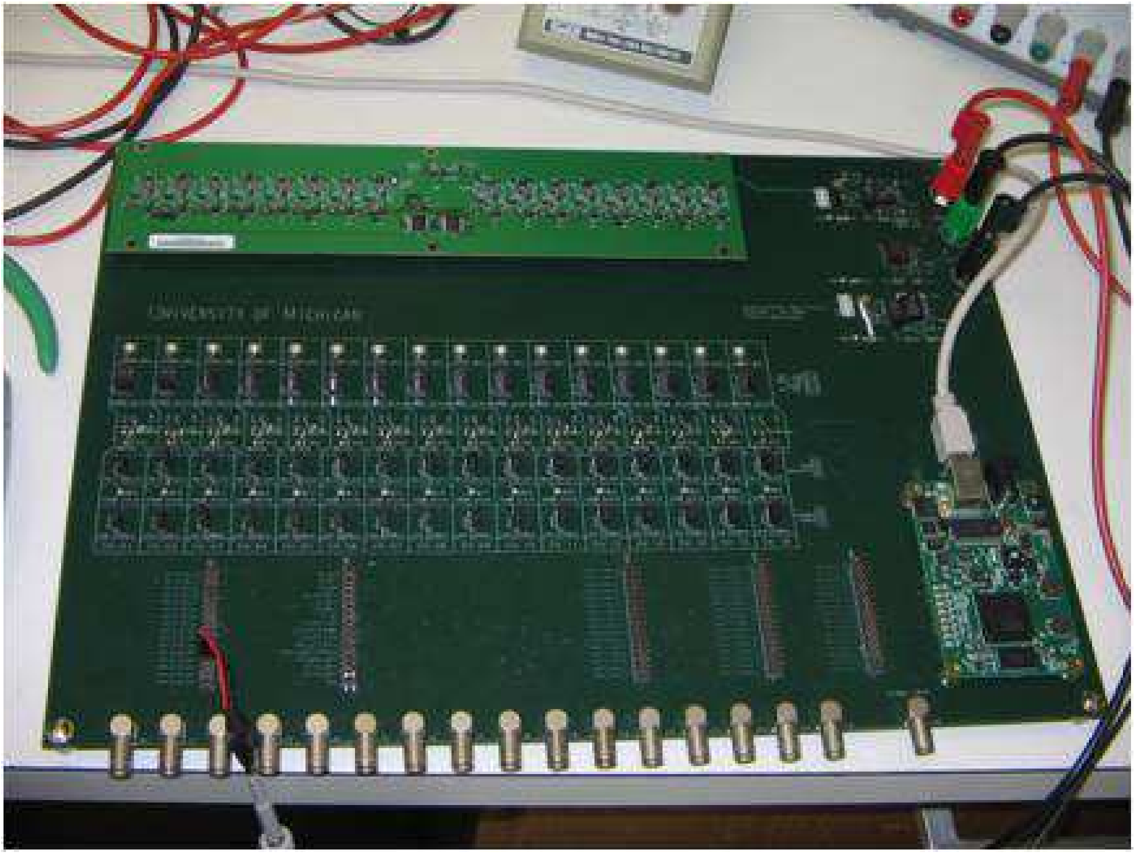

Figure 4.27: Picture of the discriminator test setup: A discriminator is attached at upper left corner of the test board. The Opal Kelly board (XEM3010), to which the USB cable is attached, is located at the bottom right corner.

both the Opal Kelly board and the discriminator board under inspection. Verilog code controlled all the chips on both the testing and discriminator boards by generating the clockings. The interface code provided the control of input parameters such as threshold settings for the Verilog code.

4.6.2 Test Results

After functional failures caused by errors in the original design of the discriminator had been fixed, the testing of the discriminator was quite promising: The 16 DAC chips (ADC5161) were able to set thresholds on individual channels, and the 2 ADCs (8 channels/ADC) were able to read off these thresholds. The ×10 gain amplifier

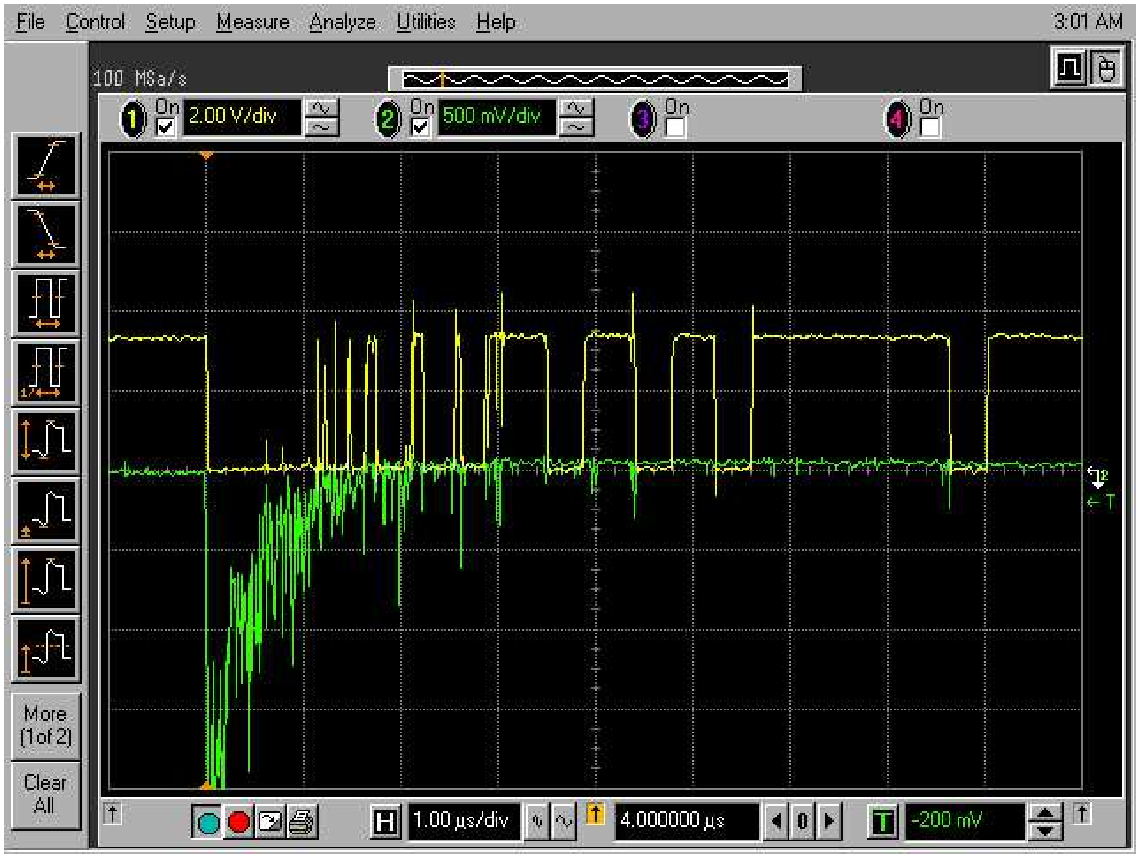

Figure 4.28: The discriminator output observed on the screen of the oscilloscope with a latch time of 400 ns. Channel 0 in yellow shows the discriminator response from the BaF_2/PMT crystal output induced by atmospheric muons (equivalent to $\sim$ 3 MeV) for the signal for channel 1 shown in green. For ease of observation, these signals are boosted by factors of 2.5× and 10× at the output and the input of the discriminator respectively.

(MAX4224) was stable and quiet. Internal noise levels were quite low (≤ -0.5 mV measured for all 16 inputs and there is no significant cross-talk among the channels). Therefore, the discriminator threshold for the anode of a PMT with a gain of 3×10^6 can be successfully set to -4.0 mV (a third of a photo-electron). The timing resolution of the input trigger generated by the pulse generator (Ortec 419) was $\leq$ 80 ps on average. Lastly, the power consumption of the board was measured to be 700 mW during regular operation and 750 mW at maximum.

The behavior of the output of the discriminator had to be carefully studied, since the photo-electron time distribution from the analog output signal of the BaF_2/PMT assembly is quite sparse. The screen shot, (Fig. 4.28), at the oscilloscope captured this feature: The output from the discriminator (shown in yellow) was caused by atmospheric muon depositing ∼3 MeV (shown in green). Once the discriminator unlatches, ∼20 ns separation between two subsequent photo-electrons from the BaF_2/PMT assembly is required of the discriminator to maintain the latch for a prescribed length of time. This feature was observed at ∼1.5 μs after the discriminator triggered in Figure 4.28, and was the cause of multiple triggering from a single hit. Observed behaviors of the CREST discriminator are as follow:

- When a signal comes for the first time, the discriminator holds low (active low) for the length of a latch time. If a part of the signal still continuously exists after the latch time has passed, the discriminator stays low until it discontinues.
- After the discriminator is unlatched, but there are still photo-electrons dribbling in, the discriminator either

  1. keeps low for the latch time if there is more than 20 ns between two subsequent photoelectrons or
  2. keeps low for ∼10 ns (the time length of one photo-electron) between two subsequent photoelectrons

  until there is no signal.

This behavior of the discriminator was used to optimize and to estimate the CREST front-end electronics dead time for the Antarctic CREST flight using a Geant4 simulation (See Sec. 6.1).

CHAPTER V

CREST-I Flight and Analysis

Figure 5.1: CREST-I Instrument at launch

To validate our detection technique, the first CREST instrument, CREST-I, was flown from the Columbia Scientific Balloon Facility (CSBF) at Ft. Sumner, New Mexico in fall 2005. The primary objectives of this flight were to measure diffuse and atmospheric X/γ-rays as well as to test the CREST electronics and the crystal/PMT assemblies under the extreme flight environment.

The importance of the detection of the diffuse and atmospheric X/γ-rays is that they introduce background to the electron events, since the detection method of the CREST instrument relies on measuring synchrotron photons from high energy CR electrons. It is therefore important to investigate the effect of X/γ-ray backgrounds on the CREST instrument.

5.1 Diffuse and Atmospheric X/γ-Rays

The X/γ-rays observable in the atmosphere have both primary and secondary components. The primary component mainly originates from both Galactic diffuse X/γ-rays and from discrete compact objects such as active galactic nuclei (AGNs). The secondary component of X/γ-rays is produced by interaction of primary CRs with the atmosphere, and this component is dominant at balloon altitudes ($\sim$130,000 ft).

5.2 Diffuse X/γ-Rays

The primary component of Galactic X/γ-rays consists of continuum and discrete components. For the continuum between Galactic hard X rays ($\sim$ 12 to 120 keV) and soft γ rays ($\sim$ 30 keV to a few MeV), three physical processes are mainly responsible: non-thermal bremsstrahlung from interstellar gas by interactions with primary cosmic rays, inverse Compton scattering of cosmic ray electrons by radiation from sources such as the cosmic microwave background, and the positronium continuum, which arises from positron annihilation at 511 keV [57]. The energy range where the CREST instrument is interested in detecting synchrotron radiation from high energy primary CR electrons is expected to be dominated by inverse Compton radiation from electrons. The recent observation by the INTEGRAL experiment [58] showed that the power index of the diffuse spectrum is -1.55 ± 0.25 for the energy

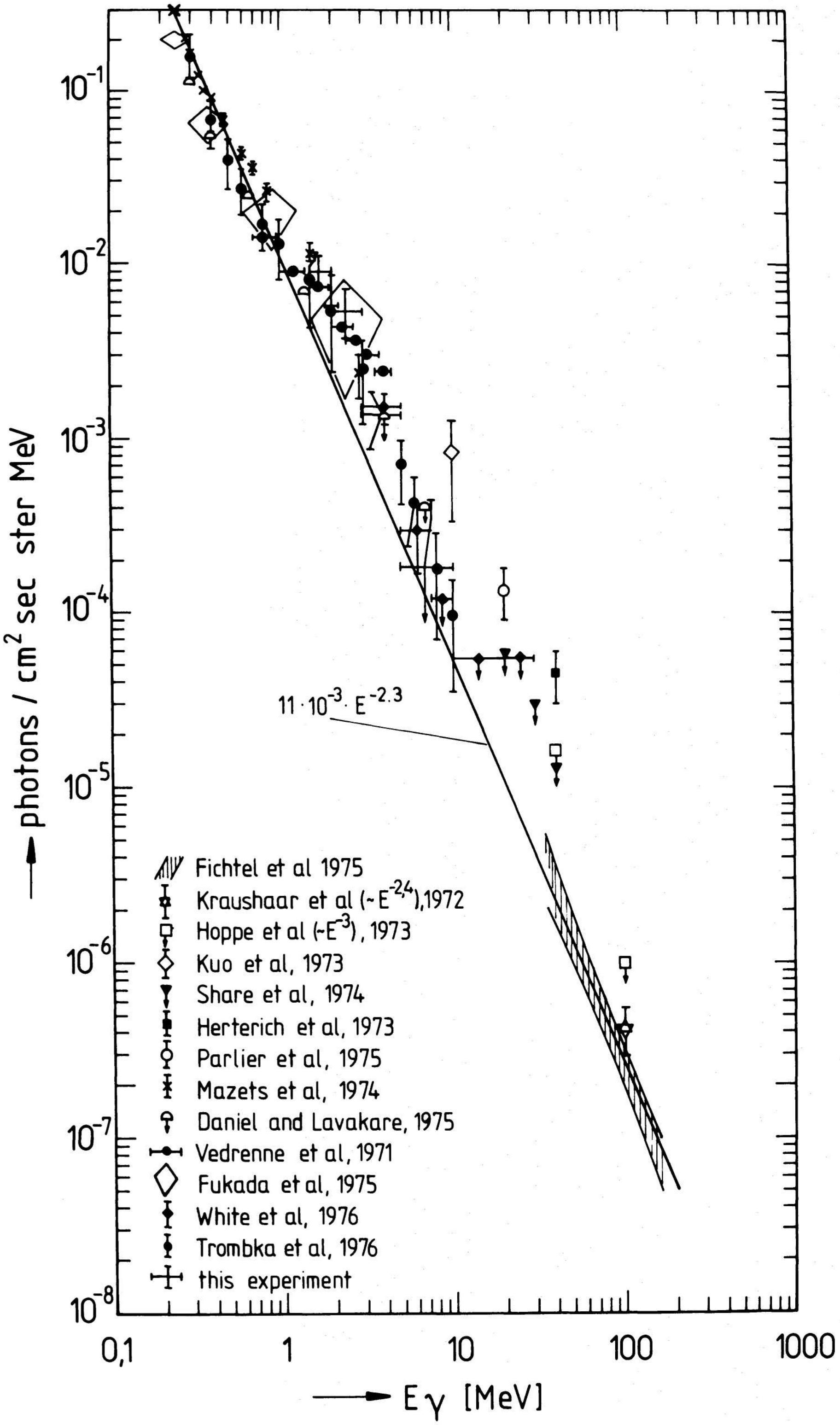

Figure 5.2: Diffuse cosmic γ-ray spectrum normalized at the atmospheric depth 3.5 g/cm^2 from various balloon and satellite experiments with the result from Schöenfelder et al. measured in 1973 and 1974 [56].

range from 50 keV to 2 MeV in the Galactic central region (|l| < 30° and |b| <15°).

Compact objects have been identified in the Galactic center region as the sources of the X/γ-rays in this energy range, and these objects coincide with previously cataloged objects such as black holes and neutron star binary systems. The integrated spectrum from all of the compact sources observed in the Galactic center region by the INTEGRAL experiment has a power index of ~ -2.67 in the energy range from 20 keV to 1 MeV.

Diffuse X/γ-rays have been measured extensively since the late 60's by balloon and satellite experiments. Figure 5.2 shows the integrated spectrum of primary X/γ-rays, whose power law index is approximately -2.3 from a few hundredths of keV to a few tens of MeV. Because the power index seems to vary with energy, Mizuno et al. [59] suggested fitting the more current results from EGRET observations [60] piecewise in a wider energy range. The resulting power law indices are -1.86 from 30 keV to 50 keV, -2.75 from 50 keV to 1 MeV, and -2.15 from 1 MeV and above (Refer to Appendix B. for their functional forms).

5.3 Atmospheric X/γ Rays

The secondary component of X/γ-rays becomes more important with increasing atmosphere depth. The dominant production processes for atmospheric X/γ-rays below 10 MeV consist of four nuclear and electro-magnetic processes: neutral pion decays, bremsstrahlung from albedo electrons and electrons from charged pions, electron and positron annihilation, and neutron capture/inelastic scattering.

The main decay mode (∼98.8%) is that of the neutral pion, π^0, which can simply decay into two gamma's in the atomsphere. For the next most probable decay mode, the π^0 can decay into one gamma plus an electron-positron pair. These electrons then

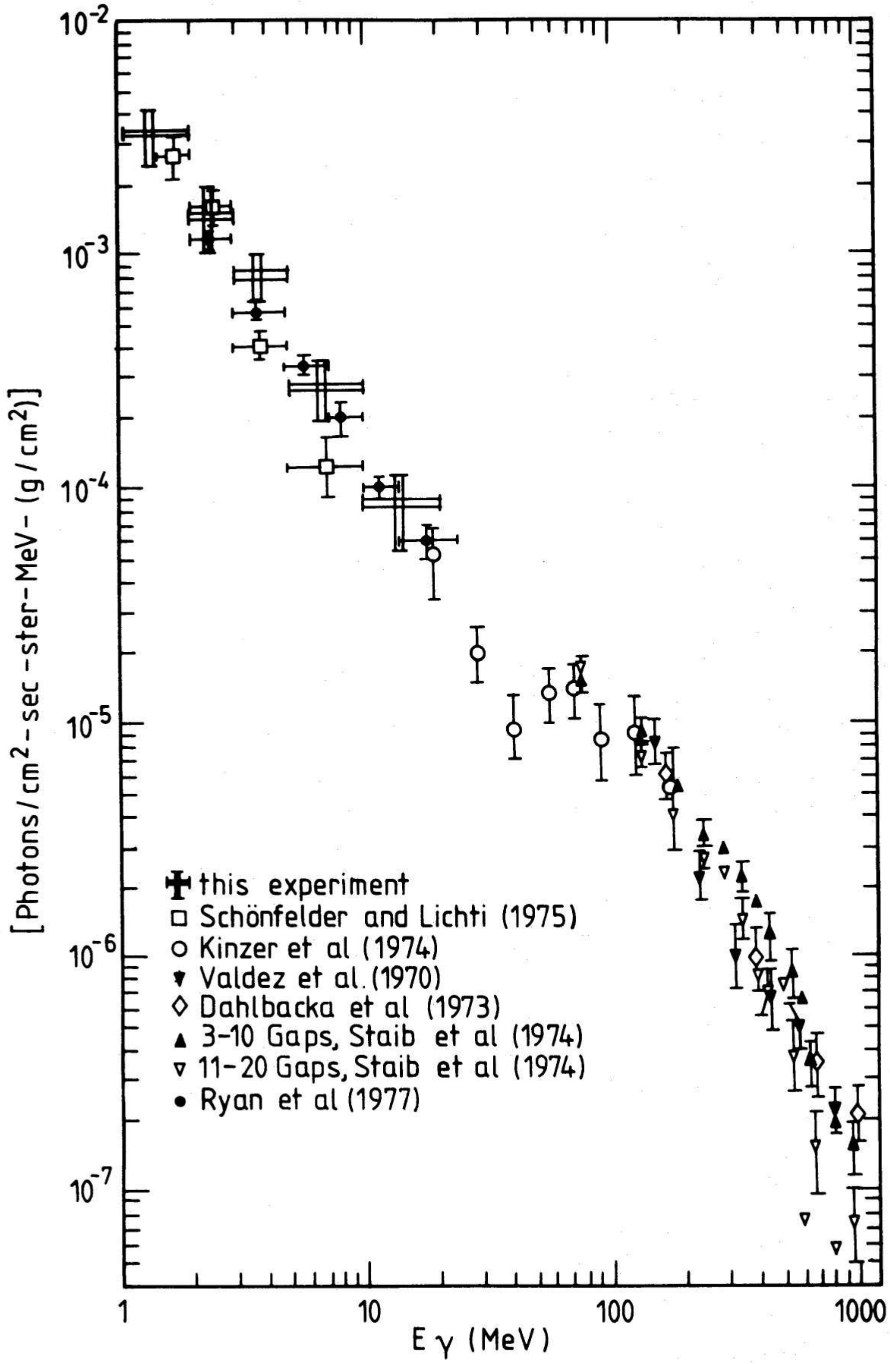

Figure 5.3: Vertically downward moving atmospheric γ ray flux with the result from Schöenfelder et al. [61]. Their data points can be fit by the function $(6 \pm 1) \times 10^{-3}$ $E^{-1.65\pm0.15}$ photons $cm^{-2}s^{-1}MeV^{-1}$ $(g/cm^2)^{-1}$ down to 1 MeV.

generate bremsstrahlung photons in the atmosphere. Charged pions, $\pi^{\pm}$, can produce electrons through the decay process ($\pi^{\pm} \rightarrow \mu^{\pm} \rightarrow e^{\pm}$), and these electrons can again generate bremsstrahlung photons. Lastly, the neutrons in the atmosphere can be captured or inelastically scatter off ^{16}O and/or ^{14}N and as a result, the neutrons become enegetically excited. From these excited states, these neutrons decay into more stable states through the emission of gamma-rays with characteristic energies.

These relatively higher energy atmospheric photons are brought down to lower energies ($\leq$ 3 MeV) by multiple Compton scattering via their interactions with the atmosphere. Each interaction decreases the energy of the photons by a small amount, and eventually this process builds up the continuum spectrum of atmospheric photons.

Atmospheric X/γ-rays have a preferential direction from below the horizon because the processes generating these photons predominately occur below balloon float altitudes [56]. This tendency becomes slightly more prominent for higher energy photons. As these photons lose their energy through scattering in the atmosphere, they become more uniform in all directions [62].

Observations of vertically downward moving atmospheric X/γ-rays at energies above ~1 MeV have been performed at balloon altitudes, and their spectrum is presented in Figure 5.3. At X/γ ray energies from ~1 MeV to ~10 MeV, this downward component of the atmospheric X/γ-ray spectrum can be modeled by a power law with an index of -1.65 ± 0.15 [56]. Below 1 MeV, there are no reliable observations [59].

Upward-moving atmospheric X/γ-rays have been observed by many balloon and satellite experiments (See. [63]). This upward moving component of atmospheric X/γ-rays has a power index of ~ -1.39. The difference index and upward moving

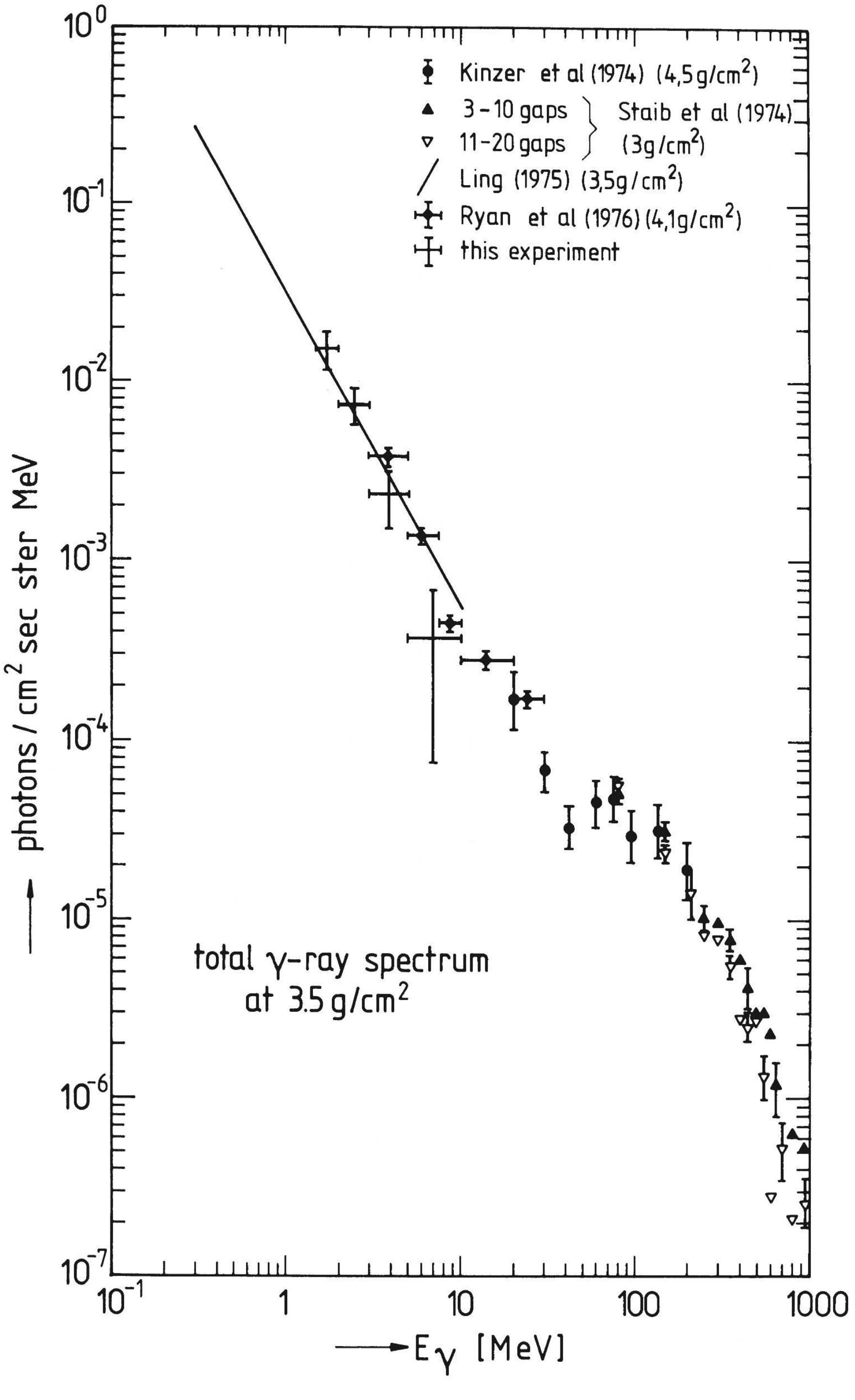

Figure 5.4: Total γ ray spectrum (diffuse and atmospheric) normalized at the atmospheric depth 3.5 g/cm^2 from the result from Schöenfelder et al. [56].

X/γ-rays in general can be inferred from the downward moving atmospheric X/γ rays [64] as follows. First, the downward moving spectrum of atmospheric X/γ rays is $\propto E^{-1.65\pm0.15}$ photons $\mathrm{cm}^{-2}\mathrm{s}^{-1}\mathrm{MeV}^{-1}$ as determined from the observations [61] from 1 to 20 MeV. By taking this spectrum as the source of the atmospheric γ-ray emissivity from secondary, albedo, and primary electrons, it has been shown that the up-going atmospheric γ ray spectrum is $\propto \mathrm{E}^{-1.34}$ at the polar region (where the rigidity cutoff is $\sim$ 3 GV at 750 km above the ground). This result agrees with both the measurement of upward-going X/γ-rays by Imhof et al. [63] from 40 keV to 2.7 MeV, and the semi-empirical model of atmospheric X/γ-rays based on previous measurements by Ling [62]. Figure 5.4 shows the spectrum of the total diffuse and atmospheric X/γ-rays at 3.5 g/cm^2 along with the Ling semiemperical model with power index of -1.39.

A summary of the power indices of the primary and atmospheric X/γ-rays at balloon altitude (Fig. 5.5) is:

1. Primary X/γ rays
    - Continuum and discrete components:
        - -2.3 (a few hundredths of keV to a few tens of MeV, Figure 5.2, [56])
        - -1.86 from 30 keV to 50 keV, -2.75 from 50 keV to 1 MeV, and -2.15 from 1 MeV and above, [59]
    - Continuum: -1.55 ± 0.25 (50 keV to 2 MeV, [58])
    - Discrete: -2.67 (20 keV to 2 MeV, [58])
2. Secondary atmospheric X/γ rays
    - Upward: $-1.39 \sim -1.34$ (40 keV to 2.7 MeV, [63])
    - Downward: -1.65 ± 0.15 ($\geq$ 1 MeV, [56])

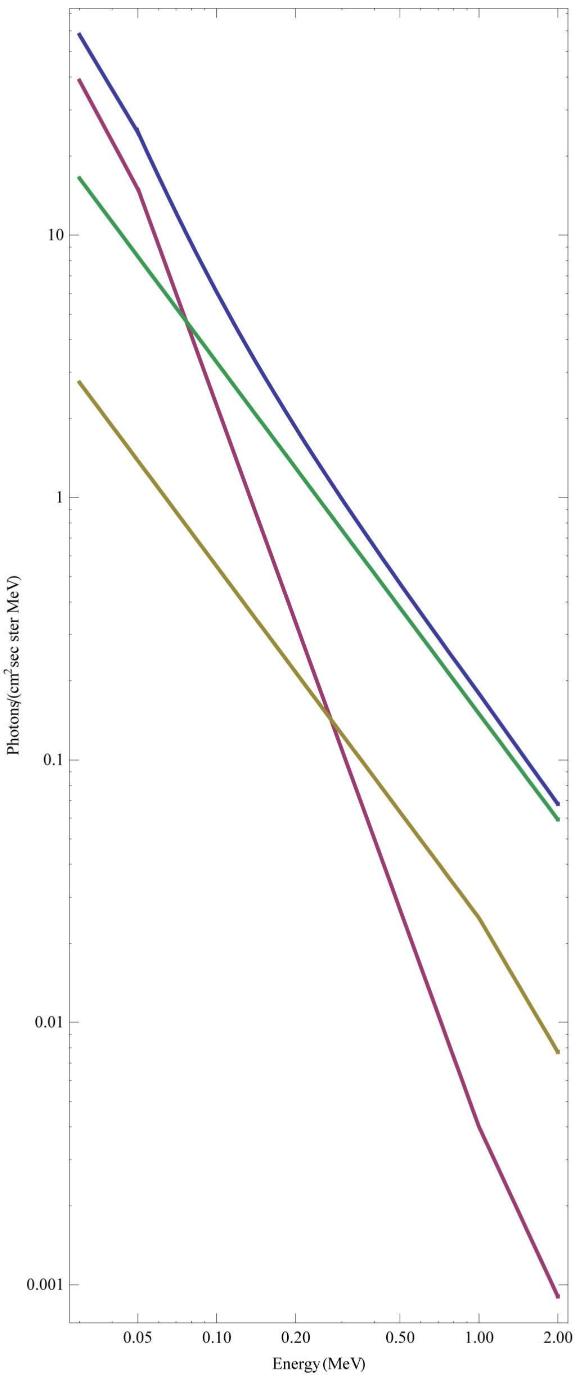

Figure 5.5: Total X/γ ray spectrum in blue and its components (primary in pink, and downward/upward moving atmospheric in yellow and green, respectively) at an atmospheric depth of 3.8 g/cm^2 and rigidity cutoff of 4.46 GV [59]. See the model functions of these components in Appendix A. They assume that the power index of the downward-going X/γ spectrum is -1.34 instead of -1.65.

Note that the CREST-I instrument was not sensitive to the direction of these photons, and it measured an integrated spectrum. However, most of the components it measured were coming from below the instrument, as shown in Figure 5.5.

The power index is a strong indication of the origin of the observed X/γ-rays and is relatively robust to variation in longitude, latitude, altitude, and cutoff rigidity. On the other hand, the normalization factor of the observed spectrum can be significantly affected by the location of the payload. As primary X/γ-rays attenuate as they travel through the atmosphere, more secondary X/γ-rays are produced. Consequently, the secondary production of X/γ-rays overtakes the primary component (at $\leq$ a few g/cm^2, depending on the energy [56]). As a result, the intensity of X/γ-rays increases at lower altitudes. The geometrical location (longitude and latitude) is also an important factor for the normalization of the X/γ-ray flux, since the magnetic field of the Earth affects the entry of primary CRs into the atmosphere. In the polar regions, more primary cosmic rays can penetrate the magnetic field of the Earth, and therefore the intensity of secondary atmospheric X/γ-ray production increases by the mechanisms described previously. Applying this principle to estimate the normalization difference between the continental US and Antarctic CREST balloon flights, the intensity normalization is expected to increase by $\sim$ 70% [64] in Antarctica.

5.4 CREST-I Detector

5.4.1 Mechanical Description of the CREST-I Instrument

The CREST-I instrument was a miniature version of the full size Antarctic CREST instrument. The total physical size of the CREST-I instrument (the outside frame size) was 82” × 66” × 34” as shown in the schematic diagram and the picture in Figure 5.6 and 5.7, respectively. The major components of this instrument are the crystal/PMT assemblies, the veto scintillators and the other supporting electronics

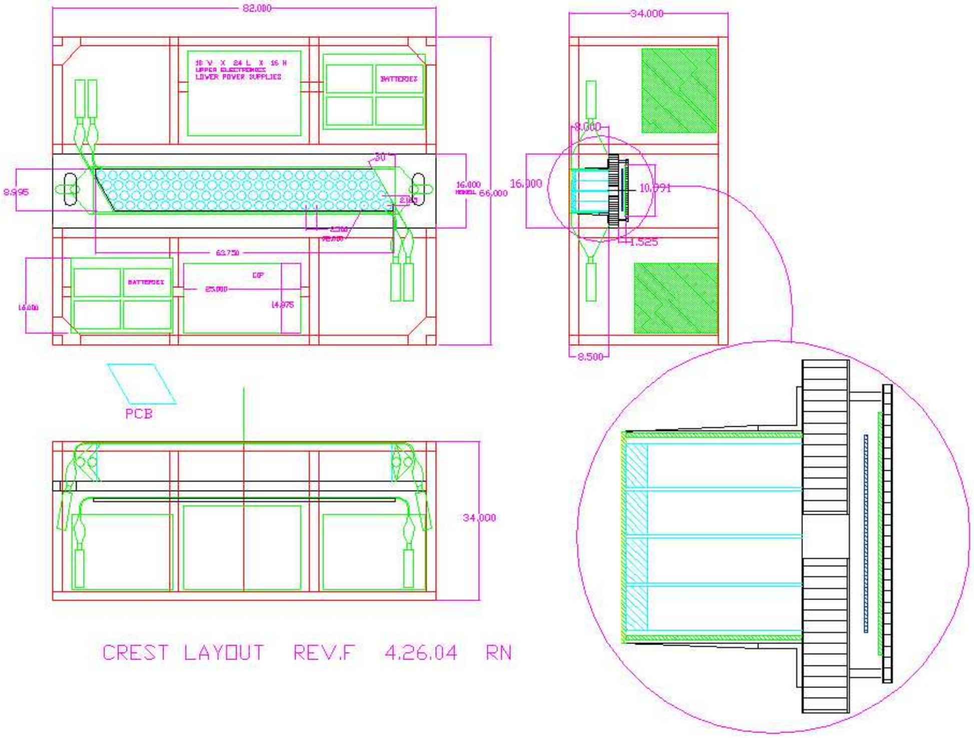

Figure 5.6: Mechanical schematic diagram of the CREST-I instrument. In the left top picture, the 96 crystal/PMT assemblies shown in light blue circles are surrounded by four veto scintillators. (Lengths are in inches.)

(similar to those described in the previous chapter).

The details of the crystal/PMT assemblies for the CREST-I flight were described in Chapter IV. The 96 crystal/PMT assemblies were close-packed with a PMT center-to-center distance of 2.5” inside foam on the supporting structure as shown in Fig. 5.8. Among these 96 assemblies, 80 PMTs had 2.54 cm radius × 1 cm tall cylindrical BGO crystals attached, while the rest of them had 2.54 cm radius × 1 cm tall cylindrical DPS vacuum-coated BaF_2 crystals. Half of the PMTs were manufactured by Burle, and the other half were manufactured by Photonis. Sixteen BaF_2 crystals were coupled to Photonis PMTs.

Manufactured by Bicron, the four plastic veto scintillators were placed to surround the crystal/PMT assembly channel in order to detect charged CR particle

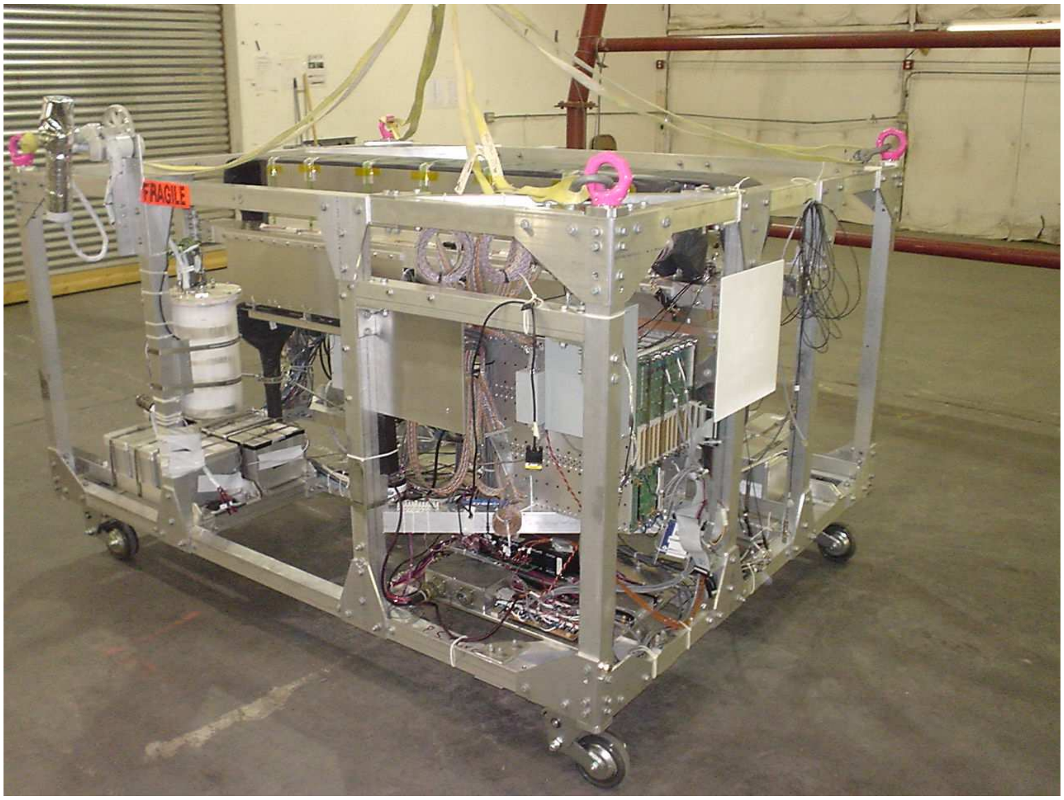

Figure 5.7: The CREST-I instrument at the CSBF facility in Ft. Sumner, NM. This photograph was taken just as it was about to be carried to the runway prior to launch.

background coming from all the sides of the instrument. Due to the mechanical difficulty of positioning one plastic veto scintillator per side on the CREST-I instrument, Bicron produced two bent plastic scintillators; one of which covers the two sides of the crystal/PMT channel. One veto scintillator was placed right on the top of the crystal/PMT channel. For bottom coverage, the veto scintillator was placed underneath the channel with a slight space, which provided space for the electronic cables that connect the crystal/PMT assemblies and front-end electronics to the coincidence logic module and the main flight computer. To collect the photons generated by these scintillators, two Burle PMTs were utilized (one per end) for each plastic scintillator. There were a total of eight Burle PMTs utilized for the CREST-I flight.

The basic functionalities and data flow of the electronics used for the CREST-I

Figure 5.8: The array of crystal/PMT assemblies in the CREST-I instrument. These crystals were covered by thin aluminum caps.

flight were quite similar to the Antarctic CREST instrument as described in Chapter IV. Hence, the physical locations of these electronics were: the discriminator and the charge collecting boards were mechanically attached directly underneath the crystal/PMT assembly channel (as seen from the right top and bottom pictures with vertical green lines in Figure 5.6). The coincidence logic module, the main flight computer, and the LED pulser were located in the same quadrant (If it were shown, they would be on the right bottom side of the left top picture).

5.4.2 Basic Data Flow and the Operational Characteristics

Data flow for the CREST-I flight was in the following order:

1. A X/γ-ray photon or/and a charged CR particle interacts with one of the crystals in the array.

2. The crystal generates scintillation photons according to the energy deposited inside of the crystal. Then, the PMT optically-coupled to that crystal generates an analog signal by first converting these scintillation photons into photo-electrons, and, then, multiplying these photo-electrons using inter-dynode voltage differences. These PMTs were operated at nominal gain of 1×10^6.

3. The discriminator triggers a signal at about the one photo-electron level and it outputs logic signals to both the coincidence logic module and the main flight computer.

4. The coincidence module makes a request to all the ADC modules of the crystal/PMT and scintillator/PMT assemblies to collect their charges when one of the following conditions is satisfied:

    - four coincident single crystal/PMT hits (each hit should fall within a 50 ns window)
    - multiple crystal/PMT hits within a 50 ns coincidence window

    Note that only the crystal/PMT assembly can actively participate in the coincidence logic. The veto scintillator/PMTs assemblies are passive to the coincidence.

5. After reading off all the charges from the ADC modules, the main flight computer matches and packages TDC data from the discriminators and the ADC data from the ADC charge collecting boards. The main flight computer records all the data onto a flash disk on board and sends a partial data package to the ground computer through the CSBF provided communication link.

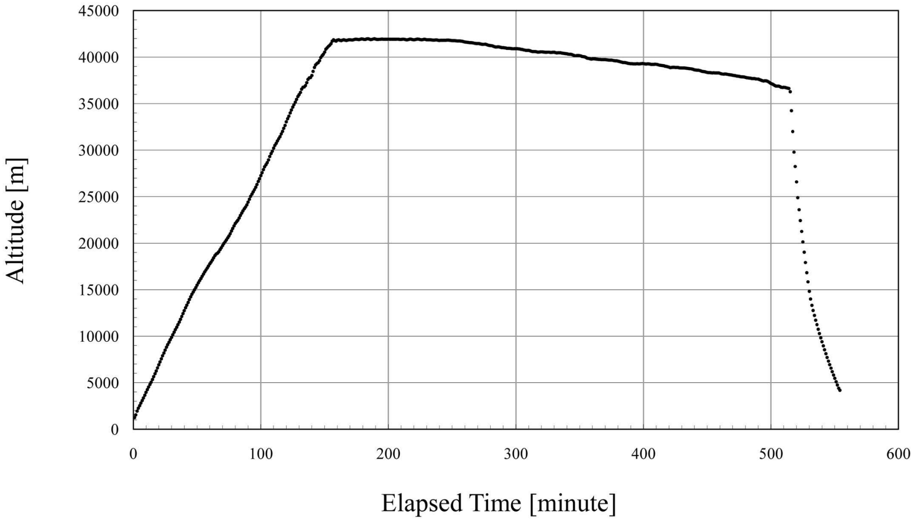

(a)

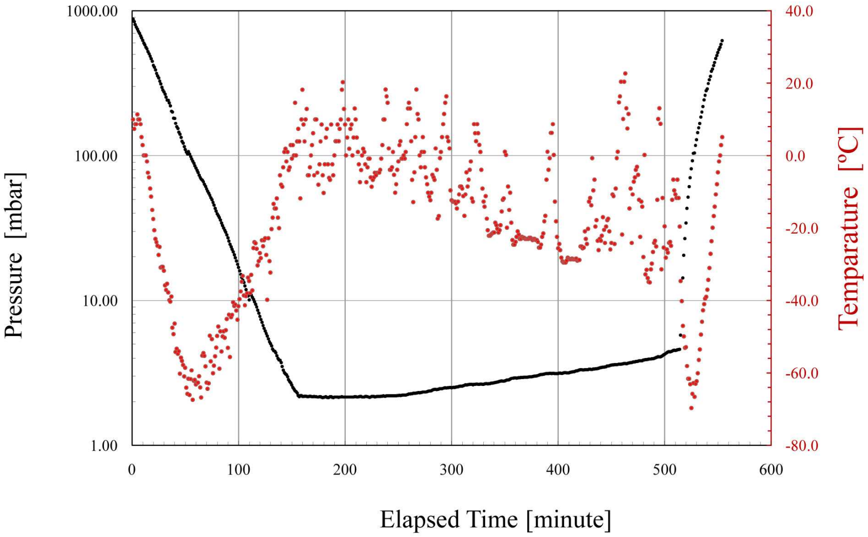

(b)

Figure 5.9: CREST-I flight (a) altitude profile and (b) pressure and temperature profiles.

5.5 CREST-I Flight

The CREST-I instrument was launched at 7:30 am MDT on October 8th, 2005 from the CSBF at Ft. Sumner, New Mexico (34^o N, 104^o W). At launch, 91 out of the 96 crystal/PMT assemblies and all of the veto plastic PMT assemblies were successfully read out. After reaching shower maximum ($\sim$80 kft) during ascent the housekeeping module malfunctioned. Hence, the CSBF provided altitude, pressure, and temperature profiles after the flight as shown in Figure 5.9. Furthermore, just before the CREST-I instrument reached float altitude, one module (16 BaF_2 crystal/PMT assemblies) malfunctioned. The total time of the ascent was 2 hours and 45 minutes.

Around 10:15 am, the CREST-I instrument had reached float altitude (41,972 m, 2.14 mbar where it achieved the record for the highest altitude for a CSBF scientific payload). After floating for 1 hour and 15 minutes at that altitude, the balloon began a valve-down, and started descending slowly and continuously from 11:30 am. During this slow descent, the entire electronics system malfunctioned. After an attempt to recover by power cycling the instrument and then waiting a half hour, contact was regained with the CREST-I instrument. This persisted for the rest of the flight, and data taking continued for 15 minutes followed by 30 minutes of rest. Float was terminated at 4:05 pm and the instrument touched down on the ground at 4:53 pm. The total duration of the flight was 563 minutes, and the coordinates of the touchdown were (35^o 2.37” N, 102^o 25.8” W).

Even though the CREST-I instrument had experienced hardware difficulties as described above, the collected data served to quantify the functionality of the electronics, which will be useful for the Antarctic flight. In addition, the diffuse and

Table 5.1: Selected data from the CREST-I flight

File name	File Size (MB)	Altitude (km)	g/cm^2	Local Time (GMT)
r0000127.dat	22	30.48 $\sim$ 33.53	11.45 $\sim$ 7.32	15:20:45 $\sim$ 15:31:45
r0000128.dat	24	33.53 $\sim$ 36.58	7.32 $\sim$ 4.77	15:31:45 $\sim$ 15:41:46
r0000129.dat	31	36.58 $\sim$ 39.62	4.77 $\sim$ 3.19	15:41:46 $\sim$ 15:55:47
r0000130.dat	35	39.62 $\sim$ 41.76	3.19 $\sim$ 2.42	15:55:47 $\sim$ 16:05:47
r0000131.dat	74	$\sim$ 41.76	$\sim$ 2.42	16:05:47 $\sim$ 17:37:51
r0000132.dat	70			
r0000133.dat	64			

atmospheric X/γ-ray energy spectra were measured.

5.6 CREST-I Data and Event Selection

5.6.1 Recorded Raw Data

The data taking of CREST-I started before its flight when the instrument was carried from the hangar onto the runway. The run number of the data files started from r0000122.dat and ended at r0000139.dat. Each file is separated manually from the ground computer during the flight according to the altitude of the instrument as provided by the CSBF. Because of the failure of the housekeeping module in the very beginning part of the flight, the altitude and absolute times of the data files were matched with the CSBF provided data after the flight. Some of the data files (shown in Table 5.1) are discussed in a later section, since these data were taken after the instrument had passed through the shower maximum (where the electronics on board was comfortably able to handle the background rates).

5.6.2 PMT Gain Stability during the CREST-I Flight and Energy Calibration

The recorded event data had to be calibrated and selected for further analysis. First, the gain stabilities of all the PMTs during the CREST-I flight were monitored by LED pulses (See Section 4.1.4 for the development of the LED calibration system). Light pulses from a LED were directed through fiber optic cables to the photocath-

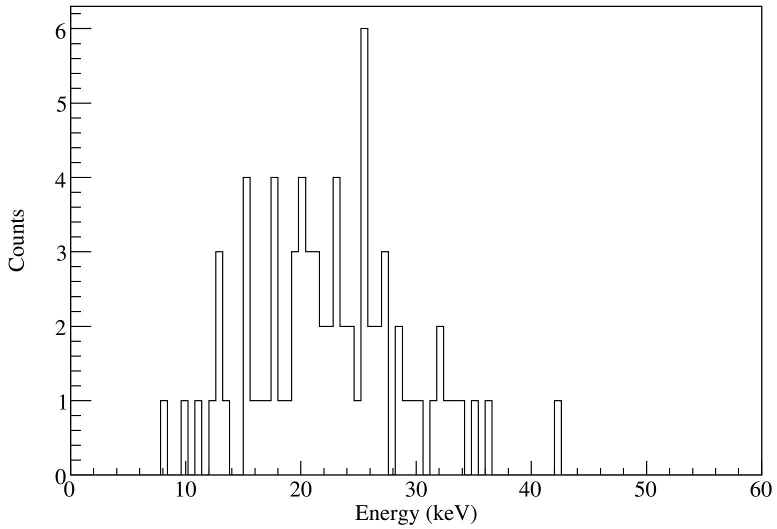

Figure 5.10: Energy cutoff values as determined by an energy calibration performed at room temperature at Indiana University. The mean energy cutoff value is 22.7 keV with $\sigma = 6.6$ keV.

odes of the PMTs. The LED was flashed at a fixed constant rate of 10 Hz, and light pulses arrived at all the PMTs simultaneously. The ADC values of these flashes were strong enough not to coincide with the low energy X ray range, where incident rates were expected to be high. These data were treated as real events and was simply read off in the regular data stream. Throughout the CREST-I flight, the mean deviation of the PMT gains were approximately 2.0% for all the 78 active PMTs with BGO crystals.

The energy calibration was performed after the CREST-I instrument was brought back to Indiana University. Two radioactive sources with three distinct X/γ ray energies were utilized for this calibration: One of them was ^{232}Th with 75.5 keV and 238 keV X/γ-rays, and the other source was ^{137}Cs with 662 keV γ-rays. Using these X/γ ray sources and the identical configuration as the first CREST flight, all of the ADC values for the BGO/PMT assemblies were calibrated. This calibration was merged with the CREST-I flight data, and revealed energy cutoff values (Figure 5.10)

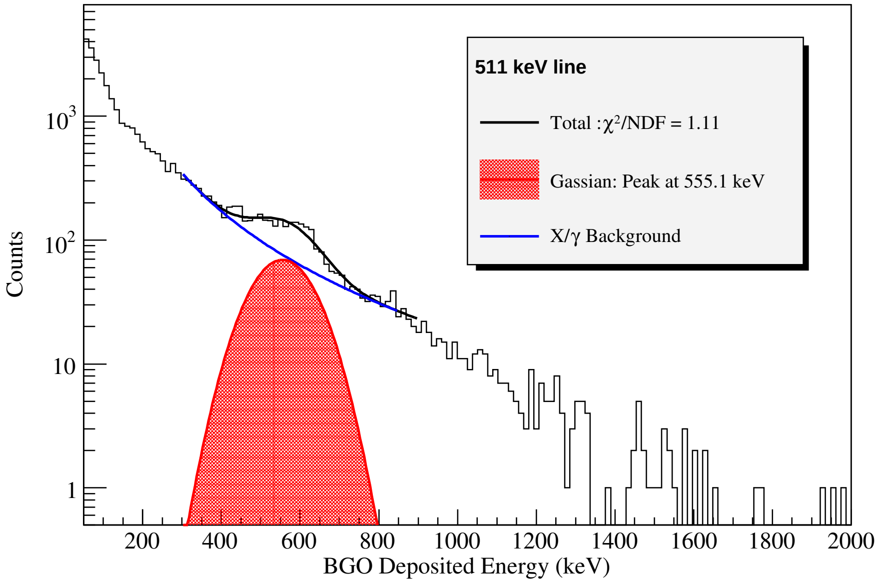

Figure 5.11: X/γ ray BGO deposited energy spectrum at an average overburden 2.81 g/cm^2. The Galactic 511 keV line is quite noticeable. Background radiation from the local atmosphere and diffusive galactic X-ray components were subtracted as a power law, and the peak of the 511 keV line was fit by a Gaussian distribution with a mean and standard deviation of 555.1 ± 6.9 keV.

of 22.7 ± 6.6 keV for the CREST-I data at room temperature. Note that radioactive sources on balloon flights are restricted due to the possibility of contamination to the environment.

The energy calibration on the ground had to be slightly adjusted in order to apply it to the flight data, since the light output of BGO crystals depends on temperature. Due to the unfortunate failure of the housekeeping module in the very beginning of the CREST-I flight, the mean temperatures of the BGO crystals throughout the flight were not completely captured. The ambient air and radiation temperatures could be quite different from those of the crystals. To accomplish the energy calibration during the flight, the peak of the 511 keV line generated from the Galactic e^+e^- annihilation line was utilized (Fig. 5.11).

Table 5.2: Event selection.

File name	Average g/cm^2	Total Number of Events	4 Single Crystal Hit Events (≤ADC=13,000)	
			x keV[1] ≤	50 keV[2] ≤
r0000127.dat	9.39	156,166	24,230	19,326
r0000128.dat	6.05	175,172	27,423	20,983
r0000129.dat	3.98	225,218	36,373	26,861
r0000130.dat	2.81	257,800	42,984	30,368
r0000131.dat	2.42	542,281	92,293	64,734
r0000132.dat		513,110	88,989	61,929
r0000133.dat		495,486	86,578	60,119

5.6.3 Event Selection and Cuts

The raw CREST-I data mainly consists of five kinds of physical events: four consecutive single crystal hits (each hit is separated by more than 50 ns), more than two crystal hits within 50 ns coincidence window, the calibration LED pulses, any events with ADC values lower than the ADC threshold and/or TDC values lower than the TDC threshold, and any of the events above with veto scintillator hits. To extract X/γ-ray induced events, four consecutive single crystal hit events (where each single hit is separated more than 50 ns) were selected. Among these events, the events with either an energy lower than 50 keV or ADC count higher than 13,000 (where the ADC saturates) were excluded. Table 5.2 shows the results of this event selection, and these events are the subject of the analyses in the subsequent sections.

---

[1] The number of events are used to extract the X/γ ray rate per BGO crystal in Sec. 5.7.1. The average energy cutoff, x, depending on energy calibration due to temperature fluctuation of the BGO crystal, is shown in Table 5.3.

[2] Section 5.7.2 uses this number of events to reconstruct the diffuse and atmospheric X/γ ray spectra.

5.7 CREST-I Flight Results and Analysis

Here, the results of the CREST-I flight will be given. First, the X/γ-ray rate per BGO crystal as a function of altitude will be shown. Next, the observed total (diffuse and atmospheric) X/γ-ray spectra observed at different altitudes will be presented.

5.7.1 X/γ-Ray Rate per BGO crystal

The X/γ-ray rate for the BGO crystals in the CREST-I instrument can be used to estimate the x/γ background rate (as well as the accidental false synchrotron radiation rate) for the Antarctic CREST instrument. Note that as previously shown (Table 4.1), the number of radiation lengths of the 1 cm thick BGO crystals used for the CREST-I instrument is almost the same as that for the 2 cm thick $\mathrm{BaF_2}$ crystal that will be used for the Antarctic CREST instrument. To extract the rate for a single BGO crystal, the distribution of the time difference between consecutive events will be used. This distribution with the scaled number of (multiple) events, as in the case of the CREST-I flight, follows a Gamma distribution [65] with density function,

$$f(\mathrm{t}) = \frac{\mu \mathrm{e}^{-\mu \mathrm{t}} (\mu \mathrm{t})^{\alpha - 1}}{(\alpha - 1)!} \tag{5.1}$$

where t is the elapsed time since the last output was generated, μ is the mean rate into, and α is the multiplicity ($\alpha = 4$ for the CREST-I flight). The use of the time difference between consecutive scaled events is quite advantageous, since this distribution is independent of the dead time of the electronics at low input rates.

Figure 5.12 shows an example of the histogram of the time differences between the scaled events and its fit with a Gamma distribution using the χ^2 method. Each error bar was estimated from both the number of single crystal hits and the number of

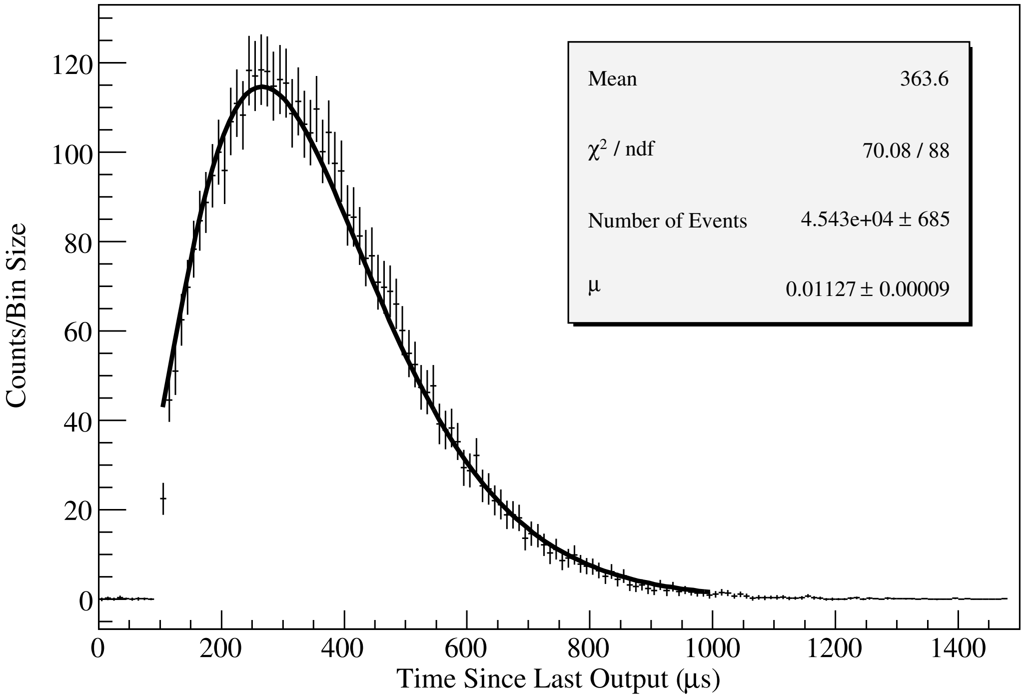

Figure 5.12: Data and χ^2 fit to a Gamma distribution at an average overburden of 2.81 g/cm^2.

multiple crystal hits in the histogram bin. There are two parameters in Eq. (5.1) to fit this distribution: the normalization of counts (Number of Events) and the mean input rate (μ) into the scaler from the 73 active PMTs. Note that there are no events less than 100 μs due to the fact that this was the time required for the coincidence module to clear its own scaler counting memory.

Table 5.3: X/γ Ray Rate (Hz)/BGO crystal with 88 dof

Ave. g/cm^2	Average Energy Cutoff (keV)	χ^2 method		Log Likelihood method	
		Rate (Hz)	χ^2/dof	Rate (Hz)	χ^2/dof
9.39	24.4	173.4 ± 1.2	56.9/88	175.8 ± 1.8	61.0/88
6.05	24.7	163.3 ± 1.4	42.7/88	165.1 ± 1.6	41.9/88
3.98	24.8	157.8 ± 1.0	52.3/88	159.0 ± 1.4	54.2/88
2.81	24.7	153.4 ± 1.4	68.7/88	154.4 ± 1.2	70.1/88
2.42	24.0	151.0 ± 0.3	137.7/88	151.4 ± 0.5	138.4/88

Figure 5.13 shows the X/γ-ray rate per BGO crystal (Hz) for the CREST-I flight.

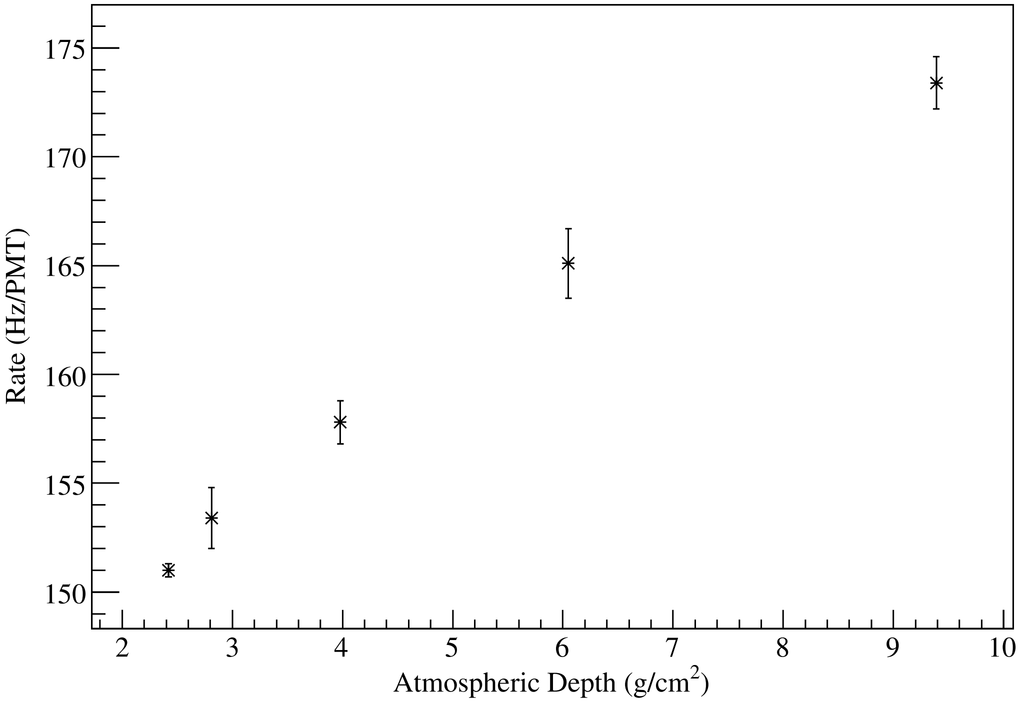

Figure 5.13: Growth curve of the counting rate per BGO crystal. The rate with lower χ^2 value is used for each data point from Table 5.3.

Table 5.3 shows the results of the Gamma distribution fits using both the χ^2 and log likelihood methods. The χ^2 method gives slightly better results, but both methods agree within each other. As expected, the X/γ-ray rate decreases as the atmospheric depth decreases.

5.7.2 Diffuse and Atmospheric X/γ Ray Spectrum from CREST-I data

To obtain the total (diffuse and atmospheric) X/γ-ray spectra in Figure 5.4, the absolute differential flux can be expressed as,

$$F = \frac{N}{\Delta \mathrm{E}} \times \frac{\beta}{\mathrm{GF} \cdot \epsilon_{\mathrm{det}} \cdot T} \quad (\frac{\text{photons}}{\text{cm}^2 \text{ second ster MeV}}), \tag{5.2}$$

Here, N is the *true* number of photons in the energy bin size ΔE. This is generally different from the measured number of photons, M in ΔE, because M includes the information regarding the response of the BGO crystal to X/γ rays. β is the multiplicity of the coincidence logic module ($\beta = 4$). GF and ϵ_{det} are the geometrical factor (cm^2 sr) and detection efficiency of a single BGO crystal, respectively. T is the live time of the CREST-I detector in seconds. Calculation of the absolute differential flux requires an energy deconvolution to unfold the true number of photons, N in Eq. (5.2).

5.7.2.1 Energy Deconvolution

To recover the true number of the photons, N, in Eq. (5.2), it is necessary to understand the detector response to X/γ-ray photons. Generally speaking, the spectrum of the measured deposited energy, $\varphi\left(E_d\right)$, in the detector is related to the primary spectrum, $\phi(E)$, by the Fredholm integral equation of the first kind:

$$\varphi\left(E_d\right) = \int_{E_{\min}}^{E_{\max}} A\left(E_d, E\right)\phi\left(E\right)dE \tag{5.3}$$

where $A\left(E_d, E\right)$ is the response function of the detector with primary energy $E \in [E_{\min},\, E_{\max}]$, and E_d is the measured deposited energy in the detector.

To solve Eq. (5.3), one divides the primary energy range from $E_{\min}$ to $E_{\max}$ into n energy bins, and discretizes this integral equation into a matrix equation:

$$M_i = \sum_{j=1}^{n} a_{ij} N_j, \quad i = 1, 2, ...n \tag{5.4}$$

with the correspondence between Eq. (5.3) and Eq. (5.4) given by

$$A\left(E_d, E\right) \Leftrightarrow a_{ij}, \quad \varphi\left(E_d\right) \Leftrightarrow M_i, \quad \phi\left(E\right) \Leftrightarrow N_j$$

Here M_i is the measured number of counts in energy bin i, N_j is the number of primary X/γ-ray counts in energy bin j, and the matrix element, a_{ij}, describes the probability that the events in the measured energy bin i come from the primary X/γ-ray energy bin j. In general the matrix equation solution for N_j is an ill posed inverse problem. To overcome this problem, I used the numerical method called Tikhonov's regularization[1].

5.7.2.2 Tikhonov's Regularization

By introduction of the weight, τ, *parameter of regularization*, it is possible to convert the problem of solving an ill-posed matrix equation into a minimization problem [66],

$$\tilde{S}\left(N_1, N_2, ..., N_n\right) = \sum_{i=1}^{n}\left(\frac{\sum_{j=1}^{n} a_{ij}N_j - M_i}{\sigma_i}\right)^2 + \tau \times \sum_{j=2}^{n-1}\left(\frac{\triangle N_j - \triangle N_{j-1}}{\sigma_j}\right)^2 \quad (5.5)$$

where $\triangle N_j = N_{j+1} - N_j$ is the difference operator and σ_i is the standard deviation of the measured value, M_i. Here, minimization of the first term of Equation (5.5) is equivalent to the solution of Equation (5.4), while the second term of Equation (5.5) is a regularization term that enforces smoothness of the solution N_j. In fact, the second term is a square norm of the numerical second derivative of the solution. The minimization of Equation (5.5) is equivalent to the compromise between the exact solution and the smoothness of the solution.

The second term of Eq. (5.5) can be improved by applying a priori knowledge of the solution. The shape of the solution should be a power law spectrum as in Figure 5.4 with an index of -1.34 for equidistant bins or -0.34 for logarithmic bins. Equation (5.5) can be transformed into more convenient form:

$$S\left(x_1, x_2, ..., x_n\right) =$$

---

[1] The text of the method of Tikhonov's regularization is closely referenced from [67].

$$\sum_{i=1}^{n}\left(\frac{\sum_{j=1}^{n} a_{ij}R_j^0 x_j - M_i}{\sigma_i}\right)^2 + \tau\times\sum_{j=2}^{n-1}\left(\frac{\alpha_{j+1}R_{j+1}^0 x_{j+1} - 2R_j^0 x_j + \alpha_{j-1}{}^{-1}R_{j-1}^0 x_{j-1}}{\sigma_j}\right)^2 \tag{5.6}$$

where $\alpha_{j+1} \equiv (E_{j+1}/E_j)^{0.39}$, $N_j \equiv x_j R_j^0$ and R_j^0 is an initial approximation of the expected result, N_j.

5.7.2.3 Regularization Parameter τ and Error on Regularization

The regularization parameter, τ, is a parameter which controls the minimization of $S\left(x_1, x_2, ..., x_n\right)$ and determines the solution, N_i. The following method [67] gives a systematic way of determining the parameter, τ, and at the same time it gives an estimation of the error from the Tikhonov regularization method.

First, we approach to the estimation of the error from Tikhonov's regularization. For a fixed τ, the minimization of Eq. (5.6) gives the set of solutions ($x_1^\star$, $x_2^\star$, ..., $x_n^\star$). From this set, we seek the restored measured value, $\tilde{M}_i$, by,

$$\tilde{M}_i = \sum_{j=1}^{n} a_{ij}N_j^\star, \quad N_j^\star = x_j^\star R_j^0, \quad i = 1, 2, ..., n \tag{5.7}$$

with matrix elements, a_{ij}, and initial approximation, R_j^0.

Now by Monte Carlo simulation with standard deviations, σ_i and standard errors, σa_{ij} for $\tilde{M}_i$ and a_{ij} respectively, a set of L species of the simulated experimental data $\{M_i^r, a_{ij}^r\}$, where r = 1, ..., L, can be generated. Again, minimization by the Tikhonov regularization method for each set of simulated experimental data, $\{M_i^r, a_{ij}^r\}$, allows the generation of a set of L simulated solutions (x_1^r, x_2^r,...,x_n^r). This results in the solution, ($x_1^\star$, $x_2^\star$, ...,$x_n^\star$), and simulated solutions, (x_1^r, x_2^r,...,x_n^r) where r = 1, ..., L.

Investigating a distribution of a set of simulated solutions (x_1^r, x_2^r,...,x_n^r) imparts a statistical property to the solution ($x_1^\star$, $x_2^\star$, ...,$x_n^\star$) characterized by the covariance matrix,

$$\mathrm{Cov}_{lm} =< (x_l - x_l^\star)\,(x_m - x_m^\star) > , \quad l,\, m = 1, 2, ..., n, \tag{5.8}$$

Standard deviations of $x_i^\star$ and errors of $N_j^\star$ are defined as,

$$\sigma x_j^\star = \sqrt{\mathrm{Cov}_{jj}} \tag{5.9}$$

$$\Rightarrow \sigma N_j^\star = \sigma x_j^\star R_j^0 = \sqrt{\mathrm{Cov}_{jj}} R_j^0 \tag{5.10}$$

For a fixed regularization parameter, τ, errors in the true X/γ-ray counts in Δ E by the Tikhonov regularization method can be easily estimated. The optimization of τ can be accomplished through the use of the correlation matrix,

$$\mathrm{Corr}_{lm} = \frac{\mathrm{Cov}_{lm}}{\sqrt{\mathrm{Cov}_{ll}\mathrm{Cov}_{mm}}} \in [-1, 1],\ \ \mathrm{Corr}_{ll} = 1, \tag{5.11}$$

which shows the degree of correlation between different energy bins, l and m. The mean correlation matrix is defined as,

$$\mathrm{C}(\Delta\mathrm{j}) = \frac{1}{\mathrm{K}(\Delta\mathrm{j})} \sum_j \mathrm{Corr}_{j,j+\Delta\mathrm{j}},\ \ \mathrm{C}(\Delta\mathrm{j}) = \mathrm{C}(\text{-}\Delta\mathrm{j}),\ \ \Delta\mathrm{j} = 0, \pm 1, \pm 2, ... \tag{5.12}$$

where $\mathrm{K}(\Delta\mathrm{j}) = \mathrm{n} - \mid \Delta\mathrm{j} \mid$ is the number of elements of the correlation matrix in the sum and the value, $\mathrm{C}(\Delta\mathrm{j})$, gives the mean correlation between all the bins for a given Δj.

To get a reasonable estimate of the regularization parameter, τ, by the mean correlation function, $\mathrm{C}(\Delta\mathrm{j})$, consider the following: When the mean correlation function of neighboring bins, $\mathrm{C}(1) \sim -1$, all the neighbor bins are anti-correlated. The resulting spectrum will not be smooth, and the regularization term of Eq. (5.6) is ignored. This is equivalent to a small value of τ. On the other hand, when $\mathrm{C}(1) \sim +1$, neighboring bins get smooth and the overall spectrum becomes close to a power law. When τ is large, the first term of Eq. (5.6) has less influence on the minimization. As a consequence, C(1) should be between -1.0 and 1.0, but it should not be too close to both ends, -1 or 1.

The restored measured values, $\tilde{M_i}$, from the real data and simulated measured values, M_i, should deviate around $\sqrt{< \left(M_i - \tilde{M_i}\right) >} \sim \sigma_i$, and, therefore, this means that the reduced chi-square, $\tilde{\chi^2} \sim 1$. This, in turn, corresponds to a mean correlation value of C(1) $\sim$ 0.5.

To summarize the strategy of the energy deconvolution:

1. For a fixed value of the regularization parameter, τ, minimize the modified Tikhonov function (Eq. (5.6)) with the initial approximation, $R_j^0, = M_j$ to find the solution, $(x_1^\star,\ x_2^\star,\ ...,\ x_n^\star)$.
2. With this solution, find the restored values of $\tilde{M_j}$ by the use of the finite Fredholm equation (Eq. (5.7)).
3. Generate a set of the L simulated experimental data $\{M_i^r,\ a_{ij}^r\}$ where r = 1, ..., L with standard deviations, σ_i and standard errors, σa_{ij} for $\tilde{M_i}$ and a_{ij} respectively.
4. Solve the energy deconvolution again by minimizing Eq. (5.6) to find a set of the simulated solutions $(x_1^r,\ x_2^r, ..., x_n^r)$ where r = 1, ..., L.
5. Calculate the mean correlation for neighboring bins, C(1), from the solution and the simulated solutions and check if C(1) $\sim$ 0.5.
6. Repeat the procedures above (1. to 5.) until C(1) $\sim$ 0.5 is found.

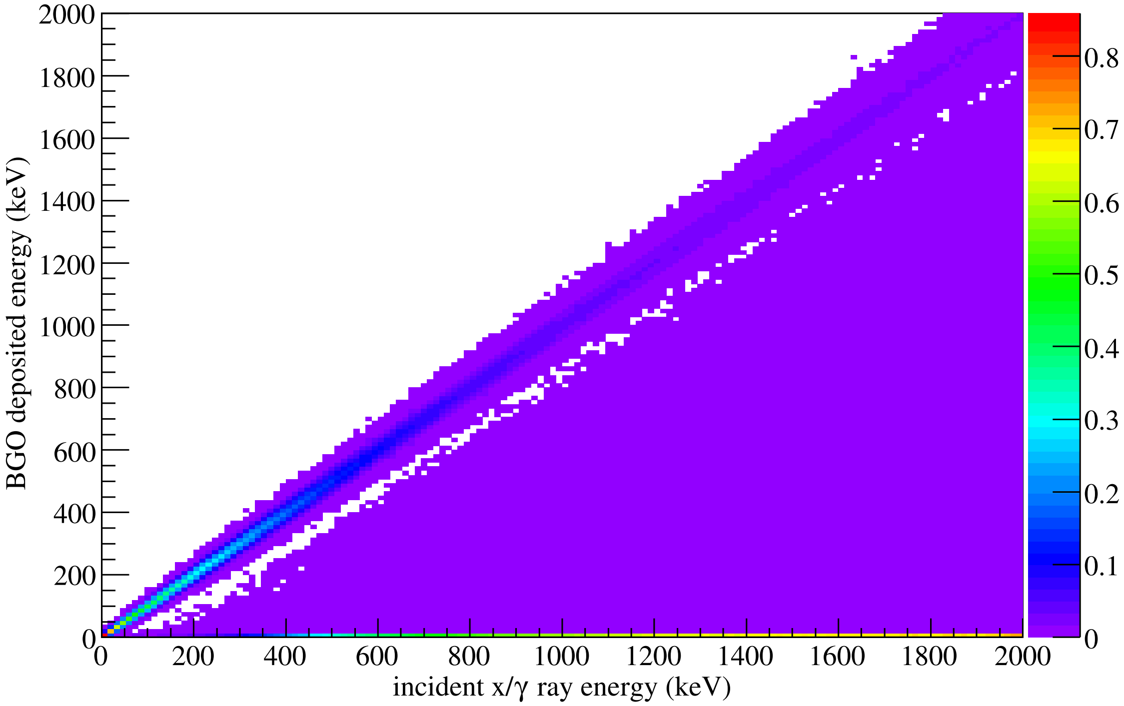

Figure 5.14: 2.54 cm radius × 1.00 cm cylindrical BGO response matrix, a_{ij} with respect to 1,000 isotropic X/γ-ray photons/keV. Note that this contour graph is normalized in incident X/γ-ray energy (keV).

5.7.2.4 Instrument Response Function Simulation

The instrument response matrix, a_{ij}, in Equations (5.4), (5.5), (5.6), and (5.7) can be calibrated by actual measurement with known energy sources or it can be estimated by Monte Carlo simulation (the indices i and j represent i^{th} and j^{th} energy bins for deposited energy in the crystal and incident photon energy, respectively). In the CREST-I analysis, a Geant 3 based program was used to simulate the interaction of X/γ ray photons with a single BGO crystal. In the simulation, photons with energies in the range from 0 to 2 MeV are generated isotropically in the 2.54 cm radius × 1 cm cylindrical BGO crystal. The energy bins were chosen to have a width of 1 keV, with 1000 photons generated per bin. The resulting deposited energies in

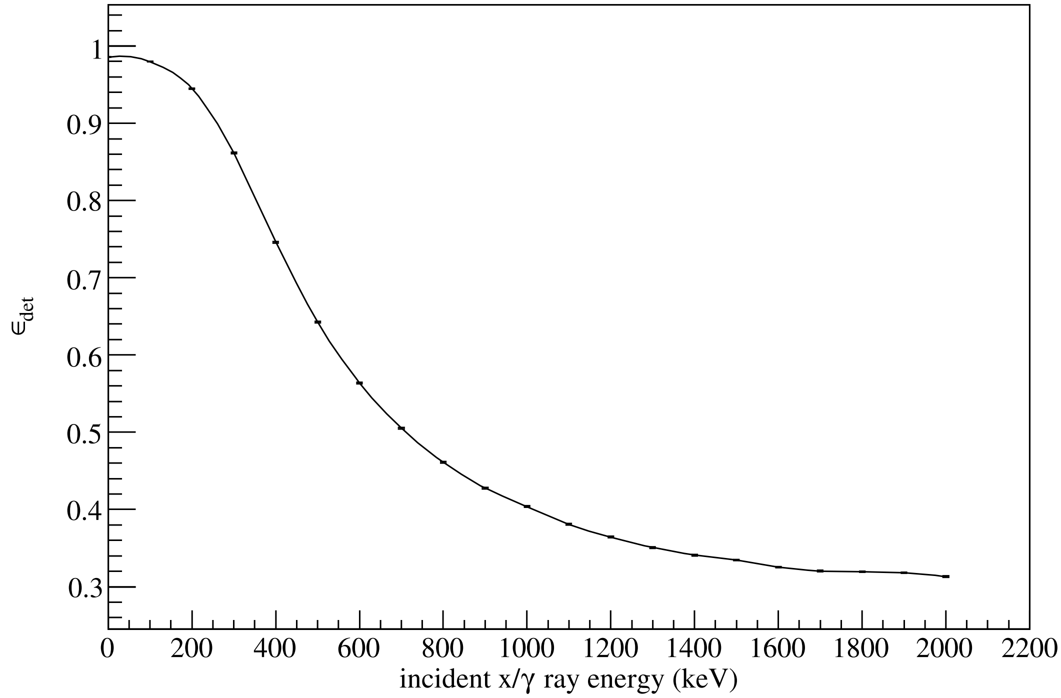

Figure 5.15: Simulated detection efficiency for the 2.54 cm radius × 1 cm cylindrical BGO crystal for 0 to 2.2 MeV incident photons.

the crystal with respect to the incident photon energy are shown in Figure 5.14. Note that at zero$^{\text{th}}$ order, the detector response function can be approximated as linear ($a_{ij} = \delta_{ij}$).

Using the results of the Monte Carlo simulation, the detection efficiency of the BGO crystal, ϵ_{det} in Eq. (5.2), to incident photons was estimated. Figure 5.15 shows that the larger the energy of the incident photon, the lower the interaction cross section between the incident photon and the BGO crystal.

5.7.2.5 Geometrical Factor

The general concept of the geometrical factor (GF: cm^2 ster-radian) is the ratio of rate (Hz) to flux (particles/cm^2 ster-radian second), which describes the geometrical characteristic of the detector used to quantify how well the detector can *see* the particles, and does not require detection nor interaction with these particles. In the case of an isotropic flux of particles the GF can be expressed as [68],

$$\mathrm{GF} = \int_{\Omega_0} d\Omega \int_{S_0} d\boldsymbol{\sigma} \cdot \hat{\mathbf{r}} \tag{5.13}$$

where dΩ is an element of solid angle, and Ω_0 is the subtended angle of the detector. $d\boldsymbol{\sigma} \cdot \hat{\mathbf{r}}$ is an area element in the direction of Ω, and S_0 is the total area of the detector.

Although the CREST-I instrument consists of an array of BGO crystals, we calculate the GF of a single BGO crystal and multiply the single crystal GF by using the number of active crystals as an approximation for the whole array. In the case of a simple geometry of the detector such as a two-dimensional rectangular plane or two circular plates separated by a distance, Equation (6.2.2) can be solved explicitly. On the other hand, there is no explicit analytical solution of the geometrical factor for a three dimensional cylindrical shape. First, we can roughly estimate the geometrical factor by taking the average subtended area of the cylinder as follows,

$$\mathrm{GF}_{\mathrm{cylinder}} \simeq 2\pi \times \overline{A} \simeq 2\pi \times \frac{\pi r^2 + 2\pi L r}{2} \simeq 113.81 \ \ (\mathrm{cm}^2 \ \mathrm{ster}) \tag{5.14}$$

where r = 2.54 cm and L = 1.00 cm for the radius and the thickness of the BGO crystal, respectively.

However, we can perform the Monte Carlo simulation to obtain a better estimate for the GF. For the case of the Monte Carlo simulation, Eq. (6.2.2) can be rewritten as,

$$\mathrm{GF}_{\mathrm{cylinder}} = \int_{-1}^{1} \int_{0}^{2\pi} d\mathrm{cos}\theta d\phi \int_{S_0} \mathrm{cos}\theta d\sigma \overset{\mathrm{M.C.}}{\Rightarrow} \left(\frac{1}{2} \int_{-1}^{1} \int_{0}^{2\pi} d\mathrm{cos}^2\theta d\phi \right) \left(f \int_{\tilde{S_0}} d\sigma \right) \tag{5.15}$$

The point of this conversion is from the surface area, S_0, into $\tilde{S}_0$ with an additional factor of f. The surface area, S_0, of the detector is estimated by the fractional intersecting volume from the particles generated from the surface $\tilde{S}_0$. Therefore, pseudo particles in the simulation can be generated from the coordinates (x, y, and z) of the surface of $\tilde{S}_0$ with a direction given by ϕ, and $\cos^2\theta$ in a 4π steradian solid angle, and a fraction, f, of these particles have trajectories that intersect with the volume of the crystal. In the case where particles are generated from a sphere enclosing the crystal, Eq. (5.15) can be further simplified,

$$\mathrm{GF}_{\mathrm{cylinder}} = 2\pi \times f \times 4\pi\tilde{r}^2 = 8\pi^2\tilde{r}^2 \times f \tag{5.16}$$

where $\tilde{r}$ is the radius of the particle generating the sphere in the simulation. A total of 10^6 particles were generated in the Geant4-based simulation, and the GF of one BGO crystal was found to be 171.28 (cm^2 ster). The simple geometrical estimation of Eq. (5.14) is off by 34% from the Monte Carlo simulation result. Since the uncertainty of the Monte Carlo simulation has a dependence of $\sim 1/\sqrt{N}$, where N is the number of the simulated events, the uncertainty of the GF for the cylindrical crystal is approximately 0.1%.

5.7.2.6 Counting Rate Spectra

Figure 5.16 presents the spectrum of average energy deposited per BGO crystal, measured by CREST-I at different altitudes. These spectra are the measured counting rates of a BGO crystal, before the energy deconvolution and the geometrical factor are taken into consideration. To generate these spectra, ten logarithmic bins (Table 5.4) were used to cover the energy range from 30 keV to 2 MeV. Since the housekeeping module failed in the early part of the flight (See Section 5.5), the live

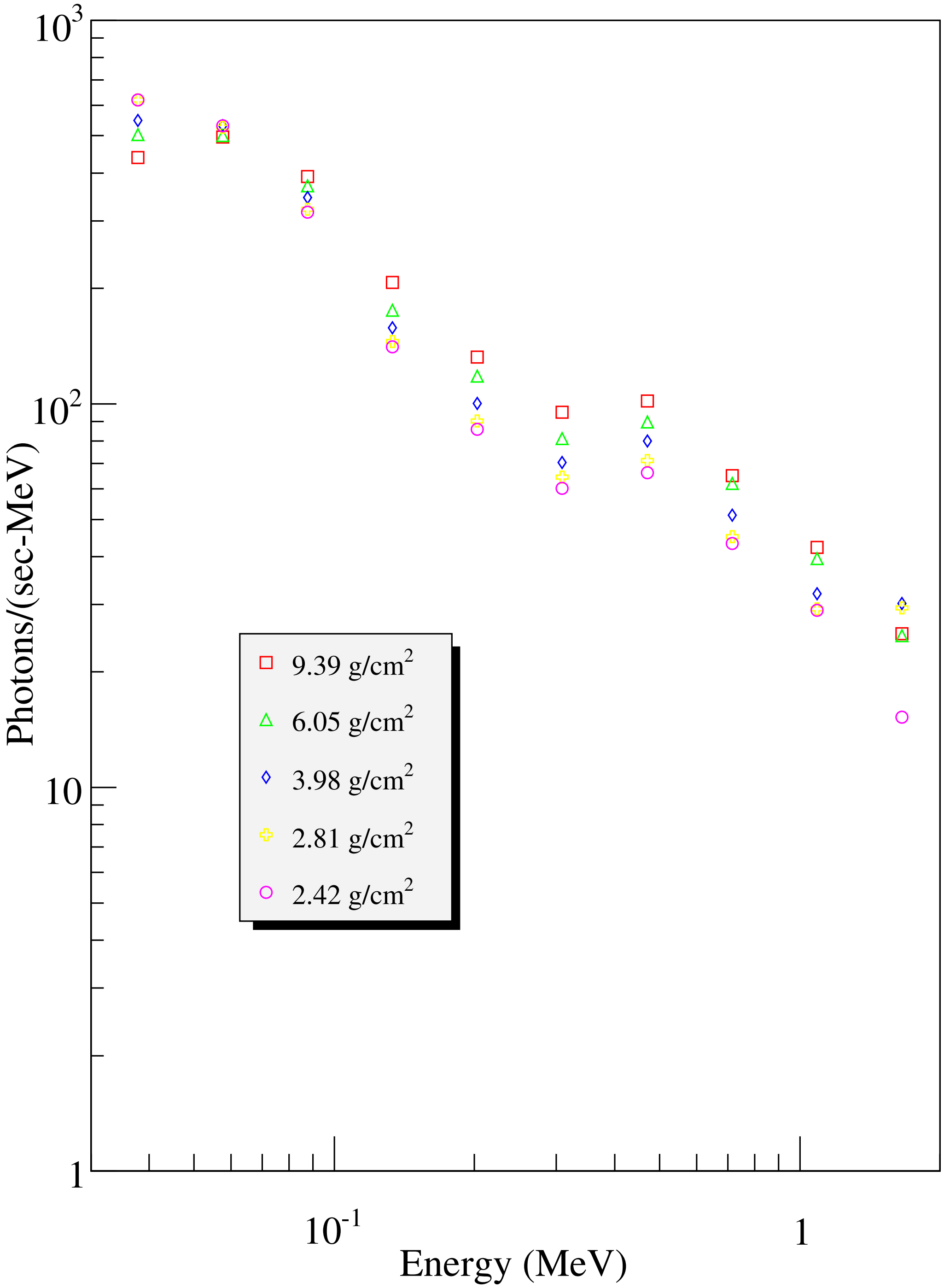

Figure 5.16: Deposited energy spectra for one 2.54 cm radius × 1 cm cylindrical BGO crystal from X/γ-rays at different flight altitudes.

Table 5.4: Energy Intervals

Energy (keV)	$\overline{E}$ (keV)	ΔE (keV)	Energy (keV)	$\overline{E}$ (keV)	ΔE (keV)
30.0 - 45.7	37.8	15.7	244.9 - 372.8	308.9	127.8
45.7 - 69.5	57.6	23.8	371.8 - 567.4	470.1	194.6
69.5 - 105.8	87.6	36.3	567.4 - 863.5	715.4	296.1
105.8 - 160.9	133.4	55.2	863.5 - 1314.1	1088.8	450.7
160.9 - 244.9	202.9	84.0	1314.1 - 2000.0	1657.1	685.9

time of the instrument was simply extracted from the X/γ-ray rates from Sec. 5.7.1.

There are a few noticeable structures in these power spectra. First, the 511 keV peaks can be observed, as it has been exploited to calibrate energies during the flight. Second, the signatures of the primary diffusive components of X/γ-ray photons can be seen in the lower energy region ($\leq$ 70 keV). On the other hand, the rates increase at higher energies ($\geq$ 100 keV) due to the production of secondary photons in the atmosphere.

5.7.2.7 Optimization of Regularization Parameter

Now, we are in a position to utilize Tikhonov's regularization method (Sec. 5.7.2.2) to recover the diffuse and atmospheric X/γ-ray spectra from the energy deposition spectra obtained from the CREST-I data in the previous Section 5.7.2.6 and the simulated BGO crystal response function (Sec. 5.7.2.4). Tikhonov's regularization method requires optimization of the regularization parameter, τ, which controls the balance between the solutions of the discretized Fredholm equation of the first kind (Eq. (5.4)) and the smoothness of the discrete data points. The optimization procedure was described in detail in Section 5.7.2.3 to obtain the mean correlation of nearby bins, C(1), $\sim$ 0.5 by varying the parameter τ.

Figure 5.17 shows the mean correlation of nearby bins as a function of τ obtained by minimizing Eq. (5.6) for different altitudes. As claimed, C(1) is a monotonically

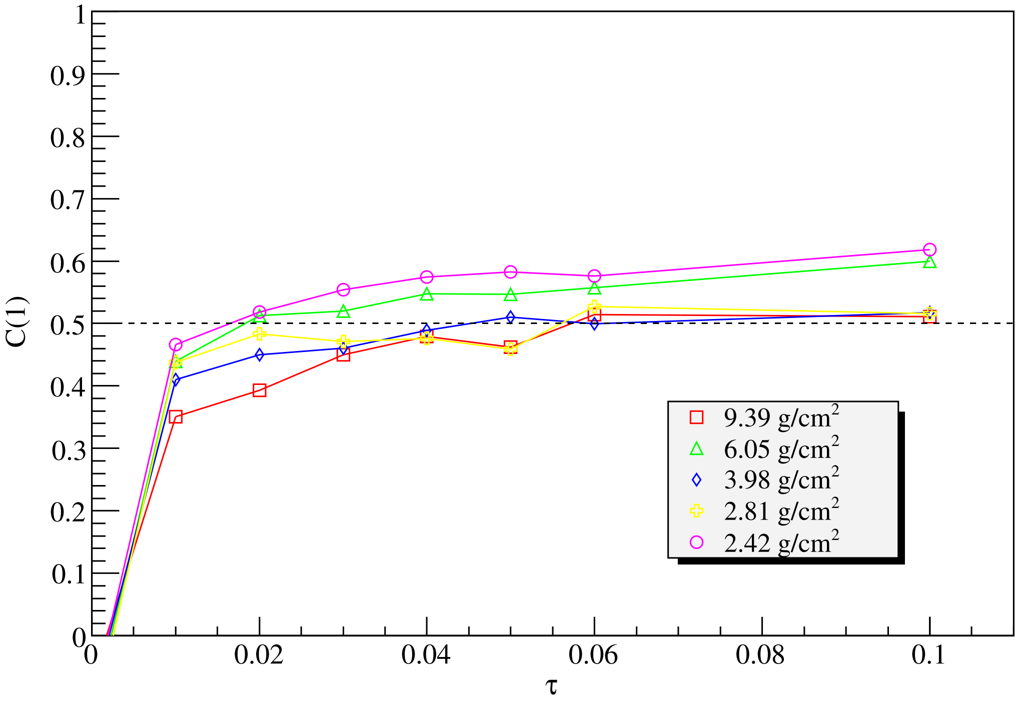

Figure 5.17: Mean correlation of nearby bins C(1) as a function of τ for the measured energy deposition spectra. At C(1) $\simeq$ 0.5, the value of τ gives the optimization between the solutions and smoothness of the Tikhonov regularization method.

increasing function of τ within statistical deviations from the Monte Carlo simulation.

5.7.2.8 Diffuse and Atmospheric x/γ Ray Spectra

The total diffuse and atmospheric X/γ-ray spectra measured during the CREST-I flight are presented in Figure 5.18. From the deposited energy spectra, these spectra were reconstructed using energy convolution with the optimized regularization parameters (Sec. 5.7.2.7) and estimates of both the geometrical factor (Sec. 6.2.2) and the total detection efficiency (Sec. 5.7.2.4) of a BGO crystal obtained from the Monte Carlo simulation. The uncertainties of these data were estimated from the numbers of counts in the logarithmic bins. Statistical errors and systematic errors were obtained by reconstruction of the total X/γ-ray spectra by energy deconvo-

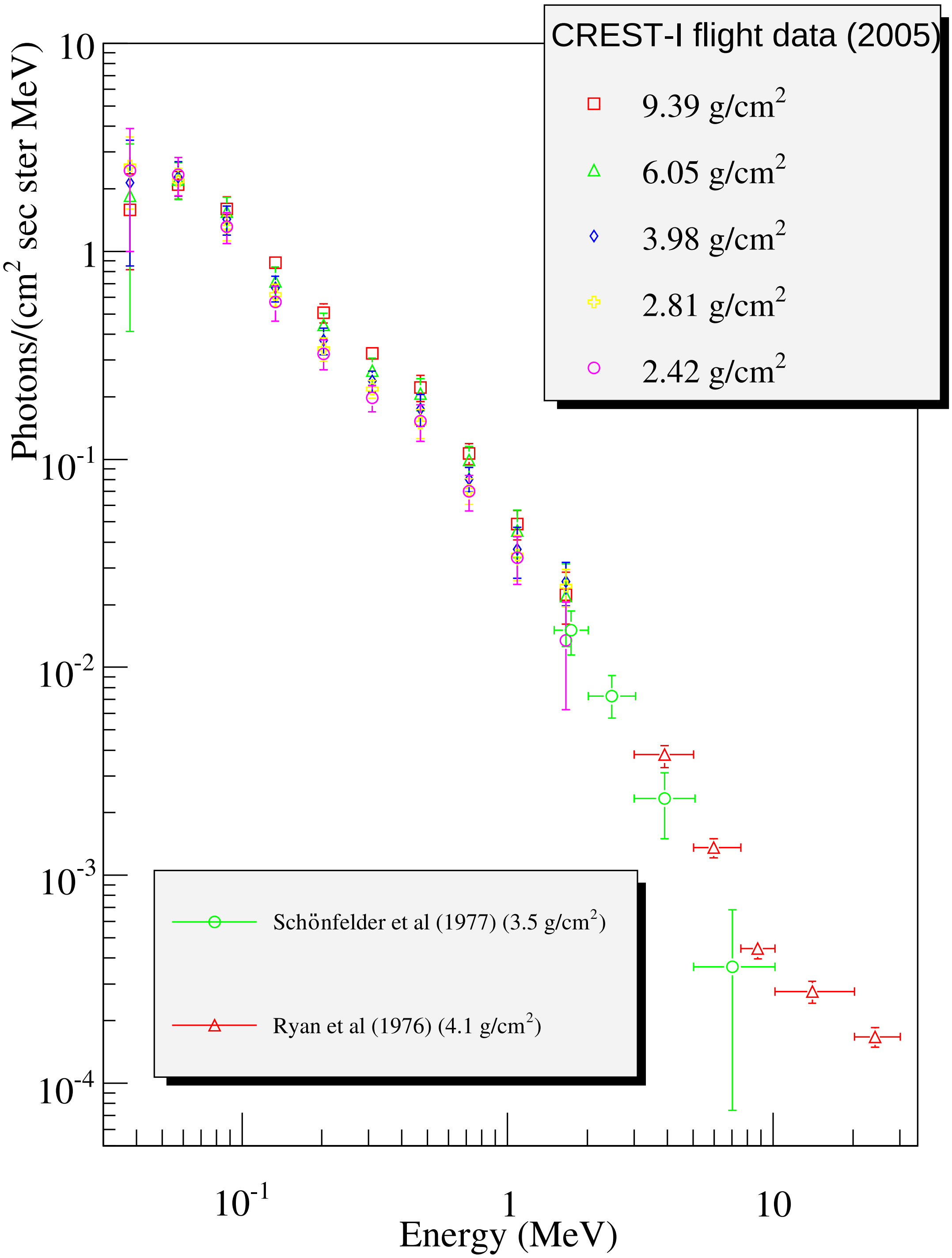

Figure 5.18: Total (diffuse and atmospheric) X/γ-ray spectra at different altitudes, compared with previous experimental data [56].

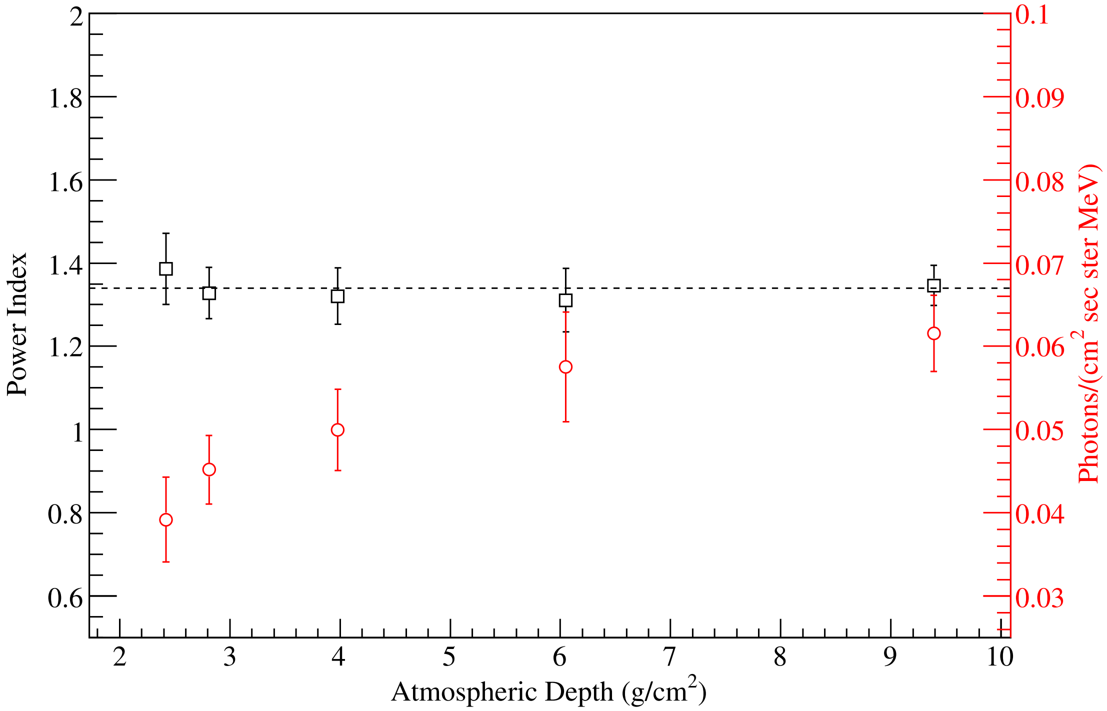

Figure 5.19: Power indices and normalizations from maximum likelihood fitting.

lution (Sec. 5.10). Lastly the statistical error was obtained from the Monte Carlo simulation for both the geometrical factor and the total detection efficiency.

Figure 5.18 also contains the data points from previous balloon experiments [56] measured at Palestine, TX for comparison with the CREST-I flight data points. These data points were obtained at similar geomagnetic rigidity cutoff ($\sim$ 4.46 GV and $\sim$ 4.3 GV, respectively) and solar modulation potentials (425 MV extracted from [69] and 430 MV from CERCLe (`http://www.obspm.fr/`), respectively) as the CREST-I flight. Our results and their results are very compatible with each other.

Figure 5.19 presents the power law fit obtained by the maximum likelihood method for the X/γ-ray spectra at different atmospheric depths (g/cm^2) from 70 keV (third data point) to 2.0 MeV (the last data point). The values of χ^2 for these power law fits range from 0.57 to 0.77. Maximum likelihood is a robust method for fitting the power spectrum [70]. First, the power indices at different altitudes agree with the previously measured value of -1.34 at all altitudes. At the lowest atmospheric depth, the power index becomes slightly harder, which could result from primary components. On the other hand, the normalization (photons/(cm^2 sec ster MeV)) of the fit increases due to the increase of secondary photons generated in the atmosphere. The CREST-I flight confirmed the previous experimental measurements for the total X/γ-ray spectra, and extended these results to lower energy.

CHAPTER VI

Detector Simulation Performance

This chapter will present the Geant3/Geant4 simulation results for the Antarctic CREST flight. First, the response of the CREST instrument to background cosmic rays (proton and X/γ-rays) was studied. This result was used to determine the hold time of the discriminator in order to minimize the dead time of the front-end electronics and the whole instrument. Second, synchrotron radiation from high energy CR electrons in the Antarctic magnetic field was simulated in order to study the geometrical factor of the CREST instrument. In the last section, the performance of the instrument in response to synchrotron photons will be presented.

6.1 Background Cosmic Ray Flux and Optimization of Discriminator Hold Time

6.1.1 Background Cosmic Ray Flux: Protons and X/γ-rays

Cosmic ray protons and X/γ-rays are the main background sources for the Antarctic CREST instrument. These CR protons are primary cosmic rays, and their interaction with the atmosphere produces secondary cosmic rays as well. Background X/γ-rays, as previously discussed in Sec. 5.1, are the primary components from both Galactic diffusion and discrete compact objects, and the secondaries result from the decay of mesons and Bremsstrahlung of e$^{\pm}$ produced in the atmosphere.

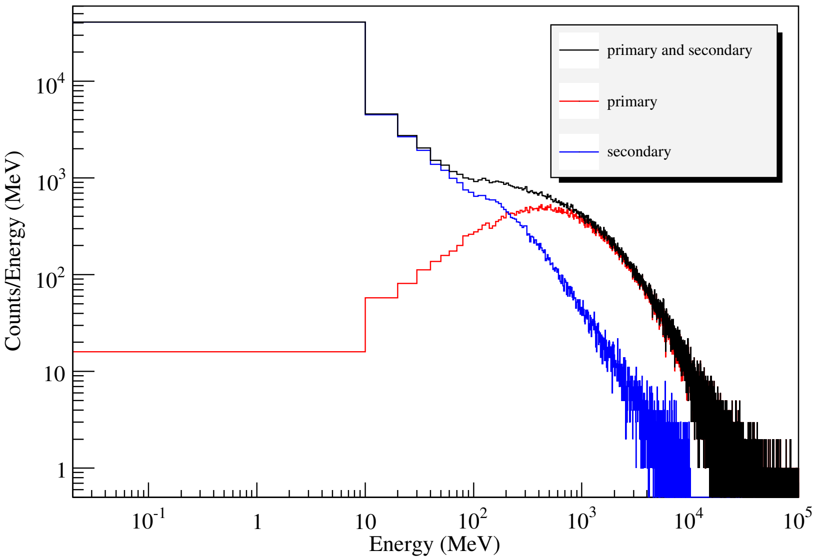

(a)

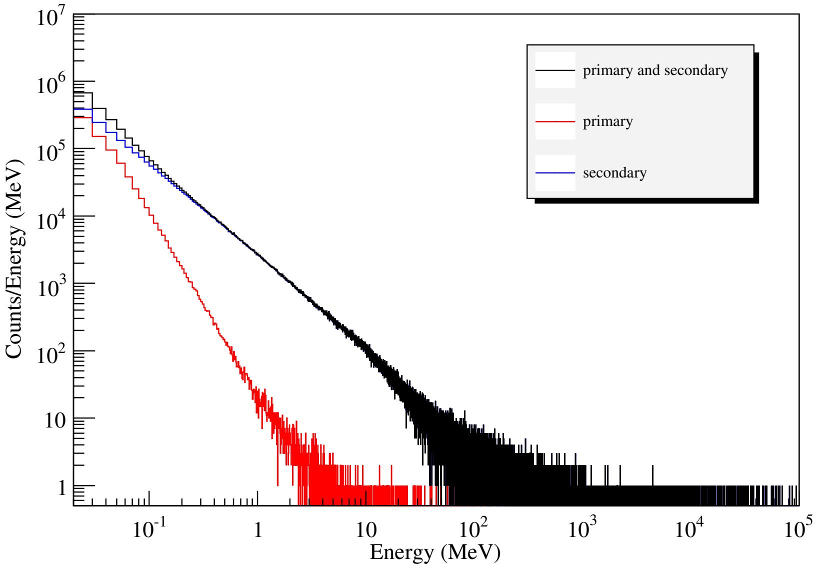

(b)

Figure 6.1: Distributions of the background spectra (arbitrary counts) for (a) CR protons and (b) X/γ-rays.

To generate background CR protons and X/γ-rays with the expected energy spectra, the GLAST Geant4 simulation package [59] was utilized. Originally, this package generates cosmic rays for the cutoff rigidity of 4.46 GV at Palestine, TX, in July 2001 but it was modified to simulate the background CRs at $\sim$0 GV ($\sim$0.05 GV at the McMordo station in Antarctica) for the Antarctic magnetic field configuration. At 0 GV cutoff rigidity, the CREST instrument could be exposed to a worse background environment. Additionally, there are two environmental parameters which influence the energy spectra of the CR proton and X/γ-ray background. One of these parameters is the solar modulation potential, determined by the activity of the Sun. The activity of the Sun influences the energy distribution of CRs through its magnetic field. From a cosine curve interpolation between solar maximum (1100 MV) and minimum (540 MV), the solar modulation potential, Φ, is expected to be $\sim$793 MV in December 2010 for the Antarctic CREST flight. The other parameter that affects the energy spectra of CRs is the flight altitude of the instrument. For simplicity, this simulation study assumes that the atmospheric depth above the CREST instrument only affects the normalizations of the CR spectra, and was set at 4 g/cm^2 (approximately 121,000 ft from the ground).

The histograms (Fig. 6.1) present simulated distributions of CR proton and X/γ-ray spectra from both primary and secondary components above 20 keV with cutoff rigidity of 0 GV and solar potential of 793 MV. Generating functions of primary and secondary components as well as their angular distributions for this simulation were extrapolated from previous balloon and satellite experiments, and the details will be discussed in Appendix B. These energy spectra served as inputs for the Geant4 simulation (with expected rates of 1.87 kHz/m^2/sr and 34 kHz/m^2/sr for CR protons and X/γ-rays respectively).

6.1.2 CREST Simulated Instrument

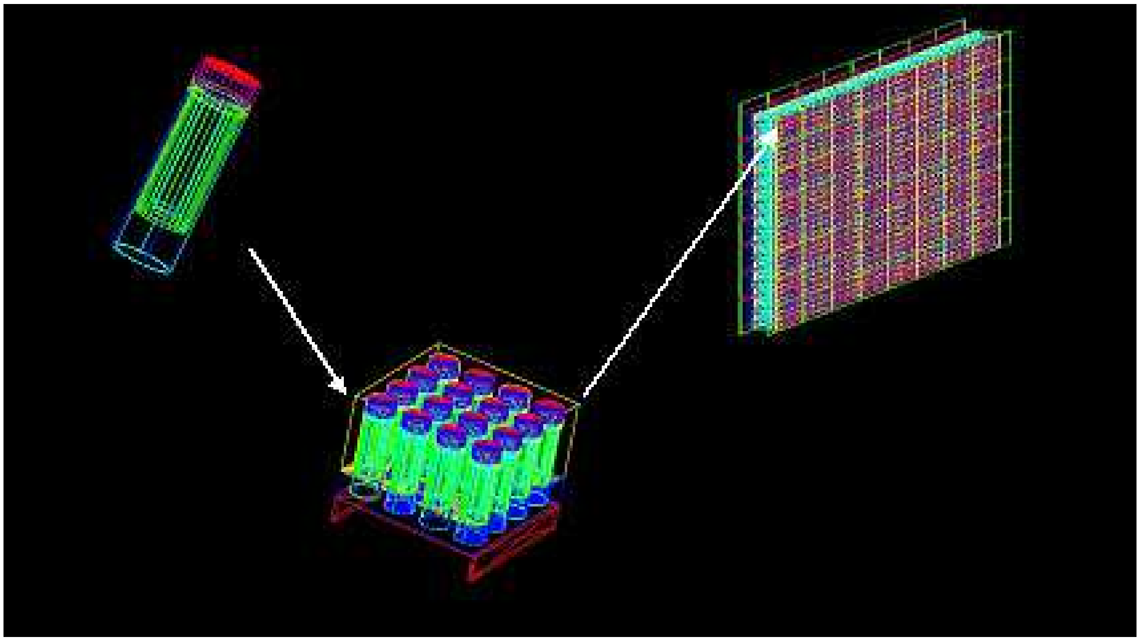

Figure 6.2: Geant4 Monte Carlo model of the CREST instrument for the Antarctic flight.

Based on the detector description in Chap. IV, the Antarctic CREST instrument was modeled in the simulation: Each crystal/PMT assembly was created in as much detail as described in Fig. 4.9, and one module of 16 crystal/PMTs was assembled on the aluminum supporting channel. A total of 1024 BaF_2 crystal/PMT assemblies were modeled for the CREST instrument. These assemblies were completely covered by 20 plastic veto scintillators (instead of the current 21 scintillators for the real CREST instrument). In this simulation, the aluminum frame structure that is used to support the weight of the 1024 crystal/PMT assemblies and 8 aluminum channels of the instrument was not included. The BaF_2 crystal and veto scintillators recorded both deposited energies and timings for all the interactions of the particles in the crystals.

The simulated CREST instrument (Fig. 6.2) was bombarded with CR protons and X/γ-rays. The geometrical acceptance of this rectangular box shape, made out of veto scintillators, [68] was calculated to be 51.19 m^2sr, and input rates of 96 kHz and 1.76 MHz of protons and X/γ-rays respectively were thrown into the instrument. With these input background rates, the detected rates of both the BaF_2 crystals and the plastic scintillators are shown in Table 6.1.

Table 6.1: Monte Carlo instrument response rates

	Proton	X/γ
Crystal PMT Hits		
Single PMT Rate (Hz/PMT)	25	270
Multiple PMT Rate (Hz/PMT)	75	60
S/M PMT Rate (Hz/PMT)	100	330
Veto Plastic Scintillator Hits		
Veto PMT Rate (kHz/PMT)	9.3	19.6
Multiple PMT $\cap$ Veto (Hz/PMT)	15	11

We are concerned with the effects of these estimated rates on the CREST front-end electronics. The rate of crystal/PMT assembly hits determines the discriminator TDC input rate. Therefore, ∼430 Hz per discriminator input with a deposited crystal energy cutoff of 10 keV is expected for both proton and X/γ-ray backgrounds. Similarly, ∼28.9 kHz is expected without an energy cutoff for each veto discriminators (Note that there are two PMTs at each end of the veto scintillator). The ADC rates for the crystal/PMT assemblies and the veto scintillators are more complex, since the charge readout by the VARC chips are initiated only when the coincidence logic (≥ 2 crystal hits) is satisfied. From this simulation, the expected rates of the crystal/PMT assembly and veto scintillator are ∼135 Hz and ∼26 Hz per VARC input, respectively.

6.1.3 Discriminator and sADC

The optimization of the CREST instrument dead time via the front-end electronics and the subsequent readout electronics requires an understanding of the CREST data chain, starting from incident background particles and their rate, to the BaF_2

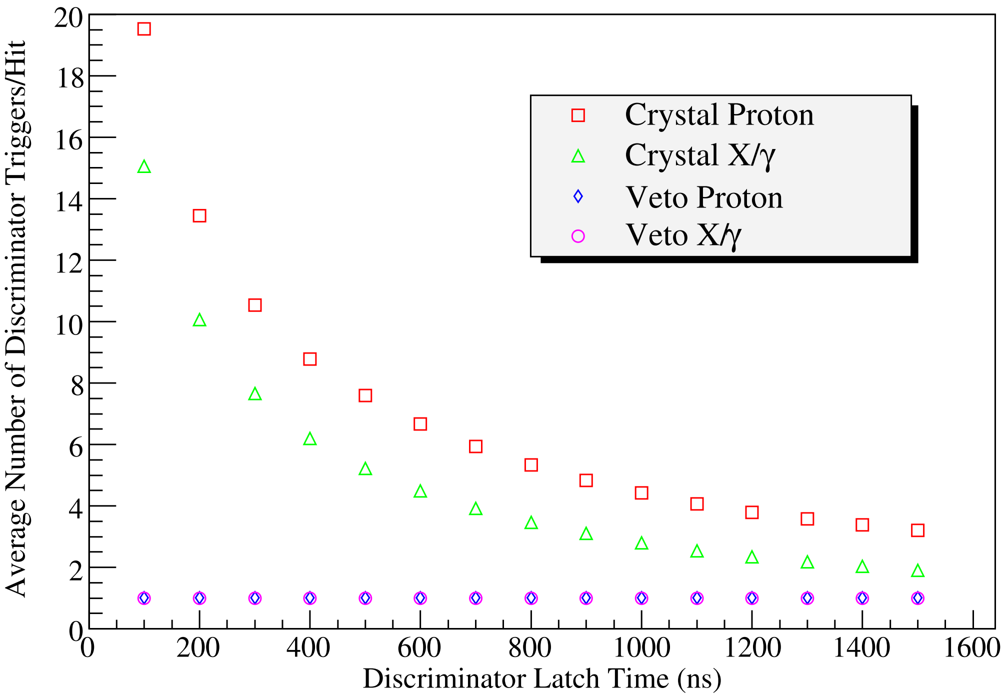

Figure 6.3: Average number of discriminator triggers per crystal or veto scintillator hit in response to input from CR proton and X/γ-ray spectra.

crystal/PMT assemblies, to the discriminator, to the VARC, to the STAC, and finally to the CRESTBUS at the end of the chain. (The details of the CREST data chain have already been discussed in Sec. 4.1.1). In this section, both the timing dead times (TDC section) and the charge recording dead times (ADC section) that result from the discriminator hold time and the VARC charge read out time are considered.

Latching of the discriminator by responding to an analog signal output from the PMT results in timing dead time. The only independent variable in optimization of the front-end electronics dead time is the hold time of the discriminator, which can be varied from 100 ns to 1.5 μs without affecting the other parts of the discriminator electronics. On the other hand, the sequential charge readout for the 32 channels of the VARC chip causes dead time for the ADC. This sequence requires 3 μs once the

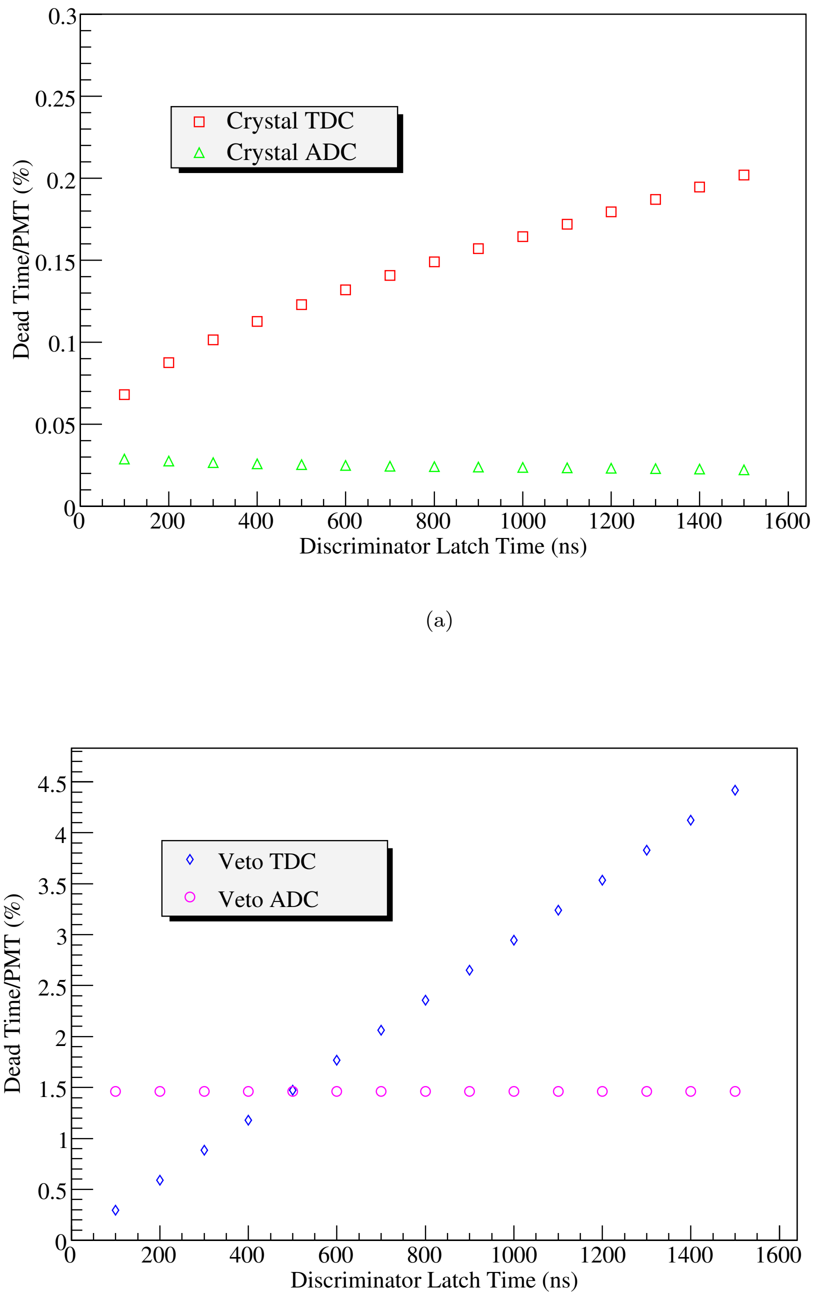

(a)

(b)

Figure 6.4: Dead time in percent per PMT for (a) TDC and ADC for the crystal/PMT assemblies and (b) TDC and ADC for the veto/PMT assemblies from expected CR proton and X/γ-ray fluxes for the Antarctic flight (Fig. 6.1) with 500 Hz PMT internal noise included.

coincidence logic (≥ 2 crystal PMT hits within a 48 ns coincidence window on the whole PMT array) is satisfied.

To understand these interrelated TDC and ADC dead times, the instrument response resulting from the Geant4 Monte Carlo simulation was fed into a discriminator C/C++ program. With the deposited energy and the interaction time of an incident particle from this Geant4 simulation, the discriminator program first generates a simulated photo-electron signal by converting deposited energy into the equivalent number of photo-electrons (10% FWHM resolution at 662 keV $\simeq$ 0.8 PEs/keV). Next, this signal is distributed in time with exponential decay times of 0.8 and 400 ns (at the fast to slow ratio of 15 to 85) for the BaF_2 crystal, assuming a 10 ns width of a single photo-electron pulse from the anode of the PMT. Then, a few discriminator signals (inducing the TDC dead time) are generated, according to the actual CREST disciminator response (See Sec. 4.6.2).

Figure 6.3 shows the simulated result for the average number of discriminator triggers for either a crystal or a veto scintillator hit in response to an incident particle (either proton or X/γ-rays). Multiple triggering per crystal hit occurs due to the long decay time of the BaF_2 crystal. This results in the sparseness of the signal as shown and discussed in Section 4.6.2. For lower discriminator hold time, more triggers per crystal hit are necessary to cover the entire timing range of the signal. Hence, the fast decay time of the plastic scintillator causes a single trigger for any type of incident particle. This assumes 12 photo-electrons per hit as measured for one end of the plastic scintillator generated within the 9 ns decay time of the Kurary fiber discussed in 4.1.1.

Combining TDC dead time results from multiple discriminator triggering with the ADC dead time from the VARC, the average TDC/ADC dead times per PMT are shown in Fig. 6.4 for the crystal/PMT assemblies and veto plastic scintillator/PMT assemblies. The ADC dead times for both cases (crystal and veto) are comparable for different values of the discriminator latch time. This observation suggests that it is much less likely for multiple triggering of the BaF_2 crystal/PMT assembly to cause multiple ADC readouts. On the other hand, TDC dead times for both cases monotonically increase. The TDC dead time for the crystal/PMT assembly is quite complex, because discriminator triggerings are generally composed of a long initial triggering and a small latch time followed by 10 ns quick transition triggerings as observed in Fig. 4.28 and discussed in Sec. 4.6.2. The Veto TDC dead time linearly increases with the discriminator latch time, since a single trigger is enough to cover the timing distribution of the photo-electrons from the plastic scintillator. With the expected background rates from CR protons and X/γ-rays, the TDC/ADC dead times of the crystal/PMT assemblies are quite small ($\leq 0.2\%$). On the other hand, the TDC/ADC dead times for the veto plastic scintillators with no energy cutoff are large ($\sim$ few percent).

At first glance, a 100 ns discriminator latch time seems optimum for the crystal and veto plastic scintillator/PMT assemblies. However, the influence of this latch time on the electronics (the STAC and the CRESTBus) after the front-end electronics in the CREST data chain have to be considered as well.

6.1.4 STAC and CRESTBus

Following the front-end electronics, the limitations of the CREST data handling system appears in two forms: the data buffer in the STAC and the data transmission rate in the CRESTBus. The STAC buffer can hold 128 data words per PMT, where one ideal hit occupies two ADC words and one TDC word (without multiple discriminator triggering). On the other hand, the readout cycle of the data words by

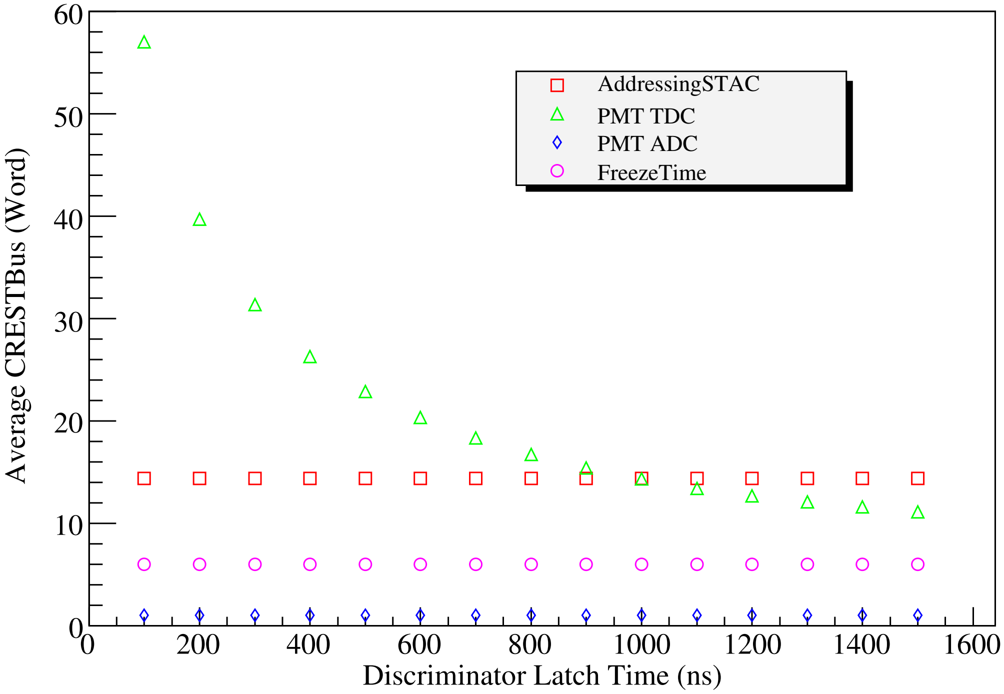

Figure 6.5: Average number of data words per CRESTBus (with 8 STACs) read cycle. The CRESTBus requires 3.0 μs = 6.0 words and 7.2 μs = 14.4 words for broadcasting freeze/accumulate commands and their addresses to communicate with the 8 STACs in a chain. There are a total of 110 data words per read cycle.

the CRESTBus from the STACs has a 60 μs window where one data word occupies 0.5 μs. Some words are already assigned for CRESTBus functionalities: 3.0 μs for broadcasting freeze/accumulate commands to all the STAC boards and 0.9 μs per STAC for its address. The time required for the VARC chips to read all the charges and for the STAC boards to obtain these ADC values in response to a freeze/accumulate command is 3.0 μs. For the entire CREST instrument, there are 8 CRESTBusses and 8 STACs per CRESTBus. Figure 6.5 shows the average number of data words used per CRESTBus read cycle for the entire BaF_2 crystal/PMT assembly. There are a total of 110 words available per CRESTBus read cycle. Again, due to multiple triggering of the discriminator (Fig. 6.3), the TDC

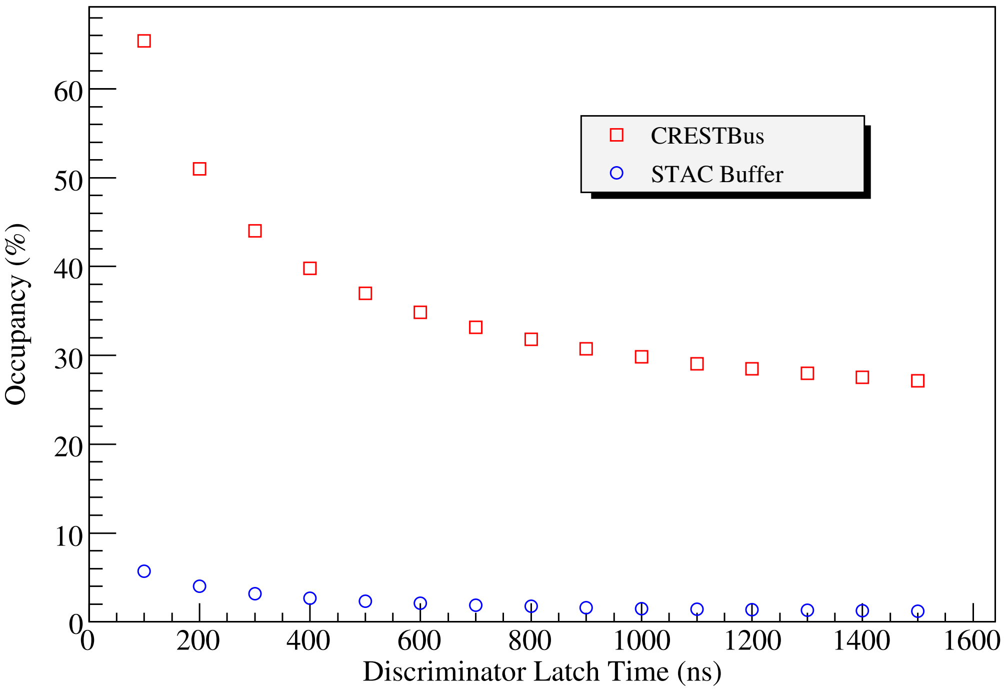

Figure 6.6: Occupancies of the Crystal PMT STAC buffer and CRESTBus in percent per CRESTBus read cycle for the Antarctic CREST instrument as a function of discriminator latch time.

words per CRESTBus read cycle increase at lower latch times of the discriminator. In summary the expected occupancy for both STAC buffer and CRESTBus from CR proton and X/γ-ray backgrounds is shown in Figure 6.6.

So far, in this section, we were only concerned with the data from the array of the crystal/PMT assemblies. At the time when this simulation study was performed, the positioning and number of both the veto scintillators and their STACs were still uncertain. Furthermore, since the background CR rates are different (depending on the positions of the scintillators), the way in which the veto STACs connect with the VETOBus affects the occupancy of the data transmission in the VETOBus. As a result, the veto section of the occupancies of the data buffer in the STACs as well as the data transmission in the VETOBus have become subjects of further study.

6.1.5 Optimization Result

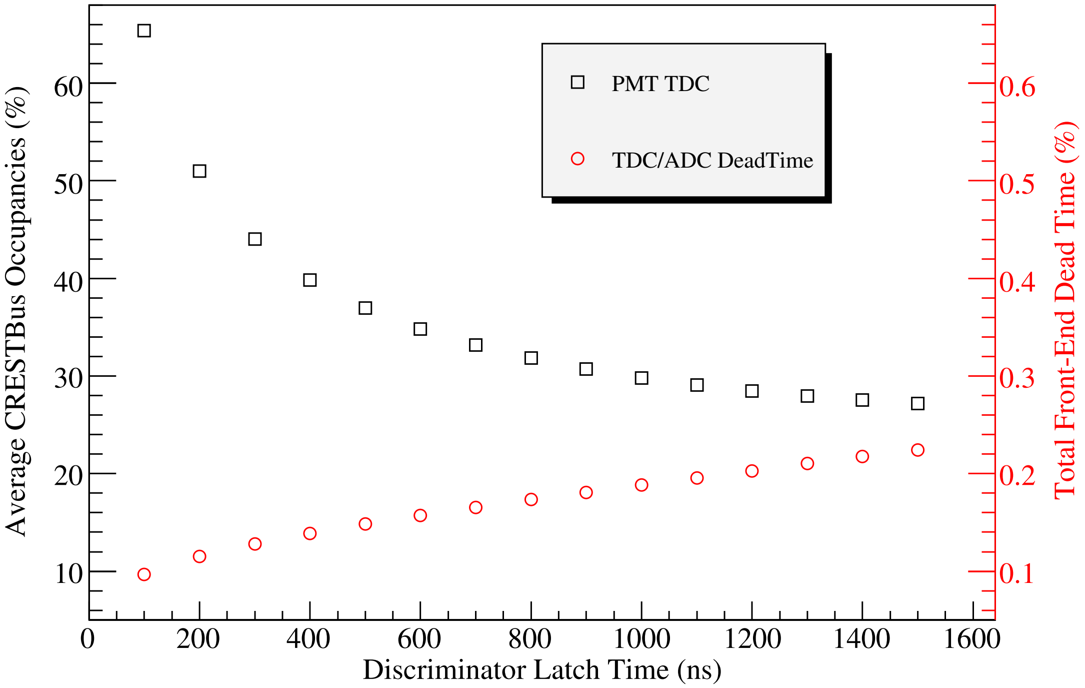

Figure 6.7: Dead time of the front-end electronics (discriminator and VARC chips) and CRESTBus occupancy in percent.

Figure 6.7 presents the results of the optimization study of the dead time from the front-end electronics (discriminator and VARC) and the occupancy of the CRESTBus when the CREST instrument is exposed to the expected backgrounds from CR protons and X/γ-rays during its Antarctic flight. Since the STAC data buffer is deep enough, and its data occupancy is $\leq 10\%$ for any discriminator latch time, it is not included in Figure 6.7 for comparison. It is quite apparent that the bottleneck of the data chain is the transmission rate of the CRESTBus. On the other hand, the dead time of the front-end electronics for the crystal/PMT assemblies is quite insignificant. Based on the result of this study, I had recommended 800 ns for the discriminator latch time. This yields an average TDC/ADC dead time of 0.17%,

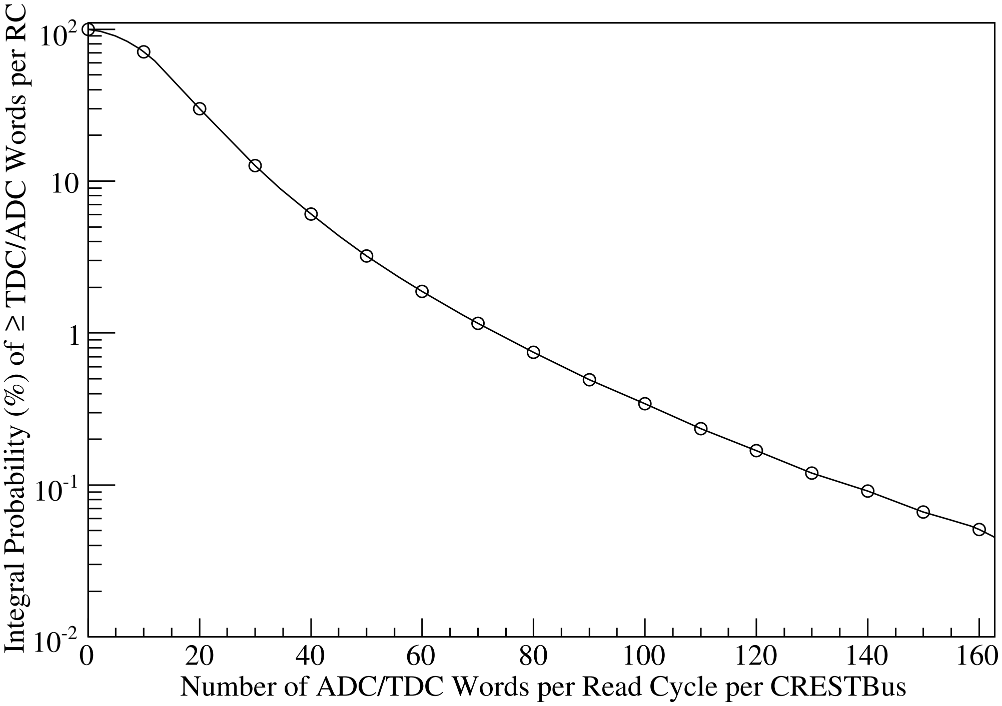

Figure 6.8: Integral probability of number of TDC/ADC words per CRESTBus read cycle. For 10% of the read cycle, CRESTBus has $\geq \sim$35 TDC/ADC words. For 1% of the read cycle, the bus has $\geq \sim$ 75 TDC/ADC words, where a total of the 110 words per read cycle is the maximum transmission rate.

and the TDC and ADC dead times are 0.15% and 0.02% respectively. An average of ∼32% of data transmission in the CRESTBus is occupied, which allows ∼80 extra words within 60 μs for the 128 crystal PMTs. The integral probablity of the number of the data words per CRESTBus read crycle for an 800 ns discriminator latch time is presented in Fig. 6.8. This was used for the firmware development.

6.2 Synchrotron Radiation Simulation and Geometrical Factor

6.2.1 Synchrotron Radiation Generator

I will now investigate the response of the Antarctic CREST instrument to synchrotron photons generated by high energy CR electrons passing through the atmosphere and the Earth's geomagnetic field. First, I will examine the geometrical factor of the CREST instrument as estimated by the simulation.

The production of synchrotron photons via interaction with the Earth's magnetic field were performed by a Fortran-based Geant3 simulation code. This code was first implemented by Jim Musser from Indiana University. Then, I implemented the shareware code from the National Geo-spatial Intelligence Agency (`www.nga.mil`) to account for the configuration of the magnetic field at the Antarctic location and altitude on a given date (including future dates).

6.2.2 Method of the Geometrical Factor by Simulation

Since the CREST instrument aims to detect secondary synchrotron photons instead of the primary high energy CR electron, the geometrical factor must be understood through simulations. The geometrical factor is not the physical size of the instrument, but is a function of the primary energy of CR electrons (TeV), the magnetic field (latitude and longitude), atmospheric overburden (g/cm^2), and the number of detected synchrotron photons. In this study, the procedure to determine the geometrical factor of the CREST instrument is as follows:

1. The synchrotron photons are generated as high energy CR electrons passing through the Earth's atmosphere from 2000 km to the measured altitude (37 km $\simeq$ 4g/cm^2) and interacting with the Antarctic magnetic field for December 2010. For an isotropic geometrical factor, the incident direction of the electron in spherical coordinates, (θ, ϕ), was generated at random angles of ϕ and $\cos^2\theta$ [68, 71]. For this simulation, it is important to ensure that these electrons travel in a downward direction through the atmosphere.

2. These synchrotron photons generated at some specific altitude travel down to the measured altitude. During this travel, these photons experience attenuation

by the atmospheric overburden.

3. The plane square (the size of the CREST instrument: 2.33 m by 2.33 m) was moved around at 4g/cm^2, and the number of the detected synchrotron photons by the BaF$_2$ crystals were counted. Deposited energies in the crystals are also calculated.

4. If the conditions of more than the required number of the synchrotron photons (≥ 3 or ≥ 4) were met, these areas were recognized as detectable. These areas were added, and the total area became the geometrical factor of the CREST instrument in the simulation study.

A total of 100 high energy electrons per TeV were released downward from 2000 km to 37 km at 0, 45, and 60 degree angles from nadir angle in this simple study. The minimum number of synchrotron photons to be considered a detected area was three or four, and the energy cutoff was set at 20 keV.

6.2.2.1 Electron Primary Energy Dependence

Figure 6.9 presents the geometrical factor as a function of the primary electron energy at (75°S 135°E) at different incident angles. It is apparent that as the primary electron energy increases, the geometrical factor increases as well (roughly linearly). This is because the CREST instrument needs to intercept only a portion of the line-like synchrotron photon signature. With 16.97 m^{2}sr as the geometrical factor of the plane, a significant detection advantage of the CREST instrument occurs at all energies $\geq \sim$10 TeV for three or more photon detection. At low primary electron energy the effect of air attenuation becomes significant, and the geometrical factor is reduced. Note that the minimum detection electron energy of the CREST instrument is therefore determined by the attenuation of synchrotron photons by the

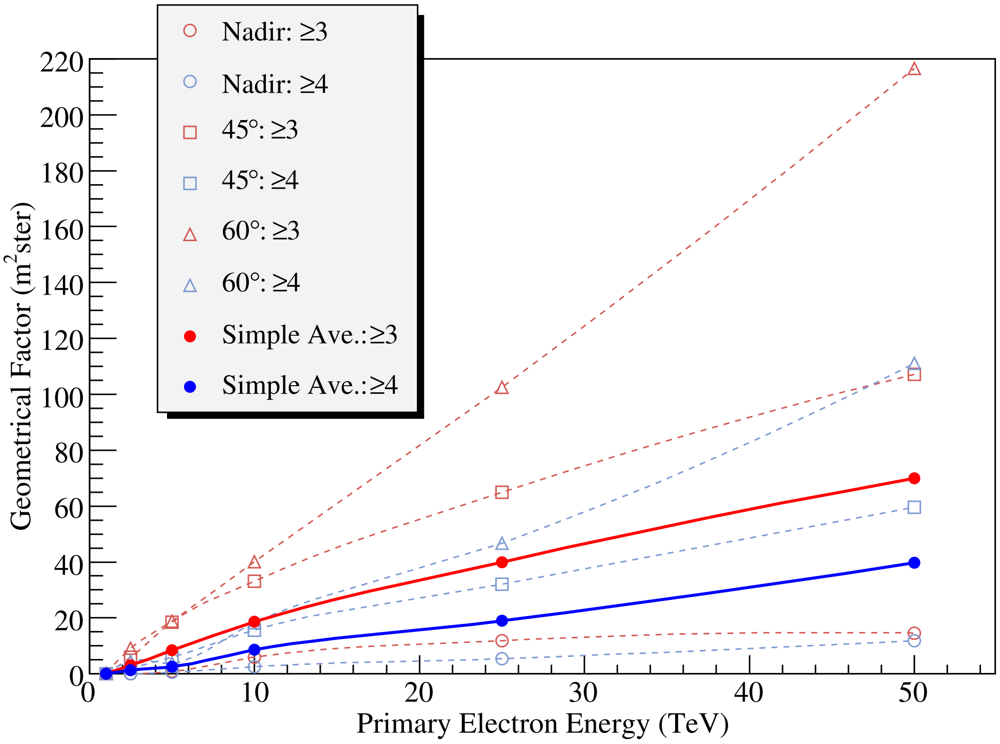

Figure 6.9: Geometrical factor dependence on the energy of the primary electron. At 0, 45, and 60 degree from nadir angle, the geometrical factors for three or more synchrotron photon detection are shown in red, and these for four or more synchrotron photon detection are shown in blue. Incident angle weighted geometrical factors, which will be used in later sections, were also presented (in thick lines).

atmosphere.

From this simulation study, it is evident that the geometrical factor of the CREST instrument strongly depends on the primary energy of CR electrons. Further study will be necessary to investigate the sensitivities of the geometrical factor on both the magnetic field (latitude and longitude) and overburden (g/cm^2).

6.3 CREST Detector Response and Performance

In this section, the responses of the Antarctic CREST instrument to synchrotron photons will be presented. Here, high energy electrons were followed from 400 km to ∼37 km (4 g/cm^2) above the surface of the Earth at (135^{o}S, 70^{o}E) in Antarctica, and the configuration of the magnetic field was set for December 2010 when the Antarctic CREST flight is planned. At the release point, the strength of the magnetic field is 0.60 G, and its normalized magnetic field direction is (north, east, up)=(-0.102, -0.031, -0.868). This corresponds to a zenith angle of 150 degrees. In this simulation, 10,000 electrons of each fixed energy (5, 10, 25, and 50 TeV) were generated at fixed relative angles (10, 20, 30, 45, 55, 65, and 75 degrees) with respect to the direction of the local magnetic field. These relative angles correspond to zenith angles of 163, 153, 143, 128, 118, 108, and 98 degrees respectively.

The synchrotron photons at specific times, directions, locations and an altitude of 4 g/cm^2 were followed into the Antarctic CREST instrument in the Geant4 simulation. The instrument is randomly rotated in the x-y plane, since the instrument cannot control its directionality with respect to the incident synchrotron photons (during flight, its directionality will be determined to obtain maximum solar illumination for power). Each BaF$_2$ crystal/PMT assembly has a 10% FWHM energy resolution and $\sigma = 1$ ns timing resolution with 1 ns digitization, unless otherwise stated. From the simulated response of the CREST instrument to synchrotron photons, the expected energy resolution for primary electrons and azumuthal and zenith angle resolutions can be estimated.

6.3.1 Detector Response to Synchrotron Radiation

As a first example of the response of the simulated Antarctic CREST instrument to synchrotron photons, the average number of emitted synchrotron photons (dotted lines) and the average number of BaF$_2$ crystal hits (thick lines) are shown in Figure 6.10. The average number of synchrotron photons is counted as the number of photons which fall inside of the CREST instrument aperture (2.33 m by 2.33 m square). The average number of detected photons includes scattered photons by

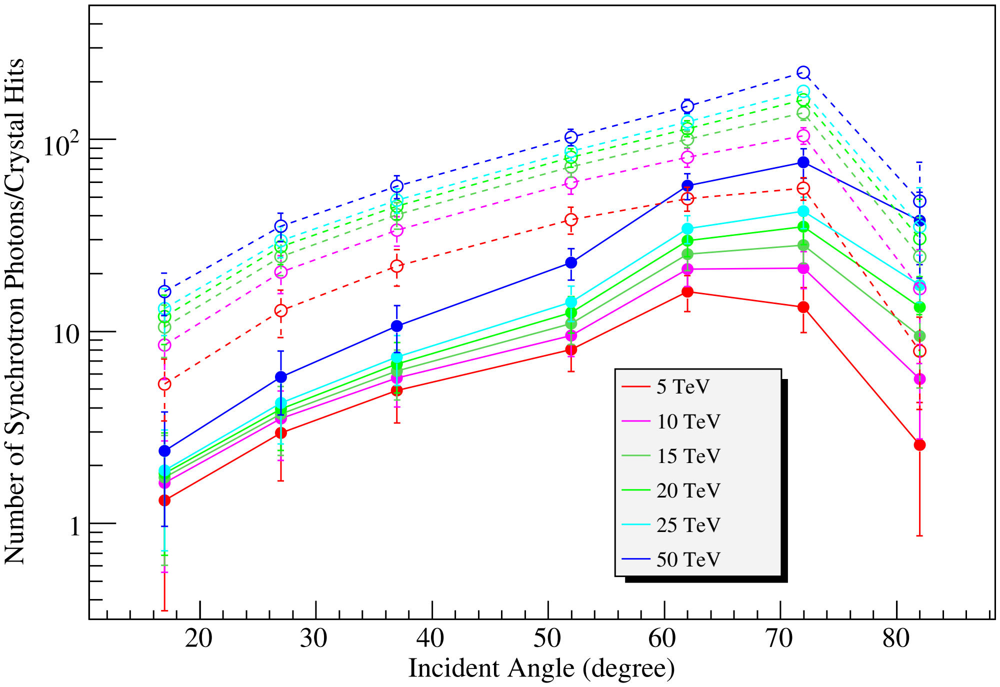

Figure 6.10: The number of synchrotron photons falling in the CREST instrument aperture (dotted lines) and the number of crystal hits (thick lines) from synchrotron photons with different primary electron energies.

the BaF_2 crystals and the photons that first interact with the instrument and then Compton-scatter into the crystals. Note that the incident angle is defined as the angle to the horizon (complement of the zenith angle).

It was shown in Sec. 2.6 that the number of synchrotron photons per path length (Eq. (2.33)) is only proportional to the magnetic field perpendicular to the instantaneous direction of the electron, $B_{\perp}$. This feature can be seen with an increase in the number of these photons as the incident angle becomes steeper (the direction of the local magnetic field is almost vertical). In the ultra-relativistic regime, the number of synchrotron photons per path length should not depend on the energy of the primary electron. In this simulation, however, there is attenuation from the atmosphere and lower energy photons are more attenuated. This is not strictly true when the energy of the photon becomes larger than ∼6 MeV where the cross section from electron pair production increases. As a result, the more synchrotron photons survive through the atmosphere, the higher the energy of the electrons.

There is a sudden decrease in the number of synchrotron photons at incident angles from 72 to 82 degrees. The reason for this feature is that when the incident angle becomes steeper, the number of synchrotron photons going into the fixed detectable area decreases. This is simply due to the projected physical size of the instrument. Furthermore, it is apparent that not all synchrotron photons falling inside the aperture of the instrument are detected by the BaF_2 crystals. Some of them fall in the space between the crystals, and some of them do not even interact with the BaF_2 crystals, since the number of radiation lengths seen by a photon in a crystal depends on the incident direction. This results in apparent decrease in the number of crystal hits, as compared with the number of synchrotron photons.

6.3.2 Energy Resolution

Figure 6.11 shows the average energies of input synchrotron photons (thick line) and the deposited energies in the crystals (dotted line) in the simulation for different primary electron energies. As shown and discussed previously in Eq. (2.37), the most convenient feature of the synchrotron radiation to reconstruct the energy of the primary electron is that (in the limit of the infinite number of the synchrotron photons) the energy of the primary electron is proportional to the square root of the mean energy of the synchrotron photons and inversely proportional to the square root of $B_\perp$. At fixed electron energy, the characteristic of the average energy of the synchrotron radiation being proportional to $B_\perp$ can be observed in Figure 6.11 for magnetic fields that are almost vertically downward. Note that the incident angle is pointing upward from the CREST instrument.

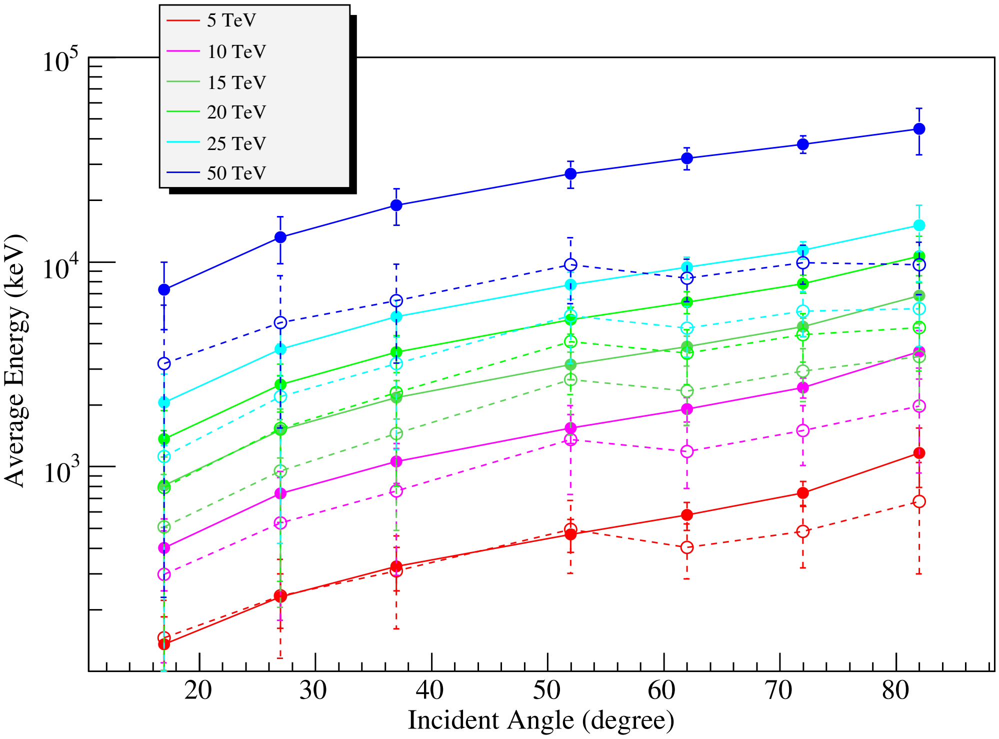

Figure 6.11: Average energies of synchrotron radiation (thick lines) and deposited energies in the crystals (dotted lines) as a function of the incident angle where this angle is pointing up (the CREST instrument's point of view). On the other hand, the magnetic field, where the electrons were generated at (135^o S, 70^o E), is almost vertical downward.

There are two noticeable features in Figure 6.11: First, there are differences between the average energies of the synchrotron radiation and the average deposited energies in the crystals. The reason for this feature is due to the fact that not all of the energy of the synchrotron photon is deposited in the 2.54 cm radius × 2 cm tall cylindrical BaF_2 crystal. This is caused by the limitation of the size (or effectively g/cm^2) of the crystal as well as by the energy dependent interaction cross section of the X/γ-ray photons, since the photon energy has to be deposited by Compton scattering and the photo-electric effect inside the crystal. A higher energy of the primary electron results in a higher energy of synchrotron radiation and thus, this feature of the differences between the average energies (of the synchrotron radiation

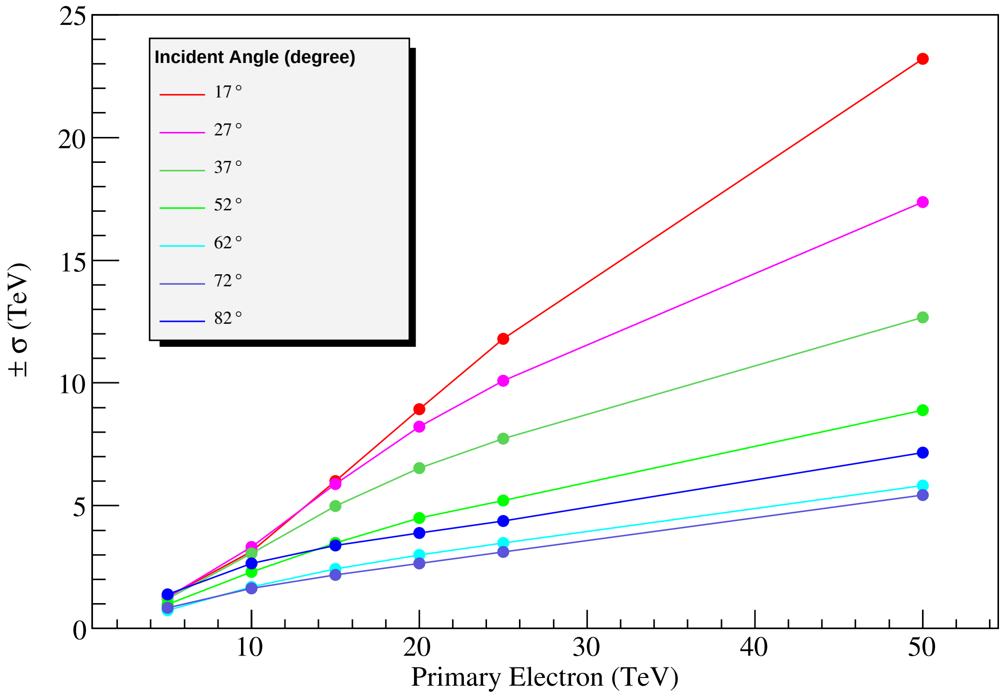

Figure 6.12: Standard deviation of the average deposited energy in a crystal from synchrotron radiation.

and crystal deposited) becomes more evident.

There are also moderate decreases in the average detected energy for incident angles from 52 to 62 degrees across all primary electron energies. This is due to the change in the photon interaction probability as a function of the crystal orientation. They become more likely to enter the sides (instead of the top surface) of the crystal at steeper incident angles.

Aside from these systematic errors, Figure 6.12 presents the energy resolution of the average synchrotron photon measurements. The degradation of the second moment of Eq. (2.35) ($=\sigma$ for infinite numbers of synchrotron photons) mainly comes from four factors: the first two are the finite number of synchrotron photons entering the CREST instrument, and the fact that some of them are not even detected by the crystals. The third factor is that not all of the individual synchrotron photon energy is deposited in the crystal. Finally, the BaF_2 crystal itself has a finite PHR (10% in this simulation). Among these, the most important factor is the number of synchrotron photons detected. Fig. 6.10 shows that at smaller incident angles, fewer synchrotron photons are detected by the CREST instrument, and as a result the energy resolution grows.

6.3.3 Azimuthal Resolution

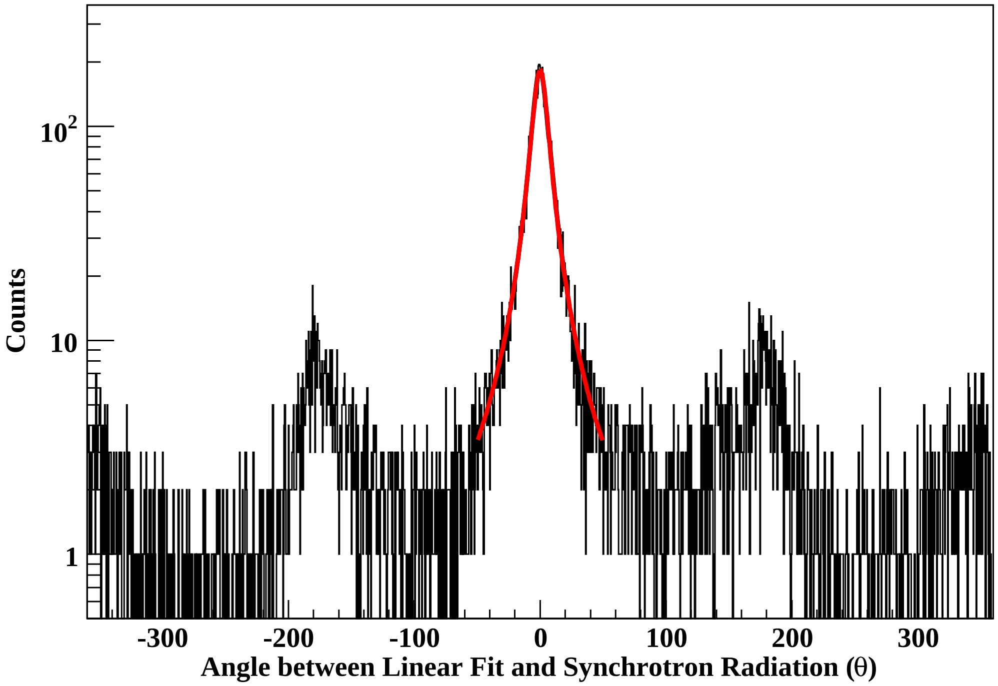

Figure 6.13: The angle difference between the known incident azimuthal angle and the reconstructed angle for 50 TeV primary electrons with a 45 incident angle. This distribution was fit by a Cauchy-Lorentz function with reduced χ^2 = 88.88/77 for this example.

For the reconstruction of azimuthal angles of synchrotron radiation, a linear χ^2 fit was performed to the locations of the crystals with energy deposition. Since we do not know the exact locations where the photons interact with the BaF_2 crystals in the real experiment, we assume that the geometrical center of the PMTs are the locations

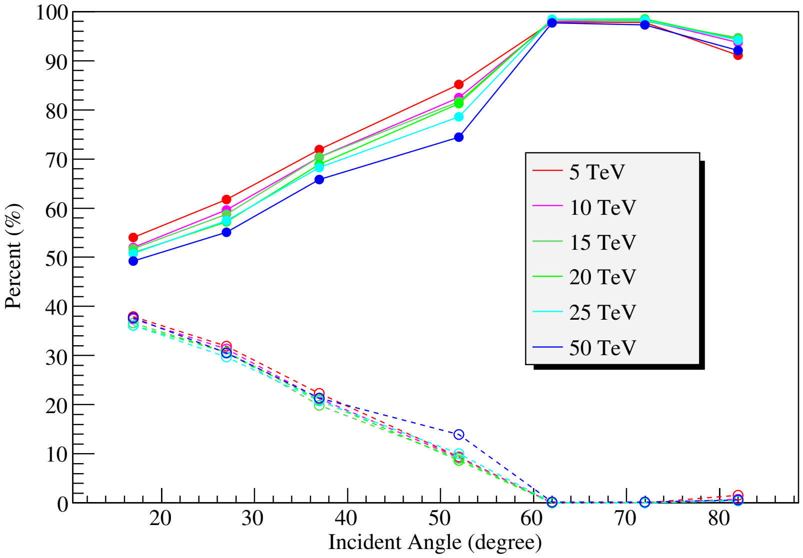

(a)

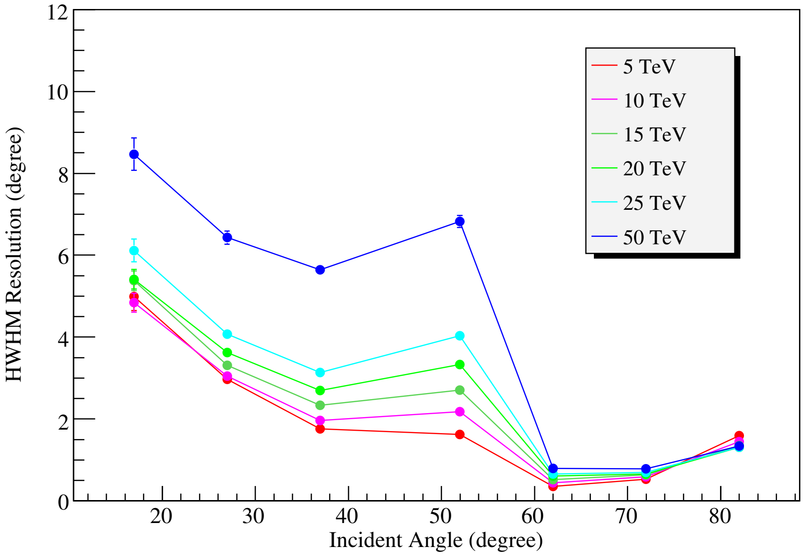

(b)

Figure 6.14: Azimuthal angle reconstruction for (a) percentage of total events that have directions within 95% of the Cauchy-Lorentz distribution peak. The thick lines show the percentages with the correctly indentified direction, and the dotted lines show the percentage of misidentified directions by 180 degrees (b) HWHM resolution for correctly indentified peaks.

of the crystal hits. To determine the directionality of these points, the timings of the geometrical end points were compared. As in the real experiment, the σ_{timing} of the BaF_2 crystal/PMT assemblies is set to be 1 ns, slightly larger than reality. In addition the timing is *digitized* in 1 ns bins for this simulation (the fractional parts of the decimal numbers are rounded off).

Figure 6.13 shows the simulated results of the difference between the known azimuthal angle of the synchrotron photons and the reconstructed angle obtained by a linear χ^2 fit for primary electron with energies of 50 TeV and a 45 degree incident angle. There are three peaks: For the zero degree peak, the known angle and the reconstructed angle are the same. For the two peaks around ±180 degrees the direction of the angles were misidentified. This is because the timing resolution was not good enough to distinguish the differences between the end points of the hits. That is to say, the end points need more than a 90 cm separation on the array with σ_{time} = 1 ns from the crystal/PMT assembly for 3 σ separation. (Note that the standard deviation $\sigma = 1 \text{ ns}/\sqrt{12}$ for a uniform, 1 ns wide distribution from digitization is much smaller.) The distribution of the difference of the two angles (with one fixed and one random) was fit by a Cauchy-Lorentz distribution with the log-likelihood method (shown in red in the Figure).

The two panels of Figure 6.14 show the results of the azimuthal angle reconstruction for synchrotron radiation in this simulation. The top panel shows the percentages of the total simulated events within 95% of the central Cauchy-Lorentz distribution peak (= peak ± 6.32×half-width at half-maximum(HWHM)) including small peaks close to ±360 degrees and direction-misindentified peaks. At nearly vertical incident angles of the synchrotron radiation, these photons were detected at PMTs with close spatial proximity, and as a result it is harder to distinguish the directionality. At steeper incident angles, however, it is easier, since synchrotron photon distances are much more spread out on the CREST instrument.

The last Figure 6.16.(b) shows the azimuthal angle resolution (HWHM) of the CREST instrument. Since the probability of Compton scattering increases for higher energy synchrotron photons, the simple linear fit is not as robust for higher primary electron energy and as a result, has poorer resolution. The resolution is better for steeper incident angles, because the synchrotron photons are more spread out on the CREST instrument, and the linear fit is consequently more robust to Compton scattering with some of the photons landing on off-line crystals. Hence, the slight increase of resolution at 52 degrees and the decrease from 52 to 62 degrees is mainly caused by the change of the probability that the synchrotron photons interact from the top to the side surface of the BaF_2 crystals as well as the distribution of directionality of these Compton scattered photons.

6.3.4 Zenith Resolution

The zenith angle of the synchrotron radiation from high energy electrons can now be reconstructed. Using the longest distance and the time difference between two BaF_2 crystal hits, the zenith angle can be geometrically constructed (assuming synchrotron photons are parallel to each other),

$$\theta_{zenith} = \frac{\pi}{2} - \arccos\left(\frac{ct}{d}\right) \tag{6.1}$$

where t and d are the time and distance differences between the two crystal hits, and c is speed of light. Note that the condition, $ct \leq d$, has to be satisfied for this equation to be used. This condition turns out to be rather tight, for $\sigma_{\text{timing}} = 1$ ns and 1 ns digitization. Figure 6.16(a) shows the percentage of events that satisfy ct

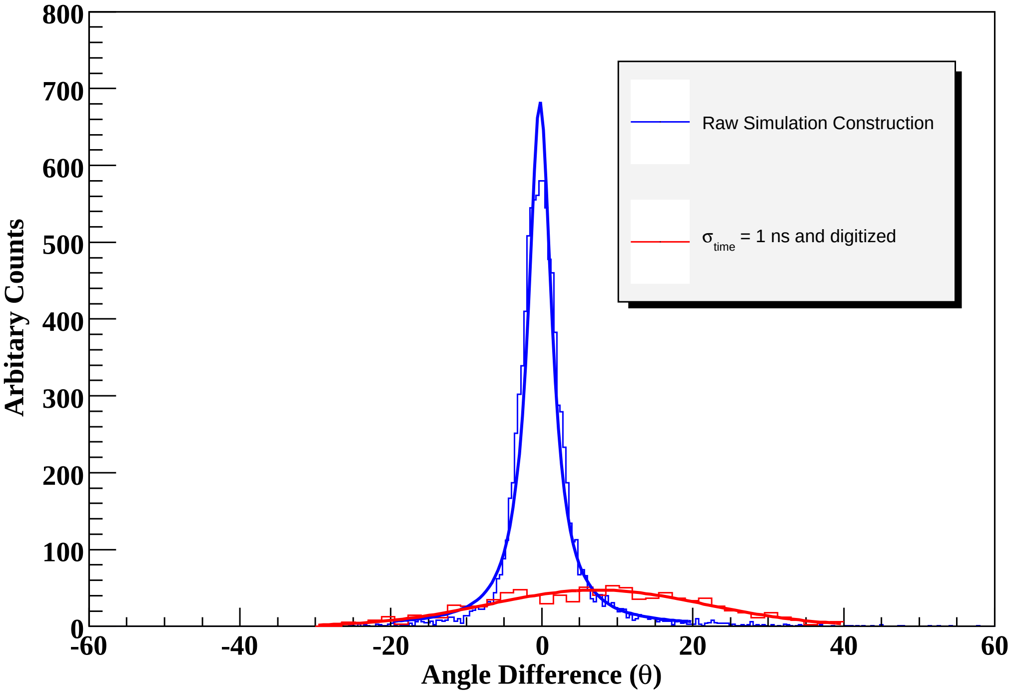

Figure 6.15: The angle difference (θ) between the known zenith and reconstructed angles. Blue histogram and its Gaussian fit do not include the timing resolution, while the red ones includes $\sigma_{\mathrm{timing}} = 1$ ns and 1 ns digitization.

$\leq d$ for $\sigma = 0$ ns (thick lines) and $\sigma = 1$ ns and 1 ns digitization (dotted lines). Note that much less than 60% of the events do not satisfy this condition including realistic software/hardware timing resolution. Since the BaF$_2$ crystals are not sensitive to the location of the photon interaction, we assume the location to be at the center of the PMT. Also, the distance between the centers of adjacent PMTs is 7.50 cm (while the diameter of the crystal is 5.08 cm). Since the speed of light is 30 cm per ns, the reconstruction requires at least 8 PMTs in principle for $\pm\ 1\sigma_{\mathrm{timing}}$ separation.

Figure 6.15 shows the differences between the known zenith and reconstructed angles (in blue) with $\sigma_{\mathrm{timing}} = 0$ ns. Also, the difference angle including $\sigma_{\mathrm{timing}} = 1$ ns and digitization (shown in red) is shown, and this difference peak looks rather small and shifted. This is solely caused by the timing resolutions of the BaF$_2$ crystal/PMT

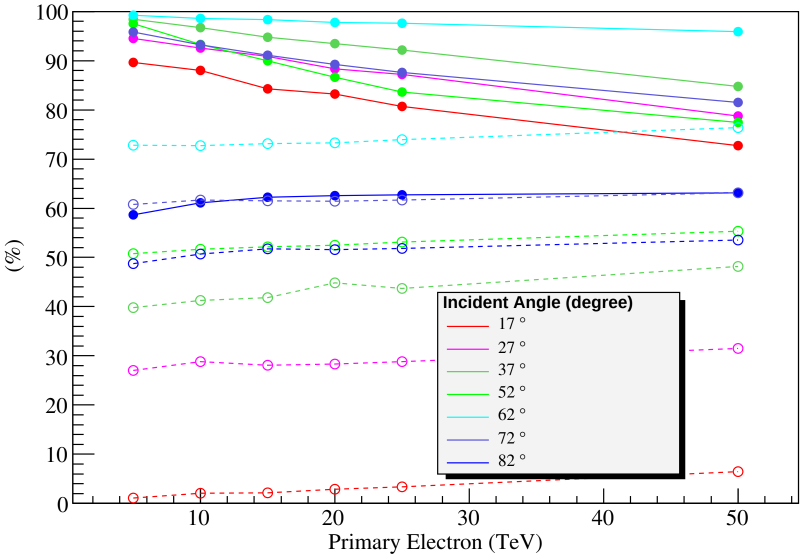

(a)

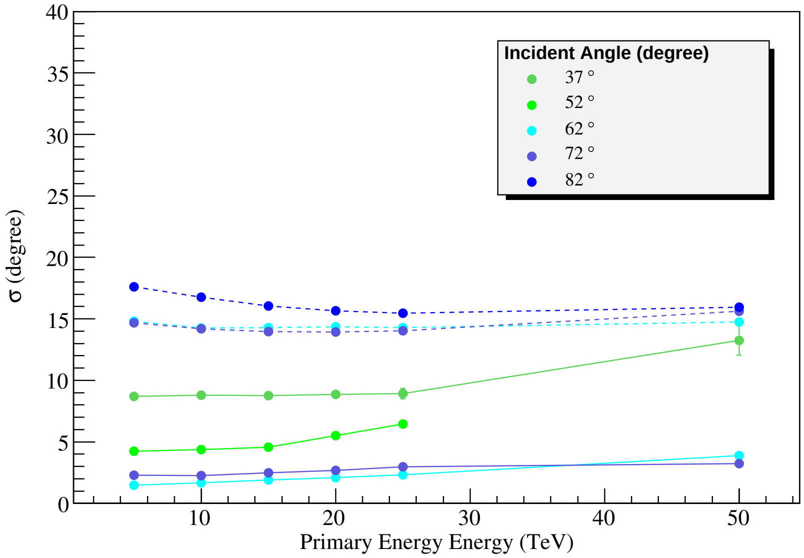

(b)

Figure 6.16: Zenith angle reconstruction results for (a) percentage satisfying Eq. (6.1) and (b) zenith angle resolution σ with $\sigma_{\text{timing}} = 0$ ns (thick line) and with $\sigma_{\text{timing}} = 1$ ns and 1 ns digitization (dotted line) for different incident angles.

assemblies and the digitization. At the same time, the shifting of the peak comes from the fact that the arc-cosine in Eq. (6.1) is not symmetric in its argument.

Figure 6.16(b) shows the zenith angle resolution from the reconstruction of zenith angle. The data points listed are the ones which can be fitted with a Gaussian distributions to extract the resolution. Only very steep incident angles (72 and 82 incident degrees) can be reconstructed, and the resolution is approximately $14 - 18$ degrees. This observation from the simulation suggests that the zenith angle reconstruction requires either better timing resolution and a larger array or a better method for zenith angle reconstruction.

6.3.5 Summary of Simulation Study

This chapter showed the simulation results of the instrument responses from background cosmic rays (proton and X/γ-rays) and synchrotron photons from high energy CR electrons. Using the expected background cosmic rays at Antarctica, deposited energies of the crystals and their rates of the background cosmic rays were simulated. With this simulated result and observed behavior (described in Section 4.6.2.) of the front-end discriminator and VARC chips, the total dead time of the instrument was optimized at 800 ns hold time of the front-end discriminator for the BaF_2crystal/PMT assemblies and 100 ns hold time for the veto scintillator assemblies.

There are many factors involved to obtain the geometrical factor of the CREST instrument. It strongly depends on the magnetic field (latitude and longitude), atmospheric overburden (g/cm^2), and primary electron energy (TeV). It was shown in Section 6.2.2.1 that the geometrical factor of the CREST instrument increases as the energy of the electrons increases. My simulations show approximately a 43% increase over the physical geometrical factor for a 25 TeV electron.

The instrument simulation shows that method of mean deposited energy can be utilized as described in Section 2.6. By understanding systematic differences between the mean energies of synchrotron photons and the mean deposited energies in the BaF_2 crystals, especially for higher energy electrons, the simulation shows that the energy resolution is ~ 17 to $\sim 47\%$ at incident angles from 17 to 82 degrees for 25 TeV electrons. The azumuthal resolution (order of a few degrees) slightly improves as incident angle increases because the synchrotron radiation is spread over the instrument, allowing a comfortable linear fit between the hits. The zenith angle resolution is quite difficult to reconstruct by the simple end to end method described in Section 6.3.4 and only for large separations between crystal hits would make this method be possible. For larger incident angles (larger than 72 degrees), this method is relatively useful, and for these angles, the zenith angle resolution is approximately 15 to 20 degrees.

Further simulation study will be needed to improve the ability of the reconstruction of the synchrotron events. Next Chapter shows expected performance of the CREST experiment and summarize this dissertation.

CHAPTER VII

Summary

In the first chapter I presented an overview of the CREST instrument and its detection of primary high energy CR electrons. In second chapter I explained the mechanisms behind the acceleration and propagation of high energy electrons and described possible sources. At the end Chapter II, some of expected electron spectra from nearby SNRs were shown. The third chapter summarized mechanical design of the instrument in order to optimize the detection of synchrotron radiation. The details of the hardware and software of the instrument and their development were introduced in Chapter IV. The prototype CREST instrument (CREST-I) and its measurement of the diffuse and atmospheric x/γ-rays measured at Ft. Sumner, NM, were shown in Chapter V. Chapter VI showed Geant4 simulation results for the Antarctica CREST instrument, response to proton and X/γ-rays backgrounds and synchrotron radiation from high energy electrons.

In this chapter, I present a short summary of the performance of the CREST instrument from the CREST-I flight and the expected number of high energy electron events for the Antarctic CREST flight. I also discuss the scientific significance of the measurement of high energy CR electrons/positrons for astro-particle and high energy physics. Lastly, the schedule of the CREST project is presented.

7.1 CREST-I flight and Background Rate to the Instrument

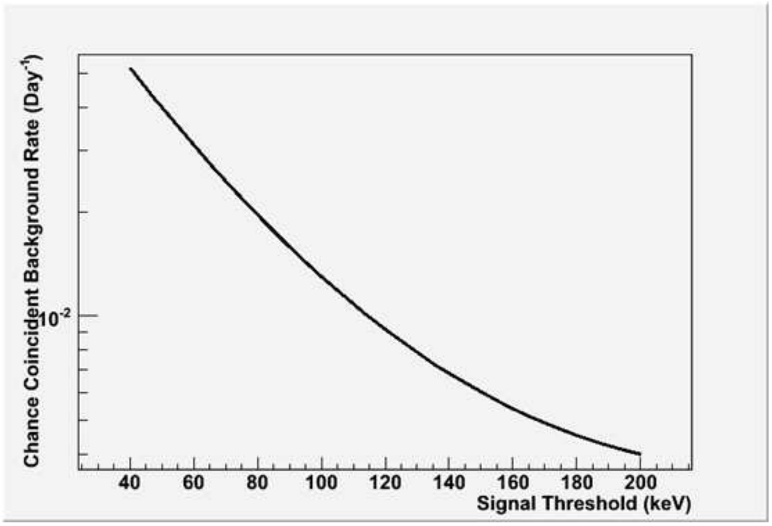

Figure 7.1: Estimated background coincident rate of Antarctica CREST flight by Jim Musser.

The CREST-I instrument was the predecessor of the Antarctic CREST instrument, but its flight at Ft. Sumner had difficulty in the functionality of some of the modules. It was beneficial however, since we were able to test the performance of the electronics logic that utilizes FPGAs with 1 GHz CPLDs responding to actual rates of incident particles and photons. The initial flight also tested the operation of the crystal/PMT assemblies with Cockcroft-Walton high voltage divider under actual near vacuum extreme conditions. Furthermore, the instrument measured the diffuse and atmospheric X/γ-ray rate and its spectrum at different atmospheric depths. This measured background rate and its spectrum was utilized to estimate the background event rate to real synchrotron event in Antarctica. Figure 7.1 shows the background event rate at Antarctica for 4-fold or greater coincidences with co-linear crystal hits with a 6 ns time window as a function of threshold energy. At a 40 keV threshold, we expect one accidental background event from diffusive and atmospheric X/γ-rays in a day flight.

The hold time of the front-end discriminator was determined to optimize the instrument dead time using a X/γ-ray and proton model from the GLAST Geant4 simulation (See Appendix B). Note that the single crystal hit rate ($\sim$ 270 Hz) of the instrument from X/γ-rays determined with this simulation package agrees with the CREST-I measured rate result ($\sim$ 1.7 (from rigidity and solar modulation) × 157.8 ±1.0 Hz (Table 5.3)= 268.3 ±1.7 Hz) at $\sim$ 4 g/cm^2 atmospheric depth.

7.2 Expected Number of Events Observed by the CREST instrument

Table 7.1: Expected Number of Events for the 100 Day Flight

Electron Energy (TeV)	Casadei and Bindi[1]		HEAT[72]		HESS[16]	Vela (Kobayashi [19])
	N_{e^-}	N_{e^+}	N_{e^-}	N_{e^+}	N_{e^-} and N_{e^+}	N_{e^-}
2.5 - 5	28.7	3.1	282	4.8	54.2	92.5
5 - 10	13.0	1.4	163	2.4	7.2	105.8
10 - 25	5.5	0.6	89	1.1	0.2	54.7
25 - 50	1.1	0.1	24	0.2	0.0	2.2
> 50	0.6	0.0	19	0.1	0.0	0.0

With different spectra, $dN/dE = J_o E^{-\alpha}$, of primary CR electrons and positrons, the expected number of events for the CREST experiment can be estimated as follows:

$$\mathrm{N}_{e^{\pm}} = T \int_{E_{\mathrm{low}}}^{E_{\mathrm{high}}} \mathrm{GF}\,(E)\, \frac{dN}{dE}\, dE \tag{7.1}$$

where T is the duration of the measurement and GF(E) is the geometrical factor as a function of primary electron energy. In this estimation, I assumed a total duration of 100 days for an Antarctic flight, and I used Figure 6.9 for the geometrical factor, where primary electrons were released at (75° South and 135° East) and synchrotron photons were detected at 4 g/cm^2. Generally, the geometrical factor, as described in Section 6.2, is a function of primary energy, atmospheric depth, latitude and longitude. The expected number of events by the different observed spectra are summarized in Table 7.1, and the CREST expected results with different power laws

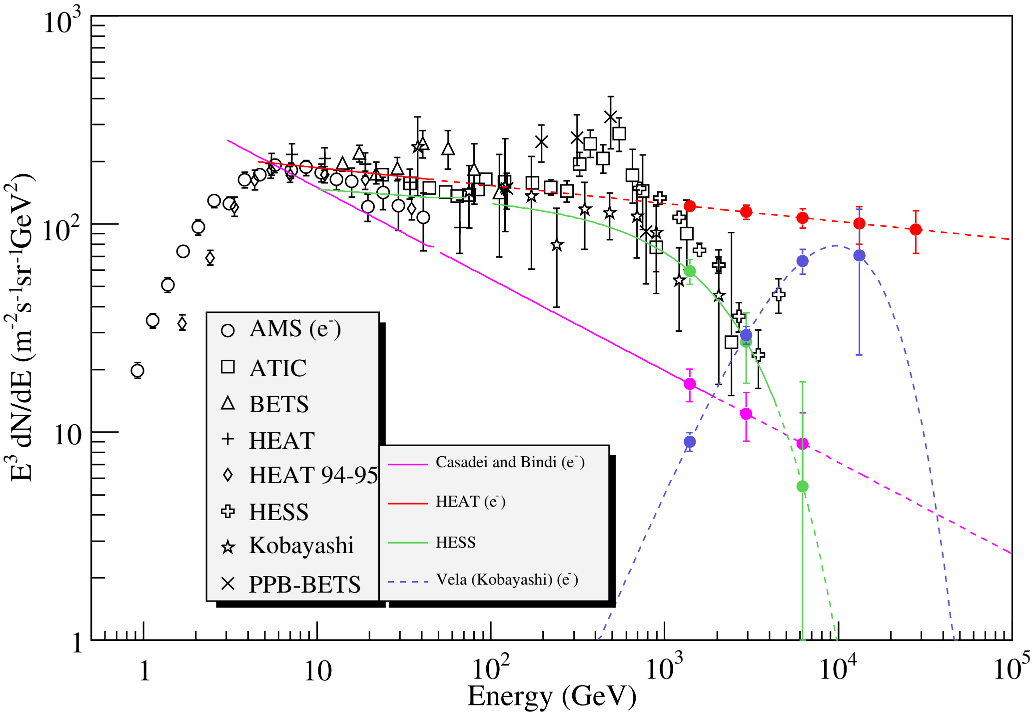

Figure 7.2: Previous measured CR electron ($e^{\pm}$) spectrum (References therein [16]) with different indices of the power-law spectra adjusted for the rigidity and solar modulation in Casadei and Bindi [1], extended from HEAT data [72], fit with exponential cutoff (Fit B in HESS [16]), and Vela spectrum from Figure 2.10. Error bars indicate expected CREST results of different models for 100 day flight and they are statistical only.

are presented with the previous experimental data in Figure 7.2. Dotted lines are simply extended from individual power law models, where their data points were fit by thick lines. The error bars on the different functional models are statistical only.

Casadei and Bindi [1] used direct measurements of CR electrons and positrons corrected for solar modulation to fit a power law with experimental data from year 1969 to 1998. Their power law fit indicates $J_o = 412 \pm 22.8$ ($\mathrm{m}^{-2}\mathrm{sr}^{-1}\mathrm{s}^{-1}\mathrm{GeV}^{2.44}$) and $\alpha = 3.44 \pm 0.03$ for CR electrons whose energies range from 3 GeV to 2 TeV, and $J_o = 41.1 \pm 2.8$ ($\mathrm{m}^{-2}\mathrm{sr}^{-1}\mathrm{s}^{-1}\mathrm{GeV}^{2.43}$) and $\alpha = 3.43 \pm 0.05$ for CR positrons whose energies range from 0.7 GeV to 66.4 GeV. For the HEAT experiment, a power law fit of their data show $J_o = 227 \pm 45$ and $\alpha = 3.086 \pm 0.081$ for CR electrons whose energy range from 4.5 GeV to 50 GeV, and $J_o = 24 \pm 12$ and $\alpha = 3.31 \pm 0.23$ for CR positrons in the same energy range. These two results yield approximations of upper and lower boundaries if their power indices are assumed to extend to higher electron energies.

The most recent published result from the HESS experiment [16] which utilizes an imaging atmospheric Cherenkov telescope shows a harder flux of $(1.17 \pm 0.02) \times 10^{-4}$ $\left(\frac{E}{1\mathrm{TeV}}\right)^{-3.9\pm0.1}$ ($\mathrm{m}^{-2}\mathrm{sr}^{-1}\mathrm{s}^{-1}\mathrm{TeV}^{-1}$) only including their CR electrons measurement and reconstruction from 600 GeV to 4.5 TeV. Combining their data points with the others above 10 GeV shown in Figure 7.2, the CR electron spectrum was expressed by a power law whose power index of -3.05 ± 0.02 with an exponential cutoff of 2.1 ± 0.3 TeV. Lastly, the expected number of CR electrons from Vela with a specific parameter set (Figure 2.10(b)) is calculated and shown as an example. This Vela estimate shows that the CREST instrument will be able to observe a further increase in CR electron spectrum around 10 TeV with significant numbers of events.

7.3 Meaning of measuring high energy CR electrons

Since high energy CR electrons lose energy very rapidly during propagation through the interstellar medium, their detection would indicate the existence of sources which are nearby on a galactic scale as shown in Fig. 2.10. Simultaneously, we will be able to observe the exponential cutoff of the diffusive component of the spectrum as in Section 7.2. The power indices of this measurement will restrict the acceleration mechanisms of CR electrons (Section 2.3.2). Although it is unfortunate that the CREST instrument will not be able to perform the separation between CR electrons and positrons, the measurement of the positron fraction at TeV energies may suggest the existence of new physics and/or the nature of positron/electron acceleration in new astrophysical objects. For instance, among many possible causes of the increase in the positron fraction observed in various experiments, the annihilation of weakly interacting massive particles (WIMP's) in the Galactic halo are the one of the candidates at energies from ten to a few hundred's of GeV. Super-symmetric particles are one of the WIMP candidates which, if sufficiently heavy, will annihilate into either Z° or $W^\pm$, which then decay into positrons and electrons. These particles may represent the dark matter of the universe. This signature was first observed by the HEAT experiment [3] and recently confirmed by the PAMELA experiment [5]. Although these energies are much lower than what CREST can measure, even a crude measurement of the positron fraction at TeV energies would have profound implications. If a few CR electrons or positrons pass throught the CREST instrument, then the presence of γ-ray hit on only one side of the electron or positron could identify the charge sign. It remains an open question as to whether any such events will be seen by CREST.

7.4 CREST Project Schedule

CREST experiment was initially proposed in 2004-2005. The first engineering flight (CREST-I) was performed in fall 2005 at Ft. Sumner, NM. The current CREST flight schedule is to have another engineering flight from Ft. Sumner, NM in spring 2009. Simultaneously, we have started designing and construction of a larger 1024 crystal/PMT array that will be flown in Antarctica in December 2010 with a second Antarctic flight in December 2011.

APPENDICES

APPENDIX A

Photomultiplier Tube Package Specification

CREST Photomultiplier Specifications[1]

May 3, 2004

Dear Photomultiplier Tube Vendors,

You are invited to bid on the development on photomultiplier tubes for the Cosmic Ray Electron Synchroton Telescope (CREST). CREST is a balloon experiment that will measure the energy spectrum of TeV (1-50 TeV) electrons in the primary cosmic rays. CREST will employ an array of cylindrical BGO detectors (5 cm D x 1 cm thick) to record gamma rays in the range (20 keV to 20 MeV) originating from synchrotron radiation from primary electrons bending in the Earth's magnetic field. The signature of these electrons will be a string of gamma ray hits in the array occurring in a row and within 5 ns of each other. Each BGO crystal will be viewed by a nominal 2" diameter PMT optically coupled with a 1 mm thick silicone "cookie." The balloon environment places a number of constraints on the PMT design. The low pressure (∼3 mbar) will require protection from corona. The PMTs and base will need to be potted to prevent corona discharge for pressures as low as 2 mbar. Power is a concern. The base should synthesize the high voltage (Cockroft-Walton

---

[1] Written by Greg Tarlé to the photomultiplier tube vendors

or equivalent) from a low voltage source provided on a connector that will not result in corona discharge. The low voltage can either be a precision reference with PMT bases internally adjusted to match gains or an individual precision voltage reference signal can be used to control an unregulated low voltage provided on a bus. Total power consumption should be less than 60 mW per PMT. Weight is also a concern. To reduce weight and allow for close packing, the shield shall consist of no more than two layers of 0.004" thick mu-metal of minimum diameter at kept at ground potential. The base should be positive high voltage to eliminate discharge problems between the shield and photocathode. We wish to determine the timing of the gamma ray hits to = 1 ns so that we can distinguish the direction of the hits in the array and separate positrons from electrons using the East-West effect. Our gain requirements are modest. We will use a nominal gain of 1×10^6 to obtain good timing but will attenuate the signal to put 20 MeV gamma rays at the full scale of our ADCs.

CREST has been funded for a prototype flight from North America in summer 2005. Development of a full long-duration CREST balloon instrument has been pre-approved, conditional on a successful demonstration of the prototype instrument.

The prototype array will consist of 96 PMTs (+ 5 % spares). An additional 8 PMTs will be required for an anticoincidence counter made of organic plastic scintillator. The anticoincidence PMTs need not have their photocathodes green enhanced but we understand that using the same PMT for both applications may reduce cost and complexity. The PMTs should have the following characteristics:

- 2" nominal diameter
- Gain: adjustable to 10^6. 5 % by external control or by matching bases.
- Photocathode: Green enhanced to match BGO emission spectrum. The PMTs

for the anticoincidence counter need not be green enhanced.

- Quantum efficiency should be comparable to standard multi-alkali photocathodes.
- Timing resolution: $\sim$ 1 ns for 20 p.e. integrated light output and pulse shape compatible with BGO detectors.
- Minimum ”linear” dynamic range 1000 (20 p.e. to 20,000 p.e.).
- Linearity: $<$ 10 % integral nonlinearity (roll off at high end acceptable)
- Pulse Height Resolution $<$ 5 % FWHM (We achieve 9.7 % FWHM for a 662 keV 137Cs photopeak and we do not want the tube or base design to degrade this significantly.)
- Magnetic Field sensitivity: With a thin (two layers of 0.004”) mu-metal foil wrap extending 1.1 cm beyond the face of the PMT, the PMT gain should not deviate by more than 5 % for any orientation relative to the Earth’s field
- Potting: The tube and base shall be potted in such a way to operate at any pressure between 2-1000 mbar. The PMT will need to be manufactured with flying leads, attached to the base, tested, cleaned and potted. Enclosure shall be grounded cylindrical μ-metal foil mentioned above. Except for the top cover, the rest of the assembly should be light tight. Aluminum tape can be used to seal the μ-metal joint and the bottom cap to the μ-metal cylinder.
- Base: Potted active base with low V input. Controllable +HV with low V reference level (see Pulse Height Resolution requirement above) 60 mV max power consumption per base.

- Vendor shall be responsible for providing a complete potted and tested PMT/base/shield unit. The customer shall attach the BGO crystal to these units, provide a light tight lid and perform final verification.

Cost of complete PMT/base assembly should be < $ 500 US ea (in lots of 100 units or more). This is a goal.

When considering these specifications you may need to know the singles rates that we will be encountering. We have flown a single prototype crystal as a piggyback payload on an Antarctic Balloon flight last December. The integral rate measured above our threshold of 20 keV is 1 kHz.

Construction of the Prototype will begin in Fall 2004. After a successful prototype demonstration flight in Summer 2005, the plan is to build the Antarctic Long Duration Balloon (LDB) payload. It will consist of 1600 PMTs with identical specifications. This will likely fly in December 2007 with construction beginning in Jan 2006.

Vendors should bid on the following three phases:

1. One demonstration unit meeting all the specifications above by Aug. 1, 2004. We expect to test units from multiple vendors during the month of August and make a selection on Sept. 1, 2004. We expect to place an order for phase 2, with the selected vendor on that date.

2. 110 units to be delivered Oct. 1-Dec. 20, 2004 (staged delivery desired). Successful performance by the selected vendor in this phase will be a deciding factor in the selection of the vendor for phase 3.

3. 1,600 additional units to be delivered Jan. 1, 2006 - Dec. 20, 2006 (Staged delivery desired)[2].

We expect to receive all bids by June 1, 2004. Orders for the single demonstration units will be placed by mid-June.

---

[2] In the orignial proposal, the number of PMTs was 1,600.

PMT Package Specifications for CREST II Payload[3]

Indiana University Physics Department

4/4/06

CREST II has been funded for the construction of a Long Duration Balloon payload consisting of 1024 PMTs. The following specifications will be required for the PMT package.

1. 52 mm. diameter envelope ± 0.25 mm
2. Gain of not less than 5×10^6
3. Minimum dynamic range of 10^3 with less than 10 % nonlinearity in that range.
4. Pulse Height Resolution of less than 10 % FWHM at 662 KeV for NaI crystal, (Cs 137 photo peak) for tube and base.
5. The output referenced noise level at the anode from the active base shall be less than the amplitude of a 1/2 photoelectron pulse at 5×10^6 gain into 50 Ω with a rate of less than 1 kHz of pulses of 1/2 p. e. amplitude.
6. The single photoelectron timing jitter sigma shall be less than 1.0 n.s. at 5×10^6 gain.
7. Magnetic field sensitivity such that a field of 1 Oersted entering the tube from any angle produces no more than a 30 % loss in anode current from that of the maximum current when operating the tube at 5×10^6 gain.
8. Tube base and +HV supply to be encapsulated in an opaque material ensuring no corona or significant leakage current is developed at maximum gain in an atmosphere of 2mbar absolute pressure. The tube shall operate at this pressure

---

[3] Written by Mark Gebhard to The Hamamatsu Corp.

for three months with no change in characteristics and should operate at any pressure between this and one atmosphere for the same length of time. The specification for opacity is such that every PMT assembly operated at 5×10^6 in a darkened lab will have a rate of less than 1 kHz triggers at a threshold of 1 mV. when stabilized and will maintain that rate when the room lights are switched on.

9. The power input lines, the control line, the monitor line and the three signal lines shall exit the potting at a radius of 0.4 cm ± 2mm from the centerline of the long axis of the tube. The anode and dynode signal lines will be of coaxial cable, type RG-178 B/U. and extend 8 cm beyond the exit from the potting. The power input cables and the control and monitor cables shall be 22-24 ga. PTFE insulated wire and if termination is provided it must be the following: At 8 cm from the potting a Molex receptacle housing 43645-0400 shall be installed using Molex 43030-0009 terminals, crimped and soldered before insertion.

10. Signal outputs to be: Anode, 10th dynode, and 7th dynode each having a safety resistance of between 10 KΩ and 1 MΩ. A schematic of the output connections will be required.

11. Active base to provide HV derived from 12V ± 1V input voltage and controlled by external control voltage with a 1:1000 control voltage: HV ratio. A monitor output with a 1000:1 ratio of HV: monitor output voltage will also be provided. The base will consume no more than 60 mW of power at the specified gain.

12. Delivery of finished assemblies at the rate of about 500 per year. We intend to begin testing PMTs and installing crystals in this calendar year. Staged delivery of assemblies is required.

13. The vendor shall be responsible for providing a complete potted and tested PMT/base unit to the customer at a mutually agreeable rate. The customer will provide fiber optic cable assemblies as specified in item 16. The customer will then assemble a crystal to the PMT unit and light tight the assembly and retest the assembly. Any PMT unit found to be defective will be returned to the manufacturer for replacement at no charge.

14. Optical fiber: Fully prepared 1 mm diameter optical fibers for injection of light into the photocathode will be provided by the customer as follows: These shall be sheathed with optically opaque material and terminated by an optical coupling connector at one end. The other end will be cut at 45 degrees and this face shall be polished and aluminized. Vendor will need to glue (with clear epoxy or other optical cement) the region of the fiber facing the angled cut to the side of the PMT at a location next to the photocathode. (Supplementary picture provided) The sheathed fiber will extend along the side of the PMT and out of the back of the PMT assembly at a point within 12 degrees of the direction of maximum magnetic sensitivity of the dynode structure.

15. Each PMT assembly will be identified with a barcode label placed vertically on the side of the unit. Code type 128 is preferred and the format of the label should be "CRESTPMT-B-[serial number].

16. A grounded magnetic shield will be incorporated into the design. It should be constructed of 1 turn of μ -metal or equivalent, of 0.1 mm thickness and beginning at the termination of the potting material at the base of the tube and extending to the photocathode plane but not beyond.

17. The storage temperature of the PMT shall be -30 C. to +40 C. and the operating

temperature shall be -10 C. to +40 C.

APPENDIX B

Background Cosmic Ray Spectra: Proton and X/γ-rays

B.1 Primary and Secondary Proton Flux Model

The functional forms used for the primary and secondary flux models[1]are:

$$\text{Primary}(E) = \frac{23.9}{1+\left(\frac{R}{R_{\text{cutoff}}}\right)^{-12.0}} \times \left(\frac{R\,(E+e\Phi)}{\text{GV}}\right)^{-2.83} \times \frac{(E)^2-(Mc^2)^2}{(E+e\Phi)^2-(Mc^2)^2} \quad (/\text{s/m}^2/\text{sr/MeV}) \tag{B.1}$$

$$\text{Secondary}(E) = \begin{cases} \text{if } 20 \text{ keV} < E < 100 \text{ MeV} \\ \quad 4.36 \times 10^{-2} \times \left(\frac{E_k}{\text{GeV}}\right)^{-1.0} \\ \text{if } 100 \text{ MeV} < E < 100 \text{ GeV} \\ \quad 3.65 \times 10^{-2} \times \left(\frac{E_k}{\text{GeV}}\right)^{-1.98} e^{-\left(\frac{E_k}{0.211\text{GeV}}\right)^{-0.98}} \end{cases} \quad (/\text{s/m}^2/\text{sr/MeV}) \tag{B.2}$$

where primary and secondary protons were generated from 20 keV to 100 GeV. The first term of the primary proton flux model function (Eq. (B.1)) describes the

---

[1] Taken from the Cosmic Ray Generator for GLAST Geant4 Simulation [59] for both proton and X/γ-rays

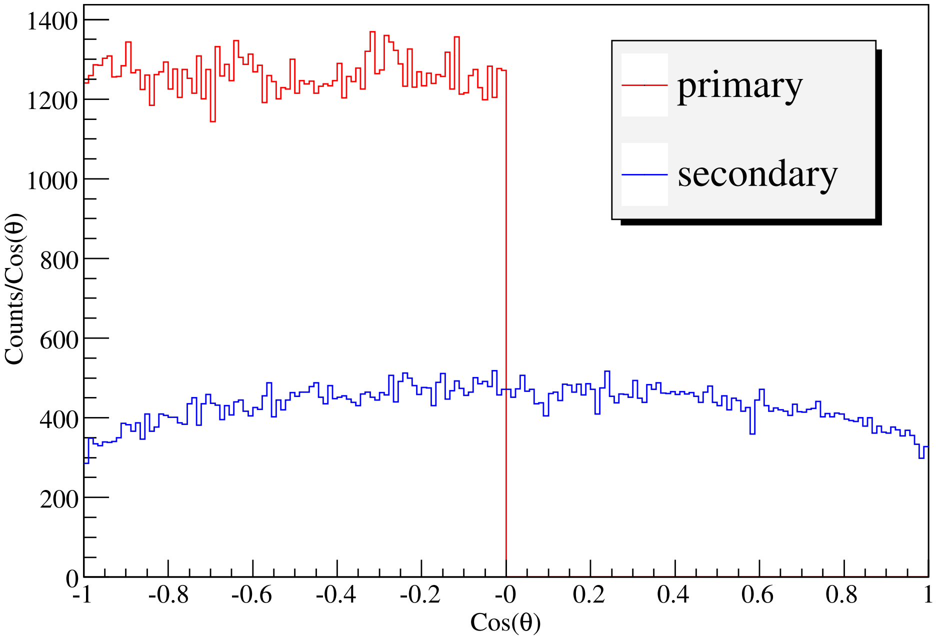

Figure B.1: Angular distributions of the primary and secondary proton fluxes in arbitrary units: the primary protons were generated with zenith angle, θ, isotropically from 0 to 180 degree, while a 1 + 0.6 Cos(θ) angular dependance was imposed on secondary proton generations.

spectrum reduction factor due to the geomagnetic cutoff effect where $R = Pc/Z|e|$ and R_{cutoff} are the magnetic rigidity of the particle and rigidity cutoff due to the Earth's magnetic field respectively. The second term describes the primary proton power law spectrum slightly modified solar activity ($E \rightarrow E{+}e\Phi$). Also, the third term modifies this spectrum by solar activity, where Φ, E, Mc^2, and e are the solar modulation potential, total energy and rest mass and electronic charge of the proton, respectively. To simulate the Antarctic flight environment, the two parameters, R and Φ are set at $R = 0$ (no modification due to the geomagnetic cutoff effect) and $\Phi = 793$ MV at December 2010. On the other hand, the secondary proton flux model function (Eq. (B.2)) was simply constructed by extrapolating the data points from AMS, BESS, IMAX, and CAPRICE experiments, and data by Pennypacker and Verma (References therein [59]). Both primary and secondary proton spectra are shown in Figures 6.1.

Figure B.1 shows the angular distributions of the primary and secondary input proton fluxes for this simulation. The angular distribution of the primary proton spectrum is assumed to be isotropic from 0 to 180 degrees. On the other hand, the distribution of the secondary proton spectrum has a $1 + 0.6 \cos(\theta)$ angular dependenace where θ is zenith angle [73].

B.2 Primary and Secondary X/γ-ray Flux Model

$$\mathrm{Primary}(E) = \begin{cases} 570.8 \times \left(\frac{E}{\mathrm{MeV}}\right)^{-1.86} & \text{if } 20 \text{ keV} < E < 50 \text{ keV} \\ 40.0 \times \left(\frac{E}{\mathrm{MeV}}\right)^{-2.75} & \text{if } 50 \text{ keV} < E < 1 \text{ MeV} \\ 40.0 \times \left(\frac{E}{\mathrm{MeV}}\right)^{-2.15} & \text{if } 1 \text{ MeV} < E < 100 \text{ GeV} \end{cases} \quad (/\mathrm{s}/\mathrm{m}^2/\mathrm{sr}/\mathrm{MeV}) \tag{B.3}$$

$$\mathrm{Secondary}(E) = \begin{cases} \text{if } 20 \text{ keV} < E < 1 \text{ MeV}, \\ \quad 250.0 \times \left(\frac{E}{\mathrm{MeV}}\right)^{-1.34} \\ \text{if } 1 \text{ MeV} < E < 1 \text{ GeV}, \\ \quad 250.0 \left(\frac{E}{\mathrm{MeV}}\right)^{-1.70} + 1.14 \times 10^5 \left(\frac{E}{\mathrm{MeV}}\right)^{-2.5} e^{-\left(\frac{E}{120\mathrm{MeV}}\right)^{-1.5}} \\ \text{if } 1 \text{ GeV} < E < 100 \text{ GeV}, \\ \quad 2.15 \times 10^4 \times \left(\frac{E}{\mathrm{MeV}}\right)^{-2.2} \end{cases} \quad (/\mathrm{s}/\mathrm{m}^2/\mathrm{sr}/\mathrm{MeV}) \tag{B.4}$$

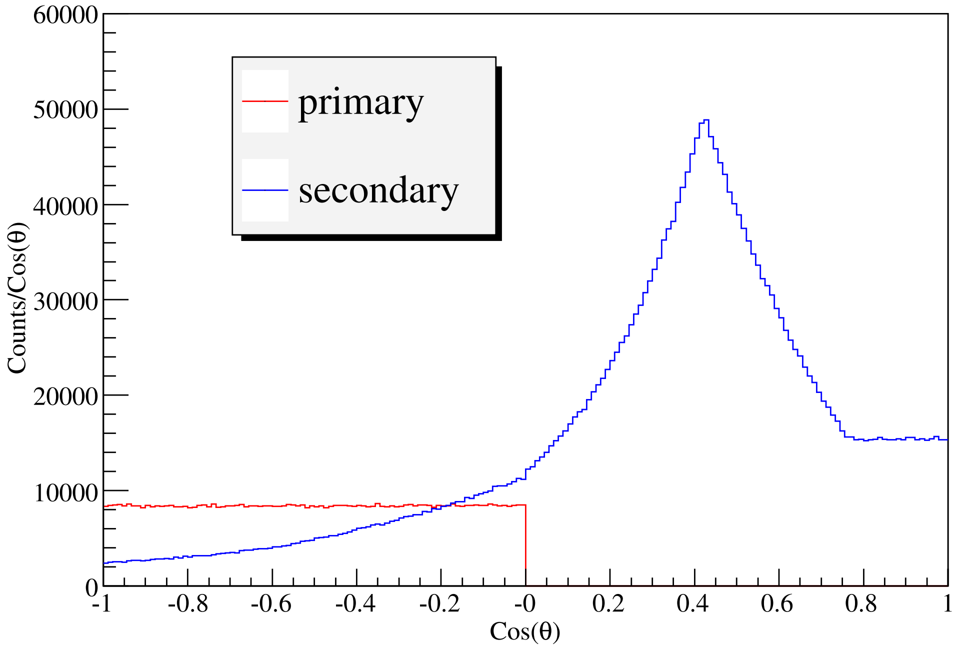

Figure B.2: Angular distributions of the primary and secondary X/γ-ray fluxes in arbitrary units. In this histogram, the angular dependance of the secondaries is based on Schöenfelder et al. [56] with their observed energy range extended from 1.5 to 10 MeV at 2.5 g/cm^2.

$$\text{Secondary}(E) = \begin{cases} 1500 \times \left(\frac{E}{\text{MeV}}\right)^{-1.34} & \text{if } 20 \text{ keV} < E < 10 \text{ MeV} \\ 4854 \times \left(\frac{E}{\text{MeV}}\right)^{-1.85} & \text{if } 10 \text{ MeV} < E < 1 \text{ GeV} \\ 5.29 \times 10^4 \times \left(\frac{E}{\text{MeV}}\right)^{-2.20} & \text{if } 1 \text{ GeV} < E < 100 \text{ GeV} \end{cases} \quad (/\text{s}/\text{m}^2/\text{sr}/\text{MeV}) \tag{B.5}$$

The primary and secondary X/γ-ray fluxes were constructed from the experimentally observed data points from the various experiments (refer to [59] for the details). Note that the secondary spectra separated into two components: downward Eq. (B.4) and upward Eq. (B.5) where the downward component is more dominant. The, angular distribution of the primary flux is assumed to be isotropic. On the other hand, the distribution of secondary photons has a distinct feature as seen in Figure B.2

based on the observation [56], where their observed energy range extends from 1.5 to 10 MeV at 2.5 g/cm^2. Even though the angular distribution of the secondaries is observed to be more isotropic at lower energies, it was taken to have the same angluar distribution over the whole energy range from 30 keV to 100 GeV in this simulation.

The normalizations of the X/γ-ray model functions (Eqs. (B.3), (B.4), and (B.5)) were modified to simulate at expected for the CREST experiment in Antarctica. Based on the rigidity normalization factor calculation performed in [64], the primary component was assumed to be the same as that observed in Ft. Sunmer, NM. On the other hand, the normalization factor of the secondary component is slightly modified. Eqs. (B.4) and (B.5) were simply multiplied by 1.7 to accomodate the Antarctic flight, where the geomagnetic cutoff is approximately 0 GV.

APPENDIX C

Compton Scattering and Lead Shield

The CREST instrument detects secondary synchrotron radiation from primary CR electrons traveling through the magnetic field of the Earth. The signature of a high energy electrons is a series of time-ordered x/gamma-ray hits along a line in the segmented CREST detector. X/γ-ray background photons in the atmosphere can mimic this signature through random linear hits of x/gamma-ray photons combined with Compton scattering of these photons off the underlying structure. These background photons detected in one crystal, for instance, can scatter into the other crystals. They can equally be scattered by the surrounding electronics and/or the gondola structure, and then they can interact with different crystals. When this event happens to have a linear structure on the crystal array within a certain time window and with a certain threshold number of the crystal hits, it can be misidentified as a synchrotron radiation event. These types of Compton scattering induced false events are inevitable. To reduce this false event rate, a lead (Pb) shield (high Z) wrapped around the crystal/PMT assemblies (Figure C.1 without lead shield) can be used. However, we are limited in the amount of lead shield we can use, because any additional weight of the balloon payload decreases the flight altitudes. In turn, this reduces the geometrical area of the instrument, and at the same time it increases the atmospheric X/γ-ray background rate. To optimize the thickness and positioning of the lead shield, a simulation study was performed by Jim Musser.

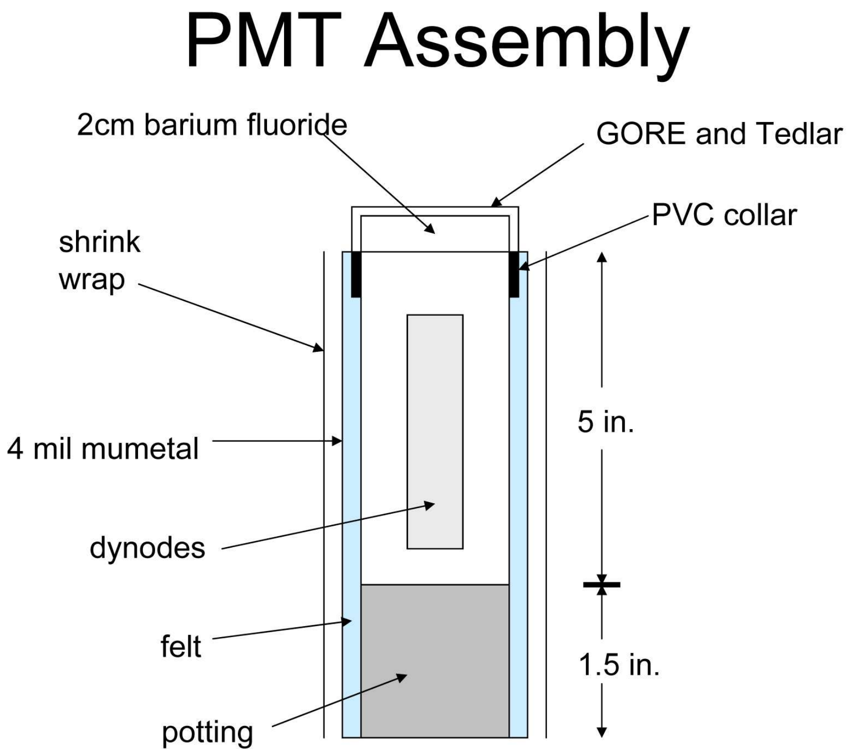

Figure C.1: Mass model for the BaF_2 crystal/PMT assembly.

In addition to the previous Geant4 study performed on the instrument (Section 6.1.2), the front-end electronics, the batteries/CIP/other electronics, and a cylinder of Pb around the crystal/PMT assemblies is included in this simulation. To make the simulation simpler, the front-end electronics, located beneath of the Al channel (Figure 4.3(b)), is modeled by simply increasing the thickness of the Al channel by 2.2 mm. The other electronic modules are also modeled by Al slabs with a size of 1 × 1 × 0.076 m placed 75 cm below the array of the crystal/PMT assemblies. Side vetos, veto PMTs, external frame, solar panels, and crush pads are not included in this study.

In his simulation, the objective was to reduce the number of *cluster*s by defining a *cluster* to be isolated group of crystal hits, where the isolation is defined as the distance of crystal hits that are larger than 20 cm (more than 2 crystals between hits). The random coincident probability for 1024 crystal/PMT assemblies exposed in the 200 Hz background of X/γ-rays with a 3 ns timing window are calculated to be 6×10^{-4} (= 200 Hz × 1024 crystals × 3 ns). On the other hand, the probability of Compton scattering event having more than two clusters has to be much smaller than the random coincident probability. The probability of the Compton scattering cluster event was calculated by convolving the X/γ-ray energy spectrum ($\mathrm{d}N/\mathrm{d}E \propto E^{-1.7}$) with the probability of the energy dependent Compton scattering obtained by the simulation,

$$\mathrm{Probability}_{\mathrm{Compton}} = \int \frac{\mathrm{d}N}{\mathrm{d}E} \times \mathrm{Probability}_{\mathrm{Compton}}(E)\, dE \tag{C.1}$$

First, the directionality of scattered photons are studied to determine where the lead shields have to be placed around the crystal/PMT assemblies. At lower energy (less than ~ 1 MeV), most of the background events come from these photons: They are first scattered by the crystal, then are scattered off the top veto, and then finally back into the crystal array. For higher energy incident photons, these Compton scattered photons are equally likely coming up from the bottom of the crystals. For an isotropic photon flux with incident photon energies larger than 1 MeV, these scattered photons are coming from slightly below the horizon. As a result, the lead shield is placed slightly below from the bottom surface of the crystal (Section 4.1.4 for the crystal/PMT assembly).

Studies of the X/γ photon energy dependence as well as the effect of varying the thickness of the Pd shield show that for greater photon energies, the probability of producing more than 2 clusters increases. This probability becomes dominant above

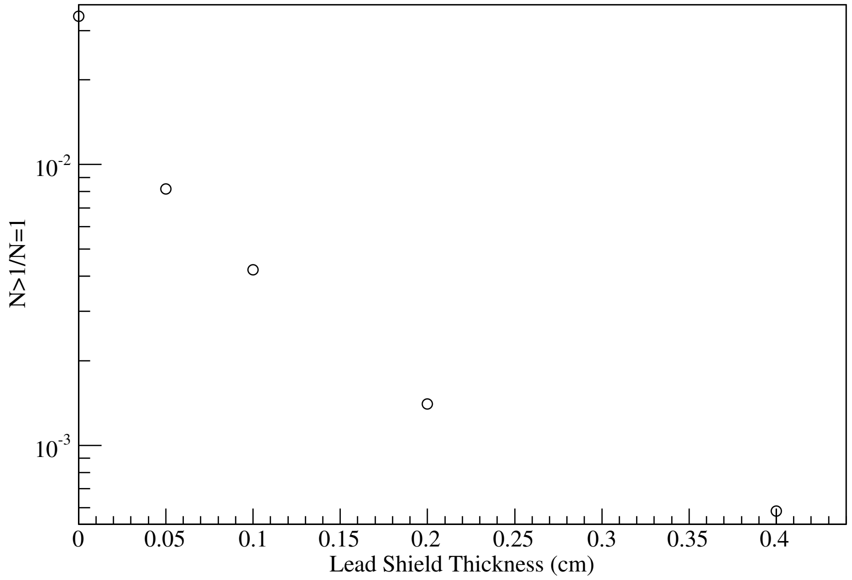

Figure C.2: The ratio of the probabilities of Compton scattering with the number of cluster, N, > 1 to the number of cluster = 1 vs. the shield thickness at 2.5 MeV.

photon energies of 1 MeV. Figure C.2 shows that without any shielding, Compton scattering results in a rate that is ∼30 times higher than random coincidence backgrounds at 2.5 MeV (In general, this is 20−50 times higher, depending on photon energy). With a shield thickness of 0.2 cm, 12 cm high from the top of the PMT (whose length is 17 cm), the probability of a Compton induced event having more than two clusters is ∼1.2 $\times 10^{-4}$. With 0.4 cm thickness shielding, the probability goes down to the level of random coincidence. Considering the weight limitations and the mechanical difficulty of molding Pb wrapping and positioning the lead shield onto the crystal/PMT assembly, a Pb shield 0.5 cm thick and 6 cm long was selected as described in Section 4.1.4.

BIBLIOGRAPHY

BIBLIOGRAPHY

[1] D. Casadei and V. Bindi. The origin of cosmic ray electrons and positrons. *ApJ*, 612(1): 262–267, 2004.

[2] K. Koyama, R. Petre, E. V. Gotthelf, U. Hwang, M. Matsuura, M. Ozaki, and S. S. Holt. Evidence for shock acceleration of high-energy electrons in the supernova remnant SN1006. *Nature*, 378:255, November 1995.

[3] J. J. Beatty, A. Bhattacharyya, C. Bower, S. Coutu, M. A. DuVernois, S. McKee, S. A. Minnick, D. Müller, J. Musser, S. Nutter, A. W. Labrador, M. Schubnell, S. Swordy, G. Tarlé, and A. Tomasch. New measurement of the cosmic-ray positron fraction from 5 to 15GeV. *Phys. Rev. Lett.*, 93(24):241102–+, Dec 2004.

[4] AMS-01 Collaboration. Cosmic-ray positron fraction measurement from 1 to 30 GeV with AMS-01. *Physics Letters B*, 646:145–154, March 2007.

[5] O. Adriani, G. C. Barbarino, G. A. Bazilevskaya, R. Bellotti, M. Boezio, E. A. Bogomolov, L. Bonechi, M. Bongi, V. Bonvicini, S. Bottai, A. Bruno, F. Cafagna, D. Campana, P. Carlson, M. Casolino, G. Castellini, M. P. De Pascale, G. De Rosa, N. De Simone, V. Di Felice, A. M. Galper, L. Grishantseva, P. Hofverberg, S. V. Koldashov, S. Y. Krutkov, A. N. Kvashnin, A. Leonov, V. Malvezzi, L. Marcelli, W. Menn, V. V. Mikhailov, E. Mocchiutti, S. Orsi, G. Osteria, P. Papini, M. Pearce, P. Picozza, M. Ricci, S. B. Ricciarini, M. Simon, R. Sparvoli, P. Spillantini, Y. I. Stozhkov, A. Vacchi, E. Vannuccini, G. Vasilyev, S. A. Voronov, Y. T. Yurkin, G. Zampa, N. Zampa, and V. G. Zverev. Observation of an anomalous positron abundance in the cosmic radiation. *ArXiv e-prints*, October 2008.

[6] V. K. Balasubrahmanyan and S. A. Stephens. Earth's magnetic field as a radiator to detect cosmic ray electrons of energy greater than 10 to the 12^{th} eV. *Journal of Geophysical Research*, 88:7811–7822, October 1983.

[7] T. Gaisser. From the Knee to the Ankle, Theory and Experiment. In *Physics at the End of the Galactic Cosmic Ray Spectrum 2005 conference*, 2005.

[8] K. Greisen. End to the cosmic-ray spectrum? *Phys. Rev. Lett.*, 16(17):748–750, Apr 1966.

[9] G. T. Zatsepin and V. A. Kuz'min. Upper Limit of the Spectrum of Cosmic Rays. *Soviet Journal of Experimental and Theoretical Physics Letters*, 4:78–+, August 1966.

[10] R. U. Abbasi, T. Abu-Zayyad, M. Allen, J. F. Amman, G. Archbold, K. Belov, J. W. Belz, S. Y. Ben Zvi, D. R. Bergman, S. A. Blake, O. A. Brusova, G. W. Burt, C. Cannon, Z. Cao, B. C. Connolly, W. Deng, Y. Fedorova, C. B. Finley, R. C. Gray, W. F. Hanlon, C. M. Hoffman, M. H. Holzscheiter, G. Hughes, P. Hüntemeyer, B. F Jones, C. C. H. Jui, K. Kim, M. A. Kirn, E. C. Loh, M. M. Maestas, N. Manago, L. J. Marek, K. Martens, J. A. J. Matthews, J. N. Matthews, S. A. Moore, A. O'Neill, C. A. Painter, L. Perera, K. Reil, R. Riehle, M. Roberts, D. Rodriguez, N. Sasaki, S. R. Schnetzer, L. M. Scott, G. Sinnis, J. D. Smith, P. Sokolsky, C. Song, R. W. Springer, B. T. Stokes, S. B. Thomas, J. R. Thomas, G. B. Thomson, D. Tupa, S. Westerhoff, L. R. Wiencke, X. Zhang, and A. Zech High Resolution Fly's Eye Collaboration.

First observation of the greisen-zatsepin-kuzmin suppression. *Physical Review Letters*, 100(10): 101101, 2008.

[11] The Pierre Auger Collaboration. Correlation of the Highest-Energy Cosmic Rays with Nearby Extragalactic Objects. *Science*, 318(5852):938–943, 2007.

[12] A. M. Hillas. The Origin of Ultra-High-Energy Cosmic Rays. *Annual Review of Astronomy and Astrophysics*, 22:425–444, 1984.

[13] A. Bamba. A detailed spatial and spectral study of synchrotron x-rays from supernova remnants with chandra. *Ph.D. Thesis*, 2003.

[14] K. T. Gaisser. *Cosmic Rays and Particle Physics*. Cambridge University Press, Cambridge, 1990.

[15] J. A. Earl. Cloud-chamber observations of primary cosmic-ray electrons. *Phys. Rev. Lett.*, 6 (3):125–128, Feb 1961.

[16] F. Aharonian et al. The energy spectrum of cosmic-ray electrons at TeV energies. *Phys. Rev. Lett.*, 101:261104, 2008.

[17] K. Yoshida. High-energy cosmic-ray electrons in the Galaxy. *Advances in Space Research*, 42: 477–485, August 2008.

[18] M.S. Longair. *High energy astrophyiscs*, volume 2 Starts, the Galaxy and the interstellar medium. Cambridge University Press, Cambridge, 2004.

[19] T. Kobayashi, Y. Komori, K. Yoshida, and J. Nishimura. The most likely sources of high-energy cosmic-ray electrons in supernova remnants. *ApJ*, 601(1):340–351, 2004.

[20] F. C. Jones. Inverse compton scattering of cosmic-ray electrons. *Phys. Rev.*, 137(5B):B1306–B1311, Mar 1965.

[21] F. C. Jones. Calculated spectrum of inverse-compton-scattered photons. *Phys. Rev.*, 167(5): 1159–1169, Mar 1968.

[22] G. R. Blumenthal and R. J. Gould. Bremsstrahlung, Synchrotron Radiation, and Compton Scattering of High-Energy Electrons Traversing Dilute Gases. *Reviews of Modern Physics*, 42: 237–271, 1970.

[23] D.J. van der Walt and R Steenkamp. The inverse Compton scattering of cosmic ray electrons in the Galaxy. *Mon. Not. R. Astr. Soc.*, 251:142–147, 1991.

[24] A. Castellina and F. Donato. Diffusion coefficient and acceleration spectrum from direct measurements of charged cosmic ray nuclei. *Astroparticle Physics*, 24:146–159, September 2005.

[25] S. I. Syrovat-Skii. The Distribution of Relativistic Electrons in the Galaxy and the Spectrum of Synchrotron Radio Emission. *Soviet Astronomy*, 3:22–+, February 1959.

[26] C. Y. Mao and C. S. Shen. Anisotropy and diffusion of cosmic ray electrons. *Chinese Journal of Physics*, 10:16–28, 1972.

[27] M. Hareyama Y. Hirakawa M. Ichimura N. Inoue E. Kamioka T. Kobayashi V.V. Kopenkin S. Kuramata A.K. Managadze H. Matsutani N.P. Misnikova R.A. Mukhamedshin S. Nagasawa R. Nakano M. Namiki H. Nanjo S.N. Nazarov S. Ohta H. Ohtomo D.S. Oshuev P.A. Publichenko I.V. Rakobolskaya T.M. Roganova G.P. Sazhina H. Semba T. Shibata D. Shuto H. Sugimoto L.G. Sveshnikova R. Tanaka N. Yajima T. Yamagami I.V. Yashin E.A.Zamchalova G.T. Zatsepin I.S. Zayarnaya M. Furukawa, V.I. Galkin. Primary Heavy Components Spectra and 2-yr/1-yr Ratio Observed by RUNJOB Collaboration. *Proceedings of ICRC 2003*, 2003.

[28] V.I. Galkin M. Hareyama Y. Hirakawa Y. Horiuchi N. Inoue E. Kamioka T. Kobayashi V.V.Kopenkin S. Kuramata A.K. Managadze H. Matsutani N.P. Misnikova R.A. Mukhamedshin S. Nagasawa R. Nakano M. Namiki M. Nakazawa H. Nanjo S.N. Nazarov S. Ohta H. Ohtomo V.I.Osedlo D.S.Oshuev P.A. Publichenko I.V.Rakobolskaya T.M. Roganova C. Saito G.P.Sazhina H. Semba T.Shibata D. Shuto H.Sugimoto R. Suzuki L.G.Sveshnikova V.M. Taran N.Yajima T. Yamagami I.V. Yashin E.A.Zamchalova G.T. Zatsepin I.S.Zayarnaya M. Ichimura, V.A. Derbina. Heavy component spectra and secondary to primary ratios obtained by RUNJOB experiment. *Proceedings of ICRC 2005*, 2005.

[29] M. A. Malkov and L. O'C Drury. Nonlinear theory of diffusive acceleration of particles by shock waves . *Reports on Progress in Physics*, 64:429–481, April 2001.

[30] R. D. Blandford and J. P. Ostriker. Particle acceleration by astrophysical shocks. *ApJ*, 221: L29–L32, April 1978.

[31] A. R. Bell. The acceleration of cosmic rays in shock fronts. I. *Mon. Not. R. astr. Soc.*, 182: 147–156, January 1978.

[32] J. Skilling. Cosmic ray streaming. II - Effect of particles on Alfven waves. *Mon. Not. R. astr. Soc.*, 173:245–254, November 1975.

[33] T. Jones. Cosmic Particle Acceleration: Basic Issues. In C.-M. Ko, editor, *The 7th Taipei Astrophysics Workshop on Cosmic Rays in the Universe*, volume 241 of *Astronomical Society of the Pacific Conference Series*, pages 239–+, January 2001.

[34] F. C. Jones and D. C. Ellison. The plasma physics of shock acceleration. *Space Science Reviews*, 58:259–346, December 1991.

[35] J. G. Kirk and P. Duffy. Particle acceleration and relativistic shocks. *Journal of Physics G Nuclear Physics*, 25:165–+, August 1999.

[36] J. G. Kirk, A. W. Guthmann, Y. A. Gallant, and A. Achterberg. Particle Acceleration at Ultrarelativistic Shocks: An Eigenfunction Method. *ApJ*, 542:235–242, October 2000.

[37] L. O. Drury and J. H. Voelk. Hydromagnetic shock structure in the presence of cosmic rays. *ApJ*, 248:344–351, August 1981.

[38] E. G. Berezhko and D. C. Ellison. A Simple Model of Nonlinear Diffusive Shock Acceleration. *ApJ*, 526:385–399, November 1999.

[39] M. Zhang. A path integral approach to the theory of heliospheric cosmic-ray modulation. *ApJ*, 510(2):715–725, 1999.

[40] V.S. Berezinskiĭ, S.V. Bulanov, V.A. Dogiel, V.L. Ginzburg, and V.S. Ptuskin. *Astrophysics of Cosmic Rays.* Elsevier Science, 1990.

[41] C. S. Shen. Pulsars and Very High-Energy Cosmic-Ray Electrons. *ApJ*, 162:L181+, December 1970.

[42] A. M. Atoyan, F. A. Aharonian, and H. J. Völk. Electrons and positrons in the galactic cosmic rays. *Phys. Rev. D*, 52(6):3265–3275, Sep 1995.

[43] J.D. Jackson. *Classical Electrodynamics.* John Wiley & Sons, Inc, New York, 1998.

[44] Geant4. *Physics Reference Manual*, Version Geant4 9.0, June 2007.

[45] H. Hofer and M. Pohl. Charge determination of high energy electrons and nuclei by synchrotron radiation with AMS. *Nucl.Instrum.Meth.A*, 416:59, 1998.

[46] A.W. Strong and I.V. Moskalenko. Galprop. URL `http://galprop.stanford.edu/web_galprop/galprop_home.html`.

[47] M.S. Longair. *High energy astrophyiscs*, volume 1 Particles, photons and their detection. Cambridge University Press, Cambridge, 2004.

[48] R. Schlickeiser. *Cosmic Ray Astrophysics.* Springer-Verlag Berlin Heidelbere, 2002.

[49] R. Blandford and D. Eichler. Particle acceleration at astrophysical shocks: A theory of cosmic ray origin. *Phys. Rep.*, 154:1–75, 1987.

[50] S. E. Derenzo and W. W. Moses. Experimental efforts and results in finding new heavy scintillators. In *Presented at the Crystal 2000 International Workshop on Heavy Scintillators for Scientific and Industrial Applications, Chamonix, France, 22-26 Sep. 1992*, pages 22–26, September 1992.

[51] G. F. Knoll. *Radiation Detection and Measurement.* John Wiley & Sonds, Inc., New Jersey, 2000.

[52] Y. Yoshizawa, H. Yamaguchi, N. Ooishi, H. Suzuki, and S. Suzuki. The study of countrate stability of photomultiplier tube withdifferent types of voltage dividers. *Nuclear Science, IEEE Transactions*, 43:1656–1660, 1996.

[53] D.N. McKinsey, C.R. Brome, J.S. Butterworth, P.R. Huffman, J.M. Doyle, R. Golub, K. Habicht, and S.K. Lamoreaux. Fluorescence efficiencies of thin scintillating films in the extreme ultraviolet spectral region. *Nuclear Instruments and Methods in Physics Research Section B: Beam Interactions with Materials and Atoms*, 132:351–358(8), November 1997.

[54] E. Lorenz, R. Mirzoyan, F. Steinbuegl, A. Chilingarian, D. Ferenc, and S. Borngrebe. Deconvolution of Energy Spectra in the ATIC Experiment. *Proceedings of ICRC 2001*, 2001.

[55] P. Kozma and Č. Hradečný. Diphenylstilbene as a wavelength shifter. *Nuclear Instruments and Methods in Physics Research A*, 254:639–639, March 1987.

[56] V. Schoenfelder, U. Graser, and J. Daugherty. Diffuse cosmic and atmospheric MeV gamma radiation from balloon observations. *ApJ*, 217:306–319, October 1977.

[57] S. E. Boggs, R. P. Lin, S. Slassi-Sennou, W. Coburn, and R. M. Pelling. Diffuse Galactic Soft Gamma-Ray Emission. *ApJ*, 544:320–329, November 2000.

[58] L. Bouchet, E. Jourdain, J. P. Roques, A. Strong, R. Diehl, F. Lebrun, and R. Terrier. INTEGRAL SPI All-Sky View in Soft Gamma Rays: Study of Point Source and Galactic Diffuse Emissions. *ArXiv e-prints*, 801, January 2008.

[59] T. Mizuno, Y. Fukazawa, K. Hirano, H. Mizushima, S. Ogata, T. Handa, T. Kamae, T. Lindner, M. Ozaki, M. Sjogren, P. Valtersson, and H. Kelly. Geant4 based cosmic-ray background simulator for balloon experiments. *Nuclear Science Symposium Conference Record, 2001 IEEE*, 1:442–446 vol.1, 4-10 Nov. 2001. ISSN 1082-3654.

[60] P. Sreekumar, D. L. Bertsch, B. L. Dingus, J. A. Esposito, C. E. Fichtel, R. C. Hartman, S. D. Hunter, G. Kanbach, D. A. Kniffen, Y. C. Lin, H. A. Mayer-Hasselwander, P. F. Michelson, C. von Montigny, A. Muecke, R. Mukherjee, P. L. Nolan, M. Pohl, O. Reimer, E. Schneid, J. G. Stacy, F. W. Stecker, D. J. Thompson, and T. D. Willis. EGRET Observations of the Extragalactic Gamma-Ray Emission. *ApJ*, 494:523–+, February 1998.

[61] V. Schoenfelder, F. Graml, and F.-P. Penningsfeld. The vertical component of 1-20 MeV gamma rays at balloon altitudes. *ApJ*, 240:350–362, August 1980.

[62] J. C. Ling. A semiempirical model for atmospheric γ rays from 0.3 to 10 MeV λ at = 40. *Journal of Geophysical Research*, 80:3241–3252, October 1975.

[63] W. L. Imhof, G. H. Nakano, and J. B. Reagan. High-resolution measurements of atmospheric gamma rays from a satellite. *J. Geophys. Res.*, 81(16):2835–2843, 1976.

[64] A. J. Dean, L. Fan, K. Byard, A. Goldwurm, and C. J. Hall. The gamma-ray emissivity of the earth's atmosphere. *Astronomy and Astrophysics*, 219:358–361, July 1989.

[65] P. B. Roe. *Probability and statistics in experimental physics.* Springer-Verlag, New York, 1992.

[66] A. N. Tikhonov and V. Y. Arsenin. *Solutions of Ill-Posed Problems.* John Wiley, New York, 1977.

[67] K. E. Batkov, A. Panov, J.H. Adams Jr., H.S. Ahn, G. Bashindzhangyan, J. Chang, M. Christl, A. Fazely, O. Ganel, R. Gunasingha, T.G. Guzik, J. Isbert, K.C. Kim, E.N. Kouznetsov, M. Panasyuk, W.K.H. Schmidt, E.S. Seo, N. Sokolskaya, J.P. Wefel, J. Wu, and V. Zatsepin. Deconvolution of Energy Spectra in the ATIC Experiment. *Proceedings of the 29th International Cosmic Ray Conference, Pune*, 3:353–356, 2005.

[68] J. D. Sullivan. Geometrical factor and directional response of single and multi-element particle telescopes. *Nuclear Instruments and Methods*, 95:5–11, 1971.

[69] K. Alanko-Huotari G. A. Kovaltsov Usoskin, I. G. and K. Mursula. Heliospheric modulation of cosmic rays: Monthly reconstruction for 1952-2004. *Journal of Geophysical Research*, 110: A12108, 2005.

[70] M. L. Goldstein, S. A. Morris, and G. G. Yen. Problems with fitting to the power-law distribution. *European Physical Journal B*, 41:255–258, September 2004.

[71] S.B. Ricciarini. Development of tracking system acquisition electronics and analysis of first data for the pamela experiment. *Ph.D. Thesis*, 2005.

[72] S. W. Barwick, J. J. Beatty, C. R. Bower, C. J. Chaput, S. Coutu, G. A. de Nolfo, M. A. Duvernois, D. Ellithorpe, D. Ficenec, J. Knapp, D. M. Lowder, S. McKee, D. Mueller, J. A. Musser, S. L. Nutter, E. Schneider, S. P. Swordy, G. Tarle, A. D. Tomasch, and E. Torbet. The Energy Spectra and Relative Abundances of Electrons and Positrons in the Galactic Cosmic Radiation. *ApJ*, 498:779–+, May 1998.

[73] J. A. van Allen and A. V. Gangnes. The cosmic-ray intensity above the atmosphere at the geomagnetic equator. *Phys. Rev.*, 78(1):50–52, Apr 1950.